



Quantum Chemistry in Nanoscale Environments: Insights on Surface-Enhanced Raman Scattering and Organic Photovoltaics

Citation

Olivares-Amaya, Roberto. 2012. Quantum Chemistry in Nanoscale Environments: Insights on Surface-Enhanced Raman Scattering and Organic Photovoltaics. Doctoral dissertation, Harvard University.

Permanent link

<http://nrs.harvard.edu/urn-3:HUL.InstRepos:9453699>

Terms of Use

This article was downloaded from Harvard University's DASH repository, and is made available under the terms and conditions applicable to Other Posted Material, as set forth at <http://nrs.harvard.edu/urn-3:HUL.InstRepos:dash.current.terms-of-use#LAA>

Share Your Story

The Harvard community has made this article openly available.
Please share how this access benefits you. [Submit a story](#).

[Accessibility](#)

© 2012 - Roberto Olivares-Amaya
All rights reserved.

Quantum Chemistry in Nanoscale Environments: Insights on Surface-Enhanced Raman Scattering and Organic Photovoltaics

Abstract

The understanding of molecular effects in nanoscale environments is becoming increasingly relevant for various emerging fields. These include spectroscopy for molecular identification as well as in finding molecules for energy harvesting. Theoretical quantum chemistry has been increasingly useful to address these phenomena to yield an understanding of these effects.

In the first part of this dissertation, we study the chemical effect of surface-enhanced Raman scattering (SERS). We use quantum chemistry simulations to study the metal–molecule interactions present in these systems. We find that the excitations that provide a chemical enhancement contain a mixed contribution from the metal and the molecule. Moreover, using atomistic studies we propose an additional source of enhancement, where a transition metal dopant surface could provide an additional enhancement. We also develop methods to study the electrostatic effects of molecules in metallic environments. We study the importance of image-charge effects, as well as field-bias to molecules interacting with perfect conductors. The atomistic modeling and the electrostatic approximation enable us to study the effects of the metal interacting with the molecule in a complementary fashion, which provides a better understanding of the complex effects present in SERS.

In the second part of this dissertation, we present the Harvard Clean Energy Project, a high-throughput approach for a large-scale computational screening and design of organic photovoltaic materials. We create molecular libraries to search for candidate structures and use quantum chemistry, machine learning and cheminformatics methods to characterize these systems and find structure-property relations. The scale of this study requires an equally large computational resource. We rely on distributed volunteer computing to obtain these properties.

In the third part of this dissertation we present our work related to the acceleration of electronic structure methods using graphics processing units. This hardware represents a change of paradigm with respect to the typical CPU device architectures. We accelerate the resolution-of-the-identity Møller-Plesset second-order perturbation theory algorithm using graphics cards. We also provide detailed tools to address memory and single-precision issues that these cards often present.

Contents

Abstract	iii
Table of contents	iv
Citations to previously published work	vii
Acknowledgments	ix
1 Introduction	1
I Chemical effects in surface-enhanced Raman scattering	29
2 On the chemical bonding effects in the Raman response: Benzenethiol adsorbed on silver clusters	30
2.1 Introduction	30
2.2 Computational details	33
2.3 Results and discussion	34
2.4 Conclusions	48
2.5 Appendix	50
3 Can Mixed-Metal Surfaces Provide an Additional Enhancement to SERS?	56
3.1 Introduction	56
3.2 Experimental methods	58
3.3 Theoretical methods	59
3.4 Results	60
3.5 Conclusions	67
3.6 Appendix	68
4 Anion stabilization in electrostatic environments	70
4.1 Introduction	70
4.2 Results	71
4.3 Discussion	78
4.4 Conclusions	79
4.5 Appendix	80
5 Electronic structure calculations in arbitrary electrostatic environments	95
5.1 Introduction	95
5.2 Theory and implementation	98

5.3	Benchmarks and applications	108
5.4	Conclusion	118
5.5	Appendix: A variational scheme for electrostatic environment effects	119
II The Harvard Clean Energy Project		121
6	Large-scale computational screening and design of organic photovoltaic materials	122
6.1	Introduction	122
6.2	The Harvard Clean Energy Project	123
6.3	Conclusions	133
7	Accelerated computational discovery of organic photovoltaic materials by means of cheminformatics	134
7.1	Introduction	134
7.2	Bulk-heterojunction solar cells	135
7.3	Organic photovoltaic materials	137
7.4	Cheminformatics modelling	142
7.5	Discussion and conclusions	151
7.6	Appendix	152
III Accelerating quantum chemistry algorithms using graphics processing units		167
8	Accelerating resolution-of-the-identity second order Møller-Plesset calculations with graphical processing units	168
8.1	Introduction	168
8.2	General-purpose computing on graphical processing units	170
8.3	Computational setup and matrix multiplication comparison	171
8.4	Speedups of RI-MP2 calculations on a series of alkanes	173
8.5	Conclusions	177
9	Accelerating correlated quantum chemistry calculations using graphical processing units and a mixed-precision matrix multiplication library	180
9.1	Introduction	180
9.2	GPU acceleration of RI-MP2	182
9.3	GPU acceleration of GEMM	184
9.4	MGEMM benchmarks	186
9.5	RI-MP2 acceleration benchmarks	194
9.6	Conclusion	197

10 Accelerating correlated quantum chemistry calculations using graphical processing units	199
10.1 Introduction	199
10.2 Quantum chemistry theory	201
10.3 GPU acceleration of GEMM	204
10.4 MGEMM benchmarks	208
10.5 RI-MP2 acceleration benchmarks	213
10.6 Conclusion	215
IV Conclusions and future directions	217
11 Conclusions and future directions	218
A On the electron localization function	221
A.1 Motivation	221
A.2 Curvature	221
A.3 The Fermi hole and its curvature	223
A.4 Laplacian of the pair density matrix	224
A.5 The electron localization function	226
A.6 Solution of a spherically-averaged Taylor expansion	227
B Resolution of the identity approximation	228
References	230

Citations to previously published work

Chapters 2, and 4–10 have, apart from minor modifications, appeared as the following publications:

“On the chemical bonding effects in the Raman response: Benzenethiol adsorbed on silver clusters,” Semion Saikin, Roberto Olivares-Amaya, Dmitriy Rappoport, Michael Stopa and Alán Aspuru-Guzik, *Phys. Chem. Chem. Phys.* **11**, 9401 (2009).

“Anion stabilization in electrostatic environments”, Roberto Olivares-Amaya, Michael Stopa, Xavier Andrade, Mark A. Watson, and Alán Aspuru-Guzik, *J. Phys. Chem. Lett.* **2**, 682 (2011).

“Electronic structure calculations in arbitrary electrostatic environments,” Mark A. Watson, Dmitriy Rappoport, Elizabeth M.Y. Lee, Roberto Olivares-Amaya and Alán Aspuru-Guzik, *J. Chem. Phys.* **136**, 024101 (2012).

“The Harvard Clean Energy Project: Large-scale Computational Screening and Design of Organic Photovoltaics on the World Community Grid,” Johannes Hachmann, Roberto Olivares-Amaya, Sule Atahan-Evrenk, Carlos Amador-Bedolla, Roel Sanchez-Carrera, Aryeh Gold-Parker, Leslie Vogt, Anna Brockway, and Alán Aspuru-Guzik. *J. Phys. Chem. Lett.* **2**, 2241 (2011).

“Accelerated computational discovery of high-performance materials for organic photovoltaics by means of cheminformatics,” Roberto Olivares-Amaya, Carlos Amador-Bedolla, Johannes Hachmann, Sule Atahan-Evrenk, Roel S. Sanchez-Carrera, Leslie Vogt, and Alán Aspuru-Guzik. *Energy Environ. Sci.* **4**, 4849 (2011).

“Accelerating resolution-of-the-identity second-order Møller-Plesset calculations using graphical processing units,” Leslie Vogt*, Roberto Olivares-Amaya*, Sean Kermes, Yihan Shao, Carlos Amador-Bedolla, and Alán Aspuru-Guzik, *J. Phys. Chem. A* **112**, 2049 (2008).

“Accelerating correlated quantum chemistry calculations using graphical processing units and a mixed-precision matrix multiplication library,” Roberto Olivares-Amaya*, Mark A. Watson*, Richard Edgar, Leslie Vogt, Yihan Shao and Alán Aspuru-Guzik, *J. Chem. Theory Comput.* **6**, 135 (2010).

“Accelerating correlated quantum chemistry calculations using graphical processing units,” Mark A. Watson, Roberto Olivares-Amaya, Richard Edgar and Alán Aspuru-Guzik, *Comput. Sci. Eng.* **12**, 40 (2010).

Chapter 4 is based on a submitted manuscript.

“Can mixed-metal surfaces provide an additional enhancement to SERS?” Roberto Olivares-Amaya , Dmitrij Rappoport, Philip Munoz, Paul Peng, Eric Mazur and Alán Aspuru-Guzik. **Submitted** (2012).

Other work I was involved in but not explicitly included in the thesis is the article

“Theory of Excitation Broadening using Time-Dependent Density Functional Theory for Open Quantum Systems,” David G. Tempel, Mark A. Watson, Roberto Olivares-Amaya and Alán Aspuru-Guzik, *J. Chem. Phys.* **134**, 074116 (2011).

Acknowledgments

I want to begin by acknowledging the guidance, motivation, friendship of my advisor, Prof. Alán Aspuru-Guzik, as well as his ability to create such an amazing research environment. This seems to be sustained both by challenging us to undertake extremely interesting scientific ideas, but also by his contagious enthusiasm. I thank Profs. Eric J. Heller and Xiaoliang Sunney Xie for taking part in my graduate advising committee and challenging me to answer the difficult questions that often seemed out of reach.

Such a collaborative environment has led me to work directly with many scientists in very diverse projects. These interactions have been the most enriching and empowering during my Ph. D. These include: Adrián Jinich, Aidan Daly, David Tempel, Dmitriy Rappoport, James Whitfield, Jimmy Zhu, Joel Yuen-Zhou, Joey Goodknight, Johannes Hachmann, Leslie Vogt, Mark Watson, Mike Stopa, Philip Munoz, Roel Sánchez-Carrera, Sean Kermes, Semion Saikin, Sergio Boixo, Şule Atahan-Evrenk, Suleyman Er, Supriya Shrestha, Xavier Andrade, and Yihan Shao.

Scientific discussions of seemingly unrelated topics are a characteristic of the group, though many interesting ideas emerged. I owe many illuminating conversations to: Alejandro Perdomo, Ali Najmaie, César Rodríguez, Ivan Kassal, Jacob Krich, Jacob Sanders, Jarrod McClean, John Parkhill, Man-Hong Yung, Patrick Rebentrost, Ryan Babbush, Salvador Venegas-Andraca, Sangwoo Shim, Sarah Mostame, and Stéphanie Valleau.

I extend my appreciation to Dr. Nancy Dickson and Profs. Bill Clark and Venky Narayanamurti for teaching me the importance of use-inspired basic research. Alex, Andrés, Edgar, Elisita, Julián, Luisa, Mauricio, Ricardo, and Roger, have offered me countless support during my time in Cambridge. For most of my life, Chino, Mónica and Turi have provided me with friendship and brotherhood in the best of times and the worst of times.

I am grateful to my previous advisors, Profs. Carlos Amador-Bedolla and William A. Lester, Jr. for providing me the opportunity to begin the path of a theoretical chemist. I hope I can now refer to Prof. Amador as Carlos. My friends at UNAM Diego, Fernanda “Hija”, Armando and Borau have unquestionably enriched my path; especially Diego and our countless conversations. Finally, I am grateful for the guidance of teachers and friends such as Susana Aburto and Agustín Tello.

My infinite appreciation goes out to my family, though words cannot describe such thankfulness. Their support at all times has been unquestioned. I honor the memory of my “abuelos” and cherish the times with my “abuelas”. My brother, Diego, is the bigger brother of the two and I look up to him. My father and mother will always have my admiration and love.

A mi familia

Chapter 1

Introduction

One of the main areas of the rapidly emerging field of nanotechnology is the development of plasmonic materials [43, 89, 323]. When interacting with visible light, these materials yield a plasmon resonance; a longitudinal excitation of the free electrons. This effect gives way to an enhancement of the local electric field. The enhancement can be exploited to identify analytes attached to these substrates, as is done in surface-enhanced Raman scattering (SERS), whether they are molecules or more complex systems [359, 580].

The study of these systems is multiscale in nature. Some of the plasmon properties can be understood through classical electrodynamics, while others, such as the dynamical effects of the molecule, explicitly need to be described through quantum mechanics. Quantum theory has been applied to chemical phenomena since its initial developments [131]. Indeed, trying to reduce the complexity of the equations to study larger systems has been one of the main objectives of electronic structure quantum chemistry [222, 405].

An additional difficulty arises when one considers that molecules interact with surrounding media. Solving the Schrödinger equation for so many degrees of freedom becomes not only unfeasible but undesirable, since it is likely that only few of these will contribute significantly to the understanding of the system. Moreover, system-environment interactions present phenomena of relaxation and dephasing, which are not easy to calculate [79, 518, 602]. Though many of these approximations have been phenomenological in nature, atomistic approaches have been proposed and tested to consider the environment degrees of freedom classically, as in quantum-mechanical and molecular mechanical models (QM/MM) [148, 476], or in other cases, considering the environment as a continuum [265, 532, 565].

At the molecular level, quantum chemistry methods must yield an accurate representation of the electronic structure and its properties. To this effect, post-Hartree-Fock (HF) methods and density-functional theory (DFT) based methodologies have been developed to increase the accuracy of the calculations [214, 222]. As these theories are able to obtain

more accurate results, the scaling factor begins to scale to higher polynomial order.

The advent of more powerful supercomputers has partially enabled a workaround to calculating molecules of greater size. These architectures are oftentimes difficult to access and have come at a much larger, and somewhat prohibitive cost. Recent work has been focused on taking advantage of heterogeneous and intrinsically parallel hardware architectures such as graphics processing units (GPUs) and field-programmable gate arrays [84, 179, 411]. In contrast to supercomputers, GPUs have the advantage that the development of this hardware is driven by videogame users desiring better graphics. The economies of scale have also helped that price of these devices remain low. Although these tools were not initially intended for scientific computing, they have provided the ability to parallelize simple, but cost-intensive calculations such as linear algebra operations, prevalent in quantum chemistry.

The development of heterogeneous architectures has increased the performance of calculations for large systems across all fields. Meanwhile, the concept of distributed computing [66, 108, 185] has allowed for an exponential growth in available computer time for scientific computing. Under this framework, volunteers donate their spare computer time for scientific applications. Distributed computing has grown to allow vastly different scientific areas to perform computational research.

One area where distributed computing can be exploited is in the field of high-throughput screening of chemical compounds. The field of drug discovery has been increasingly dependent on designing leads as an initial step in the search of new drug candidates [141, 256]. In recent years, materials discovery research has become increasingly important [242, 506], and the impact on the search for new ceramics, batteries and energy-materials will begin to resonate as *in silico* predictions begin to be translated into successes at the workbench [491]. These projects are data-intensive by nature and have been enabled by the exponential increase of computational resources, whether they come principally from supercomputers or available heterogeneous architectures.

The development of organic-based solar cell materials [74, 217] becomes a prime application where high-throughput screening and data-intensive techniques can be exploited. It is widely known that solar energy could account for world's energy needs [303]. The difficulty is that harnessing the sun's resources is by no means a simple undertaking. Silicon and other inorganic-based solar cells have proven successful, and while prices are decreasing, they are still too costly for extensive use [152]. Recently, conjugated polymers mixed with fullerene-based molecules have shown promise to provide low-cost mass-production of photovoltaics [509]. Therefore, with the appropriate analytical and computational tools, the search for solar cell materials can become a high-throughput discovery endeavor for molecules with ideal characteristics.

Despite the wide scope of the work presented in this dissertation, there is an intrinsic connection between developing quantum chemistry algorithms, and applying these tools: whether they involve multiscale phenomena, or the high-throughput screening of molecules. This work is divided into three parts to account for the different developments. In Part I, we develop the multi-scale approaches to understand the chemical effects in SERS. In Part II, we present the Harvard Clean Energy Project (CEP), which is the high-throughput approach to finding organic-photovoltaic (OPV) materials. In Part III, we explain the methods used to accelerate quantum chemistry algorithms using graphics processing units. In Part IV, we summarize our conclusions and detail future directions.

Part I: Chemical effects in surface-enhanced Raman scattering

The Raman process refers to the inelastic dispersion present as a laser scatters from a substance. Specifically, when a monochromatic radiation source of frequency ω_I , such as a laser pulse, is incident on a system, some scattering of radiation occurs. When the scattered radiation is studied, besides the frequency ω_I (known as Rayleigh scattering), there will be pairs of frequencies $\omega_I \pm \omega_S$. The latter corresponds to the inelastic dispersion process known as Raman scattering [315, 583].

The Raman lines have their origin in an exchange of energy between photons and the molecular system. Therefore, $\hbar\omega_S$ corresponds to energies in the range of rotational, vibrational and electronic levels. The vibrational regime roughly corresponds to the frequency range of 400–4000 cm^{-1} . This reflects that incoming energy is being transferred to the vibrational modes of the molecule. Molecular spectra at this shifted frequency (known as the Stokes-shifted frequencies) have been effective to elucidate and identify diverse molecules, just as is the case for vibrational spectroscopy. As Raman scattering is intrinsically a second order process, its cross-section is orders of magnitude smaller compared to other spectroscopies at the same incident frequency such as fluorescence. This has led to limited applications beyond the research laboratory.

The discovery of the surface-enhancement of the Raman signal took place over 35 years ago [150, 244]. SERS is considered to be an ideal analytical technique since it reveals information about the molecule’s vibrational modes and its intensity under ideal conditions can identify single-molecules [270, 376]. Its instrumentation is relatively simple compared to other techniques such as high-performance liquid chromatography and is potentially portable. Despite its promise, SERS has not yet been able to become a turnkey analytical tool, as we will explain below.

SERS sensors could be useful to monitor water pollution in the form of pesticides, fertilizers and metal ions [15, 423]. As we expect population to increase to 9 billion by

2050, and developing countries continue their growth, pesticide use is expected to have a two-fold increase by 2050. This will come hand-in-hand with increases in the use of fertilizers to grow crops [528]. An excess in these two families of chemicals will certainly reduce the ecosystems' capacity to deliver goods and services if their use does not grow sustainably. Although there are available analytical techniques to probe for substances in the *part-per-billion* regime, these are often expensive or rely on heavy equipment. SERS, whether at the purification plant or on the field could be an ideal tool for monitoring these pollutants.

One of the main reasons SERS has not become widely available is due to the irregularities in the enhancement factor. This is brought about by the difficulty in obtaining reliable substrates, along with the lack of control of adsorption of molecules in the substrates. Current development in nanofabrication have given SERS the potential to have substrates that relay a homogeneous response. However, the diversity of molecules that can interact with metal substrates makes having a uniformly strong signal for all systems difficult. Controlling this effect proves to be a great challenge at the experimental scale, due to the (sub-)nanometer size of these phenomena. It is the role of quantum chemistry to aid in the understanding of how the molecular vibrational, electronic states and binding are affected in the metal environment [43, 336], and to bring forth new ideas for the development of SERS.

In the case of SERS, the enhanced electric field, provided by the plasmon excitation of the nanoparticles, is the main contributor to the enhancement of the Raman signal. The electric field in SERS is proportional to the product of the incoming electric field, E_0 , the enhancement factor at the incident frequency, $g(\omega)$, the enhancement factor at the Stokes-shifted frequency, $g'(\omega')$, and an appropriate combination of the components of the Raman tensor, α_R [362],

$$E_{\text{SERS}} \propto \alpha_R g(\omega) g'(\omega') E_0. \quad (1.1)$$

In turn, the SERS intensity is the square of the field:

$$I_{\text{SERS}} \propto |\alpha_R|^2 |g(\omega) g'(\omega')|^2 I_0. \quad (1.2)$$

The enhancement factors, $g(\omega)$ and $g'(\omega')$, have been understood by classical electrodynamics and account for about 5–6 orders of magnitude of the enhancement [246, 455]. Through nanostructured methods, it is even possible to tune the substrate to an appropriate incident and Stokes-shifted frequency [104, 106]. Since Raman scattering is a quantum effect [223, 297, 315], one either needs to account for the quantum effects of an extended system coupled with a molecular (*i.e.*, localized) system, or consider a multi-scale model where the metal can be appropriately simulated as an environment. In Chapters 4–5 we consider an electrostatic approximation of the environment, where the metal is considered

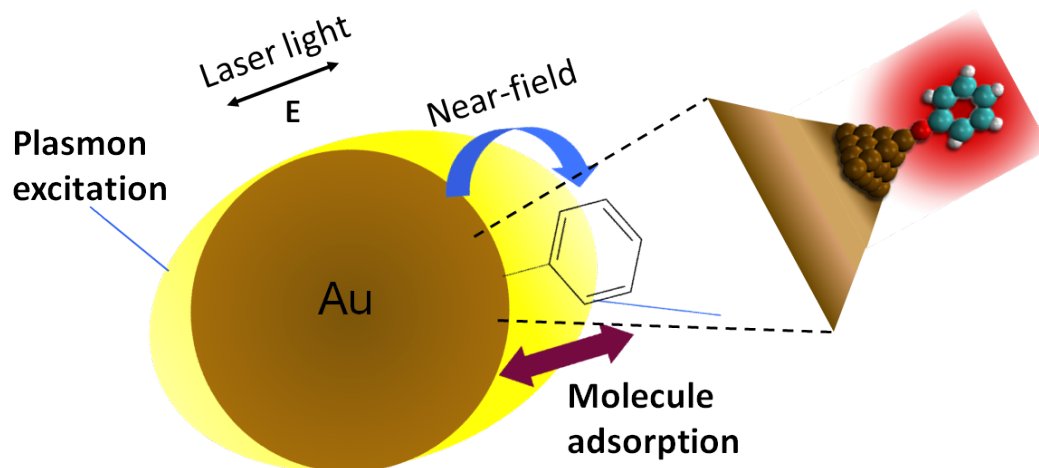


Figure 1.1: The plasmonic excitation causes a collective oscillation of electrons in the metal nanoparticle. In turn, this induces a strong near-field at the molecule's position. The right hand side depicts the approach used to simulate the chemical effects in SERS. We assume the chemical effect is localized around the molecular absorption site of the chemical bond between metal atoms and the analyte molecule.

as a perfect conductor. We are able to study image-charge effects that are present when a molecule (or any set of particles) interacts with metal surfaces.

The term given by the components of the Raman tensor, α_R , is dependent upon the Kramers-Heisenberg-Dirac polarizability tensor and the normal mode components [12, 297]. The Raman tensor is also modified by the presence of the metal. It is known to contribute around 1–3 orders of magnitude to the Raman enhancement, so it cannot be altogether ignored. In this case, the environment surrounding the molecule, including parts of the metal atom becomes increasingly important. In Chapters 2–3 we consider the study of chemical effects of SERS by doing an atomistic modeling of metal molecule interactions.

Chapters 2–3: Atomistic modeling of metal–molecule interactions

Since SERS essentially relies on substrate-analyte interaction, the chemical enhancement must also be considered when studying this phenomenon, though it has often been overlooked [360]. After all, although the chemical effect is dwarfed by the electromagnetic one, there can be fluctuations in the order of 100–1000 with respect to different molecules. This is by no means a small quantity if one desires to control the enhancement to provide for reliable instrumentation across different analytes.

The SERS system is represented in Fig. 1.1. A surface plasmon excitation takes place when light interacts with a substrate composed of a coinage metal, *e.g.*, gold or silver. This

resonance causes an increase in the local electric field due to the longitudinal excitation of the electrons. Molecules attached to the surface of these nanostructures will respond to the enhanced field. The chemical effect, on the other hand, takes place in the vicinity of the analyte [455]. It is related to the formation of chemical bonds between the molecule and the surface metal atoms [246, 248, 358, 398, 399, 456]. We therefore restrict our simulations to the metal atoms to those around the molecule, to study this enhancement contribution. Although this approximation does not allow us to study the electromagnetic effect (metal clusters cannot sustain plasmons), it allows us to grasp chemical effects present in the metal–molecule interactions [11, 246, 616].

In Chapter 2, we study the chemical bonding effects in the Raman response of benzenethiol bound to silver clusters. We choose benzenethiol since it readily binds to silver to form a thiolate-Ag bond. We use the time-dependent density functional formalism (TDDFT) [432, 453] to explore both the change in the Raman response, and the electronic excitations of the mixed molecule-cluster system.

We use a set of Ag_n clusters of different sizes ranging from $n=6$ –11 to explore the relationship between the binding effects and the time-dependent properties. We find that the binding geometry of benzenethiolate is important, as there are several differences between on-top and a bridging motif. More importantly, benzenethiol does not present electronic transitions in the range of visible excitation energies between 1.6–3.0 eV (400–750 nm) used for Raman analysis. When this molecule is attached to a cluster, electronic excitations appear in this spectral region. The change of electronic structure leads to changes in the polarizability, and therefore we can expect also a modification to the Raman tensor.

For each of these systems, it is possible to generate a Raman excitation profile (REP), where we sweep the incident frequency through a certain region and follow the Raman signal of specific Raman modes [127, 614]. By exploring over the 1.6–3.0 eV region, one is able to observe an additional enhancement of the order of 100. Although the Raman scattering calculations took place in the non-resonant regime, we are able to observe, through transition density calculations, that this enhancement comes from resonant transitions of the mixed metal–molecule states.

This work motivated the study of the potential of surface-enhanced coherent anti-Stokes Raman scattering in clusters [404], and also the development of a simplified sum-over-states approach for predicting resonance Raman spectra [433]. Moreover, a collaboration between theory and experiment showed the effective separation between the electromagnetic and chemical contributions of SERS when using a highly nanostructured plasmonic substrate [455].

Chapter 2 provided us with an understanding of the chemical enhancement using a molecule that is chemisorbed to the metal by exploring the cluster space, and different

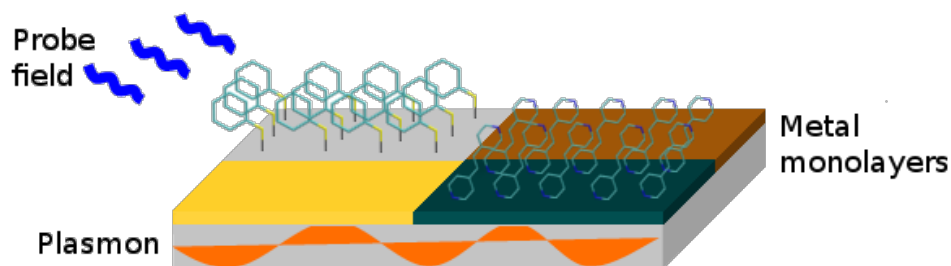


Figure 1.2: Image depicting different *roughened* surfaces and the binding of two molecules (benzenethiol on silver, upper left and BPE on nickel, lower right). The other surfaces are platinum (upper right) and gold (lower left), which show favorable interactions with other analytes.

incident frequencies. More importantly, it showed that mixed metal–molecule excitations are the main contributors to the enhancement. However, there will be a host of molecules that will not bind favorably to silver or gold, but would to another transition metal, as is the case for pyridine on platinum.

In Chapter 3 we pose the question if a mixed-metal surface can provide an additional enhancement to SERS. We venture to ask if adding a nanometer thick layer of a transition metal on top of the plasmonic substrate can provide an additional enhancement. This would effectively mean that the chemical contribution would be compensating from the loss of electromagnetic enhancement due to the thickness of the dopant transition metal. If this is the case, then one can propose creating SERS-based sensors using different transition metals. Molecules would bind to the metals which have the highest binding energy, and due to an increased chemical enhancement, signal could be homogeneous across a large part of the molecular space. The representation of such sensor is shown in Fig. 1.2.

The concept of adding a secondary metal on top of the SERS-active substrate is not new [570, 625]. For instance, SERS has been used to monitor reactivity of H_2 on Pt surfaces. In this case, a platinum layer is added on top of the plasmon-active substrate. Van Duyne and Haushalter proposed the term “SERS borrowing” [547], to obtain a Raman signal of molecular species adsorbed on non-SERS active materials [523]. What we posit is in fact the opposite effect, where an additional source, in the form of dopant metal can *provide* an additional chemical enhancement. Therefore, we propose and coin the term of a *SERS lending* effect.

There have also been efforts to expand SERS effects beyond plasmonic effects. For instance, Tian *et al.*, took advantage of advances in instrumentation, such as charged-coupled devices to obtain a surface enhancement of the Raman signal from transition metals that

do not exhibit a plasmon excitation in the visible range, *e.g.*, Pt [1, 524, 525]. More recently non-metallic nanostructures from silicon and germanium have also shown to provide an enhancement [562, 563]. The enhancement from these structures can be explained using a photoinduced charge-transfer model, which provides evidence that there can be an enhancement despite not having plasmon-based substrates.

In Chapter 3 we present experimental evidence, as well as quantum chemistry insights using metal clusters that point towards the existence of a *lending* effect under favorable conditions. These considerations include favorable molecule-dopant metal interactions. Since it is difficult to fully characterize the mixed-metal substrate experimentally, we can only point at the analytical enhancement (*i.e.*, per-concentration instead of per-molecule enhancement).

The theoretical evidence takes a role in this research to “fill the gaps” in our understanding of this nanoscale phenomenon [469]. In this case, we reduce the metal environment to study localized effects in molecules by looking at just the part which directly interacts with the molecule. We show it can provide the right intuition to understand phenomena, such as the chemical effect in SERS. This approach also helps us to demonstrate the feasibility of enhanced monitoring tools by using different SERS substrates.

Chapters 4–5: Chemistry in electrostatic environments

In Chapters 2–3, we used metal clusters to improve our understanding of the chemical enhancement of SERS. Since this effect takes place only in the vicinity of the molecule, we could approximate the nanostructure as a cluster of metal atoms. However, when studying field effects of the nanoparticle on the molecule, it is important to consider the environment differently to account for effects that may take place farther away from the molecule. These interactions have overarching implications in the fields of electronics, detection, and catalysis [187, 259, 294].

As in the case of molecules in solution, or interacting with complex structures (*e.g.*, proteins), there needs to be a proper accounting for the degrees of freedom that affect the relevant subsystem since solving for all of them is neither feasible nor desirable. The formalism to separate system and environment in quantum chemistry dates back to Löwdin [317]. As mentioned above, QM/MM and continuum methods have been used to study different systems, with a specific emphasis to biomolecules or solvation reactions.

Metal environments are decidedly different from the situations mentioned above. Moreover, there is considerable interest to study electron transfer and electronic excitations of molecules interacting with nanoparticles or surfaces [305, 360, 440]. The traditional approach to studying these systems classically solves Maxwell’s equations, with the most recent implementation being either the discrete dipole approximation [428, 594] or the finite-

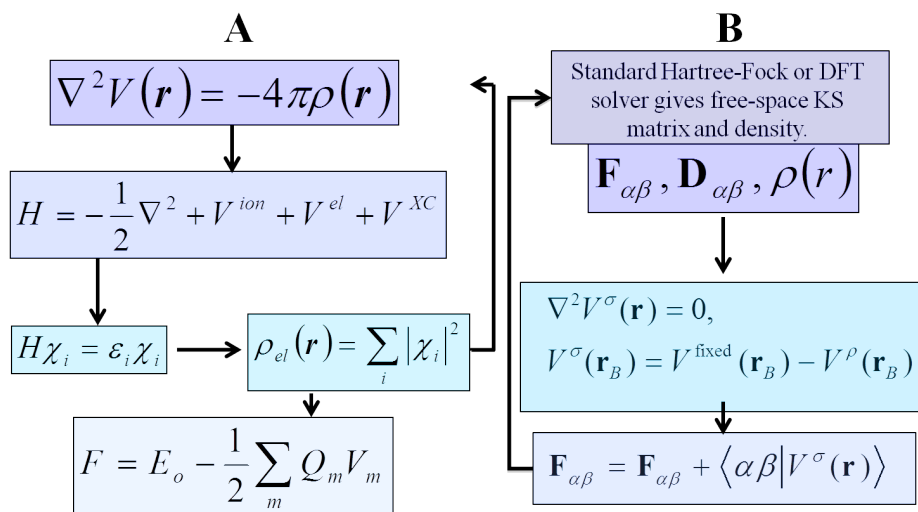


Figure 1.3: The two CheESE schemes presented in this work: **A. Full Poisson-Schrödinger approach**, as detailed in Chapter 4. The final step details the calculation of the free energy, as we are able to obtain the induced charges on the metal plates; **B. Laplace-corrected approach**, as detailed in Chapter 5. One can obtain the surface charge potential V^σ by recognizing that the charge of the surfaces inside the plates is zero, thus turning the problem into a Laplace approach. In turn, this potential is added to the KS system of equations.

difference time-domain method (FDTD) [514, 598]. McMahon *et al.*, employ a non-local approximation to consider nonlocal effects at nanometer-sized lengthscales [339, 340].

To fully consider quantum effects, one needs to partition the space and attempt a multiscale separation of the relevant degrees of freedom. In this vein, there have been FDTD/QM implementations [97] as well approximations of considering a metal dielectric function [116, 117]. The latter is an extension of the PCM model [531, 532]. In these models, solvation is described by a single bulk component, characterized by a dielectric or screened conductor, rather than explicit solvent molecules. Specifically, the metal–molecule interaction is derived from the mutual polarization of the neutral metallic surface and the electron density of the molecule.

We developed two different strategies to account for the electrostatic effects (including a strong applied static field) that a metallic surface exerts upon a molecule. These approaches are based on the metallic surface acting as a boundary condition. Therefore, there is a clear separation between system and environment. We termed this scheme as CheESE (chemistry in electrostatic environments).

The change of boundary conditions in the boundary region, \mathbf{r}_b , leads us to couple the

Poisson equation:

$$\nabla^2 V(\mathbf{r}) = -4\pi\rho(\mathbf{r}), \quad (1.3)$$

with the given boundary condition: $V(\mathbf{r}_b)$, with the potential V , and the Schrödinger equation. The Schrödinger equation naturally enables us to obtain the density, which in turn can lead us to obtain a better representation of the potential, by iteratively solving the Poisson-Schrödinger scheme (*i.e.*, applying the new density to Eq. 1.3), as shown in Fig. 1.3A. This scheme can be coded in a straightforward fashion representing space in a finite difference (FD) approach [435, 503], and couple it with existing FD quantum chemistry codes, such as `octopus` [93]. Chapter 4 contains more details of the development of this methodology.

In this approach, we assume that constant potential generators are attached to power supplies. As such, the system is open and we must include the work done by the environment as a free energy F . The finite-difference real-space approach enables us to obtain the contribution of the induced charges on the gates (Q_m), when we have an applied voltage (V_m) in this region. The finite difference approach enables the calculation of Q_m , given by the normal derivative of the total electrostatic potential at each of the surfaces. This is effectively the last step of Fig. 1.3A and is a major difference of the two approaches, as shown in Table 1.1.

The Laplace-corrected CheESE scheme developed in Chapter 5 stems from recognizing that the potential has two components, as shown in Fig. 1.3B: V^σ , the potential due to the surface charge; and V^ρ , the potential of the system (*i. e.*, electrons and nuclei). At the boundary, the total potential at the plates must be a constant. Then V^σ can be defined as a solution of Laplace’s equation inside the cavity:

$$\nabla^2 V^\sigma(\mathbf{r}) = 0 \quad \forall \mathbf{r} \in \text{cavity}, \quad (1.4)$$

where the cavity indicates the space within the metal plates. V^σ , under the Dirichlet boundary conditions, is in turn determined by the sum of the fixed potential at the plates (*i. e.*, the bias), and the inverse of the system potential V^ρ . This entails that V^σ can be directly determined without knowledge of ρ . As shown in Fig. 1.3B, this correction can be added to the modified Kohn-Sham (or Hartree-Fock) operator.

Chapter 5 makes an in-depth analysis of the parameters involved in V , and specifically V^σ , including the effect of the bias potential on the plates, but also image-charge effects on molecules that present charges, dipoles or induced quadrupoles: benzene anion, glycine and neutral benzene, respectively. On the other hand, Chapter 4 covers the effect of anion stabilization under electrostatic environments. Namely, the image charge effect causes an excess electron in benzene to be more stable than its neutral counterpart.

Type	Real Space	Basis set
Calculation type	Full Poisson equation	Correction to free-space
Space representation	Finite difference	Finite element
Solver type	Poisson solver	Laplace solver
Grid in molecular region	Fine grid required	Modest grid required
Induced charges	Calculated	Not calculated

Table 1.1: Comparison between the basis-set based Laplace correction of CheESE and the real-space based Poisson-equation Cheese approach.

The Laplace-corrected scheme was implemented as a standalone library using a wavefunction based approach, and can in principle be integrated to other quantum chemistry codes. Table 1.1 refers to a comparison of both methods. There are striking differences between both approaches. While one relies on a real-space approach, the other represents space in terms of basis sets. Moreover, the real space approach relies on finite-differences to solve the Poisson equation, while the basis set one uses a finite-element Laplace solver, which enables the grid around the molecular region to be more modest. On the other hand, the finite-difference approach allows the induced charges to be calculated in a facile manner.

Our work has been so far focused on simulating two metallic plates and having a molecule between them. However, the Poisson or Laplace-corrected solvers are more powerful tools as they can provide the potential for any geometry with just the appropriate boundary conditions as input. Therefore, the development of methods for arbitrary structures should aid in the understanding of roughened surfaces, such as those used in SERS.

The understanding of dynamic effects of molecules physisorbed to surfaces is also essential in the field of plasmonics, whether it is to enhance the electric field [323] or to understand excitonic effects [32]. The next step could include adding a complex metal dielectric function, as developed by Corni *et al.* [116, 117]. However, one must consider more higher-order effects, such as the interaction of charge between the surface and the substrate. Therefore, a more intricate jellium-like model for the surface would need to be implemented for the metallic environment [289].

Several important components of the chemical effects in surface-enhanced Raman scattering are described either using atomistic approximations of the metal, as well as boundary-condition based approaches. It is possible to readily study localized dynamic effects of metal-molecule interactions with the atomistic models, at a loss of bulk-like effects. Meanwhile, the image-charge models allow the potential of studying effects at a larger length scale.

Part II: The Harvard Clean Energy Project

At the moment, human energy use amounts to 550 EJ per year. The current sources that satisfy this demand are mainly based on fossil fuels. Oil is responsible for one third of the yearly energy demand. However, it is becoming scarcer and more expensive to extract. Coal, on the other hand, is readily available and present in countries with large energy consumption such as the United States and China. If fossil-based fuels are continued to be used at the current rate, we will continue to head towards the worst-case scenario paths of climate change as presented by the Intergovernmental Panel for Climate Change [493].

It then becomes increasingly important to start searching for prominent sources of non-carbon emitting sources. Saudi Arabia, the world's leading exporter of oil, recently launched an initiative to cover 50% of its energy demand using both nuclear and solar power. Regardless of the climate consequences to greenhouse gases, approximately 1 billion people still live without electricity. This part of the population often resides in remote regions where access to the grid is difficult [236]. The sun's input exceeds the global consumption by 4 orders of magnitude and it is a well known fact that an hour's irradiance exceeds mankind's yearly energy needs [357]. When conditions are favorable, local methods of power generation like solar power are ideal, as they can effectively bypass the connection to the grid and can *in principle* provide all the necessary energy.

Solar cells harness the sun's energy by converting the incident photons into energy. Currently, the most prevalent solar cells are made up of crystalline silicon. Its mechanism has been widely known [370], as well as its efficiency limits [482]. Despite these findings, the cost of generating electricity with solar cells is still not competitive with other sources of electricity. Even if there was a short-term adoption of this technology, crystalline silicon solar cells tend to be heavy and thick, which hinder its overall access for building-integrated architectures, either for rural or urban environments. Nonetheless, widespread adoption of solar panels and economies of scale are consistently driving prices of silicon solar cells down [169].

To reduce material costs, as well as to enhance the solar cell's use in non-traditional locations (e.g., beyond rooftops and solar harvesting plants), thin-film inorganic solar cells have been termed as the second generation of solar cells [509]. Similarly, the field has gone beyond studying inorganic materials and has also developed hybrid inorganic-organic photovoltaics such as dye-sensitized solar cells [397] and organic photovoltaic materials, which we will detail below [218]. The main goal becomes reaching a higher efficiency cost ratio, and not necessarily going after a higher efficiency than crystalline silicon, at 25% [615].

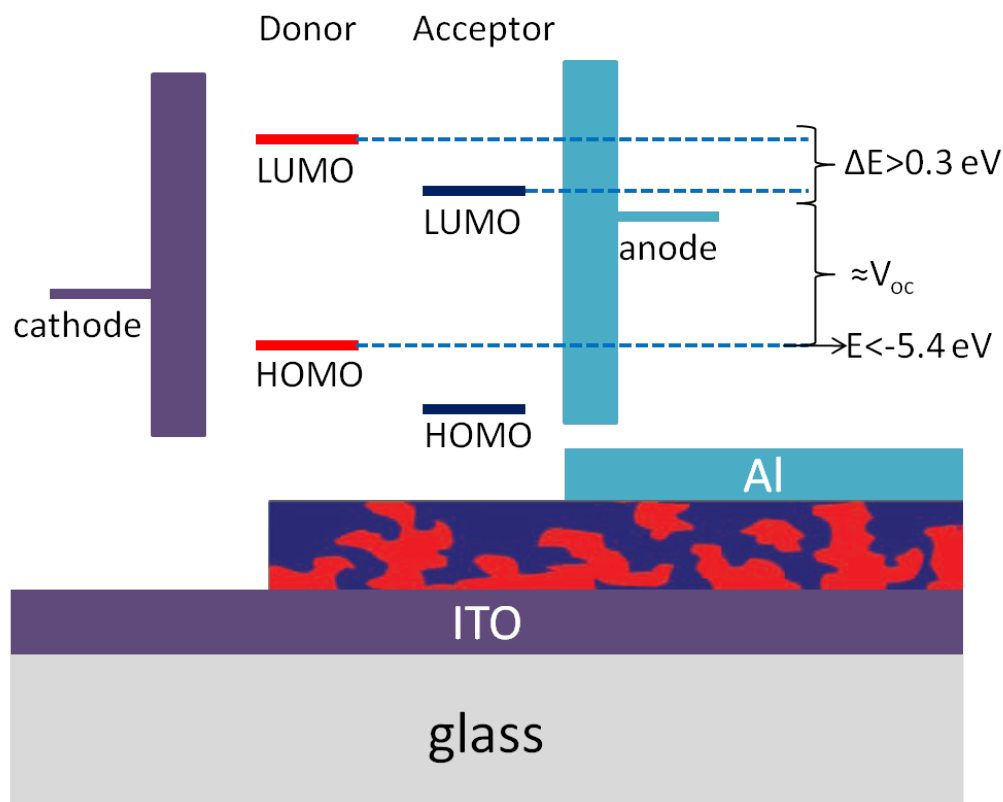


Figure 1.4: Organic photovoltaic device architecture layout and material energetic parameters. The bulk heterojunction is a mixture between the donor (red) and the acceptor (blue), and is capped by the electrodes at both ends.

Materials for organic photovoltaics

Organic photovoltaic solar cells have lately represented a new set of possibilities for solar cell materials. Although their discovery dates from the mid 1980's [516], it is not until the past decade that there have been considerable improvements [98, 218, 478, 521]. The development of these materials has gone from using single crystals as the active substance (akin to crystalline silicon), to crystalline bilayers of donors and acceptors to the bulk-heterojunction (BHJ) model. The latter seems to be the most successful thus far, though several problems in fabrication and scaling still remain. Yet another problem for OPV materials is the solar cell lifetime. As these materials are plastic-based, they degrade much faster than Si or other crystalline systems. Laboratory studies have reported a record lifetime of 7 years [419], and we expect lower yields at real-life conditions. Though, there is hope that as efficiency increases (the current record is 9.2% [478]), and production costs

of these solar cells decrease, lifetime issues will also become less relevant [35].

For organic-based solar cells, the cathode and anode are composed of indium tin oxide (ITO) with a layer of the PEDOT:PSS conductive polymer and aluminum, respectively. The device architecture of the bulk heterojunction solar cells is represented in Fig. 1.4. The bulk heterojunction lies between the electrodes and is a mixture of an acceptor material, typically a fullerene-based molecule, and a donor material, either a small molecule or a polymer.

Acceptor materials are characterized by having a high electron affinity and also good electron-transport properties. They require appropriate electronic levels to couple efficiently with the donor material. Other properties that are also necessary include having good solvation properties in the heterojunction medium, and potentially having good optical absorption properties. Finding a better acceptor is a field of active research [213, 298, 443, 451]. However, the most successful acceptor molecules have been fullerene-based ones, specifically PCBM¹ [230]. Although this molecule has a weak absorption, and its LUMO level is not ideal, there has as of yet not been more suitable acceptor materials as PCBM presents good affinity and electron transport properties. Therefore, it has often been the case that the search for improved BHJ materials has been in the realm of donors, with PCBM as acceptor.

Donor materials are characterized for having good hole-transport properties. It is also essential for them to have a favorable optical absorption as most of the excitons are generated in the donor phase. Since the advent of BHJ, donor materials have typically been conjugated polymers [600], principally due to favorable electronic properties and packing interactions. These have yielded the highest-recorded efficiencies for BHJs [96, 478]. However, donor materials can also be small molecules [556, 575]. The latter have the advantage of having higher processing control, and thus the possibility of a higher efficiency at the commercial scale. However, polymer-based BHJ still have a higher efficiency with respect to small-molecule counterparts.

In Chapter 7 we detail the photophysics of OPVs. The BHJ architecture is essential for the organic photovoltaic mechanism to take place. Briefly, the process begins with light absorption, principally at the donor phase, as mentioned above. This creates an exciton, which must diffuse to the donor-acceptor interface. At this point, if the exciton has not recombined, exciton dissociation takes place and there is charge carrier (*i.e.*, hole and electron) migration to the electrodes, which translates into an electric current. One of the main bottlenecks in OPVs is the exciton diffusion. As the diffusion length is typically in the order of tens of nanometers, the donor-acceptor interface must be located well inside

¹1-(3-methoxycarbonyl)propyl-1-phenyl-[6,6]C₆₁

this threshold. In the case of bulk heterojunctions, the donor and acceptor mix to create connected domains in the order of tens of nanometers, thus permitting charge-transfer [109].

Power conversion efficiency

As the relevant parameters for the development of BHJ OPVs are essentially known [74, 78, 225], the search for materials with these features becomes one of the essential parts of the problem. The power conversion efficiency (PCE) is given by the product of the maximum current density and voltage over the incoming power (typically set at 100 W m^{-2}). In order to cast the power characteristics into material properties, we represent PCE as:

$$\%PCE = \frac{FF \cdot J_{sc} \cdot V_{oc}}{P_{in}} \times 100 \quad (1.5)$$

In the formula above, V_{oc} represents the open-circuit voltage; J_{sc} is the short-circuit current density; and FF is the fill-factor. J_{sc} and V_{oc} can be obtained under device illumination measurements. In turn, the fill factor is the ratio of the maximum voltage-current over the product of J_{sc} and V_{oc} . The FF is a parameter that measures the capacity of the device to obtain the most power available.

The short-circuit current density is the photocurrent generated by a solar cell under illumination at short circuit. It is related to the incident spectrum and the cell's external quantum efficiency, EQE. The latter represents the probability that an incident photon of wavelength λ will deliver one electron to the external circuit at a given wavelength. The J_{sc} can be represented as:

$$J_{sc} = qA_{cell}^{-1} \int_{\lambda=0}^{\lambda_{max}} N_{phot}(\lambda) EQE(\lambda) d\lambda, \quad (1.6)$$

where q is charge of the electron; A_{cell} represents the area of the cell; and $N_{phot}(\lambda)$ is the incident number of photons (*i.e.*, the photon flux) at a given wavelength [370, 477]. The integral is bound by the largest absorbed wavelength. In the case of BHJ, this is normally the bandgap of the donor material, a property that can be estimated using quantum chemistry methods.

The EQE is related to the internal quantum efficiency, the capacity of every absorbed photon in the material to generate carriers, and the optical transmittance (related to the ITO/glass spectrum) [477]. Recent work on device architectures has enabled IQE of 100% at certain frequencies [403]. Exciton diffusion is typically responsible for small internal quantum efficiencies.

In order to obtain the N_{phot} spectrum in Eq. 1.6, one needs to specify its position with respect to that of the air mass (AM): the path length through the atmosphere relative to the zenith [196]. At sea-level and measuring directly above, the spectrum is named AM

1. The measurement standard was given by a tilt angle representing 37 degrees, which is equivalent to the average latitude of the continental United States. This is equal to a path length of 1.5 with respect to sea level and its spectrum is thus labeled AM 1.5 [180].

The V_{oc} is a function of the electrical and chemical potential gradients present in the cell [192]. In BHJ devices holes and electrons are formed within the donor and acceptor phases. This leads for the V_{oc} to be related to the energetics of the donor-acceptor interface [118]. In fact, it has been found that V_{oc} is related to the highest occupied molecular orbital (HOMO) of the donor and the lowest unoccupied molecular orbital (LUMO) of the acceptor [73]:

$$V_{oc} \sim \frac{1}{q} |E_{HOMO}^D - E_{LUMO}^A|. \quad (1.7)$$

In the case of silicon-based solar cells, V_{oc} is mainly determined by the electrode work functions. This is due to the holes and electrons being generated in the same semiconducting phase, and thus require a classical built-in potential to generate charge carrier separation [118]. The difference in potential between the electrodes is typically smaller than in BHJ materials. However, the J_{sc} in Si-based solar cells is larger than in organic photovoltaic solar cells.

The Scharber model: A simple tool for predicting organic photovoltaic efficiency

The Scharber model relies on frontier orbital energetics to determine PCE [467], and thus depends only on time-independent properties. Although this model entails working with several approximations, it is a useful starting point to start assessing orbital-dependent properties and its relationship to the material's performance. The model includes a linear relationship between the difference of the donor's HOMO and the acceptor's LUMO. They use the V_{oc} in Eq. 1.7 and approximate it as:

$$V_{oc} = \frac{1}{q} |E_{HOMO}^D - E_{LUMO}^A| - 0.3. \quad (1.8)$$

The offset value, 0.3 V, in Eq. 1.8 is an empirical factor. Scharber, *et al.*, attribute these losses to photocurrent effects present in bulk-heterojunctions. In practical terms, it is a loss to the overall efficiency of the system. The J_{sc} relies on approximating the EQE as: EQE (λ) = 0.65, for all λ ; and, λ_{max} as the wavelength related to the gap between the donor's HOMO and LUMO: ΔE_g^D . The LUMO of the acceptor also plays a role in this calculation, since we must consider the exciton dissociation process. We consider that there needs to be an energy gap of 0.3 eV between the LUMO of the donor and the LUMO of the acceptor, as shown in Fig. 1.4. This gap is necessary because we need to provide the energy

necessary for exciton dissociation. Therefore, Eq. 1.6 becomes an integral of the incoming solar spectrum (*e.g.*, AM 1.5), given the associated donor bandgap wavelength, λ_g^D :

$$J_{\text{sc}} = qA_{\text{cell}}^{-1}\text{EQE} \int_{\lambda=0}^{\lambda_g^D} N_{\text{phot}}(\lambda) d\lambda.$$

Lastly, the fill factor is also approximated to $\text{FF} = 0.65$, and so we are able to calculate the efficiency of the material (Eq. 1.5). Since PCBM is the lead acceptor, it is typical to perform a search of the donor, given the acceptor’s parameters. After accounting for all the losses of the material under this model (due to V_{oc} , FF, EQE and exciton dissociation), we find that it has a maximum efficiency of 11.1% and its ideal bandgap is 1.4 eV. Since PCBM’s LUMO is -4.3 eV, then the ideal donor LUMO is -4.6 eV and its HOMO is -6.0 eV. Therefore, it is possible to search for donors by using the orbital values given by the ground-state DFT calculations.

In Chapter 6, we provide an overview of the Harvard Clean Energy Project, a high-throughput approach for a large-scale computational screening and design of OPV materials. These include efforts in several directions including cheminformatics, machine learning, quantum chemistry, while keeping a tight integration with experimental researchers. In Chapter 7, we present our initial efforts in cheminformatics and machine learning for materials discovery. These include developments of inference methods as well as the generation of molecular libraries to find new OPV materials.

Chapter 6: Large-scale computational screening and design of organic photovoltaic materials

The development of materials is a time-intensive process, where synthesis and characterization may have a turnaround time in the order of months or years. Moreover, the molecular space is limited as researchers often work with systems that belong to the same family of molecules [63, 620]. Theory has been able to aid in the understanding of the parameters for organic optoelectronic materials [177, 355, 458, 459], and has also been successful in predicting new materials for organic electronics [491]. However, as in the case of synthetic characterization, theoretical studies has thus far been limited to a small set of candidates.

Proof-of-principle studies have given a positive indication that it is feasible to go from an *in silico* prediction of materials to translate them to the workbench [491]. Therefore, it is possible that expanding the search across the relevant molecular space could yield molecules that exceed the current record efficiency for solar cell materials. Relationships between materials parameters such as V_{oc} and orbital values enable for the initial rank and characterization of potential candidates [467]. A successful initial screening of these materi-

als requires the following components: i) an appropriate molecular space; ii) analytical and statistical tools to discriminate and predict successful candidates; iii) and a cyberinfrastructure to withstand a large scale project. We begin by introducing our infrastructure efforts, and continue detailing the quantum chemistry tools we use for our large-scale screening approaches. In the next section, we overview the details of the molecular space, along with the statistical tools we utilize.

Knyder’s Law [557] predicts disk space doubling roughly every year. This law shows no signs of slowing down as storage densities are still far from its fundamental limits [282]. This has brought forth a paradigm prevalent in many scientific, as well as technological areas of “Big Data”, or data-driven projects [10]. These are defined by the size of the data itself as being part of the problem [316]. Examples of these projects abound and vary from the culturomics project [347], which aims to digitize all books ever printed, to the dynamomics efforts to collect a comprehensive database on protein dynamics [545]. The CEP aims to screen millions molecules for finding organic photovoltaic materials, thus making this project a data-driven one.

The infrastructure needed for this kind of approach is based on the fact that this project relies heavily on available computer time, but this has moved away from the large super-computer centers, and into the households and offices around the world. The SETI@Home² project revolutionized this idea and started the paradigm of distributed computing. Nowadays, the Berkeley Open Infrastructure for Network Computing (BOINC) is the software that enables countless others scientific projects [20, 66]. The CEP partnered with World Community Grid [108], which is a philanthropic arm of IBM and hosts around 500,000 volunteers for various projects. As of March 2012, the CEP has used over 8,000 computer years for this endeavor and has done 10,000,000 calculations on different molecular configurations. We are currently obtaining properties for 30-40,000 molecules per day.

As an initial screening, we perform a set of HF and DFT calculations [271, 405] using various different functionals, and basis-set configurations. We develop these in detail on Chapter 6. We use a customized version of Q-Chem 3.2 [480] and users around the world run the calculations in a fully automated fashion during their idle time. Although DFT and HF methods are a time-independent approximation to the Schrödinger equation, this is a starting point to probe for necessary conditions for successful OPV materials. Needless to say, the properties addressed in the initial pruning will not be sufficient considerations for predicting a new material.

As we mentioned above, the Scharber model relies on time-independent quantities as an initial approximation for power conversion efficiencies. As such, this is our first step

²Search for Extraterrestrial Intelligence @ Home, <http://setiathome.ssl.berkeley.edu/>

in the screening process. There is a myriad of information that can be extracted both for theoretical and experimental use. For example, instead of doing a search of a donor, with respect to PCBM, one can undertake a coupled donor-acceptor approach. Similarly, to go beyond 11% efficiency in the Scharber model, one would need to consider more complicated architectures such as tandem solar cells, where two (or more) donors absorb at different frequencies. It will be useful to perform a complementary search of donors to find systems with higher efficiency [17].

Chapter 6 also details the theoretical methods needed to go beyond the initial screening. More accurate methods are needed to account for the vibrational effects on these molecules. This is specifically important to address electron-phonon coupling [460], which may lead to dissipation of energy; charge transport via the calculation of cations and anions [371]; and excited states to address the absorption spectra of the candidates [459, 489].

So far we have addressed the cyberinfrastructure of the CEP, along with some of the analytical tools we use in this project. Chapter 7 details our initial advances on the field of cheminformatics. We explore the modelling of an appropriate space, as well as the machine learning tools we have been using and developing for this materials discovery endeavor.

Chapter 7: Accelerated computational discovery of organic photovoltaic materials by means of cheminformatics

High-throughput approaches for discovery of new molecules has mainly been concentrated in the realm of drug discovery [40, 41, 193]. For the last 40 years, this field has also developed machine learning approaches to find new drug-like molecules [193, 338]. Research in drug discovery led to the creation of cheminformatics (chemical informatics), which allows for the “transformation of data information and information into knowledge” [82]. More specifically, it is a field that combines machine learning and statistics in a chemistry-oriented context [295].

Machine learning involves creating algorithms so a computer can take in knowledge from empirical data (such as a dataset) and be able to make decisions based on the data. Supervised learning algorithms involve training a set of target values, using a set of features (or independent variables) [434]. When the outputs are real values, this setting is known as a regression; while if the targets are a logistic function (*e.g.* to discriminate between photoactive and inactive materials), then the setting is known as a classification. One of the main objectives of these algorithms is to find an underlying structure between the features and targets [62, 321].

The drug discovery community has extensively used the linear regression model. In linear regression, one tries to fit an output using a set of features (or inputs) and parameters

(or weights):

$$f(\mathbf{x}) = \mathbf{x}^\top \mathbf{w}, \quad y = f(\mathbf{x}) + \varepsilon, \quad (1.9)$$

where \mathbf{x} is the input vector, \mathbf{w} is a vector of weights, f is the function value, y is the target value, and ε is the deviation from a perfect fit [434]. The objective becomes minimizing the error in Eq. 1.9, by tuning the weights vector and using an error metric, such as the sum-of-squares error function [62]. One of the goals of the drug-discovery community is to exploit structure-activity relationships (QSAR), though these can also be obtained with non-linear regressions and other machine learning methods. However, the ease of interpretation and implementation of linear methods enhanced their stature in this community. As it is perhaps clear, what it has of simplicity, it lacks in flexibility as it is not always the case that there is a linear relationship between inputs and output. The field, however, has been progressing towards using more complex non-linear regression methods [387, 434, 519].

Non-linear regression methods can be expanded to include quadratic terms between the different features, or even higher-order polynomials. However, one notices the quadratic features grow as $n^2/2$, while we expect that cubic and higher terms scale even higher. Therefore, machine learning has focused on methods that have attempted to circumvent these issues by using complex adaptive basis functions or adapting parametric forms of these basis functions [62]. These methods have strongly relied on Bayesian statistics. As these methods grow in complexity, their prediction models might improve, but the underlying interpretation may be easily lost.

Our initial machine learning approach consists on using a linear regression models to find better donor materials, as detailed in Sec. 7. We collected target values from reported data. Secondly, we turned our attention to which features we could choose for these materials. In this case, we utilized properties that could be calculated in a facile matter. These are called descriptors (which we will use interchangeably with features) and these correspond to both structural properties, such as connectivity, elemental analysis and simple electronic structure properties, such as those based on extended Hückel theory [95, 237]. These properties are easy to calculate and provide both an initial indication of structure-property relationships, as well as an effective testing ground for developing machine-learning methods. Turning quantum chemistry-based data into descriptors will be one of the most important steps in order to provide more accurate inference tools for predicting new molecules.

There are some properties that are heavily dependent upon fabrication, such as the fill-factor. Therefore, we exclude this property from our analysis, where our regression with highest confidence will then be the product of V_{oc} and J_{sc} . We provide a summary of our scheme in Fig. 1.5. We start with a set of OPV donor materials with known parameters. These are our target values we used to train with the cheminformatics features developed

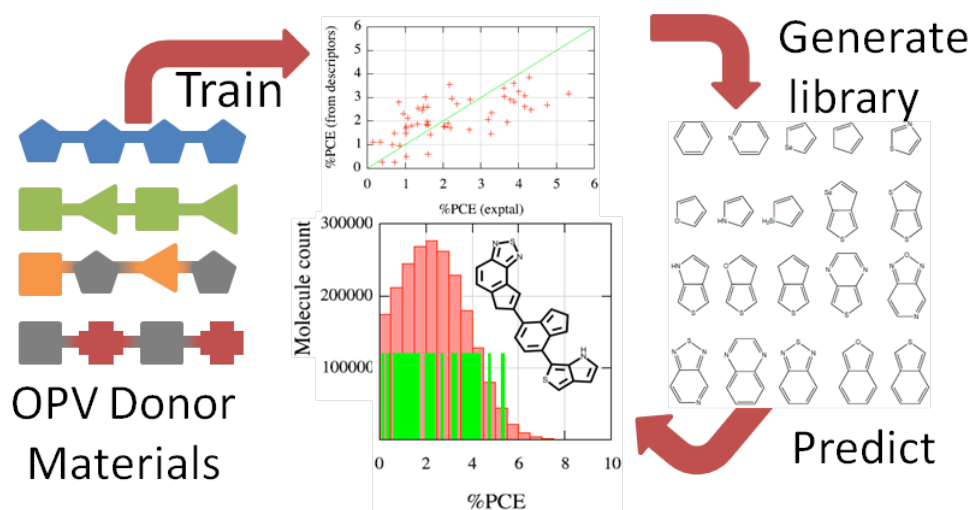


Figure 1.5: Machine learning approach to donor organic photovoltaics materials discovery. OPV donor materials, with known parameters are used as target values to train a regression model. We virtually generate a molecular library, which we apply our model to find new candidate molecules.

above. With a virtually generated library (*vide infra*), we can apply our trained regression model to find new candidate molecules.

The last component in our cheminformatics approach is related to generating a library of potential candidate molecules. The chemical space is extremely vast. For instance, it has been estimated that there are far more than 10^{60} organic-like molecules [65]. Although the donor molecule space is likely not as large, since donors require certain electronic properties, typically provided by conjugation, we can expect that the whole space cannot be computed. Generating a database of lead molecules should be related to the available screening capability of the project, but it should be bound by the interest in the available space, as well as the potential use of the non-successful leads. In our initial approach, we generate a combinatorial library starting with building blocks provided with experimental input from the group of Zhenan Bao at Stanford University to ensure synthetic feasibility [356].

There is not always a need to explore the largest computational space available. As molecules grow larger, the combinatorial possibilities grow exponentially, and there may not be available computer time. Furthermore, as successful candidates are found in the molecular space, it may be more useful to concentrate on specific areas. O’Boyle *et al.*, have studied a library of donor OPV materials using a stochastic method (*i. e.*, genetic algorithm) to create combinations of the building block materials [386] and test them using semi-empirical quantum-mechanics methods.

Our approach initially explores around 3.5 million molecules [394, 391]. We have found that around 0.3% of these candidates are above the 10% mark using the Scharber model, as shown in Sec. 6. This sparsity indicates that it is indeed difficult to find successful candidates. Similarly, the median lied at around the 6% efficiency, which means that chemical intuition might not necessarily lead to high efficiency yields, but instead must rely in these high-throughput methods. On the other hand, our machine learning approach, shown in Sec. 7 has enabled us to perform a ranking of molecules, which in our future analysis will be coupled to appropriate statistical validation schemes [2, 122], along with more complex descriptors and learning algorithms such as Gaussian processes [387, 434], and classification schemes [375].

Part III: Accelerating quantum chemistry algorithms using graphics processing units

One of the main interests for electronic structure theory is to find approximate solutions to the non-relativistic time-independent Schrödinger equation:

$$\hat{H}(\mathbf{r}, \mathbf{R}) \Psi(\mathbf{r}, \mathbf{R}) = E \Psi(\mathbf{r}, \mathbf{R}) \quad (1.10)$$

where $\psi(\mathbf{r}, \mathbf{r})$ represents the wavefunction for the Hamiltonian, \hat{H} , which depends on both the nuclei and electron position vectors \mathbf{r} and \mathbf{R} , respectively [513]. For a system with M nuclei and N electrons, Eq. 1.10 involves solving an eigenvalue equation in $3M + 3N$ independent variables, *i.e.*, the coordinates of all the particles. It is well known that this is impossible to solve exactly [496]. Approximate solutions are therefore necessary.

The first approximation consists in considering that since electrons are much lighter than nuclei, they move faster. Therefore, one can consider the electrons acting in the field of fixed nuclei. We can then separate the components of Ψ into a product of an electronic wavefunction $\psi(\mathbf{r}; \mathbf{R})$, which depends explicitly on the position of the electrons and parametrically on the nuclear coordinates; and a nuclear wavefunction $\chi(R)$: $\Psi(\mathbf{r}, \mathbf{R}) = \psi(\mathbf{r}; \mathbf{R}) \chi(R)$. This is the ansatz proposed by Born and Oppenheimer [69] and it allows Eq. 1.10 to be decomposed into an equation for the electronic wave function and another for the nuclei, which describes vibrations, rotations and translations of the nuclei. We will concentrate on the electronic wave function [496].

$$\hat{H}_{\text{el}} \psi_{\text{el}}(\mathbf{r}; \mathbf{R}) = E_{\text{el}}(\mathbf{R}) \psi_{\text{el}}(\mathbf{r}; \mathbf{R}), \quad (1.11)$$

where now the energy also depends parametrically on the nuclear coordinates; and the

electronic Hamiltonian is given by:

$$\begin{aligned}\hat{H}_{\text{el}} &= -\frac{1}{2} \sum_i \nabla_i^2 - \sum_i \sum_A \frac{Z_A}{\mathbf{r}_{iA}} + \sum_i \sum_{j>i} \frac{1}{\mathbf{r}_{ij}} \\ &= \sum_i \hat{h}_i + \sum_i \sum_{j>i} \frac{1}{\mathbf{r}_{ij}}.\end{aligned}\tag{1.12}$$

Effectively, we have reduced the Schrödinger equation on a $3N$ dimensional problem, for each nuclear configuration. For most molecular systems, it is still not possible to find an analytical solution to Eq. 1.11. Since the development of the Schrödinger equation, the electronic structure community has focused on a hierarchy of methods to solve Eq. 1.11 approximately. This has led to systematic improvements to yield properties of increasing accuracy. The starting point in the hierarchy is the Hartree-Fock (HF) method, which describes the electron-electron interactions (*i.e.*, the second term in Eq. 1.12) within a mean-field approach [388].

The Hartree-Fock method relies on the expansion of a wave-function in a Slater determinant, an antisymmetrized product of one-particle spin orbitals: $\psi(\mathbf{r}_1, \mathbf{r}_2, \dots, \mathbf{r}_N) = |\phi_1 \phi_2 \phi_3 \dots \phi_N\rangle$. Broadly speaking, and we provide more details of this derivation on Sec. 10, we calculate the expectation value of Eq. 1.11 and obtain the Hartree-Fock energy. Minimizing the expectation value in terms of expanding $\phi_i(\mathbf{r})$ into fixed basis leads to solving a pseudo-eigenvalue problem. This is coupled with constructing the density matrix out of the optimized coefficients and self-consistently using these values for a better expression of the HF energy. The eigenvalue problem is typically solved by diagonalization, which scales cubically with system size: $\mathcal{O}(M^3)$, though for small molecules, the scaling is typically $\mathcal{O}(M^4)$.

The HF method is able to recover up to 99% of the exact energy. The neglected energy is known as correlation energy and can be systematically recovered using post-HF methods. These methods increase in accuracy at a higher scaling price. These include coupled-cluster methods, which modifies the single-determinant ansatz, as well as multi-determinant approaches [222, 513]. For completeness, we mention that DFT approaches scale similarly to HF as it is also a self-consistent field [271, 405]. DFT offers a good compromise between accuracy and computational cost, but to date does not yet provide a systematic way of improving upon the result, as post-HF methods do.

The post-HF method we focus on is perturbation theory. Møller and Plesset (MP) used Rayleigh-Schrödinger perturbation theory to obtain a second-order solution (MP2), where the zeroth order eigenvalues are given by the HF approach [354, 388]. The expression for

computing second-order energy is:

$$E^{(2)} = \sum_{ijab} \frac{(ia|jb)^2 + \frac{1}{2} [(ia|jb) - (ib|ja)]^2}{\epsilon_i + \epsilon_j - \epsilon_a - \epsilon_b}, \quad (1.13)$$

in terms of the eigenfunctions of the Fock operator with eigenvalues ϵ ; where the occupied molecular orbitals (MO) are labeled by i, j ; the virtual molecular orbitals are labeled by a, b ; and the MO integrals,

$$(ij|ab) = \sum_{\mu\nu\lambda\sigma} C_{\mu i} C_{\nu j} C_{\lambda a} C_{\sigma b} (\mu\nu|\lambda\sigma), \quad (1.14)$$

are obtained by transforming the atomic-orbital (AO) electron repulsion integrals (ERI),

$$(\mu\nu|\lambda\sigma) = \int \int \frac{\eta_\mu(\mathbf{r}_1) \eta_\nu(\mathbf{r}_1) \eta_\lambda(\mathbf{r}_2) \eta_\sigma(\mathbf{r}_2)}{|\mathbf{r}_1 - \mathbf{r}_2|} d\mathbf{r}_1 d\mathbf{r}_2, \quad (1.15)$$

where $C_{\mu i}$ represents the matrix elements of MO coefficients describing the expansion of each MO as a linear combination of AOs. The time-consuming part in this process is considering that the transformation from AOs to MOs formally scales as $\mathcal{O}(M^5)$. The MO coefficients in Eq. 1.14 are nonlocal and so most of the elements are significant and cannot be canceled out to reduce the order [388].

Although the scaling holds in the asymptotic limit, there have been efforts to reduce the prefactor in MP2 at a very small cost to accuracy. This method is similar to inserting a resolution-of-the-identity (RI) in the ERI's [147, 572]. In Eq. 1.15, the 2-center 4-index ERI becomes highly linearly dependent with increasing atomic orbital basis set, and so it is possible to expand the products of electrons 1 and 2 in a basis set auxiliary function P [210]:

$$\rho_{\mu\nu}(\mathbf{r}) = \eta_\mu(\mathbf{r}) \eta_\nu(\mathbf{r}) \approx \tilde{\rho}_{\mu\nu}(\mathbf{r}) = \sum C_{\mu\nu,P} P(\mathbf{r}),$$

with a dimension smaller than the original product space. If one minimizes the error in the Coulomb ERI's, then it is possible to approximate Eq. 1.15 as only 2 and 3-index quantities:

$$(\widetilde{\mu\nu|\lambda\sigma}) = \sum_{P,Q} (\mu\nu|P)(P|Q)^{-1}(Q|\lambda\sigma). \quad (1.16)$$

This method is called resolution-of-the-identity (RI) due to the insertion of:

$$I = \sum_m |m\rangle\langle m| \approx \sum_{P,Q} |P\rangle\langle P| (P|Q)^{-1} \langle Q|,$$

but it has also been referred as a density-fitting scheme [577]. We can now obtain the approximate $(ia|jb)$ integrals, as well as its elements using matrix multiplications for RI-

MP2:

$$\widetilde{(ia|jb)} \approx \sum_Q B_{ia,Q} B_{jb,Q}, \quad (1.17)$$

$$B_{ia,Q} = \sum_P (ia|P) (P|Q)^{-1/2}. \quad (1.18)$$

It is known that the RI approximation reduces the operations at least an order of magnitude for a triple-zeta basis-set calculation. Also, in RI-MP2 a larger basis set entails a larger relative speedup [210]. Therefore, RI-MP2 enables both the study of larger systems, and also a more accurate representation for the same molecule, since it allows for its study using a larger basis set. Moreover, the fact certain steps in this method are effectively matrix-matrix multiplications will enable for a facile translation into the single-instruction multiple-data calculation paradigm, and hence be further accelerated with graphics processing units (GPUs).

In Chapters 8–10, we develop our work related to the acceleration of RI-MP2 using GPUs. We detail the approaches needed for an efficient computation of this method. At the time of our initial implementation, graphics cards lacked double precision (DP) accuracy; a considerable loss for quantum chemistry methods. Eventually, GPUs started having DP, albeit slower. Moreover, most cards did not include DP. We therefore developed a mixed precision approach to be able to obtain reasonable accuracy in RI-MP2. We present these approaches in Chapters 9–10.

Chapter 8–10: RI-MP2 Acceleration Using GPUs

The development of scientific computing in graphics processing units (GPU) has exploded in the last five years, especially in the field of molecular modelling [19, 126, 500, 539, 540, 538, 541, 596, 597]. This change in computing paradigm has been enabled by the specific architecture of GPUs. GPUs were developed to display complex images, especially for videogames. The most computationally-demanding operation lies in the rasterization and shading process [500]. These two steps are inherently data-parallel. Typical CPU processors do not provide a multi-threaded or parallel architecture to meet these needs effectively

According to Flynn’s taxonomy, the single instruction, multiple data paradigm, implies that one instruction can operate on multiple data. Similarly, stream processing gathers a ‘stream’ of input, and operates on the input stream by using one or more kernels. Each kernel comprises of one or several operations [198, 251]. Typical GPUs contain multiple arithmetic units (streaming processors) arranged into groups to form multiprocessors that share fast access memory and an instruction unit; the grouped processors execute the same instruction thread simultaneously on different data streams. This is extremely useful for

visualization where, for instance, a stream of pixels are translated or rotated on a screen. GPUs are therefore well-suited to high-performance applications with dense levels of data parallelism.

Several other hardware architectures utilize the stream processing paradigm. These have had successes in implementing scientific computing tools. However, they have not always stood the test of time; especially with respect to the wide availability of GPUs. These include the Clearspeed hardware, with boards similar to those in GPUs [84]; field-programmable gate arrays [411]; and the MDGRAPE hardware for MD and N-body simulations [510].

Molecular modelling, whether it is for molecular dynamics or, quantum chemistry applications typically contain fine-grained data parallelism, which has resulted into porting these algorithms for GPUs. One of the main reasons there has been such an explosion in general purpose applications for GPU³ is due to the release programming interfaces that allow development of algorithms for the GPU using a relatively simple extension of the standard C language, namely CUDA [385] and OpenCl [367]. These two factors have combined to have production level codes for MD calculations and visualization (NAMD, VMD), a standalone quantum chemistry implementation (Terachem), and a legacy code that now enables GPU usage (Q-Chem 4.0), among others.

We implemented an acceleration of the RI-MP2 method, principally by noticing that Eqs. 1.17–1.18 can be calculated more efficiently using the stream-processing paradigm with GPUs. The most time consuming step in the RI-MP2 algorithm is Eq. 1.17 due to the evaluation of the matrices grows as $\mathcal{O}(N^2)$. These hurdles were overcome with the CUDA development toolkit and its basic linear algebra subprograms implementation, CUBLAS [383]. As we mentioned, one of the main issues is the CPU-GPU communication. Therefore, the algorithm included a method to batch the matrices up to the available GPU memory, since acceleration increases as the size of matrix grows. Lastly, since memory in the cards is typically smaller than in CPU RAM, we also devised a matrix-cleaver to enable a full RI-MP2 implementation for GPUs.

Our initial algorithm in Chapter 8 used single precision (SP) cards, as those were the only available ones at the time. The error of our RI-MP2 implementation with these cards naturally increased as we tested with larger systems, until eventually the error was beyond 1 kcal mol⁻¹ (*i.e.*, chemical accuracy). This led us to propose methods of mixed precision in Chapters 9–10. The main problem for using single precision is that when performing a product between a large and a small number, the 6-7 significant figures are often insufficient to achieve chemical accuracy. We explored two schemes of partitioning matrix elements so

³General-purpose computing on graphics processing units (GPGPU).

that they can be calculated using single precision matrix multiplication (SGEMM in BLAS library) in the GPU.

The first method is deemed *bitwise partitioning*. Consider splitting a double precision (DP) floating point number, $A = m * 2^k$,

$$A \approx A^u + A^l \quad (1.19)$$

where A^u and A^l are single precision (SP) numbers storing the uppermost n_u , and the next lowest n_l , significant bits of m , respectively. Then, if we apply the multiplication of two scalars A, B using bitwise partitioning, we can approximate the full DP multiplication as four (or three for expediency) SP multiplications.

$$\begin{aligned} AB &\approx A^u B^u + A^u B^l + A^l B^u + A^l B^l \\ AB &\approx A^u B^u + A^u B^l + A^l (B^u + B^l) \end{aligned} \quad (1.20)$$

We can generalize Eq. 1.20 for matrix multiplication:

$$\mathbf{AB} \approx \mathbf{A}^u \mathbf{B}^u + \mathbf{A}^u \mathbf{B}^l + \mathbf{A}^l (\mathbf{B}^u + \mathbf{B}^l) \quad (1.21)$$

where, we can use Eq. 1.19 for each element of $\mathbf{X} \in \{\mathbf{A}, \mathbf{B}\}$.

We implemented an heterogeneous algorithm as our second approach. It involves separating the matrix multiplication $\mathbf{C} = \mathbf{AB}$, by splitting \mathbf{A} and \mathbf{B} into ‘large’ and ‘small’ components, giving

$$\begin{aligned} \mathbf{C} &= (\mathbf{A}^{\text{large}} + \mathbf{A}^{\text{small}}) (\mathbf{B}^{\text{large}} + \mathbf{B}^{\text{small}}) \\ &= \mathbf{AB}^{\text{large}} + \mathbf{A}^{\text{large}} \mathbf{B}^{\text{small}} + \mathbf{A}^{\text{small}} \mathbf{B}^{\text{small}}, \end{aligned} \quad (1.22)$$

where we have taken the simple approach of introducing a cutoff value, δ , to define the split. That is if $|X_{ij}| > \delta$, the element is considered ‘large,’ otherwise it is considered ‘small.’ The $\mathbf{A}^{\text{small}} \mathbf{B}^{\text{small}}$ term consists entirely of ‘small’ numbers, and can be run with reasonable accuracy in single precision on the GPU. The other two terms contain ‘large’ numbers, and need to be run in double precision to achieve greater accuracy. However, since each of the ‘large’ matrices will often be sparse, these terms each consist of a dense-sparse multiplication.

We found that the bitwise implementation is less arbitrary as it depends only on the matrix size N (assuming square matrices), and not on the elements of \mathbf{A} or \mathbf{B} . Moreover, it is only 3 times faster than CPU DP matrix multiplication in the best case. In contrast, the speed of the heterogeneous approach strongly depends on the fraction of ‘large’ elements. Regarding the accuracy, the effectiveness of these methods ultimately depends on the matrix structure. As we are interested in accelerating quantum chemistry, the matrices calculated

in RI-MP2 are of large size N and contain both large and small elements which are separated by orders of magnitude. Therefore, in the case of these methods, the heterogeneous approach seemed to be most effective to tackle mixed-precision.

Single and mixed precision approaches have been recently revisited in the context of the MP2 method, using Cholesky decomposition [555], as well as for an efficient evaluation of ERI's in GPUs when using SCF methods [319]. Similarly, the matrix multiplication approach has also been extended to post-HF methods, such as coupled-cluster [126]; as well as phenomenological hierarchical equations of motion [279].

Overall, heterogeneous hardware is becoming ubiquitous, both in the PC as in the supercomputer setting. GPUs are becoming the stream processors of choice for scientific computing due to their astounding FLOP⁴ per price ratio. As mentioned above, the field of molecular modelling is actively adapting to these changes. Therefore, it should be possible to apply these techniques for nanomaterials as well, as we do in Chapter 2–5. Since GPUs are present in PCs around the world, one of the goals of the Clean Energy Project (see Chapter 6) is to be able to take advantage of these additional resources for finding organic photovoltaic materials. Indeed, the prospect of using this computational power for distributed computing is already being exploited for understanding of protein folding using molecular dynamics methods [156].

⁴Floating point operation per second

Part I

**Chemical effects in
surface-enhanced Raman scattering**

Chapter 2

On the chemical bonding effects in the Raman response: Benzenethiol adsorbed on silver clusters

2.1 Introduction

Raman scattering from molecules in proximity to a rough noble-metal surface or near a metal nanoparticle is strongly enhanced due to the interaction with surface plasmon modes and to the formation of metal–molecular complexes [360, 399]. This phenomenon, which allows for the measurement of Raman spectra of extremely low concentrations of molecules [553] with a single-molecule detection as its ultimate limit [376, 270], is very attractive for sensor applications. In particular, it could be utilized for detection and identification of hazardous materials [605, 612] or for probing of biological structures [26], for which Raman fingerprints provide unique information about molecular composition.

Recent achievements in the design of nanostructured materials demonstrate substantial progress toward resolving the long-standing problem of low reproducibility of SERS substrates. Arrays of nanoantennas fabricated with electron beam lithography [105] or nanoimprinting [33] utilize extended control of optically excited surface plasmons to tune the plasmon resonance frequency and to focus the near field in particular areas. Lithographically engineered [87, 181] or laser-engineered [127] structures allow the observation of a spatially homogeneous enhancement of the Raman signal by 7 orders of magnitude¹ when an excitation laser frequency far below intramolecular resonances is employed. However, there remains a number of open questions which are related to the formation of hot spots and to the homogeneity of the Raman response throughout a sample. The enormous Raman cross section reported for fluorescent dyes in hot spots [376] has a substantial contribution from an intramolecular resonant excitation [130]. On the other hand, many important an-

¹There is a controversy in the definition of the enhancement factor discussed recently in E. C. Le Ru *et al.* [293].

alytes do not have electronic excitations in the available range of laser frequencies. For these systems, a relevant question is whether modification of the local environment of the molecule can be used to boost the limit of Raman detection sensitivity.

The importance of the so-called chemical enhancement [360, 398, 291] has been debated since the early years after the discovery of SERS. The contributions of the electromagnetic coupling and the chemical binding are not clearly separable in the experiments [291], because the first process is essential for SERS detection. This adds to ambiguity in the interpretation of SERS experiments. Moreover, the electronic coupling effects are sensitive to the local environment of adsorbed molecules, which makes a systematic analysis of chemical effects more difficult. General theories of chemical enhancement [417, 6, 314] provide an intuitive picture of the mechanism, but rely on phenomenological parameters. In this context, first-principles modeling [246] is a useful tool that complements experimental studies and provides additional information about microscopic properties of a metal surface/adsorbed molecule interface.

Complete modeling of a molecule chemisorbed on a rough metal surface requires multi-scale simulations, in which the electronic structure of a molecule and its local environment are treated by quantum chemical methods while a larger-scale environment is accounted for by a mean-field approximation. However, to understand the chemical bonding effects in SERS, it is enough to simulate only the local environment of a molecule. This is consistent with the “adatom model” [360], which assumes that the atomic-scale roughness features determine the hot spots on a metal surface. Obviously, such an approach does not account for the electromagnetic enhancement due to the excitation of surface plasmons in the metal. An interference between the chemical and the electromagnetic effects is ignored as well. To get the total enhancement factor one has to use a conventional phenomenological relation [398] which assumes that both effects enter in multiplicative fashion. In most previous theoretical studies of SERS, only a few metal atoms were used to model the molecule/surface interaction. For instance, in Ref. [30]. the authors considered a complex with a single Ag atom to mimic a chemisorption of phthalimide on a silver surface and obtained a reasonable agreement with experiments. Recently, Schatz and co-workers reported a resonance Raman response calculation procedure using phenomenological lifetime parameters for electronic polarizability derivatives. [247] This procedure has been applied to study SERS of pyridine adsorbed on silver clusters up to a few tens of atoms [616, 248, 358]. The authors identified three different mechanisms contributing to SERS: change in static polarizability of the molecule upon adsorption, resonant enhancement due to charge-transfer transitions, and electromagnetic enhancement due to coupling with a strong excitation in a metal cluster, and discussed their role in SERS. In Ref. [358] some examples of different molecules and pyridine with substituents have been considered. However, no systematic studies of other

molecular structures have been done yet. Given the differences in the chemical bonding of pyridine and thiols to metal surfaces, it is important to know how general these findings are and whether they can be applied to other types of metal–molecular coupling or to other molecules.

In this paper, we address effects related to chemical bonding on Raman scattering from benzenethiol adsorbed on silver clusters Ag_n , $n = 6 - 11$, which is one of the most commonly used analytes in SERS experiments. We link the enhancement of Raman response to the modification of the molecular electronic structure due to adsorption. Excitation energies and transition moments of the metal–molecular complexes are substantially different from those of bare metal clusters and of isolated benzenethiol. For off-resonant excitations, Raman response is enhanced by one order of magnitude. To understand the importance of the cluster geometry, we modeled a pool of 7 different metal–molecular complexes. We identify the effects that contribute to the off-resonant Raman enhancement, such as the *molecular orientational effect*, the effect of the *local symmetry* of the adsorbate, and the effect of the *proximity* of the vibrational mode to a binding site. Stochastic modulation of these effects by thermal motion is related to “blinking” events observed in recent SERS experiments on 4-aminobenzenethiol [157, 564]. We compare the computed vibrational frequency shifts and relative Raman scattering cross sections of the the metal–molecular complexes to experimental SERS data for benzenethiol adsorbed on silver surfaces [60, 91, 7, 337].

Our theoretical approach to compute Raman scattering cross section is based on analytical derivatives of frequency-dependent polarizabilities [432]. The frequency dependence of polarizability derivatives includes resonance enhancement effects in an approximate fashion, which allows us to describe both off-resonance and resonance enhancement effects on an equal footing and to study resonance excitation profiles of Raman scattering cross sections. However, this approach does not take into account the finite lifetime of the excited states. As a result, the Raman scattering cross sections computed within our approach diverge in the strictly resonant case.

We demonstrate that formation of mixed metal–molecular electronic states results in a resonance structure in the Raman excitation profiles (REPs) for molecular vibrations within the excitation range 1.6 – 3.0 eV, which is far below the purely intramolecular transitions. Our lower-bound estimates of the Raman signal enhancement due to chemical bonding is of the order of $10^2 - 10^3$ in the absence of intramolecular resonances. The chemical bonding effect thus provides additional flexibility in controlling the enhancement of Raman scattering from chemisorbed species.

The paper is organized as follows: in Sec. 2.2 we describe the details of our computational procedure. In Secs. 2.3.1–2.3.4 the computed results are presented and different

mechanisms contributing to the Raman enhancement are discussed. In particular, we show that the orientation of the benzene ring has a substantial effect on the Raman scattering cross section. We also identify metal–molecular states responsible for the resonant enhancement of the Raman response of the computed complexes. In Sec. 2.3.5 the computed Raman spectra are compared to available experimental data. The conclusions are formulated in Sec. 2.4.

2.2 Computational details

Density functional calculations were performed using the quantum chemistry package Turbomole, version 5.10 [9, 537]. Triple- ζ valence-polarization basis sets (def2-TZVP [571]) were used for the main group elements while for silver atoms we employed split-valence basis sets with polarization (def2-SV(P) [465]) and effective core potentials (ECP) comprising the 28 core electrons and accounting for scalar relativistic effects [24]. Preliminary calculations showed that expanding the molecular basis set up to quadruple- ζ quality [571] does not significantly alter the results.

Our choice of the computed exchange-correlation functional was guided by the balance between the accuracy of the computed Raman scattering cross sections and an accurate description of electronic and geometric parameters of Ag_n clusters. We chose the hybrid functional of Perdew, Burke, and Ernzerhof (PBE0) [414] which provides good accuracy for frequency-dependent polarizabilities and Raman scattering cross sections [544, 543]. While many computational studies of metal clusters have been traditionally performed with gradient-corrected exchange-correlation functionals [209, 38], hybrid functionals were found to yield good structural parameters and band gaps in extended systems [328].

The charge-transfer error of approximate exchange-correlation functionals is a significant challenge in TDDFT calculations, although several recent works have proposed approaches to address this problem [324, 408, 588, 415]. The charge-transfer error results in an overestimation of electronic polarizabilities and an underestimation of electronic excitation energies, however these effects are ameliorated by inclusion of a fraction of non-local Hartree-Fock exchange in hybrid functionals such as PBE0 [543, 408], which we use in this chapter.

Ground state structure optimizations of silver clusters Ag_n with $n = 6$ –11 were performed using the PBE0 functional. Force-constant calculations were used to confirm that the optimized structures correspond to local minima of the electronic potential energy surface [123]. Many energetically close-lying structure minima are known to exist in small Ag_n clusters [209, 232, 233]. We concentrated on structures suitable to represent atomic-scale roughness features, especially those with pyramidal or bipyramidal shape. For instance,

for the Ag_6 cluster the pyramidal C_{5v} isomer, which might be considered as a more realistic model for atomic-scale roughness, rather than the lowest-energy planar structure of D_{3h} symmetry [209, 232] was used. For each optimized cluster structure, the 200 lowest electronic excitations were computed using TDDFT in the frequency-based linear response regime [92, 44, 161]. The obtained line spectra were broadened using an empirical Gaussian broadening parameter of 0.05 eV.

Oxidative attachment of the benzenethiol molecule [37, 241] was modeled by placing the benzenethiol radical (PhS) at different atomic binding sites and fully reoptimizing the structures of the PhS- Ag_n complexes. Raman spectra of benzenethiol and PhS- Ag_n complexes were obtained from analytical derivatives of frequency-dependent polarizabilities [432]. This approach is based on the polarizability Lagrangian and allows for efficient computation of Raman spectra of medium-sized and large molecules. Raman spectra of benzenethiol and PhS- Ag_n complexes were computed for a low-energy excitation of 0.62 eV (2000 nm) to investigate the off-resonance Raman scattering enhancement. Raman excitation profiles of benzenethiol and PhS- Ag_n were computed for the range of 1.6–3.0 eV for the four strongest vibrational modes of the benzenethiolate group. No scaling of vibrational frequencies was applied. The Raman spectra were simulated by Lorentzian broadening of the line spectra using an empirical linewidth of 5 cm^{-1} . A scattering angle of 90 degrees and perpendicular polarization of both incident and scattered radiation was assumed unless specified otherwise.

2.3 Results and discussion

2.3.1 Silver clusters and metal–molecular complexes

The computed structures of the clusters Ag_n , $n = 6 - 11$, are in agreement with results of previous works [209]. The clusters with an even number of atoms n were found to be closed-shell singlets while the odd-numbered clusters are spin doublets. The relative energies of the structures are dependent on the particular choice of the exchange–correlation functional. Among the simulated structures, several metal clusters were selected based on their similarity in geometry. In particular, the geometries derived from the bipyramidal structure of Ag_7 were chosen.

The benzenethiol molecule binds to the Ag metal surface via the thiolate bond. To construct the metal–molecular complexes the central atom of the bipyramid has been chosen as a binding site. The final optimized geometries of PhS- Ag_n , $n = 6 - 11$, are shown in Fig. 2.1. In most configurations the sulfur atom migrates to the middle of an Ag-Ag bond forming a bridging motif. This is consistent with previous theoretical studies of benzenethiol chemisorbed on Au surfaces [369]. For a better understanding of properties of

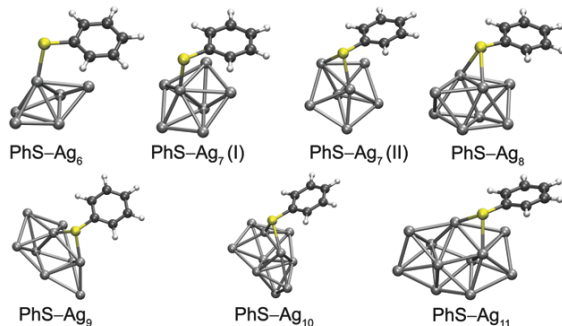


Figure 2.1: Optimized geometries of PhS-Ag_n , $n = 6 - 11$ complexes that were utilized in the study. For $n = 7$ two isomers with different types of binding for the molecule were considered.

the PhS-Ag_n complexes the simplest structure—benzenethiol bound to a single Ag atom—has been simulated. Addition of benzenethiol to the C_{5v} -symmetric Ag_6 cluster leads to a rearrangement of the metal atoms to form a C_{2v} -symmetric cluster structure, see Fig. 2.1. However, we find that the C_{2v} structure of Ag_6 does not correspond to a local minimum for the PBE0 functional. Starting with approximately similar initial conditions, two stable isomers of the PhS-Ag_7 complex with an on-top and a bridging binding motif have been obtained, respectively. The energy difference between these two structures is approximately 3 kcal/mol, with the lower configuration corresponding to the complex with the bridging motif.

The structural characteristics of the PhS-Ag_n , $n = 1, 6 - 11$, complexes are given in Table 2.1. They include the lengths of the Ag-S and the S-C bonds, the angle C-S-Ag (for the bridging motif the calculated angle is between the S-C bond and a shortest line connecting the sulfur atom with the nearest Ag-Ag bond), and the distance between the carbon atom adjacent to the S-C bond and the closest silver atom. The latter parameter characterizes the shortest non-bonding distance between the benzene ring and the Ag_n cluster. The binding energies between benzenethiol and silver clusters were estimated as

$$E_b(\text{PhS-Ag}_n) = E(\text{Ag}_n) + E(\text{PhSH}) - E(\text{PhS-Ag}_n) - \frac{1}{2}E(\text{H}_2), \quad (2.1)$$

neglecting the basis set superposition errors.² The variation of the Ag-S and C-S bond lengths for the complexes with the same type of binding is less than 4 %. The angle between the C-S and Ag-S bonds is consistent with the experimental data obtained for benzenethiol

²The basis set superposition error of a pyridine molecule attached to an Ag_{20} to be ca. 0.7 kcal/mol [616].

Complex	Binding	Ag-S	C-S	\angle C-S-Ag	C ₂ -Ag	E_b
PhS-Ag ₁	on-top	2.339	1.769	102.830	3.975	12.34
PhS-Ag ₆	on-top	2.389	1.756	101.470	2.454	7.56
PhS-Ag ₇ (I)	on-top	2.421	1.757	96.606	2.669	17.71
PhS-Ag ₇ (II)	bridge	2.521/2.589	1.768	103.673	2.629	20.67
PhS-Ag ₈	bridge	2.573/2.587	1.767	109.449	2.600	3.31
PhS-Ag ₉	bridge	2.429/2.458	1.774	109.682	3.646	25.06
PhS-Ag ₁₀	bridge	2.480/2.495	1.769	108.946	3.684	15.37
PhS-Ag ₁₁	bridge	2.544/2.546	1.768	105.044	2.523	23.32

Table 2.1: The computed structural properties of PhS-Ag_n, $n = 1, 6 - 11$, complexes. The lengths of the Ag-S and the C-S bonds, and the shortest distance between the aromatic ring and the cluster, C₂-Ag, are given in Å. The C₂ denotes a carbon atom adjacent to the C-S bond. The angle C-S-Ag is given in degrees and the binding energy of a molecule and a cluster is calculated according to Eq. 2.1 in kcal/mol.

adsorbed on Au (111) [578]. There are no obvious correlations of the structure parameters with the size of the Ag_n clusters. The binding energies vary substantially for the complexes. PhS-Ag_n complexes with odd n form closed-shell electronic configurations and have larger binding energies.

Two types of benzene ring orientation are distinguishable. In the complexes PhS-Ag_n, $n = 6, 7, 8, 11$ the benzene ring oriented towards the metal cluster, allowing several non-bonding C-Ag interactions. In the complexes PhS-Ag_n, $n = 9, 10$ the benzene ring is directed outward and the distance between the ring and the Ag_n cluster is about 40 % longer than in the previous type.

In the following sections, we provide a detailed analysis of the computed optical and Raman spectra of PhS-Ag_n complexes using representative examples of the aforementioned binding structures and molecule orientations. The spectra of the other complexes are provided in Section 2.5.

2.3.2 Electronic excitation spectra.

The electronic excitations of neat benzenethiol are in the ultraviolet spectral range. The computed energies of the two lowest a' transitions, 4.87 eV and 5.37 eV, are in good agreement with the measured values of 4.42 eV and 5.25 eV for benzenethiol in a solution, respectively [474]. The simulated absorption spectra of bare silver clusters are consistent with the experimental data from Ref. [209]. In the energy range of 3–5 eV, the clusters of higher symmetry, such as Ag₇ (D_{5h}) and Ag₁₀ (D_{2d}), have few strong transitions with oscillator strengths higher than 1. The low-frequency parts of the absorption spectra overlap

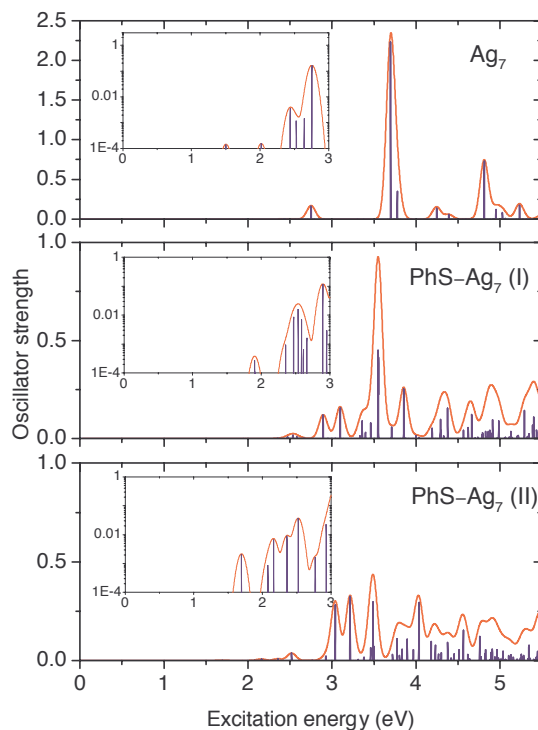


Figure 2.2: Electronic excitation spectra of Ag_7 cluster and two isomers of the PhS-Ag_7 complex with different types of binding on-top and bridge. The insets show the low-frequency parts of the spectra in logarithmic scale for the range 1.0 – 3.0 eV.

with the visible range and some extend down to 0.5 eV. They consist of weak transitions with oscillator strengths in the range $10^{-1} - 10^{-4}$. As an example, the electronic excitation spectra of the Ag_7 cluster and two isomeric complexes PhS-Ag_7 (I) and (II) are shown in Fig. 2.2. The spectra of the complexes differ substantially from the spectra of the corresponding silver clusters. In contrast to silver-pyridine complexes [248], the strong electronic transitions are quenched in most of the studied PhS-Ag_n structures. In the cases where these excitations are still identifiable, we observe a red-shift of the order of 0.1–0.2 eV, see Fig. 2.2, except for the PhS-Ag_{10} complex where the transition is blue-shifted by about 0.1 eV.

2.3.3 Off-resonance Raman spectra

Off-resonance Raman spectra of benzenethiol and of PhS-Ag_n , $n = 6 - 11$, complexes were simulated using an excitation energy of 0.62 eV (2000 nm), which is below the lowest electronic transition in these systems. Three different quantities have been computed:

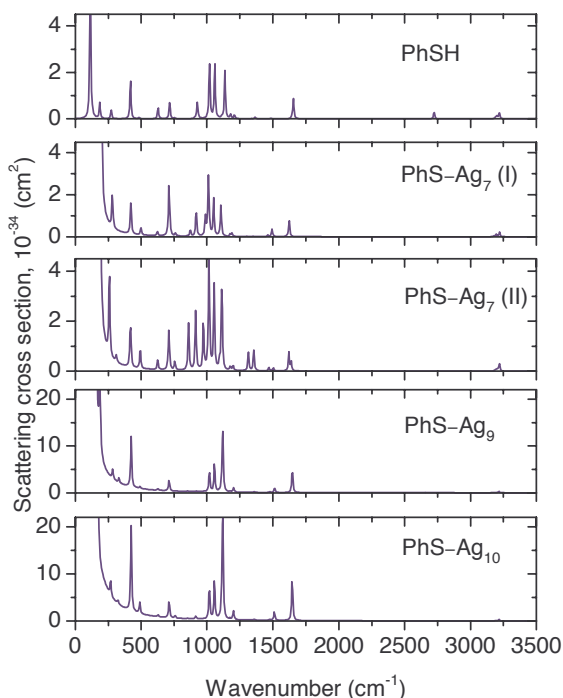


Figure 2.3: The computed Raman spectra of isolated benzenethiol (PhSH) and four different complexes PhS-Ag₇ (I) and (II), PhS-Ag₉, and PhS-Ag₁₀ for the excitation energy 0.62 eV (2000 nm), which is below all electronic transitions in the complexes.

Raman cross sections for characteristic molecular vibrational modes; the total scattering cross section of the complex, and the integrated cross section with a low-frequency cutoff at 200 cm⁻¹. The latter quantity excludes almost all vibrational modes of the metal cluster. Most important for SERS applications are molecular vibrational modes about 1000 cm⁻¹. Enhancement of the scattering cross sections of these modes is used to characterize the surface enhancement. However, the integrated cross sections are introduced to analyze the modulations of the Raman response rather than for estimation of the enhancement factor. The computed Raman spectra are given in Fig. 2.3.

The computed Raman spectrum of isolated benzenethiol is in reasonable agreement with the experimental off-resonant spectrum of neat benzenethiol recorded for a 785 nm excitation [60]. The dominant vibrational modes in the Raman spectrum of benzenethiol are totally symmetric and belong to the *a'* irreducible representation of the *C_s* point group. The computed vibrational band at $\omega_1 = 1019$ cm⁻¹ is assigned to the ring breathing mode, and the band at $\omega_2 = 1059$ cm⁻¹ corresponds to a ring deformation mode. The C-S stretching mode is computed at $\omega_3 = 1136$ cm⁻¹ while the computed Raman band at

Complex	α_{ISO}	E_{gap}	$\sigma_4 \times 10^{-33}$	σ_{tot}	w
PhSH	85.8	5.96	1.39	$3.34 \cdot 10^{-32}$	64.0
PhS-Ag ₁	130.7	3.35	16.50	$1.53 \cdot 10^{-30}$	10.2
PhS-Ag ₆	351.7	1.53	1.63	$2.16 \cdot 10^{-30}$	2.8
PhS-Ag ₇ (I)	365.2	2.80	1.35	$1.04 \cdot 10^{-30}$	2.7
PhS-Ag ₇ (II)	374.9	2.54	0.64	$1.23 \cdot 10^{-30}$	4.8
PhS-Ag ₈	425.6	1.34	0.48	$1.67 \cdot 10^{-30}$	4.3
PhS-Ag ₉	478.2	2.09	7.98	$1.35 \cdot 10^{-29}$	0.6
PhS-Ag ₁₀	529.3	1.22	14.43	$2.28 \cdot 10^{-29}$	0.6
PhS-Ag ₁₁	568.8	1.95	1.00	$1.81 \cdot 10^{-30}$	4.0

Table 2.2: Isotropic polarizabilities α_{ISO} (a.u.), HOMO-LUMO gaps (eV), Raman cross sections for the $\omega_4 = 1583 \text{ cm}^{-1}$ vibrational mode σ_4 (cm^2), integrated Raman scattering cross sections σ_{tot} (cm^2), and fractions w (%) of Raman scattering cross section from modes with frequencies larger than 200 cm^{-1} for benzenethiol (PhSH) and PhS-Ag_n complexes. The excitation wavelength is 2000 nm.

$\omega_4 = 1656 \text{ cm}^{-1}$ is associated with a totally symmetric ring stretching mode. Our results are consistent with previous assignments [188]. The computed vibrational frequencies of benzenethiol are blue-shifted by 10–50 cm^{-1} with respect to experimental data due to incomplete basis sets and neglect of anharmonicity. The totally symmetric modes assigned above correspond to the experimentally measured vibrational frequencies $\omega_1^{\text{exp}} = 1004 \text{ cm}^{-1}$, $\omega_2^{\text{exp}} = 1027 \text{ cm}^{-1}$, $\omega_3^{\text{exp}} = 1094 \text{ cm}^{-1}$, and $\omega_4^{\text{exp}} = 1583 \text{ cm}^{-1}$, respectively, for neat benzenethiol [60]. Comparison of computed Raman intensities of isolated benzenethiol to experimental data is provided in Section 2.5.

Binding of benzenethiol to Ag_n clusters leads to an overall increase of off-resonant Raman scattering cross sections and to a significant redistribution of band intensities in the Raman spectrum. This effect is known as the *static enhancement* mechanism of SERS [360]. This effect has been attributed to the decrease of the energy gap between the highest occupied molecular orbital (HOMO) and the lowest unoccupied molecular orbital (LUMO) and the ensuing enhancement of the electronic polarizability and its derivatives [358]. The Raman cross section of the molecular vibrational modes ω_{1-4} in the computed metal–molecular complexes can be up to 10 times larger than that in isolated benzenethiol. This value is comparable to the results of Ref. [616] for pyridine. However, we observe a strong dependence of the enhancement factor on the geometry of a metal cluster and the orientation of the molecule. For example, the Raman signal from the modes ω_{1-4} in PhS-Ag₇ (I and II) complexes is almost unenhanced compared to PhSH, see Fig. 2.3. Also, Raman signals from different molecular modes have different enhancement factors. To characterize the off-resonant enhancement of Raman scattering, the cross sections of the ω_4 vibrational

mode have been used. Table 2.2 shows the computed off-resonant electronic polarizabilities, HOMO-LUMO gaps, Raman cross sections corresponding to the ω_4 vibrational mode, and integrated Raman scattering cross sections of benzenethiol and PhS-Ag $_n$ complexes for the excitation energy of 0.62 eV (2000 nm). The integrated cross sections are computed by summation of Raman scattering cross sections over all vibrational modes of the complex, including the vibrations of the metal cluster. The electronic polarizabilities are to a good approximation additive and thus increase linearly with the number of Ag atoms. The integrated Raman scattering cross sections of PhS-Ag $_n$ complexes are larger than that of benzenethiol by 2–3 orders of magnitude but do not increase monotonically with the cluster size n . Molecular vibrational modes contribute only a small fraction (less than 5 % with the exception of PhS-Ag, see Table 2.2) to the integrated Raman scattering cross section while the largest part of the scattered radiation arises from vibrations within the metal cluster.

Orientation effect. We find a significant dependence on the orientation of the benzene ring: the largest integrated Raman scattering cross sections are computed for the complexes PhS-Ag $_n$, $n = 9, 10$, in which the benzene ring points outward from the cluster surface, see Fig. 2.1. In contrast, in the PhS-Ag $_n$, $n = 6 - 8, 11$ complexes the aromatic ring is oriented towards the metal cluster and non-binding C-Ag interactions reduce the integrated Raman scattering cross sections by about one order of magnitude. This orientation effect appears to be the major influence in the off-resonance Raman spectra of PhS-Ag $_n$ complexes, while the effect of increasing electronic polarizability and the characteristic alternation of HOMO-LUMO gaps in between even- and odd-numbered metal clusters Ag $_n$ seem to be less important. The non-binding interactions of the benzene ring with the Ag $_n$ cluster in the PhS-Ag $_n$, $n = 6 - 8, 11$ complexes result in an efficient quenching of Raman scattering from metal cluster modes, increasing the relative weight of molecular vibrations.

Symmetry effect. The relative intensities of vibrational modes in Raman spectra of PhS-Ag $_n$ complexes might be explained based on their symmetry and proximity to the Ag $_n$ cluster. Comparison of the Raman spectra of the isomers PhS-Ag $_7$ (I) and PhS-Ag $_7$ (II) exemplifies the effect of the local symmetry of the benzene ring on the off-resonant enhancement. The PhS-Ag $_7$ (I) isomer is, similar to the isolated benzenethiol molecule, C_s -symmetric while the local symmetry of the benzene ring in the PhS-Ag $_7$ (II) isomer is perturbed by unsymmetric bonding to the cluster. The symmetry of the benzene ring affects the aromatic C-C stretching bands in the region of 1620–1660 cm^{-1} . Only the totally symmetric aromatic C-C stretching vibration ($\omega_4 = 1656 \text{ cm}^{-1}$ in benzenethiol, denoted as $8a$ in Wilson’s notation [582]) is observed in the Raman spectra of PhSH and PhS-Ag $_7$ (I) while the corresponding non-totally symmetric vibration at lower frequency (1641 cm^{-1} in benzenethiol, $8b$ in Wilson’s notation) is at least one order of magnitude weaker and not observed in the experiment. The lower symmetry of the PhS-Ag $_7$ (II) manifests itself in

the redistribution of Raman scattering cross sections among the aromatic C-C stretching modes such that the lower-frequency $8b$ mode gains intensity. As a consequence, a doublet of vibrational bands is formed in the aromatic C-C stretching region. In the PhS-Ag $_n$, $n = 9, 10$, complexes, the interaction between the benzene ring and the Ag $_n$ cluster is weak and local C_s symmetry of the benzene ring is essentially unperturbed. This results in only one observable aromatic C-C stretching band in the Raman spectra of these complexes.

Proximity effect. The proximity effect on the Raman scattering cross section may be observed in the region between 1000–1150 cm^{-1} , including ring deformation modes at $\omega_1 = 1019 \text{ cm}^{-1}$ and $\omega_2 = 1059 \text{ cm}^{-1}$ and the C-S stretching mode at $\omega_3 = 1136 \text{ cm}^{-1}$ in benzenethiol, respectively. In both PhS-Ag $_7$ (I) and PhS-Ag $_7$ (II) clusters, the ring breathing mode at 1011–1015 cm^{-1} and the ring deformation mode at 1050–1055 cm^{-1} are strongly enhanced by the interaction with the Ag $_n$ clusters. With benzene rings further away from the Ag $_n$ clusters in PhS-Ag $_n$, $n = 9, 10$, enhancement of ring deformation modes is diminished in these clusters, while the C-S stretching mode is more pronounced.

All three effects governing off-resonant surface enhancement of Raman response of PhS-Ag $_n$ complexes, namely the relative orientation of the benzene ring with respect to the cluster, the local symmetry of the benzene ring, and the proximity of the particular vibrational mode to the binding site, are interrelated. Their modulation by thermal large-amplitude motion of the aromatic ring may serve as a simple and plausible explanation for the “blinking” events observed in SERS experiments on 4-aminobenzenethiol attached to Au bowtie nanoantennas [157] or to molecular junctions [564].

2.3.4 Raman excitation profiles

Raman excitation profiles of four strong totally symmetric benzenethiol vibrational modes, $\omega_1 = 1019 \text{ cm}^{-1}$, $\omega_2 = 1059 \text{ cm}^{-1}$, $\omega_3 = 1136 \text{ cm}^{-1}$, and $\omega_4 = 1656 \text{ cm}^{-1}$, were calculated for the excitation energy range 1.6 – 3.0 eV (413 – 775 nm). These modes are dominant in experimental SERS spectra of benzenethiol [60, 91].³

In Figs. 2.4 and 2.5 we provide REPs and electronic excitation spectra of four different complexes PhS-Ag $_7$ (I), PhS-Ag $_7$ (II), PhS-Ag $_9$, and PhS-Ag $_{10}$ in logarithmic scale. For comparison we also show REP of isolated benzenethiol averaged over all four modes. The simulated scattering cross sections for the vibrational modes ω_{1-4} in isolated benzenethiol differ by no more than a factor of two, therefore an averaged value of REP of benzenethiol (dashed line) is used to simplify the plots. The slope of the REP of benzenethiol is close to 4 and stems from the ω^4 dependence of Raman scattering cross sections [315]. The effect

³It should be noticed that the vibrational modes of neat benzenethiol are assigned incorrectly in Table I of the reference. For the correct assignment see Ref. [188].

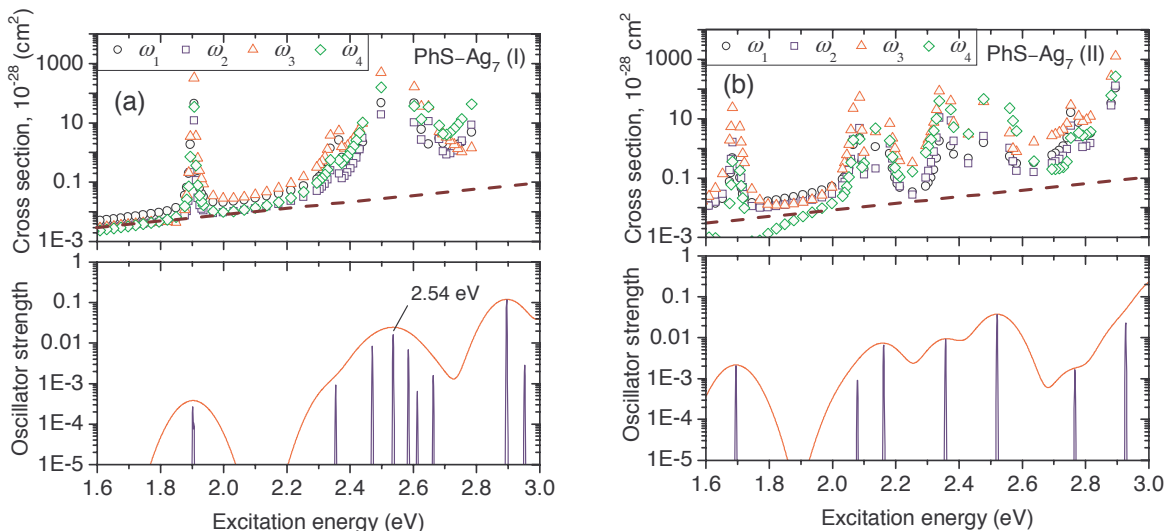


Figure 2.4: The Raman excitation profiles (REPs) together with the electronic excitation spectra for (a) the PhS-Ag₇ (I) and (b) the PhS-Ag₇ (II) complexes. The vibrational modes are $\omega_1 = 1019 \text{ cm}^{-1}$, $\omega_2 = 1059 \text{ cm}^{-1}$, $\omega_3 = 1136 \text{ cm}^{-1}$, and $\omega_4 = 1656 \text{ cm}^{-1}$. The dashed tilted line in the REPs plots corresponds to the response of isolated benzenethiol averaged over all four modes.

of intramolecular resonances is small in the studied range of excitation energies.

The isomers PhS-Ag₇ (I) and (II) in Fig. 2.4 represent two distinct bonding patterns (on-top and bridge), whereas the structure of the silver cluster remains essentially the same. The electronic excitation spectra of the complexes are quite dissimilar, which reflects the sensitivity of the electronic states to the binding pattern. For example, the lowest electronic excitation of the PhS-Ag₇ (II) complex is 0.2 eV lower in energy than that of the PhS-Ag₇ (I) complex. All transitions within the excitation range 1.6 – 3.0 eV are weak with oscillator strengths $10^{-1} - 10^{-4}$.

Cluster-molecule resonant effect. The REPs illustrate the frequency dependence of SERS and allow for identification of two different contributions to chemical Raman enhancement. These are the baseline shifts of the REPs of the complexes compared to that of isolated benzenethiol and the additional modulation by resonance-type features. The baseline shift is attributed to the off-resonant enhancement discussed in the previous section while the resonances arise from electronic transitions between metal–molecular states. This is consistent with the conventional picture of chemical enhancement [246]. The off-resonant enhancement factor for both isomers of the PhS-Ag₇ complex is of the order of 1 and can be explained by the orientational effect discussed in the previous section.

The relative enhancement for different modes depends on the excitation energy. For

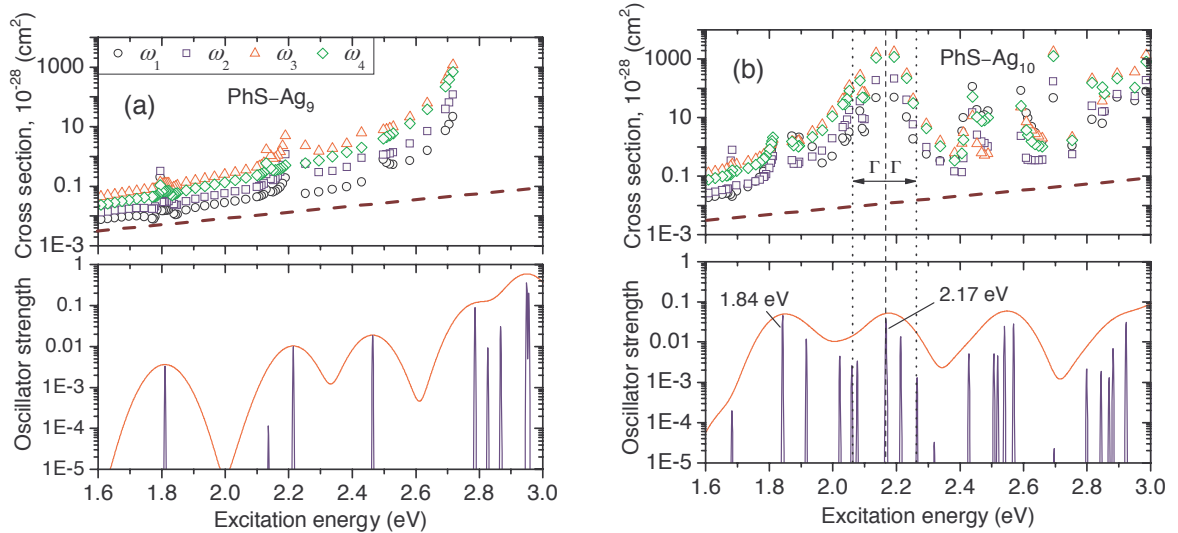


Figure 2.5: The Raman excitation profiles together with the electronic excitation spectra for (a) the PhS-Ag₉ complex and (b) the PhS-Ag₁₀ complex. The vibrational modes are $\omega_1 = 1019 \text{ cm}^{-1}$, $\omega_2 = 1059 \text{ cm}^{-1}$, $\omega_3 = 1136 \text{ cm}^{-1}$, and $\omega_4 = 1656 \text{ cm}^{-1}$. The dashed tilted line in the REPs plots corresponds to the response of isolated benzenethiol averaged over all four modes. $\Gamma = 0.1 \text{ eV}$ is a phenomenological parameter characterizing homogeneous linewidth of electronic states.

example, the ω_1 vibrational mode has the largest enhancement for the PhS-Ag₇ (I) complex in the energy range below the first electronic transition, whereas the ω_3 becomes the strongest Raman mode above it. This observation is in accord with the empirical Tsuboi rule [227]: the lowest electronic excitation in the complex PhS-Ag₇ (I) involves the Ag-S bond and has a larger impact on the C-S stretching mode (ω_3).

The structures of the PhS-Ag₉ and PhS-Ag₁₀ complexes differ only by a single Ag atom, which is located approximately 4.8 Å from the binding sites. The PhS-Ag₉ complex has a closed-shell electronic structure and shows a smaller number of electronic transitions as compared to the PhS-Ag₁₀. Both structures show 10–100 fold enhancements of Raman signals outside of resonant regions. Enhancement factors of different vibrational modes differ by about one order of magnitude. This can be seen by comparing the Raman cross sections of the complexes to that of isolated benzenethiol for the excitation energy 1.6 eV, Fig. 2.5.

Most of electronic excitations shown in Figs. 2.4 and 2.5 result in resonance-type divergences of the REP. However, Raman enhancement in pre-resonant regions cannot be characterized by the oscillator strengths of the respective electronic transitions only. For instance, in the PhS-Ag₁₀ complex the electronic transition at 2.17 eV has an oscillator

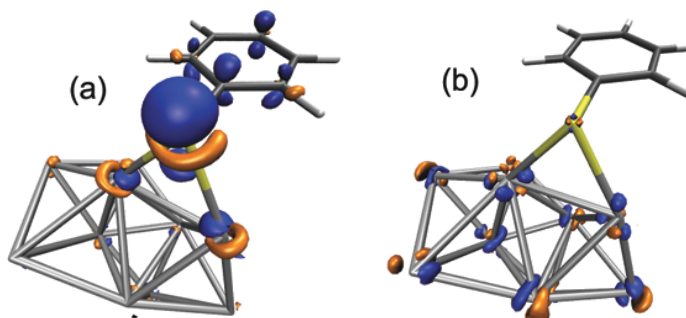


Figure 2.6: The transition electron densities for (a) the 2.17 eV electronic excitation and (b) the 1.84 eV electronic excitation in the PhS-Ag₁₀ complex. The former transition results in the strong resonant features in the REP, whereas the latter one has much weaker effect. The light grey (orange) color corresponds to the transition density of -0.002 a.u., the dark grey (blue) corresponds to the transition density of 0.002 a.u.

strength 0.04, which is smaller than that of the 1.84 eV transition (oscillator strength 0.05). Nevertheless, the former excitation induces a large peak in the REP, see Fig. 2.5 (b), while the latter has a much smaller effect. These two excitations differ by the degree to which Ag-S bonds are affected by the electronic excitations, as can be seen in Fig. 2.6. The 2.17 eV electronic excitation is localized around the bonding sites and does not involve all atoms in the Ag_{*n*} cluster, whereas the 1.84 eV electronic excitation is delocalized. This observation lends support to the underlying assumption of this chapter that the effects of chemical bonding on surface enhancement can be modeled to a significant extent using finite-size metal clusters.

The occurrence of strong resonant Raman peaks is a common feature of all considered PhS-Ag_{*n*} complexes. The strong peak in the REP of the PhS-Ag₇ (I) complex is centered around the 2.54 eV electronic excitation, and in the REP of PhS-Ag₉ a similar feature can be associated with the region 2.8 – 3.0 eV.

Our approach does not include finite-lifetime effects and is thus not applicable in a strictly resonant case. The enhancement of a Raman signal at resonances scales inversely proportional to the fourth power of the homogeneous linewidth Γ of the involved electronic states [314]. Since Γ enters as a phenomenological parameter, estimates of the corresponding enhancement factors are inherently imprecise. To obtain lower-bound estimates of resonant enhancement factors we consider the Raman scattering cross section at frequencies $\Omega_i \pm \Gamma$, where Ω_i stand for electronic excitation frequencies. For Γ we use a pragmatic value 0.1 eV, which is consistent with Ref. [616]. The estimated enhancement of Raman signal near the 2.17 eV electronic transition in the PhS-Ag₁₀ complex is of the order of 10^3 and varies about 10 times for different vibrational modes. Similar estimates are also obtained for other

structures.

Usually, in SERS literature the enhancement below intramolecular excitations is associated with charge-transfer excitations that have very small oscillator strengths. For example, in Ref. [616] electronic transitions at energies comparable to those considered here were found in a pyridine-Ag₂₀ complex, with enhancements that were also about 10³. The excitations were referred to as charge-transfer states. In our system, all electronic transitions in the excitation range 1.6 – 3.0 eV have a mixed metal–molecular character and can be associated with a partial charge transfer between the cluster and the molecule. However, most of them have only a small contribution to the resonance Raman enhancement. Thus, besides narrow singularities, the computed cross sections are relatively smooth functions of the excitation energy. For example, the 1.9 eV excitation in PhS-Ag₇ (I) complex, see Fig. 2.4, gives almost no enhancement of the Raman signal if we take into account the finite linewidth of the transition. The important excitations, such as the excitation shown in Fig. 2.6 (a), are local to the binding site and are characterized by the change of the electron density around the binding sites only. It is important to notice that the difference in the static dipole between a ground and an excited state of the complexes for such transitions is rather small. For example, the change in the static dipole moment for the excitation of the PhS-Ag₁₀ complex depicted in Fig. 2.6 (a) is 3.7 Debye.

2.3.5 Discussion

Many important features of experimental SERS results for benzenethiol [60, 91, 7, 337] are reflected in the computed Raman spectra of the PhS-Ag_n complexes. The molecular vibrational frequencies of the complexes are shifted compared to that of isolated benzenethiol. The frequency shifts of intense *a'* modes of the complexes PhS-Ag₇ (I) and (II), PhS-Ag₉, and PhS-Ag₁₀ are compared to experimental SERS data in Table 2.3. The values and the signs of the computed shifts are in good agreement with the results of measurements. The magnitudes of the frequency shifts depend on the degree to which the C-S bond is involved in the given vibration. For instance, the C-S stretching mode $\omega_3^{\text{exp}} = 1094 \text{ cm}^{-1}$ shows the largest shift on average, which is an additional manifestation of the proximity effect discussed in Sec. 2.3.3.

Comparisons of the computed Raman cross sections of the PhS-Ag_n complexes to experimental SERS data should take into account that the chemisorbed molecules are no longer freely rotating. This has the effect that the orientational averaging of the Raman tensor depends on the shape of the metal substrate and the relative orientation of the adsorbed molecules. As a model, we consider benzenethiol molecules adsorbed on a spherical nanoparticle. The computed PhS-Ag_n structures are oriented such that in the complexes with on-top binding, $n = 6, 7(\text{I})$, the Ag-S bond is orthogonal to the particle surface, and

Mode	ω_1	ω_2	ω_3	ω_4	ω_5	ω_6	ω_7
Freq. PhSH	1004	1027	1094	1583	414	701	918
PhS-Ag ₇ (I)	-7	-9	-31	-33	1	4	-8
PhS-Ag ₇ (II)	-4	-5	-24	-17	3	6	-12
PhS-Ag ₉	-1	-2	-18	-8	6	-4	-5
PhS-Ag ₁₀	-1	-3	-18	-9	5	-4	-11
Ref. [60]	-1	0	-18	-7	8	-6	-
Ref. [91]	0	1	-17	-9	6	-3	-
Ref. [7]	-1	-2	-21	-11	5	-8	-

Table 2.3: Frequency shifts of benzenethiol Raman-active vibrational modes due to binding to the metal. The values of the vibrational frequencies are taken for neat benzenethiol from Ref. [60]. The shifts for the computed complexes, calculated as $\Delta\omega_n = \omega_n(\text{PhS-Ag}_k) - \omega_n(\text{PhSH})$, are compared with the shifts of Raman lines, $\Delta\omega_n = \omega_n(\text{SERS}) - \omega_n(\text{PhSH})$, from the experimental studies, Refs. [60, 91, 7]. The frequencies are given in cm^{-1} .

in the complexes with the bridge binding motif, $n = 7(\text{II}), 8 - 11$ the plane formed by the two Ag-S bonds is orthogonal to the particle surface. The Raman intensity of a vibrational mode with frequency ω_n is [119]

$$I(\omega_n, \omega_{\text{ex}}) \propto (\omega_{\text{ex}} - \omega_n)^4 |g(\omega_{\text{ex}})|^2 |g(\omega_{\text{ex}} - \omega_n)|^2 f(\alpha_n(\omega_{\text{ex}})), \quad (2.2)$$

where ω_{ex} is the excitation frequency, and the electromagnetic enhancement factor is

$$g(\omega) = \frac{\epsilon_p(\omega) - \epsilon_{\text{env}}}{\epsilon_p(\omega) + 2\epsilon_{\text{env}}}. \quad (2.3)$$

ϵ_p stands here for the dielectric constant of the metal particle and includes the plasmon resonance, and ϵ_{env} is the dielectric constant of the environment, which is considered as not strongly frequency-dependent. $\alpha_n(\omega_{\text{ex}})$ denotes the Raman tensor of the mode n , and the orientational averaging function is given by

$$f(\alpha) = 4(\alpha_{11}^2 + \alpha_{22}^2 + 16\alpha_{33}^2) + \alpha_{11}\alpha_{22} + 4\alpha_{11}\alpha_{33} + 4\alpha_{22}\alpha_{33} + 7(\alpha_{12}^2 + 4\alpha_{13}^2 + 4\alpha_{23}^2). \quad (2.4)$$

The orientational averaging used here [119] is different from the isotropic averaging that has been utilized in the previous sections. Particularly convenient for comparison with experiment are relative Raman scattering cross sections which are defined as

$$\frac{I(\omega_n, \omega_{\text{ex}})}{I(\omega_{\text{ref}}, \omega_{\text{ex}})} = \frac{g^2(\omega_{\text{ex}} - \omega_n)}{g^2(\omega_{\text{ex}} - \omega_{\text{ref}})} \cdot \frac{(\omega_{\text{ex}} - \omega_n)^4 f(\alpha_n)}{(\omega_{\text{ex}} - \omega_{\text{ref}})^4 f(\alpha_{\text{ref}})}, \quad (2.5)$$

where ω_{ref} is a frequency of the reference vibrational mode. The first multiplier on the right-hand side of Eq. 2.5 represents the relative electromagnetic enhancement of the Raman

Mode	ω_1	ω_3	ω_4	ω_5	ω_6	ω_7
Freq. PhSH	1004	1094	1583	414	701	918
PhS-Ag ₇ (I)	1.2	1.4	2.7	0.4	0.5	1.0
PhS-Ag ₇ (II)	1.2	1.4	0.5	0.1	0.2	1.6
PhS-Ag ₉	0.6	3.4	2.8	0.7	0.2	0.0
PhS-Ag ₁₀	0.6	5.1	4.5	1.1	0.3	0.0
Ref. [60]	1.3	1.4	0.6	0.6	0.3	-
Ref. [91]	1.4	1.3	1.3	1.0	0.4	-
Ref. [7]	1.1	1.0	3.5	2.7	0.4	-

Table 2.4: Relative intensities of Raman lines, defined as $I(\omega_n)/I(\omega_2)$, $\omega_2 = 1027 \text{ cm}^{-1}$, are given for the PhS-Ag_n, $n = 7, 9, 10$ complexes and for the experimental SERS spectra from Refs. [60, 91, 7]. The relative intensities for the complexes are computed using Eq. 2.5 assuming that electromagnetic enhancement is frequency independent, $g(\omega) = \text{const}$. The mode $\omega_7 = 918 \text{ cm}^{-1}$ is not observable in the SERS experiments. The excitation wavelength is 785 nm. The vibrational frequencies of neat benzenethiol [60] are given in cm^{-1} .

scattering due to plasmon excitations in the metal particle. The chemical bonding of a molecule to a surface modifies the Raman tensor α and contributes to the second multiplier of Eq. 2.5.

The computed relative intensities of several Raman lines for the complexes PhS-Ag₇ (I) and (II), PhS-Ag₉, and PhS-Ag₁₀ are compared to the experimental data in Table 2.4. Experimental SERS cross sections depend sensitively on the structure of the surface and the roughness features of the SERS substrate and are thus strongly influenced by the preparation technique, as illustrated by the differences between the experimental data in Table 2.4. Surface enhanced Raman spectra result from the appropriate averaging over the multitude of possible local bonding configurations. An additional important effect is due to differences in plasmonic resonance structures. Comparison of the experimental data with finite-size cluster models PhS-Ag_n shows that indeed many experimental SERS features may be correlated with the models considered here. For example, all strong Raman lines observed in Ref. [60] belong to the a' representation, similar to the spectra of the PhS-Ag₉ and PhS-Ag₁₀ complexes. However, the relative intensities of the $\omega_3^{\text{exp}} = 1094 \text{ cm}^{-1}$ and $\omega_4^{\text{exp}} = 1583 \text{ cm}^{-1}$ modes are too high as compared to the experimental data. The discrepancy stems from overestimation of the computed Raman intensities for isolated benzenethiol and also from a frequency dependence of electromagnetic enhancement, which is not accounted for in the model. For instance, in Ref. [60] the excitation frequency is optimized to enhance modes about 1000 cm^{-1} .⁴ Thus, the electromagnetic enhancement

⁴ The enhancement factor for a given mode ω_n is maximal if $\omega_{\text{ex}} - \omega_{\text{pl}} \approx \omega_n/2$, where ω_{pl}

of the ω_3 and ω_4 modes is weaker as compared to the 1004 cm^{-1} mode. This trend should reduce the discrepancy between the experimental data of Ref. [60] and the computed spectra of the PhS-Ag₉ and PhS-Ag₁₀ complexes. On the other hand, Refs. [91] and [7] show some enhancement of the vibrational modes at 470 cm^{-1} and 960 cm^{-1} , respectively, which belong to the a'' representation. A possible explanation is that molecular orientations on the metal surface have irregularities and also contain binding situations similar to PhS-Ag₇ (I) and (II), which show considerable enhancement for a'' modes. For instance, the relative intensity of the 960 cm^{-1} mode in PhS-Ag₇ (II) complex is 0.8.

To get an additional verification of our model, relative enhancement factors for the 1094 cm^{-1} and 1583 cm^{-1} vibrational modes of the PhS-Ag₇ (I) and (II), PhS-Ag₉, and PhS-Ag₁₀ complexes have been compared to the enhancement factors measured in Ref. [337]. A relative enhancement factor is defined for two vibrational modes ω_n and ω_{ref} with corresponding excitation frequencies ω_{ex} and $\omega_{\text{ex}'}$ as

$$\frac{\text{EF}(\omega_n, \omega_{\text{ex}})}{\text{EF}(\omega_{\text{ref}}, \omega_{\text{ex}'})} = \frac{g^4(\omega_{\text{ex}})}{g^4(\omega_{\text{ex}'})} \left(\frac{f(\alpha_n)}{f_{\text{iso}}(\alpha_n)} \right) / \left(\frac{f(\alpha_{\text{ref}})}{f_{\text{iso}}(\alpha_{\text{ref}})} \right), \quad (2.6)$$

where $f(\alpha)$ is calculated using Eq. 2.4, $f_{\text{iso}}(\alpha)$ is a similar expression for an isotropic case [315], and the excitation frequencies have been chosen to get a maximal enhancement of corresponding vibrational modes.⁵

Near a plasmonic resonance the first multiplier on the right hand side of Eq. 2.6 can be approximated by the ratio of the extinction coefficients of the plasmonic structure. The computed relative enhancement factors for the ω_3 and ω_4 modes of PhS-Ag_{*n*}, $n = 9, 10$, complex given in Table 2.5 agree well with the experimental data from Ref. [337].

Resonant structure of Raman cross sections discussed in Sec. 2.3.4 is hardly observable in experiments of Refs. [60, 91, 7, 337], where Raman scattering is measured for an inhomogeneous ensemble of molecules with their local environment. However, it can be observed in single molecule experiments. For example, the fine structure of single-molecule REPs measured in Ref. [130] may be interpreted as a result of resonances with mixed metal–molecular states.

2.4 Conclusions

We have analyzed the Raman response of benzenethiol chemisorbed on small silver clusters and find overall enhancement of the response of the order of 10^3 as compared to isolated benzenethiol. Mixed metal–molecular electronic states are formed due to chemical

is the frequency of a plasmonic resonance [337]. At this condition $g(\omega_{\text{ex}} - \omega_n) = g(\omega_{\text{ex}})$.

⁵See Footnote 4.

Mode	ω_1	ω_2	ω_3	ω_4
Freq. SERS	1009	1027	1081	1575
λ_{ex}	705	703	700	692
$g^4(\omega_{\text{ex}})/g^4(\omega_{\text{ex}'})$	1.0	1.0	0.9	0.6
PhS-Ag ₇ (I)	1.0	0.8	1.0	1.4
PhS-Ag ₇ (II)	1.0	0.6	1.0	0.1
PhS-Ag ₉	1.0	1.7	5.3	2.9
PhS-Ag ₁₀	1.0	1.7	7.8	4.6
Ref. [337]	1	-	10	7

Table 2.5: Relative enhancement factors of molecular vibrational modes computed for the PhS-Ag₇ (I) and (II), PhS-Ag₉ and PhS-Ag₁₀ complexes using Eq. 2.6 as compared with the experimental data from Refs. [337]. The reference vibrational mode is $\omega_1^{\text{exp}}(\text{SERS}) = 1009 \text{ cm}^{-1}$. The corresponding excitation wavelength λ_{ex} is in nm. To account for frequency dependence of electromagnetic enhancement the computed values were multiplied by $g^4(\omega_{\text{ex}})/g^4(\omega_{\text{ex}'})$ estimated from the experiments. The vibrational frequencies in cm^{-1} are for benzenethiol on an Ag nanoparticle array from Ref. [337].

bonding. Raman response from the metal–molecular complexes exhibits resonance-type features even in the range far below the onset of molecular electronic excitations. We identify several mechanisms contributing to enhancement of Raman scattering in both off-resonant and resonant regimes. These include the relative orientation of the benzene ring with respect to the cluster, the local symmetry of the benzene ring, and the proximity of the particular vibrational mode to the binding site. Additional enhancement of Raman response by several orders of magnitude arises from resonant excitations localized around the binding sites, whereas response from other excitations in this range is significantly weaker. Specific properties of Raman response are strongly dependent on the local atomic environment of adsorbate. However, important features in SERS of benzenethiol on silver surfaces such as vibrational frequency shifts and relative enhancement factors may be explained using finite-size cluster models. Since the atomic structure of SERS substrates cannot currently be controlled in experiments the described effects should be averaged over a set of possible binding patterns. Nevertheless, our results might provide a guidance for optimization of SERS-active structures and are useful for interpretation of single molecule SERS measurements.

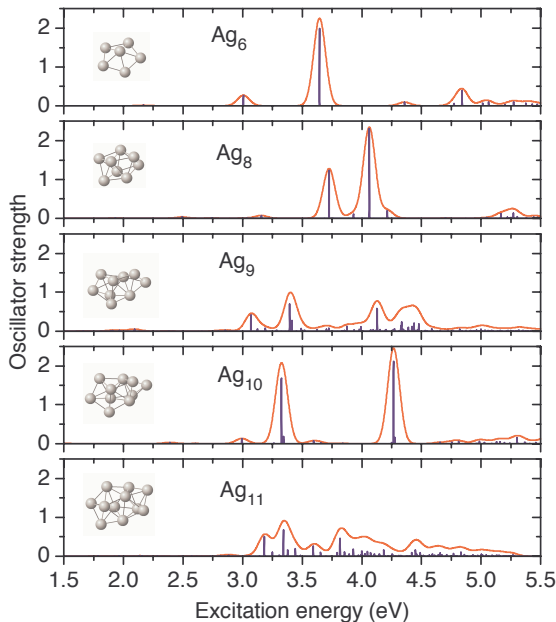


Figure 2.7: Absorption spectra of the computed Ag_n clusters, $n = 6, 8 - 11$.

2.5 Appendix

2.5.1 Electronic excitation spectra

The absorption spectra of the simulated Ag_n clusters and PhS-Ag_n complexes, $n = 6, 8 - 11$ are shown in Figs. 2.7 and 2.8. For $n = 6$, the structure of the silver cluster in the PhS-Ag_n complex differs from the one of the bare silver cluster because of the cluster reconstruction. This is discussed in Sec. 2.3.1 in more detail.

2.5.2 Off-resonance Raman spectra

The relative intensities of the computed Raman lines of isolated benzenethiol as compared to the relative Raman intensities measured for neat benzenethiol [60, 91, 7] are given in Table 2.6. The intensities are in good agreement except of the $\omega_1^{\text{exp}} = 1004 \text{ cm}^{-1}$ vibrational mode. Changing the exchange functional in DFT simulations results in minor improvements only.

The Raman spectra of PhS-Ag_n complexes, $n = 1, 6, 8, 11$ computed at the excitation energy 0.62 eV (2000 nm excitation wavelength) are shown in Fig. 2.9. The excitation energy used is below the lowest electronic transition in the structures. The complex PhS-

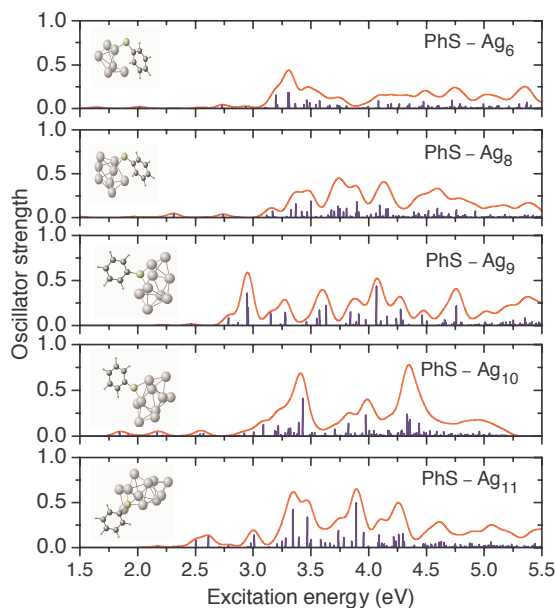


Figure 2.8: Absorption spectra of the computed PhS-Ag_{*n*} complexes, *n* = 6, 8 – 11.

Ag shows a strong enhancement of totally symmetric vibrational modes, while in the other complexes, the non-bonding interaction between the aromatic ring and the cluster results in a suppression of the integrated Raman scattering cross section and a redistribution of intensities between the totally symmetric and non-totally symmetric modes (see Sec. 2.3.2).

2.5.3 Raman excitation profiles

The Raman excitation profiles (REPs) and low-frequency electron excitation spectra for PhSH and PhS-Ag_{*n*} complexes, *n* = 1, 6, 8, 11 for the computed vibrational modes, $\omega_1 = 1019 \text{ cm}^{-1}$, $\omega_2 = 1059 \text{ cm}^{-1}$, $\omega_3 = 1136 \text{ cm}^{-1}$, and $\omega_4 = 1656 \text{ cm}^{-1}$, are shown in Figs. 2.10-2.12. The range of excitation energies is 1.6 – 3.0 eV. In logarithmic scale the REPs for isolated PhSH, Fig. 2.10, are almost linear in the excitation energy, which is consistent with the semiclassical theory of Raman scattering [315]. For the complexes PhS-Ag_{*n*}, *n* = 1, 6, 8, 11, Figs. 2.11-2.12, a resonance-type structure of REPs originates in the electronic excitations to mixed metal-molecular states.

2.5.4 Discussions

The frequency shifts of four totally symmetric vibrational modes $\omega_1 = 1019 \text{ cm}^{-1}$, $\omega_2 = 1059 \text{ cm}^{-1}$, $\omega_3 = 1136 \text{ cm}^{-1}$, and $\omega_4 = 1656 \text{ cm}^{-1}$ in PhS-Ag_{*n*}, *n* = 1, 6 – 11

Mode	ω_1	ω_3	ω_4	ω_5	ω_6	ω_7
Freq. PhSH	1004	1094	1583	414	701	918
PhSH ^{comp}	1.0	1.0	0.9	0.5	0.3	0.4
PhSH ^{exp} Ref. [60]	3.0	0.5	0.3	0.7	0.7	0.3
PhSH ^{exp} Ref. [91]	4.5	0.4	0.4	0.6	0.7	0.2
PhSH ^{exp} Ref. [7]	2.9	0.6	1.0	1.0	0.5	0.4

Table 2.6: The relative intensities of the computed Raman lines for isolated benzenethiol as compared to the experimental data for neat benzenethiol, Refs. [60, 91, 7]. The relative intensities are defined with respect to the 1027 cm⁻¹ vibrational mode. The excitation wavelength is 785 nm. The frequencies are in cm⁻¹.

Complex	$\Delta\omega_1$	$\Delta\omega_2$	$\Delta\omega_3$	$\Delta\omega_4$
PhS-Ag ₁	-0	-4	-21	-10
PhS-Ag ₆	-7	-8	-26	-28
PhS-Ag ₇ (I)	-7	-9	-31	-33
PhS-Ag ₇ (II)	-4	-5	-24	-17
PhS-Ag ₈	-5	-5	-29	-16
PhS-Ag ₉	-1	-2	-18	-8
PhS-Ag ₁₀	-1	-3	-18	-9
PhS-Ag ₁₁	-6	-6	-28	-19

Table 2.7: The relative shifts of four totally symmetric vibrational modes in PhS-Ag_n, $n = 1, 6 - 11$, complexes as compared to the unperturbed frequencies in isolated benzenethiol, $\Delta\omega_n = \omega_n(\text{PhS-Ag}_k) - \omega_n(\text{PhSH})$. The computed frequencies for isolated benzenethiol are $\omega_1 = 1019$ cm⁻¹, $\omega_2 = 1059$ cm⁻¹, $\omega_3 = 1136$ cm⁻¹, and $\omega_4 = 1656$ cm⁻¹. The values of the shifts are given in cm⁻¹.

complexes are collected in Table 2.7. On average, the values of the shifts are larger for the complexes where total Raman scattering is quenched, PhS-Ag_n, $n = 6, 7, 8, 11$.

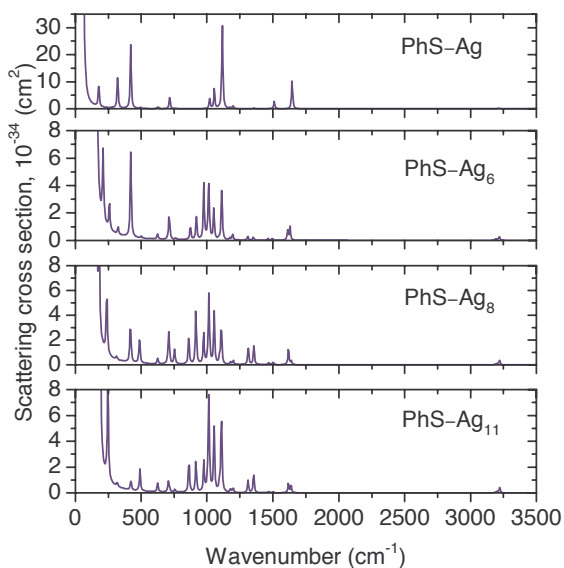


Figure 2.9: Off-resonance Raman spectra of the computed PhS-Ag_n complexes, $n = 1, 6, 8, 11$. The excitation energy is 0.62 eV, which corresponds to 2000 nm wavelength.

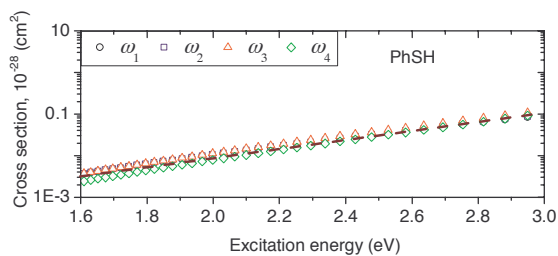


Figure 2.10: Raman excitation profile for the vibrational modes $\omega_1 = 1019 \text{ cm}^{-1}$, $\omega_2 = 1059 \text{ cm}^{-1}$, $\omega_3 = 1136 \text{ cm}^{-1}$, and $\omega_4 = 1656 \text{ cm}^{-1}$ in isolated benzenethiol.

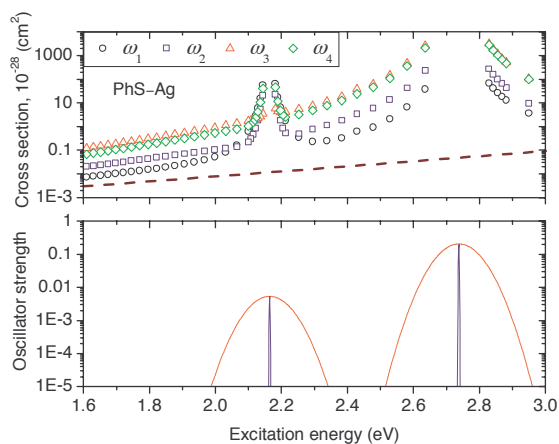


Figure 2.11: Raman excitation profile for the vibrational modes $\omega_1 = 1019 \text{ cm}^{-1}$, $\omega_2 = 1059 \text{ cm}^{-1}$, $\omega_3 = 1136 \text{ cm}^{-1}$, and $\omega_4 = 1656 \text{ cm}^{-1}$ in the PhS-Ag complex.

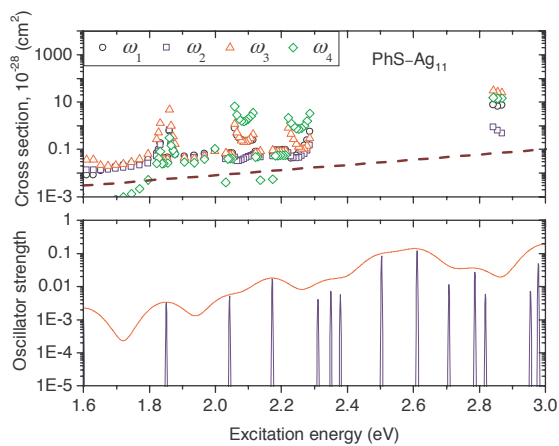


Figure 2.12: Raman excitation profile for the vibrational modes $\omega_1 = 1019 \text{ cm}^{-1}$, $\omega_2 = 1059 \text{ cm}^{-1}$, $\omega_3 = 1136 \text{ cm}^{-1}$, and $\omega_4 = 1656 \text{ cm}^{-1}$ in the PhS-Ag₁₁ complex.

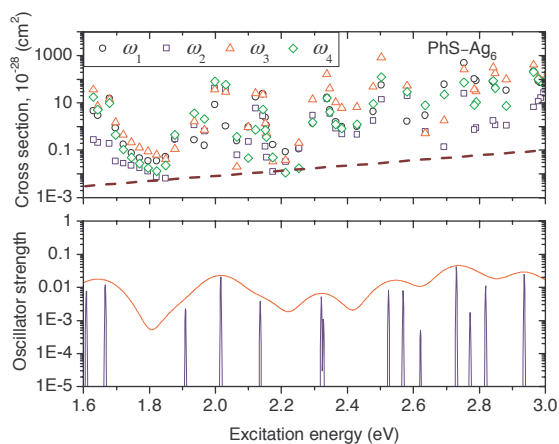


Figure 2.13: Raman excitation profile for the vibrational modes $\omega_1 = 1019 \text{ cm}^{-1}$, $\omega_2 = 1059 \text{ cm}^{-1}$, $\omega_3 = 1136 \text{ cm}^{-1}$, and $\omega_4 = 1656 \text{ cm}^{-1}$ in the PhS-Ag₆ complex.

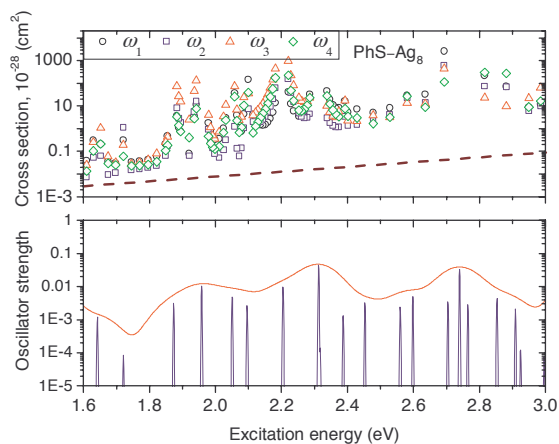


Figure 2.14: Raman excitation profile for the vibrational modes $\omega_1 = 1019 \text{ cm}^{-1}$, $\omega_2 = 1059 \text{ cm}^{-1}$, $\omega_3 = 1136 \text{ cm}^{-1}$, and $\omega_4 = 1656 \text{ cm}^{-1}$ in the PhS-Ag₈ complex.

Chapter 3

Can Mixed-Metal Surfaces Provide an Additional Enhancement to SERS?

3.1 Introduction

Surface-enhanced Raman scattering (SERS) is observed in molecules deposited on rough or nanostructured metal surfaces [150, 244, 13, 361, 88]. Over the past decade SERS has developed into a powerful analytical technique [362, 269, 294, 87, 498]. The enormous enhancement of the ordinarily weak Raman scattering cross sections in SERS is attributed to two main effects: electromagnetic and chemical enhancement. Electromagnetic enhancement is due to the presence of strong electromagnetic fields at the surface of nanoscale metal particles and is responsible for enhancements of Raman scattering cross sections of 10 or more orders of magnitude [362, 269]. Chemical enhancement is related to the formation of chemical bonds between the adsorbed molecule and surface metal atoms [399, 398, 248, 246, 358, 456]. While being much smaller in absolute magnitude than the electromagnetic effect, chemical enhancement has important implications for SERS as an analytical tool, and can provide up to 2–3 orders of magnitude of enhancement in addition to the electromagnetic contribution. Furthermore, it affects Raman-active vibrations selectively and thus alters the shapes of Raman spectra in addition to providing enhancement [455]. Lastly, the chemical effect is chemically specific and has potential for improved performance of SERS in analytical applications. The exact origin of the chemical contribution to surface enhancement remains an active area of research in both theory and experiment [162, 163, 361, 399, 398, 88, 418, 246, 358, 456, 606]. Chemical enhancement can be modeled as a combination of a static contribution connected to the redistribution of electron density between the metal and the molecule and a dynamical contribution arising from resonance enhancement due to surface excited states of mixed metal–molecular character [456].

Gold and silver are the most commonly used substrate materials for SERS applications.

Ag has been found to give highest enhancements of Raman cross sections for an excitation in the visible range, while Au is often used because of simpler processing and resistance to oxidation. Recently, Wang *et al.*, have created nanostructured silicon and germanium-based SERS substrates [562, 563]. For these structures, the enhancement is in the order of 10^2 – 10^4 . Its enhancement mechanism relies on a photon-induced charge transfer process instead of the typical plasmon-based approach. Although this effect is by no means as intense as with Ag and Au, it provides evidence that these materials can provide a SERS signal despite the lack of a plasmonic properties.

Several other metals have been explored with regard to surface enhancement [525]. Differences in the localized surface-plasmon resonances (LSPR) in scattering and absorption spectra of these metals relative to the frequencies of the incident and scattered radiation result in vastly different electromagnetic enhancements [361]. On the other hand, the richness of chemical reactivity of transition metals opens the prospect of chemically selective binding and detection.

The idea of using mixed-metal substrates, which combine the SERS activity of a majority metal (typically a coinage metal) with the chemical properties of a dopant metal (deposited as an overlayer), was proposed early on [299, 300, 624, 570]. In subsequent extensive work of Weaver, Tian, *et al.*, fabrication techniques for producing transition- and mixed-metal substrates were considerably improved and their surface enhancements were explored in great detail [623, 626, 363, 587, 527, 526, 523]. Their work was motivated by the concept of *SERS borrowing*, originally put forward by Van Duyne and Haushalter [547]. SERS borrowing refers to the fact that dopant metals are poor SERS substrates by themselves. However, when deposited as an overlayer atop effective SERS substrates, they acquire some surface enhancement “borrowed” from the coinage metal. If only the electromagnetic enhancement is taken into account, one expects the enhancement factors for these mixed-metal substrates to be *lower* than for pure coinage metals. The attenuation of the surface enhancement has been described in terms of the distance dependence of the electromagnetic fields and has been broadly explored [172, 623, 255, 566, 585]. The above picture neglects the effect of the strong coordinative bonds formed between the dopant metal and specific analytes, e. g., pyridine. Therefore, the objective of this chapter is to explore, both experimentally and using simulation, the *chemical contribution* to surface enhancement in mixed-metal SERS substrates.

We expect that stronger chemical bonding in suitably chosen mixed-metal substrates, coupled with existing advanced nanofabrication techniques, can help to balance or in ideal cases even overcome the attenuation of electromagnetic enhancement. In this case, we propose and coin the term of an additional *SERS lending* effect, where the transition-metal overlayer could contribute to the overall surface enhancement due to the strong chemical

bonding. SERS lending would open an avenue for new analytical applications of SERS. Well-known and recent results from surface chemistry [452, 381, 187, 494, 466] may serve as an inspiration for designing new mixed-metal SERS substrates. In particular, transition metals of the nickel group are known to form strong coordinative bonds with nitrogen-containing molecules and are promising candidates for their detection with SERS. In contrast, gold and silver substrates tend to bind more strongly to thiols. As mentioned above, mixed-metal substrates using nickel, palladium, and platinum were extensively studied by Weaver, Tian, *et al.* in the context of SERS borrowing [623, 626, 363, 587, 527, 526, 523]. Furthermore, molybdenum-covered SERS substrates could possibly be used for improved chemical bonding to oxygen-containing molecules.

The effect of stronger chemical bonding between the analyte and the metal surface on the Raman signal is two-fold. A stronger binding affinity results in a higher concentration of the analyte on the surface, which yields higher analytical enhancements. In addition, stronger coupling between the electronic structure of metal surface and vibrations of the molecule leads to an enhancement of the Raman cross section *per* molecule. These effects have to be balanced with the damping of the plasmonic resonance due to the presence of the dopant metal as well as changes in surface morphology in mixed-metal SERS substrates. A complete investigation of all these effects presents a number of challenges. In this chapter, we explore the chemical enhancement in mixed-metal clusters using theoretical models to describe the coupling between the analyte and the metal surface. As was shown in previous studies, chemical enhancement in SERS depends mainly on the immediate chemical environment of the binding site and can be successfully modeled using cluster models [456, 616].

In the following, we present Raman scattering calculations of *trans*-1,2-bis(4-pyridyl) ethylene (BPE) on silver-based mixed-metal clusters to theoretically characterize the chemical contribution to surface enhancement. We report experimental measurements of BPE on Ag substrates with nanometer-thick overlayers of Pd or Pt. Further computational results predict that similar effects are possible with Au as majority metal and Pd or Pt as dopant metals. Finally, we study the electronic effects of mixed-metal SERS by analyzing the Raman excitation profile of pyridine (Py) bound to silver in order to explore the dynamical contribution to the chemical enhancement in mixed-metal SERS substrates.

3.2 Experimental methods

SERS Substrate Fabrication. Experimental Raman spectra are collected from BPE adsorbed onto a femtosecond laser nanostructured SERS substrate, using the setup previously reported on Ref. [127]. This type of substrate has been previously shown to provide SERS enhancement factors of 10^9 , relative to pure analyte [127, 128]. All substrates

were fabricated using a femtosecond laser structuring process on a n-type silicon (100) wafer ($\rho=0.005\text{--}0.020 \text{ } \Omega \cdot \text{cm}$). A pulse train from a regeneratively amplified titanium:sapphire laser was used to generate 800 nm center wavelength, 100 fs pulses at a repetition rate of 1 kHz. This pulse train was frequency-doubled to a center wavelength of 400 nm using a thin BiBO₃ crystal. The second harmonic pulse width exiting the crystal was less than 200 fs. These laser pulses were loosely focused with a plano-convex lens to achieve an average fluence of 10 kJ m^{-2} at the surface of a silicon wafer fastened to the inside of a 10 mm deep cuvette filled with deionized water. The cuvette was mounted on a computer-controlled two-axis translation stage and rastered at an appropriate speed such that each point on the silicon wafer was subjected to approximately 500 pulses.

To render the surfaces SERS-active, silver was thermally evaporated onto the structured silicon. Using a quartz crystal microbalance to measure the thickness of a planar continuous film, substrates were fabricated with 80 nm of deposited silver. All films were thermally evaporated at a rate of 0.15 nm s^{-1} , with no heating or cooling applied to the substrate during deposition. A subsequent layer of 1–4 nm of platinum or palladium is added to probe the mixed-metal effects. The metal-coated substrates were submerged in $10\text{-}\mu\text{M}$ solutions of BPE made with ethanol for 1 hour and then gently rinsed in ethanol for 1 minute, followed by drying under a stream of nitrogen.

Raman Spectroscopy. Using a 5 mW, s-polarized HeNe laser, spectra were recorded through a $10\times$ microscope objective (0.25 NA) and projected onto a thermoelectrically cooled charged-couple device array using 1200 mm^{-1} diffraction grating. Individual spectra were recorded from both single spots ($1.6 \text{ }\mu\text{m}$ diameter) on the substrate, and from a $500 \text{ }\mu\text{m}$ thick cell of neat BPE for normalization.

Electron Microscopy. Secondary electron microscope images of the substrates were collected using a field-emission gun scanning electron microscope, utilizing an accelerating voltage of 5 kV. No additional sample preparation was performed prior to imaging the substrates.

3.3 Theoretical methods

Computational Details. Density-functional calculations were performed using the PBE0 functional [414]. Triple- ζ valence basis sets with one set of polarization functions (def2-TZVP) and split- ζ basis valence sets with polarization (def2-SVP) were used for the main group and transition metal elements, respectively [571]. Relativistic effective core potentials (ECP) comprising 28 core electrons for Ag and Pd and 60 core electrons were employed for Au and Pt, respectively [24]. The PBE0 functional was chosen because it has proven to be accurate for polarizabilities [4, 544] and Raman intensities [432, 543],

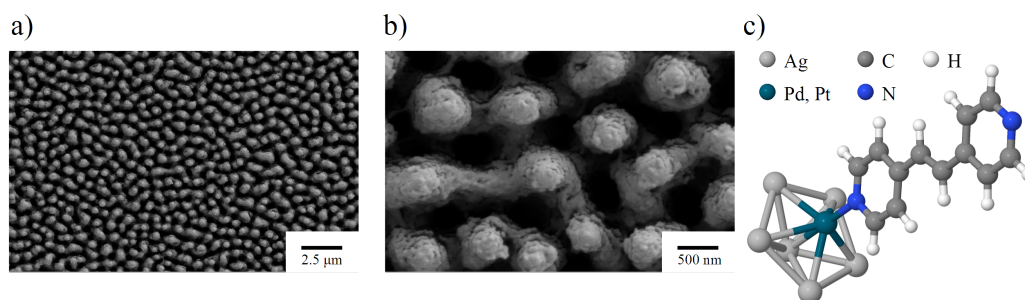


Figure 3.1: **a-b)** SEM pictures of a femtosecond laser nanostructured SERS substrate and 2 nm Pt overlayer thermally evaporated on top of the substrate. **c)** Structure of a $\text{Ag}_6\text{M} \cdot \text{BPE}$ complex.

although it is known to overestimate vibrational frequencies [346] and electronic excitation energies [5]. The TURBOMOLE package [537] was used to perform all calculations.

Raman Scattering Calculations. Raman intensities were computed using the static polarizability limit, except for the Raman intensities calculated for the Raman excitation profiles [432]. No scaling of vibrational frequencies was applied. The Raman spectra were simulated by Lorentzian broadening of the line spectra using an empirical linewidth of 5 cm^{-1} . A scattering angle of 90 degrees and perpendicular polarization of both incident and scattered radiation was employed.

Geometry Optimization. The molecular systems were relaxed using the PBE0 functional. Multiple spin geometries were studied and singlets (doublets in the open-shell case) were most stable. The molecule-cluster systems presented an imaginary mode, even after repeated attempts to relax the molecule. This mode was prevalent at the $3\text{--}15 \text{ cm}^{-1}$ region. None of the bare clusters or molecules presented imaginary frequencies.

3.4 Results

3.4.1 Enhancement effects of BPE using mixed-metal substrates

We prepared silver-based SERS substrates including a thin overlayer of Pd or Pt. Details regarding the nanofabrication of these surfaces can be found in the Experimental Methods Section. Briefly, silicon surfaces were roughened by a femtosecond laser nanostructuring process [127]. An 80 nm thick layer of silver was deposited on the roughened surfaces by thermal evaporation; subsequently, an overlayer of Pd or Pt of 1–4 nm thickness was created by the same technique. In Fig. 3.1a-b, we show scanning electron microscope (SEM) images of the silver substrate with 2 nm Pt coverage. We notice a similar quasi-uniform

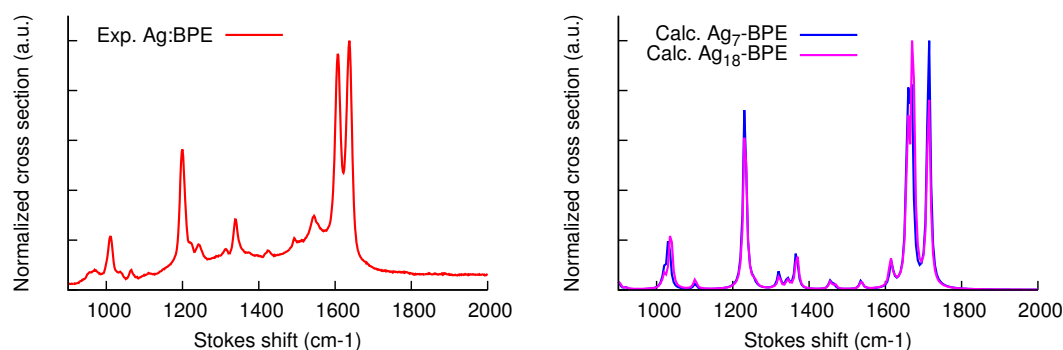


Figure 3.2: Experimental Raman spectrum of BPE and 80 nm Ag substrate using 633 nm wavelength. (left) Calculated Raman spectra of $\text{Ag}_7 \cdot \text{BPE}$ and $\text{Ag}_{18} \cdot \text{BPE}$ complexes. (right)

distribution of raised features as shown in the work by Diebold *et al.* [127]; even in the presence of an additional transition metal.

Thermal evaporation is a highly directional process that preferentially coats the top surface of the sample and may leave shadows exposed to Ag. There have been previous efforts to ensure a pinhole free surface in an electrochemical setting by Weaver *et al.* [626] The current setup to identify elemental composition of surface coverage employs the SEM setup coupled with energy-dispersive X-ray spectrometry. The latter has a micron-sized resolution, so other ways of determining surface coverage, such as chemical probes [623] are needed. The consequences of nanoscale pinholes are discussed in the theoretical section as we explore the local environment of the molecule using mixed-metal clusters.

To elucidate the role of the chemical contribution to surface enhancement in bi-metal substrates, we calculated the Raman cross sections of BPE bound to small-cluster models of SERS substrates. We use seven-atom ($\text{Ag}_6\text{M} \cdot \text{BPE}$) and a larger 18-atom cluster ($\text{Ag}_{14}\text{M}_4 \cdot \text{BPE}$) models, see Fig. 3.1c. Chemical enhancement effects appear to be well localized around the site of the chemical bond between metal atoms and the analyte molecule. In Chapter 2 and in previous work, these have been shown to provide realistic models for chemical enhancement [456, 455].

The experimental Raman spectrum of BPE at 633 nm excitation wavelength on a silver substrate and the computed Raman spectra for the $\text{Ag}_7 \cdot \text{BPE}$ and $\text{Ag}_{18} \cdot \text{BPE}$ complexes are compared in Fig. 3.2. The vibrational frequencies and relative Raman cross sections are in good agreement between the experimental and the computed spectra. The four most prominent vibrational modes are clearly identified as the ring-breathing mode of the pyridine rings at 1010 cm^{-1} , the in-plane bending of the pyridine rings at 1200 cm^{-1} , the ring

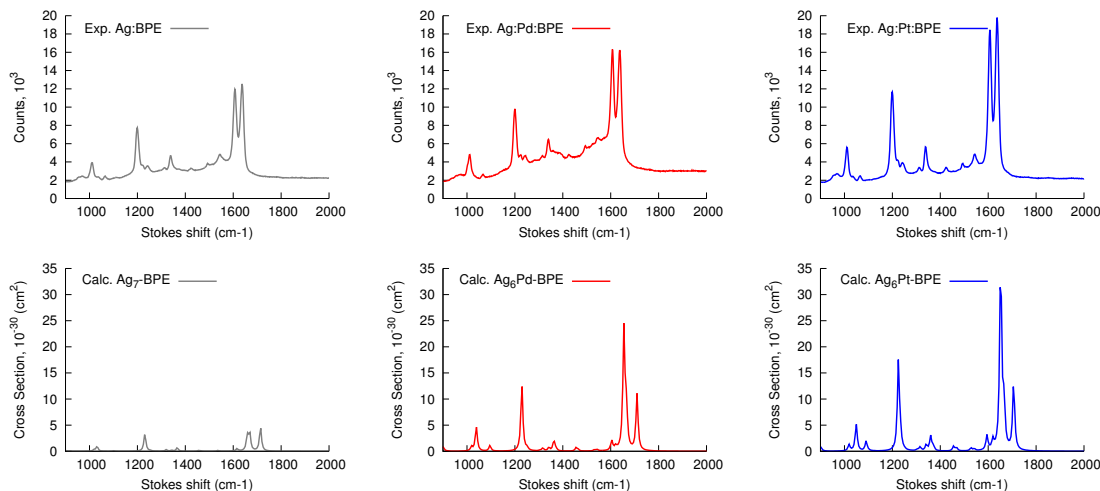


Figure 3.3: Experimental and computed SERS spectra of BPE. Experimental Raman scattering cross-sections at 633 nm incident wavelength of BPE on 80 nm Ag substrate, 80 nm Ag substrate with 1 nm Pd overlayer, and 80 nm Ag substrate with 1 nm Pt overlayer. (left) Calculated Raman spectra of $\text{Ag}_7 \cdot \text{BPE}$, $\text{Ag}_6\text{Pd} \cdot \text{BPE}$, and $\text{Ag}_6\text{Pt} \cdot \text{BPE}$, complexes. (right)

stretching mode at 1610 cm^{-1} and the ethylene stretching mode at 1640 cm^{-1} [593, 508]. The differences between these cluster models are comparatively small, with the largest deviations found in the relative Raman cross sections for the 1610 and 1640 cm^{-1} modes. The computed vibrational frequencies are overestimated by about 4% by the PBE0 functional used in this chapter, in accord with previous benchmark studies [346].

In Fig. 3.3, we show the experimental Raman spectra of BPE absorbed on the silver SERS substrate and mixed-metal SERS substrates using 1 nm coverage of Pd or Pt at 633 nm excitation wavelength. We observed a stronger Raman signal for mixed-metal SERS substrates compared to the silver SERS substrate. Also, Pt coverage of 1 nm thickness is more effective in enhancing the Raman signal than Pd coverage of the same thickness. At the same time, the relative Raman signals from different modes and the shapes of measured Raman spectra remain virtually unchanged. Measurements of Raman cross sections of BPE on SERS substrates are complicated by the fact that its surface coverage is not exactly known and might vary depending on the composition of the SERS substrate. Therefore, we consider analytical enhancement factors (AEF) as defined by LeRu, Etchegoin, and co-workers and used extensively in SERS research [86, 337, 293],

$$\text{AEF} = \frac{I_{\text{SERS}}/c_{\text{SERS}}}{I_{\text{ref}}/c_{\text{ref}}}, \quad (3.1)$$

where I is the Raman intensity and c represents the concentration of the analyte. The

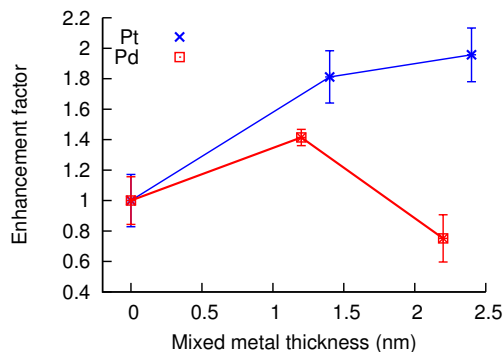


Figure 3.4: Analytical enhancement factors for the integrated signals of the in-plane bending mode of BPE on mixed-metal SERS substrates as a function of the transition-metal thickness. The analytical enhancement factors are normalized with respect to the silver SERS substrates (0 nm thickness). For Pd coverage there is only enhancement at 1.2 nm thickness, while the Pt signal is close to 1.9 at both 1.4 nm and 2.4 nm coverage.

$\text{Ag}_6\text{M} \cdot \text{BPE}$	Enhancement	ΔE (eV)	$\text{Ag}_{18} \cdot \text{BPE}$	Enhancement
$\text{Ag}_7 \cdot \text{BPE}$	1.00	-0.38	$\text{Ag}_{18} \cdot \text{BPE}$	1.00
$\text{Ag}_6\text{Pd} \cdot \text{BPE}$	3.79	-0.92	$\text{Ag}_{14}\text{Pd}_4 \cdot \text{BPE}$	2.28
$\text{Ag}_6\text{Pt} \cdot \text{BPE}$	5.08	-1.41	$\text{Ag}_{14}\text{Pt}_4 \cdot \text{BPE}$	4.25

Table 3.1: Enhancement factors of the in-plane bending mode of $\text{Ag}_6\text{M} \cdot \text{BPE}$ complexes (relative to $\text{Ag}_7 \cdot \text{BPE}$) and $\text{Ag}_{14}\text{M}_4 \cdot \text{BPE}$ complexes (relative to $\text{Ag}_{18} \cdot \text{BPE}$). Binding energies ΔE of $\text{Ag}_6\text{M} \cdot \text{BPE}$ complexes according to Eq. 3.2.

significance of the observed analytical enhancement factors is discussed extensively below.

At close to 1 nm thickness, Pd- and Pt-covered substrates show analytical enhancement factors for the 1200 cm^{-1} mode that are 1.4 and 1.8 times higher than that for the silver SERS substrate, respectively. At 2 nm thickness, this ratio drops to 0.75 when using a Pd-covered substrate. The analytical enhancement factor for the 2 nm Pt-covered substrate is 1.9 times higher than for the silver substrate; indicating that there is a sustained enhancement as the coverage thickness increases. We observe no SERS enhancement beyond a layer thickness of 3 nm layer of Pd or Pt (not shown). The dependence of the measured analytical enhancement factors on the thickness of the transition-metal overlayer is summarized in Fig. 3.4.

The computed Raman spectra of the $\text{Ag}_6\text{M} \cdot \text{BPE}$ complexes ($\text{M} = \text{Ag}, \text{Pd}, \text{Pt}$) are shown in Fig. 3.3. Increased Raman cross sections are observed in transition-metal complexes, while relative cross sections are preserved, in line with experimental results. For the in-plane bending mode at 1200 cm^{-1} , we find that replacement of the proximal Ag atom

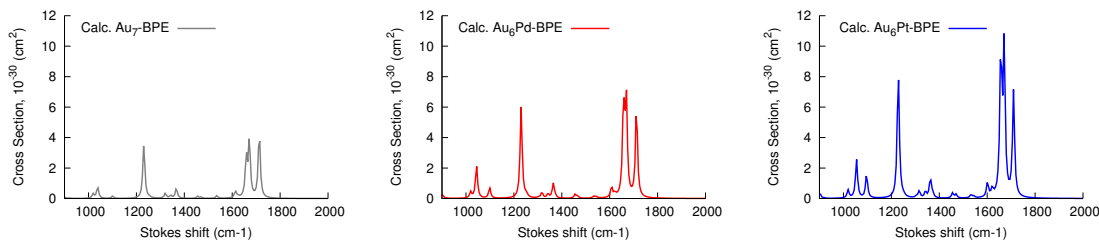


Figure 3.5: Calculated Raman spectra of $\text{Au}_7 \cdot \text{BPE}$, $\text{Au}_6\text{Pd} \cdot \text{BPE}$, and $\text{Au}_6\text{Pt} \cdot \text{BPE}$ complexes.

by a Pd atom leads to an 3.8-fold increase in Raman cross section. For the $\text{Ag}_6\text{Pt} \cdot \text{BPE}$ complex, the Raman cross section is highest, 5.1 times higher compared to the $\text{Ag}_7 \cdot \text{BPE}$ complex. The Raman spectra of the larger complexes of the form, $\text{Ag}_{14}\text{M}_4 \cdot \text{BPE}$, show a similar trend and are given in Sec. 3.6. The computed results are summarized in Table 3.1.

Nitrogen-containing heterocycles such as BPE are known to form strong coordinative bonds to transition metals of the platinum group. This strong bonding can be expected to have a significant effect on the chemical contribution to surface enhancement. Therefore, it is instructive to study the binding energies of BPE to the mixed-metal clusters as a simple measure of the metal–molecular bonding. The binding energies ΔE are computed as electronic reaction energies (without zero-point correction) of the $\text{Ag}_x\text{M}_y \cdot \text{BPE}$ complex formation,

$$\Delta E = E(\text{Ag}_x\text{M}_y \cdot \text{BPE}) - E(\text{Ag}_x\text{M}_y) - E(\text{BPE}) \quad (3.2)$$

The binding energies are given in Table 3.1 and follow the trend $\text{Ag} < \text{Pd} < \text{Pt}$. This observation is in line with complex stability of transition metals [402, 18, 284] and suggests that the mixing between electronic levels in the molecule and the metal cluster is correlated to the increase in Raman scattering cross sections. A simple explanation is that stronger bonding leads to a stronger coupling of vibrational modes in the analyte molecule to the large polarizability of the metal cluster.

Further, we computed Raman spectra of the $\text{Au}_6\text{M} \cdot \text{BPE}$ complexes ($\text{M} = \text{Au}, \text{Pd}, \text{Pt}$) and their binding energies according to Eq. 3.2 that are shown in Fig. 3.5 and Fig. 3.2. The chemical enhancement and the Raman cross sections increase in the sequence $\text{Au} \uparrow \text{Pd} \uparrow \text{Pt}$. The effect of Pd and Pt is, however, smaller than for the $\text{Ag}_6\text{M} \cdot \text{BPE}$ complexes, while the binding energies are similar for both $\text{Ag}_6\text{M} \cdot \text{BPE}$ and $\text{Au}_6\text{M} \cdot \text{BPE}$ series of complexes. It is therefore apparent that other electronic-structure considerations need to be taken into account to fully understand the origin of the mixed-metal effect.

Theory and experiment are complementary in the understanding of the molecule–metal and mixed-metal interface. In this chapter, we are able to provide analytical enhancement

Au ₆ M · BPE	Enhancement	ΔE (eV)
Au ₇ · BPE	1.00	-0.64
Au ₆ Pd · BPE	1.66	-1.05
Au ₆ Pt · BPE	2.26	-1.67

Table 3.2: Enhancement factors of the in-plane bending mode of Au₆M · BPE complexes (relative to Au₇ · BPE). Binding energies ΔE of Au₆M · BPE complexes according to Eq. 3.2.

Ag ₆ M · Py	Enhancement	ΔE (eV)
Ag ₇ · Py	1.00	-0.38
Ag ₆ Pd · Py	6.10	-0.90
Ag ₆ Pt · Py	9.27	-1.37

Table 3.3: Enhancement factors of the in-plane bending mode of Ag₆M · Py complexes (relative to Ag₇ · Py). Binding energies ΔE of Ag₆M · BPE complexes according to Eq. 3.2.

factors, but the surface coverage of BPE on SERS substrates is unknown and its measurement is far from trivial [158]. Theoretical results predict an increase in Raman cross sections *per molecule* when the analyte binds to a Pd or Pt atom, an effect that can be described by *SERS lending*. The enhanced Raman cross sections are concomitant with an increase in binding energy between the analyte and the metallic surface. Higher binding energies will however also lead to increased surface coverage of the analyte under equilibrium conditions, potentially yielding higher analytical enhancement factors. Estimating the surface coverage is therefore necessary in order to interpret the experimental findings.

Surface coverage experiments of pyridine on roughened electrodes of Ag and Pt yield a coverage of $4.5\text{--}6.5 \times 10^{-10}$ mol cm⁻² and 5.1×10^{-10} mol cm⁻², respectively [205, 206, 607]. These measurements were done for a similar bulk concentration of pyridine, though each was determined with a different method. In the case of BPE, estimations of the surface coverage on Ag have relied on a geometric area estimation of 1.16×10^{-9} mol cm⁻² [380, 313, 136], though we note this is likely an overestimate. Measurements of BPE on Pt have reported to give a coverage of 4.75×10^{-10} mol cm⁻² [197]. Although the variety of methods shrouds the comparison, the difference in surface coverage between Pt and Ag is not over a factor of two greater. Therefore, coverage cannot be the sole factor for the 1.9-fold enhancement we find experimentally. Along with robust theoretical predictions of increased Raman cross sections per molecule, we tentatively conclude that a *SERS lending* effect is present in mixed-metal substrates considered in this chapter.

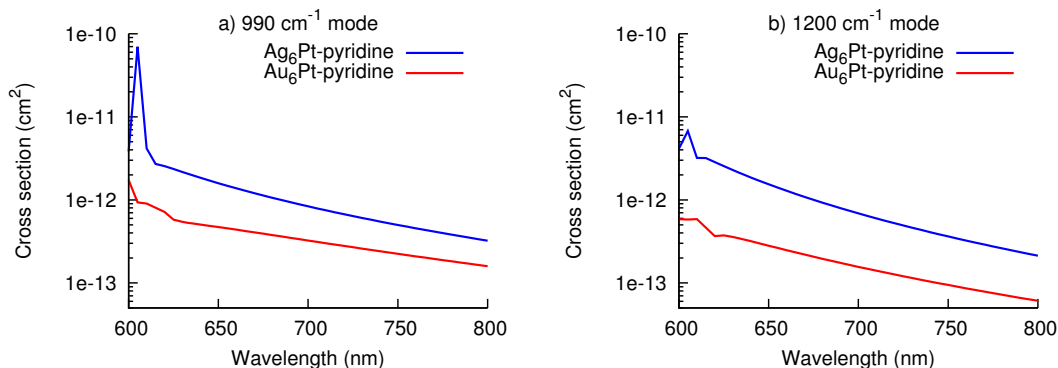


Figure 3.6: Raman excitation profiles (REP) of ring-breathing mode (990 cm^{-1} , a) and in-plane bending mode (1200 cm^{-1} , b) of pyridine in $\text{Ag}_6\text{Pt}\cdot\text{Py}$ and $\text{Au}_6\text{Pt}\cdot\text{Py}$ complexes.

3.4.2 Theoretical study of pyridine: Raman excitation profile

We proceed by investigating the importance of a dynamical contribution to chemical enhancement in mixed-metal clusters using complexes $\text{Ag}_6\text{M}\cdot\text{Py}$ as an example. Table 3.3 shows the relative Raman scattering cross sections for the 1230 cm^{-1} in-plane bending mode of pyridine as well as binding energies computed according to Eq. 3.2. This vibration corresponds to the 1200 cm^{-1} mode in BPE (spectra available in Sec. 3.6). The binding energies follow the same trends as in the case of BPE and are within 0.04 eV of the values obtained for $\text{Ag}_6\text{M}\cdot\text{BPE}$, compare Table 3.1. The Raman cross section of the 1230 cm^{-1} mode is 6 times higher in $\text{Ag}_6\text{Pd}\cdot\text{Py}$ and 9 times higher in $\text{Ag}_6\text{Pt}\cdot\text{Py}$ compared to the $\text{Ag}_7\cdot\text{Py}$ complex. However, the absolute Raman cross-section for this mode is 20 times smaller than in complexes containing BPE (shown in Sec. 3.6).

Raman excitation profiles (REPs) are a useful tool in elucidating the dynamical contribution surface enhancement and describe the dependence of Raman cross sections on the excitation frequency [456]. In Fig. 3.6, we show REPs for the ring-breathing mode (experimental frequency 990 cm^{-1}) and the in-plane bending mode (1200 cm^{-1}) of $\text{Ag}_6\text{Pt}\cdot\text{Py}$ and $\text{Au}_6\text{Pt}\cdot\text{Py}$ complexes. The silver-platinum complex has its lowest-energy electronic excitation at 607 nm , while the lowest excitation occurs at 616 nm in the gold-platinum complex. For both vibrational modes, $\text{Ag}_6\text{Pt}\cdot\text{Py}$ exhibits a large increase in Raman cross sections close to the electronic excitation at 607 nm , showing almost an order of magnitude increase in Raman cross section for the ring-breathing mode. In contrast, $\text{Au}_6\text{Pt}\cdot\text{Py}$ complex fails to show a significant increase for both of these modes at its excitation wavelength of 616 nm .

Isosurface plots of transition electron densities for the lowest-energy excitations in $\text{Ag}_6\text{Pt}\cdot\text{Py}$ and $\text{Au}_6\text{Pt}\cdot\text{Py}$ are displayed in Fig. 3.6. In the case of $\text{Ag}_6\text{Pt}\cdot\text{Py}$ (Fig. 3.7a),

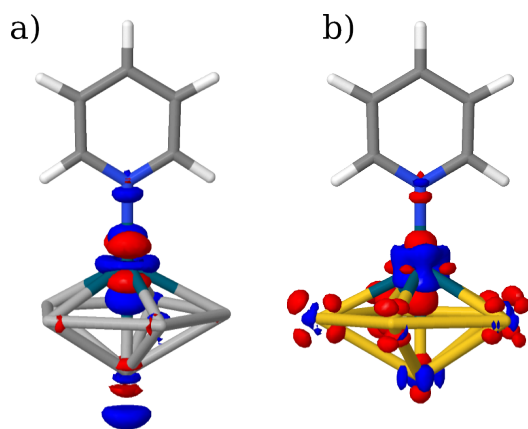


Figure 3.7: Isosurface plots of computed transition densities of lowest-energy electronic excitations in $\text{Ag}_6\text{Pt} \cdot \text{Py}$ (excitation wavelength 607 nm, a) and $\text{Au}_6\text{Pt} \cdot \text{Py}$ complex (excitation wavelength 616 nm, b) The red color indicates a transition density of -0.005 a.u., while the blue corresponds to a transition density of 0.005 a.u.

the transition density lies exactly at the metal–molecule interface. The $\text{Au}_6\text{Pt} \cdot \text{Py}$ complex (Fig. 3.7b) is characterized by a transition density that is spread out throughout the metal cluster. These observations provide a simple explanation for the computed REPs of Fig. 3.6. We note that when an excitation transition density is largely localized at the metal–molecule interface, the Raman cross sections for excitation energies close to it are strongly enhanced, as has been reported previously for $\text{Ag}_n\text{-SPh}$ complexes [456]. In contrast, excitations in the metal cluster have a much smaller effect on Raman cross sections. The differences between Au and Ag as majority metals illustrate that excited state properties are also important to understand the effects in mixed-metal systems.

3.5 Conclusions

The chemical contribution to surface enhancement in mixed-metal SERS substrates was investigated by experimental and theoretical techniques. We report an increase by up to 1.9-fold in analytical enhancement factors obtained experimentally for BPE on silver-based SERS substrates including an overlayer of Pd or Pt of 1–2 nm thickness. The analytical enhancement factors include the effect of surface coverage of the analyte, the attenuation of the electromagnetic enhancement by the transition-metal overlayer as well as changes in the chemical enhancement. The observed increase in analytical enhancement factors is unlikely to arise solely from a higher surface coverage on Pd- or Pt-containing SERS substrates. Therefore, we conclude that a *SERS lending* effect is present in mixed-metal

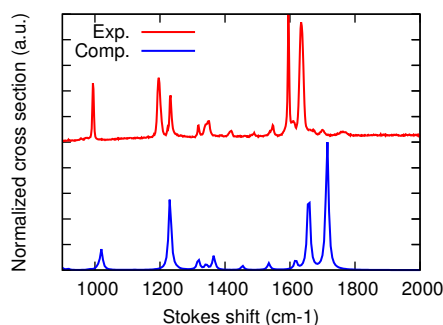


Figure 3.8: Experimental and computed spectra for BPE at 633 nm.

SERS substrates due to an increase in chemical enhancement.

These findings are further corroborated by theoretical results on small-cluster models, which consistently predict up to a 5-fold increase in Raman cross sections for BPE on Pd- or Pt-containing mixed-metal clusters. The differences in enhancement are understandable since the theoretical model does not take into account the distance-dependent decrease of electromagnetic enhancement. It is likely the issue of the attenuation of the electromagnetic effect can be alleviated [255, 566, 129]. Overall, the enhancement is a combination of the attenuation and the chemical enhancement effect. As mentioned above, the chemical enhancement can lead to observable SERS spectra without necessarily having a substrate with plasmonic properties [562, 563].

SERS lending could open an avenue for new analytical applications for monitoring and identification. Future work needs to focus on a more in-depth experimental characterization of the mixed-metal substrate, as well as expanding the use of transition metals for detecting different analytes. The experimental challenge to overcome in future work is the determination of surface coverage, which would shed some light on the quantitative relationship between the borrowing and lending effects in mixed-metal SERS substrates.“

3.6 Appendix

3.6.1 Supplementary Raman Spectra

We plot the comparison between the experimental and theoretical Raman spectrum of BPE in Fig. 3.8. We show the comparison in Fig. 3.9 between experimental and calculated spectra of SERS and mixed-metal SERS with clusters of up to 18 metal atoms and BPE (*i.e.*, $\text{Ag}_{14}\text{M}_4 \cdot \text{BPE}$, where $\text{M}=\{\text{Ag}, \text{Pd}, \text{Pt}\}$). In the case of pyridine, Fig. 3.10 shows the Raman spectrum of the three layouts: $\text{Ag}_6\text{M} \cdot \text{Py}$, where $\text{M}=\{\text{Ag}, \text{Pd}, \text{Pt}\}$.

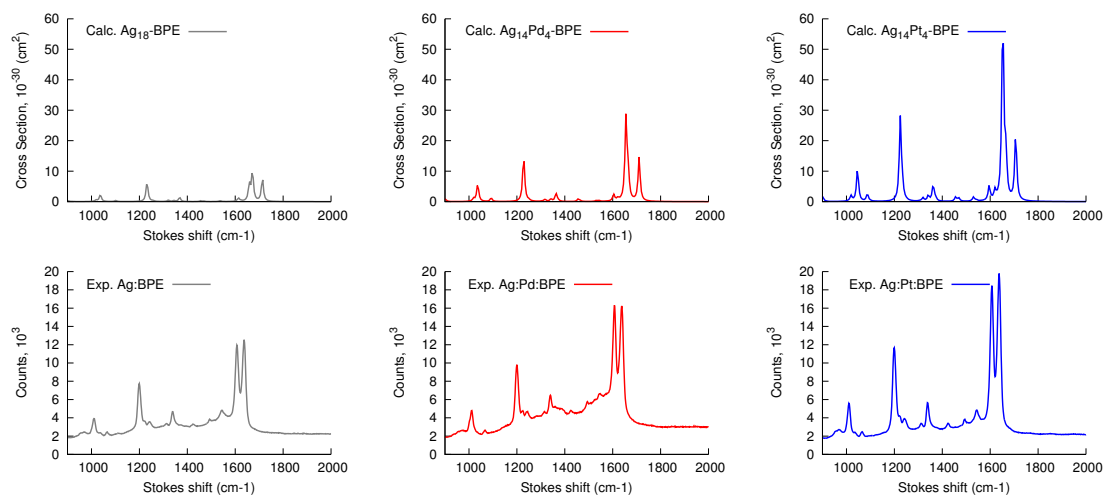


Figure 3.9: Calculated and experimental SERS spectra. **Top** Raman scattering simulations at 633 nm incident wavelength of BPE bound to Ag_{14}M_4 where M is: **left** Ag; **Center** Pd; **Right** Pt. **Bottom** Experimental Raman scattering cross-sections at 633 nm incident wavelength of BPE attached to: **Left** 80 nm Ag substrate; **Center** 80 nm Ag substrate with 1nm Pd layer; **Right** 80 nm Ag substrate with 1nm Pt layer.

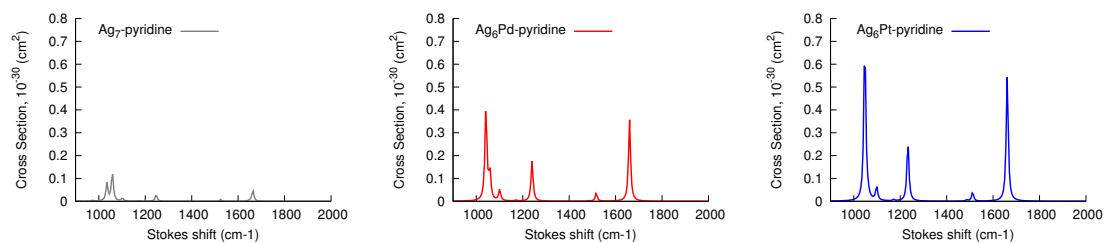


Figure 3.10: Calculated Raman spectra at 633 nm excitation wavelength for gold-containing clusters: $\text{Ag}_6\text{M}\cdot\text{Py}$. M is: **Left** Ag; **Center** Pd; and **right** Pt. There is an overall enhancement of the Raman spectra, as we modify the substrate from bare Ag to Pd, and Pt (*i. e.*, from left to right).

Chapter 4

Anion stabilization in electrostatic environments

4.1 Introduction

The stabilization of a transient electron in a molecular system by a complex nanoscale environment is relevant for the fields of molecular electronics and transport [440, 305, 378, 492, 124] as well as to the understanding of molecular properties on surfaces such as in surface-enhanced Raman spectroscopy [150, 468, 360, 116, 246, 130, 456, 455]. A major challenge is that of understanding the interaction between extended metallic systems, such as surface metal gates or a nanoparticle, and an adsorbed molecule. From a theoretical standpoint, these two components are characterized by different length scales.

Differing approaches for handling this intrinsically multiscale problem have been taken. For example, several authors have focused on the molecular system. These efforts include the PCM [532, 531, 117, 345] and COSMO methodologies [265, 264], where the metal surfaces or nanoparticles are simulated as cavity surfaces discretized into finite elements. The PCM technique has provided valuable insight into surface-enhancement processes [115, 554, 364, 461]. Recently, we have also modeled nanoscale systems using finite element and basis set methods [569]. Our approach includes partitioning the Green's function into a contribution that is effectively the interaction of the particles in vacuum (obtaining the $1/r$ potential), and an additional term, which is effectively due to the electrostatic environment [569]. A parallel formulation has been developed by one of us for quantum dots [502, 504, 503, 435]. In this case, the system is determined by the finite-difference discretization of arbitrarily shaped boundaries, where these lie at the edges of a calculation box. This treatment of gated systems has enabled the study of properties such as Coulomb blockade energetics [504], quantum-dots self-consistent structures [503] and, more recently, Förster coupling in nanoparticle excitonic circuits [435].

In this chapter we focus on molecular systems interacting with a nanoscale environment. As a representative example, we study the benzene anion. It is known that a single benzene

molecule in the gas phase is unable to bind an excess electron as shown by a negative vertical electron affinity (VEA) of -1.15 eV [67, 373]. VEA is defined as the energy difference between the neutral species at its ground-state geometry and the anion species at the neutral geometry as shown in Eq. 4.1. We use atomic units throughout to represent all quantities, unless otherwise noted.

$$\text{VEA} = E_{\text{neutral}}(\mathbf{R}_{\text{neutral}}) - E_{\text{anion}}(\mathbf{R}_{\text{neutral}}) \quad (4.1)$$

$$\text{VDE} = E_{\text{neutral}}(\mathbf{R}_{\text{anion}}) - E_{\text{anion}}(\mathbf{R}_{\text{anion}}) \quad (4.2)$$

Similar to the VEA, the vertical detachment energy (VDE) shown in Eq. 4.2 is defined as the energy difference between the neutral species at the anion’s ground-state geometry and the anion at that same geometry. The VEA and VDE represent lower and upper bounds, respectively, of the electron affinity when the nuclear configuration is not significantly different in the anionic and neutral geometry [486, 445, 280]. Specifically, Mitsui *et al.* [353] observed the formation of negatively charged benzene clusters $(\text{C}_6\text{H}_6)_n^-$. In the gas phase, the vertical detachment energy (VDE) is between 0.47 and 0.56 eV for $n = 53 - 124$ with an estimated value of 0.84 eV when n is extrapolated to infinity.

Why does a cluster of molecules bind an excess electron when a single molecule does not? One explanation is that the polarizability of the cluster is greater than the single molecule. An excess electron can therefore more readily induce a dipole in the cluster to which it can favorably interact. In a similar fashion, the polarizability of a local dielectric and conducting medium in a nanostructured system can also stabilize anionic states of molecules.

We study the stability of the benzene anion in the proximity of a conductor. We approximate the metal surfaces as perfect conductors, which are grounded and can act as voltage sources. The arbitrariness of the boundaries allow us to explore geometric effects such as metallic tips. Variations from the parallel-plate setup treated in this paper are planned for future studies. We propose a simple method to determine the total energy of a system given an arbitrary electrostatic environment. We show that the benzene anion energy is lower than the neutral benzene energy in this environment. Subsequently, we describe the effect of a voltage bias on the system and explore the effects of the environment by studying the induced charge on the metal plate and the electronic localization function.

4.2 Results

We place the molecule between two charged metallic plates, a geometry reminiscent of some single-molecule experiments. [440, 305] The total electrostatic energy of the molecule

can then be given by two terms: the interaction of the charge density, $\rho(\mathbf{r})$, with the grounded potential $\phi^{\parallel}(\mathbf{r})$, and the interaction of the density with the potential generated due to the bias voltage at the plates, $\phi^{\text{B}}(\mathbf{r})$. The grounded potential depends on the system's charge density: $\rho(\mathbf{r}) = \rho_{\text{ion}}(\mathbf{r}) + \rho_{\text{el}}(\mathbf{r})$ and is solved via the Poisson equation: $\nabla^2 \phi^{\parallel}(\mathbf{r}) = -4\pi\rho(\mathbf{r})$; having the boundary condition $\phi^{\parallel}(\mathbf{r}_b) = 0$. \mathbf{r}_b represents the position of the plates, where the potential is set to zero. We use the dielectric constant of vacuum, although this can be easily extended to adopting a position-dependent dielectric function.

The bias potential is obtained by solving Laplace's equation, $\nabla^2 \phi^{\text{B}}(\mathbf{r}) = 0$, given the voltage bias, $\phi^{\text{B}}(\mathbf{r}_b) = V_b$, in each of the gates. We use Laplace's equation as this potential is generated by charges outside the system. The expression of the total electrostatic system energy then becomes, $E_{es} = \frac{1}{2} \int d\mathbf{r} \rho(\mathbf{r}) \phi^{\parallel}(\mathbf{r}) + \int d\mathbf{r} \rho(\mathbf{r}) \phi^{\text{B}}(\mathbf{r})$.

The plate energy also contributes to the total energy, but as we currently consider an open system, the plate energy essentially becomes the work associated with charging the metal plates up to a constant bias voltage. We return to discussing the plate energy below.

Given these non-trivial potentials, we can solve for the density in a self-consistent fashion by using the Kohn-Sham [228, 273] approach to density functional theory (DFT), where one solves a system of equations, $[-\frac{1}{2}\nabla^2 + \phi^{\text{eff}}(\mathbf{r})] \chi_i(\mathbf{r}) = \epsilon_i \chi_i(\mathbf{r})$ where χ_i corresponds to a Kohn-Sham molecular orbital and ϵ_i corresponds to its energy. In addition to the ionic and electronic potentials contained in $\phi^{\parallel}(\mathbf{r})$, ϕ^{eff} includes the exchange-correlation potential, $\phi^{\text{xc}}(\mathbf{r})$: $\phi^{\text{eff}} = \phi^{\parallel}(\mathbf{r}) + \phi^{\text{B}}(\mathbf{r}) + \phi^{\text{xc}}(\mathbf{r})$. Finally, the density is determined by the occupied Kohn-Sham orbitals: $\rho_{\text{el}}(\mathbf{r}) = \sum_i |\chi_i(\mathbf{r})|^2$.

The internal energy E_{sys} is given by the expression below. The superscripts in the potential terms represent the boundary condition, and the subscripts represent the source of the potential:

$$\begin{aligned}
E_{\text{sys}} = & \sum_i \epsilon_i - \frac{1}{2} \int d\mathbf{r} \rho_{\text{el}}(\mathbf{r}) \phi_{\text{el}}^{\parallel}(\mathbf{r}) + \\
& + \frac{1}{2} \int d\mathbf{r} \rho_{\text{ion}}(\mathbf{r}) \phi_{\text{ion}}^{\parallel}(\mathbf{r}) + \int d\mathbf{r} \rho_{\text{ion}} \phi^{\text{B}}(\mathbf{r}) + \\
& + E^{\text{xc}}[\rho_{\text{el}}] - \int d\mathbf{r} \phi^{\text{xc}}(\mathbf{r}) \rho_{\text{el}}(\mathbf{r})
\end{aligned} \tag{4.3}$$

Here ϵ_i are the Kohn-Sham eigenvalues. ϕ_{el} and ϕ_{ion} are the electronic and ionic potentials that act on the electronic and ionic densities: ρ_{el} and ρ_{ion} , respectively. $E^{\text{xc}}[\rho_{\text{el}}]$ is the exchange-correlation energy. Note that the sum over Kohn-Sham eigenvalues in Eq. 4.3 implicitly contains the electrostatic interaction of the electrons: $\frac{1}{2} \int d\mathbf{r} \rho_{\text{el}}(\mathbf{r}) \phi_{\text{el}}^{\parallel}(\mathbf{r}) + \int d\mathbf{r} \rho_{\text{el}}(\mathbf{r}) \phi_{\text{el}}^{\text{B}}(\mathbf{r})$.

In free-space, the ion potential is given by $\phi_{\text{ion}}^{\circ}(\mathbf{r})$ and the ion-ion interaction,

$$\frac{1}{2} \int d\mathbf{r} \rho_{\text{ion}}(\mathbf{r}) \phi_{\text{ion}}^{\circ}(\mathbf{r}),$$

is substituted by the sum of the i th-ion interacting with all other j th-ions: $\sum_i \sum_{i>j} \frac{q_i q_j}{|R_i - R_j|}$. In arbitrary electrostatic conditions, besides considering the interaction between the i th-ion and the potential generated by the j th ion: $\sum_i \sum_{i>j} \int d\mathbf{r} \rho_{\text{ion},i}(\mathbf{r}) \phi_{\text{ion},j}^{\parallel}(\mathbf{r})$, the interaction given by an ion with the metal plates is an important energetic component. [238] This can be rationalized in physical terms as the interaction of each ion with its mirror images. This contribution is an attractive one and is fully considered in our calculations (as detailed in Sec. 4.5) and is included in Eq. 4.3.

Since we assume that the constant potential generators are attached to power supplies (or ground lines), the system is effectively open, and the work done by the environment must be included in the total free energy F . The energy of the charges on the m metal surfaces is given by the plate energy:

$$E_g = \frac{1}{2} \sum_m Q_m V_m, \quad (4.4)$$

where Q_m represents the surface charge and V_m is the applied voltage at the gates. Q_m is obtained as the normal derivative of the total electrostatic potential, $\phi(\mathbf{r}) = \phi^{\parallel}(\mathbf{r}) + \phi^{\text{B}}(\mathbf{r})$, at each of the surfaces: $Q_m = \frac{-1}{4\pi} \frac{\partial \phi(\mathbf{r})}{\partial n} \Big|_{\mathbf{r}=\mathbf{r}_b}$. The standard expression for the work done by batteries in electrical circuit analysis is

$$\begin{aligned} W &= - \sum_m \int dt I_m(t) V_m(t) \\ &= - \sum_m Q_m V_m, \end{aligned} \quad (4.5)$$

where $V_m(t)$ is the time-dependent applied voltage, and $I_m(t)$ is the current to or from the power supply, for the m th gate respectively. Equation 4.5 results from the assumption that the voltage is maintained arbitrarily close to the power supply potential throughout any charge rearrangement processes that induce a flow of current to or from the system.

Taking into account the additional energy terms of Eq. 4.4 and Eq. 4.5, the final expression for the total free energy of the system becomes

$$\begin{aligned} F &= E_{\text{sys}} + \frac{1}{2} \sum_m Q_m V_m - \sum_m \int dt V_m(t) I_m(t) \\ &= E_{\text{sys}} - \frac{1}{2} \sum_m Q_m V_m. \end{aligned} \quad (4.6)$$

For all results presented in this work, Eq. 4.6 is what we will refer to as the energy of the system.

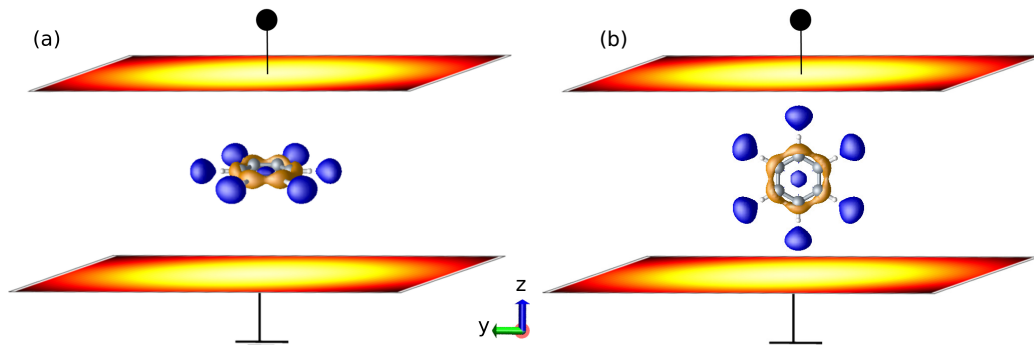


Figure 4.1: Two metallic plates acting on a molecule. Two metal plates measuring 6 nm on each side separated by 2.1 nm (figure not to scale) confine a molecular system either parallel **(a)** or perpendicular **(b)** to the plates. We present the induced charge (See Fig. 4.4 a,b). In between the plates, we show the highest occupied molecular orbital (HOMO) of the benzene anion.

We study a model system composed of two parallel-infinite plates separated along the z -axis. The gates are assumed to be connected to power supplies which can be set to arbitrary voltages. The plates confine a benzene molecule oriented either parallel or perpendicular to the metallic plates, shown in Fig. 4.1a,b, respectively.

We performed all calculations using `octopus` [93], a finite-difference real-space DFT code, which we modified to include the electrostatic boundary conditions. We modeled the system using the Perdew-Burke-Ernzerhof (PBE) functional [412, 613]. The interaction between valence electrons and the cores were modeled using Troullier-Martins pseudopotentials [535]. Method details are available on Sec. 4.5.1

We first look at the total energy of benzene with respect to the plate separation, while keeping the molecule centered and the gates grounded. The results are plotted in Fig. 4.2. When the interplate distance is 13 Å, the perpendicular orientation is 3.3 eV lower in energy than the parallel orientation. This implies that the molecule centered between the plates will tend to rotate toward the perpendicular orientation. This effect results from the charge induced, by the molecule, in the metal plates and is thus a type of Casimir effect [350, 379, 90].

The conformational stabilization of benzene with respect to the plates can be understood in the context of image charges. In the perpendicular case, the molecule is closer to the metal plates, as seen in Fig. 4.1. The image charge solution gives an opposite charge on the plates to each of the charges present inside the plates. We therefore expect that proximity to the plate translates as an additional source of energy stabilization. As the plate separation increases, at 40 Å plate distance, both orientations are within 0.1 eV of

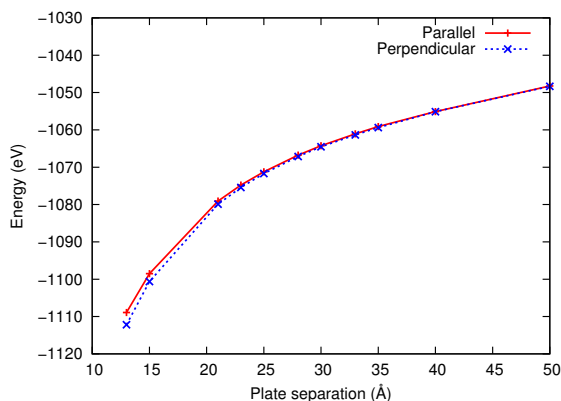


Figure 4.2: Benzene total energy with respect to plate separation. The total energy of benzene at parallel and perpendicular orientations with respect to the metal plate distance separation. The latter orientation is higher in energy at lower plate separations, but as the plates become farther apart, these energies converge and the orientational effects of energy disappear.

each other.

Next, we explore a bias sweep by varying the potential on the bottom plate (see Fig. 4.1) and keeping the top grounded. Neutral benzene presents a parabolic dependence of the energy with respect to the voltage bias centered around 0.0 V. A positive or negative bias affects the energy similarly, as shown in Fig. 4.3 where the change of energy takes a parabolic shape.

The benzene anion experiences stabilization due to the image charges in the metallic plates of an overall charged system. This leads to a stabilization of the excess electron in benzene. When the plates are grounded (*i. e.* no bias), we obtain a total energy that is 0.4 eV lower than the neutral system for both orientations. In this case, the maximum is not at 0.0 V, but rather is shifted to a potential of approximately -0.3 V for both orientations. At this potential, the excess electron has some electron density interacting with the bottom plate. The energy curves are not symmetric due to the excess electron, which causes a different response with positive and negative biases. It stabilizes under a positive bias more readily than under a negative one due to the excess negative charge. As the voltage bias increases (becomes more positive), the slope for the total energy of the anion becomes steeper than in the case of the negative bias. Finally, for large negative potential, we find that the neutral system becomes more stable than the anion at a bias of -1.0 eV and of -1.1 eV for the parallel and perpendicular cases, respectively, as is seen in Fig. 4.3.

We continue by looking at the induced charge on the metal plates due to its energetic relevance. With the anion oriented parallel to the plates the induced charge shows a round

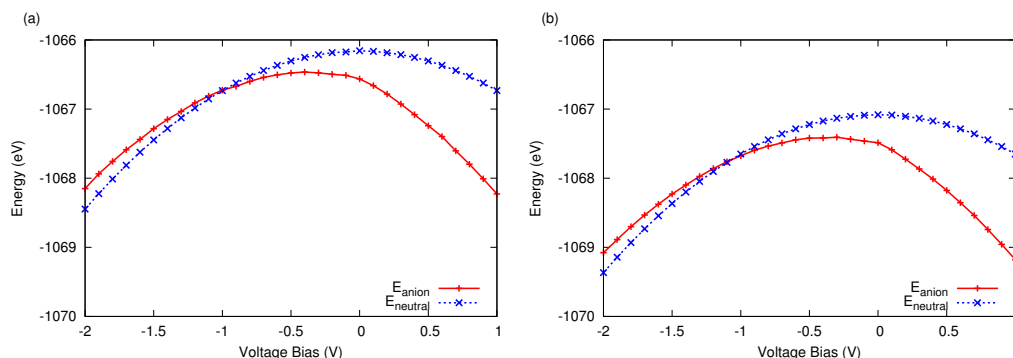


Figure 4.3: **Benzene anion energy and its neutral counterpart.** Energy between the benzene anion and its neutral counterpart when the molecule is oriented parallel (a) and perpendicular (b) to the plate and an interplate distance of 21 Å. At zero voltage bias, the energy of the anion is less than the neutral molecule. Adding a negative voltage bias moves the neutral case toward higher stability with respect to the anion.

shape, while it shows an oval shape when the molecule is oriented perpendicular to the plates (along the xz -plane) as seen in Fig. 4.4a,b, respectively. The induced charge on the molecule parallel to the plates is relatively homogeneous across the boundary, while in the perpendicular case, the induced charge is concentrated in the center and has a more pronounced response. In both cases it is positive, indicating that the excess electron is screened by the plates. The induced charge is therefore helpful to identify the areas of increased electron density along system boundaries.

We plot the highest occupied molecular orbital (HOMO) of the molecule with plates grounded and at a bias of -0.1 V as shown in Fig. 4.5a,b, respectively. The comparison of these orbitals suggests an increased polarizability of the excess electron as it diffuses when applying a bias in the electrostatic environment.

As shown in Fig. 4.5c, the anion HOMO energy at zero bias is -0.20 eV. There is a change of HOMO energy as we apply the voltage bias; decreasing in energy as the bias is increased. Changes in HOMO and lowest unoccupied molecular orbital (LUMO) levels influence charge transport calculations, and studies of these changes are planned as a future area of exploration.

One can also look at the interaction between the molecule and the plates as the system interacting with its image charges; the latter being responsible for the anion stabilization. Specifically, the image charges provide a screened potential, different than the $1/r$ potential present in vacuum, which allows the excess electron to interact more strongly with the ions. To further understand the interaction of the electrons and ions of the system, we use the electron localization function (ELF) developed by Becke and Edgecombe [53]. Description

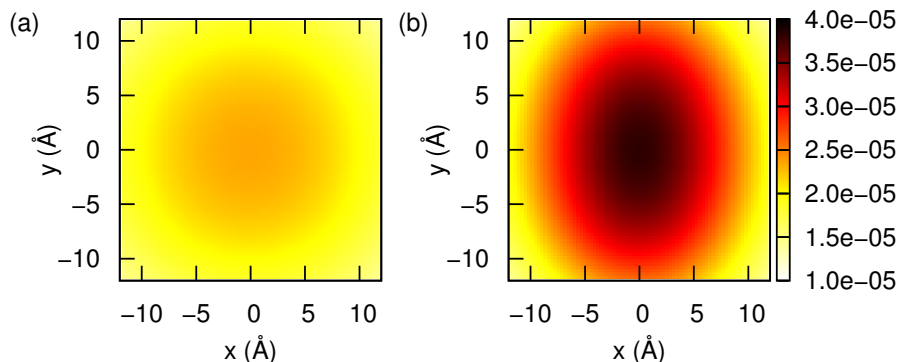


Figure 4.4: Induced charge (a.u.) at bottom plate caused by benzene anion at different orientations. (a) Parallel to the plates. (b) Perpendicular to the plates.

of the ELF can be found in Section 4.5.3.

There are clear differences in the case of the molecule in free-space and under these electrostatic conditions. In Fig. 4.6 we compare the ELF of the benzene anion between the metal plates to its free-space form. In order to highlight this, we plot the ELF difference: $\Delta\text{ELF} = \text{ELF}^{\text{=}} - \text{ELF}^{\circ}$, where the = and \circ superscripts denote the metallic plates and free-space, respectively. Two-dimensional (2D) ΔELF plots (showing the yz plane at $x=0$) for different bias potentials are shown in Fig. 4.6. Fig. 4.6b at $V=0.0$ shows crescent-shaped regions at $z = \pm 4 \text{ \AA}$ with a negative difference (blue). A negative value of ΔELF represents regions where, in the metallic plates case, the excess electron is able to penetrate closer to the ions. The difference of the ELF diagrams between benzene anion in free-space and grounded with the metal plates, shown in Fig. 4.6b, signifies that the excess electron lies closer to the nuclei in the latter case. Effectively, this causes the excess electron to be more strongly bound in this environment by 0.4 eV.

As we decrease the voltage bias, we observe the depletion of the excess electron as a negative voltage bias is added to the bottom plate of the system, as shown in Fig. 4.6b. In vacuum, this section is completely dominated by the excess electron. As we add a negative bias, this electron will tend to avoid the bottom-half area. At the same time, we obtain a negative difference in ELF at positive values of z . As we decrease the bias, the bottom region becomes depleted of the excess electron. Similarly, the top area acquires more electron density, but the ΔELF in this area remains at -0.5; as the excess electron is already dominating in this region.

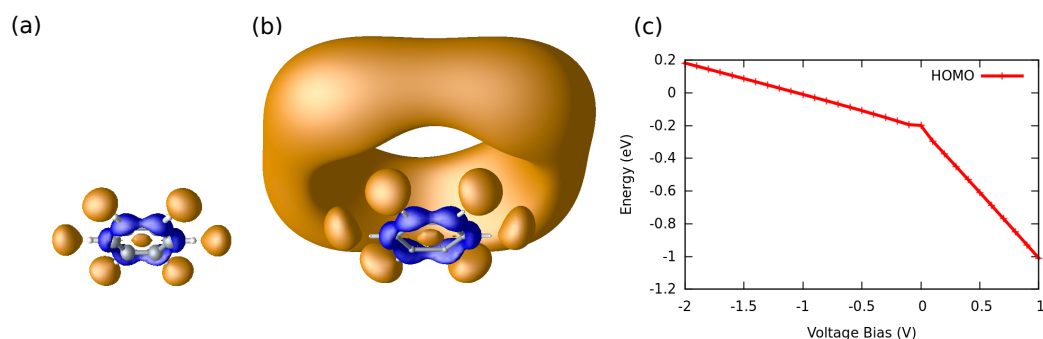


Figure 4.5: HOMO of the benzene anion. (a) Benzene anion HOMO under no bias under the electrostatic environment. (b) Benzene anion HOMO with a -0.1 V bias shows an increased localization of the orbital away from the bias. (c) HOMO eigenvalue at different voltage bias.

4.3 Discussion

The plate distance separation calculations show the relevance of image charge effects due to the plates. The energetic contribution due to the metal plates become an essential contribution to understand orientational effects. For instance, at small interplate distances, the energy differences are in the range of several eV. We notice that each ion or electron will also interact with the images of the other charged particles of the system. It can be shown by geometric arguments that the interaction with the plate(s) is attractive for a system with any number of charges when the plates are grounded.

In the case of the benzene anion, these image charges cause the excess electron to stabilize, with respect to its neutral counterpart. When applying a voltage bias, the system's total energy becomes part of an energetic interplay between the decrease in energy of the eigenvalues (particularly the HOMO energy, as seen in Fig. 4.5c), the electrostatic energies, and the plate energy.

Choi *et al.* have explored the molecular orbital shift of benzene under a electrostatic field in the order of $1 \text{ V}\text{\AA}^{-1}$ [102, 260]. The bias induced in the metallic plates produces also an electric field. In order to create such fields in this confined environment, we require a voltage bias of 21 V. In the case of the benzene anion, less voltage is needed to observe effects similar to those studied by Choi *et al.*, such as molecular orbital tuning, as shown in Fig. 4.5c. We observe the effect of a small field $\sim 0.1 \text{ V}\text{\AA}^{-1}$ as it causes the excess electron distribution to move away from the plate with negative voltage.

The work of Mitsui *et al.* [353] showed the stabilization of an excess charge in benzene clusters of 53–124 molecules. We observe that a similar effect takes place in an metallic environment: the VEA becomes positive, and thus an excess charge in benzene is stabilized.

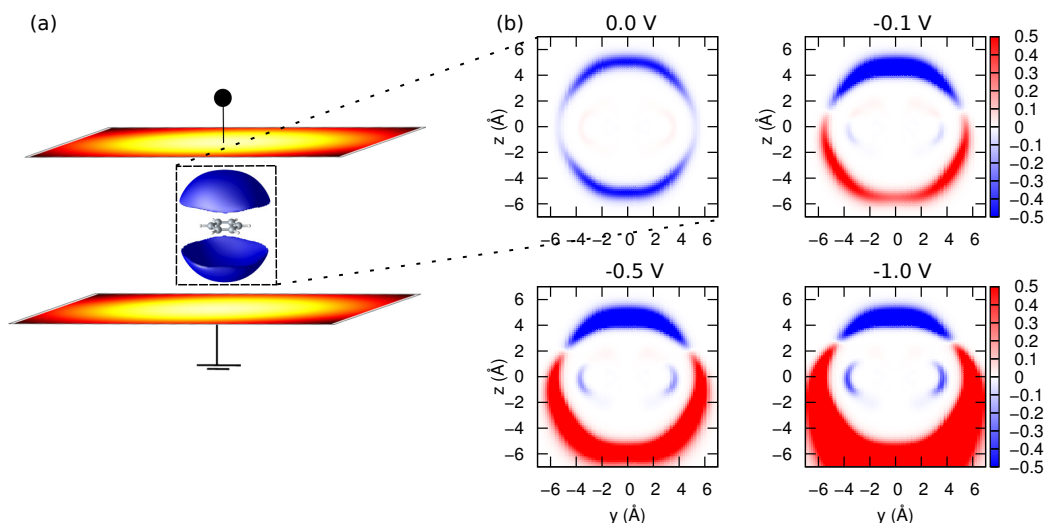


Figure 4.6: Difference of metallic-environment ELF: $\Delta\text{ELF} = \text{ELF}^{\equiv} - \text{ELF}^{\circ}$, where \equiv and \circ represent the metallic plates and free-space, respectively, at different voltage biases of β spin polarization contains the excess electron. Panel a represents ΔELF . The dotted region represents the area plotted in panel b. We plot the yz -plane at $x=0$. (b) shows ΔELF for four different voltages. In $V=0.0$, the diagram shows an area (blue) where the excess electron dominates closer to the molecular region, and edges (red) where the electrons are more delocalized than the free-space case. As we decrease the bias to more negative bias the bottom region becomes more red (positive) as the excess electron begins to localize itself upward, due to the electrostatic repulsion with the plates.

Other conjugated molecules, such as polycyclic aromatic hydrocarbons, have a systematically decreasing VEA [444] as they increase in number of aromatic cycles.

4.4 Conclusions

The effects presented here by simulating a metallic environment with electrostatic boundary condition reveal the leading role of the image charge effect for stabilizing excess charge in molecular systems. This chapter shows a straightforward way of considering electron confinement in a perfect conductor system.

The use of more geometrically complex boundary conditions will allow us to obtain an even more realistic environment of the molecule interacting with an extended metallic system. Furthermore, controlling the molecule in this environment could greatly enhance the system's spectroscopic properties such as is the case for surface-enhanced and tip-enhanced Raman scattering.

The implementation of this algorithm in a versatile and widely-available software pack-

age such as `octopus` will allow for studies of time-dependent properties of the molecules and also will facilitate the simulations of higher-order physics such as many-body effects with metallic boundary conditions in the near future.

4.5 Appendix

4.5.1 Methods

Algorithm

This section details the solution of the self-consistent Poisson-Schrödinger system of equations. This method is general for wave-function-based methods or density functional algorithms. We use the latter and program it in the `octopus` code.

We solve Poisson’s equation separately for ions and electrons given the metallic boundary conditions: plate geometry, fixed voltage at each plate. Poisson’s equation is solved using an incomplete LU biconjugate gradient squared $\mathbf{Ax}=\mathbf{b}$ solver [495, 249]. The solver tolerance was set differently for obtaining the ionic and electronic potential, since the number of times the solver is called is different for each case. We obtain Poisson’s equation using Dirichlet boundary conditions at the plates. We use Neumann boundary conditions on the remaining sides of the simulation box; these are distant from the molecule and we thus consider the electric field component in each of these directions to have decayed to zero.

We solve for the nuclear potential one atom at a time, and then solve for the electronic potential in each Kohn-Sham SCF iteration, as per the `octopus` algorithm [93].

The ionic potential is determined at the beginning of the calculation. In this chapter, ion positions are taken as fixed. We explicitly determine the nuclear energy since it does not have a closed form. Instead, we integrate the product of the ion density and the ion potential over space, as mentioned in Sec. 4.1.

We find the induced charge density after obtaining a total expression of the electrostatic potential. Given the potential at the plates, an input parameter, and the potential bordering these points, then it is possible to find the surface charge by obtaining the normal derivative of the potential at the surface. We calculate the derivative by the same finite difference approach we use in computing the potential. The plate energy is then obtained by summing the product of the induced charge densities at every gate, as shown in Eq. 4.4.

The rest of the energy components (*e.g.* electronic energy, exchange and correlation contributions) are obtained using the canonical `octopus` operations to obtaining these properties.

Computational Details

We treated the molecule with `octopus` [93], a finite-difference real-space code, which we modified to include the electrostatic boundary conditions. The code including our modifications is available for download under a free software license.¹ We modeled the system using the Perdew-Burke-Ernzerhof (PBE) functional [412, 613]. The interaction between valence electrons and the cores were modeled using Troullier-Martins pseudopotentials [535].

In the plate-separation calculations, the distance was set to 0.10 Å grid spacing to ensure convergence. The plate distance is varied from a minimum of 13.0 Å (the converged distance for the free space case) to 50.0 Å. In the bias-dependence calculations, we set out a wider grid separation of 0.16 Å since we are interested in converging the difference in energy between the anion and neutral case. In this case, we used a parallelepiped box of 24 Å on the x - and y -axis and 20 Å on the z -axis to ensure that the anion wave-functions are correctly represented.

In all cases, the metal plates are located 0.5 Å away from the limits of density-containing box. In the voltage dependence case, we set the two metallic plates to be 21.0 Å apart. In order to simulate infinite plates along the x and y dimensions, we extend the mesh up to 60. Å.

We performed a set of calculations by setting the voltage at the bottom plate. This voltage varied from -2.0 V to 1.0 V. The drain voltage (i.e. the top plate) remained always grounded.

4.5.2 Ion Potential and Ion-ion Energy in Electrostatic Boundary Conditions

As mentioned in Sec. 4.2, in free-space, the ion potential is given by $\phi_{\text{ion}}^{\circ}(\mathbf{r})$ and the ion-ion interaction,

$$\frac{1}{2} \int d\mathbf{r} \rho_{\text{ion}}(\mathbf{r}) \phi_{\text{ion}}^{\circ}(\mathbf{r}),$$

is substituted by the sum of the i th-ion interacting with all other j th-ions: $\sum_i \sum_{i>j} \frac{q_i q_j}{|R_i - R_j|}$. In arbitrary electrostatic conditions, besides considering the interaction between the i th-ion and the potential generated by the j th ion: $\sum_i \sum_{i>j} \int d\mathbf{r} \rho_{\text{ion},i}(\mathbf{r}) \phi_{\text{ion},j}^{\parallel}(\mathbf{r})$, the interaction given by a single charged particle with the metal plates (*i. e.* its image charges) is an important energetic component [238].

In order to obtain a general solution of the interaction of each i th-ion with the plates, we notice that the i th-ion potential we calculate, $\phi_{\text{ion},i}^{\parallel}(\mathbf{r})$, can be partitioned into two

¹<http://www.tddft.org/programs/octopus/>

contributions: $\phi_{\text{ion},i}^{\parallel}(\mathbf{r}) = \phi_{\text{ion},i}^{\circ}(\mathbf{r}) + \phi_{\text{ion},i}^{\text{im}}(\mathbf{r})$, where $\phi_{\text{ion},i}^{\circ}(\mathbf{r})$ is the potential of the ion in free-space and $\phi_{\text{ion},i}^{\text{im}}(\mathbf{r})$ is a potential given by the image charges due to the metallic plates.

If we calculate the contribution of the ion with the metal plates, as shown in the LHS of Eq. 4.7 below,

$$\int d\mathbf{r} \rho_{\text{ion},i}(\mathbf{r}) \phi_{\text{ion},i}^{\parallel}(\mathbf{r}) = \int d\mathbf{r} \rho_{\text{ion},i}(\mathbf{r}) \phi_{\text{ion},i}^{\circ}(\mathbf{r}) + \int d\mathbf{r} \rho_{\text{ion},i}(\mathbf{r}) \phi_{\text{ion},i}^{\text{im}}(\mathbf{r}), \quad (4.7)$$

we notice that the energy contribution due to the interaction of the ion with its own potential, *i. e.* the first term in the RHS, is a spurious self-interaction. We can remove this term by separately calculating $\phi_{\text{ion},i}^{\circ}(\mathbf{r})$ and subtracting the interaction with its own potential: $\int d\mathbf{r} \rho_{\text{ion},i}(\mathbf{r}) \phi_{\text{ion},i}^{\parallel}(\mathbf{r}) - \int d\mathbf{r} \rho_{\text{ion},i}(\mathbf{r}) \phi_{\text{ion},i}^{\circ}(\mathbf{r})$. The difference yields the energy due to the interaction of the *i*th-ion with its image charge: the last term on the RHS of Eq. 4.7. This self-interaction correction is analogous to the one utilized in Ewald summation methods [330].

The energetic contribution of $\phi_{\text{ion},i}^{\parallel}(\mathbf{r})$ (after removing the self-interaction) is an attractive one. This can be rationalized in physical terms as the attraction of each ion with its mirror images. We find a similar interplay taking place in the case of the electrons, where the self-interaction is removed to a lesser or greater extent by the exchange-correlation potential; the interaction of the plates with the electron density should also provide a stabilizing effect to the overall system.

4.5.3 Electron Localization Function

To better understand the behavior of the excess electron of the molecule between two metal plates, we will examine the changes in the electronic distribution and localization with respect to the applied voltage. One useful tool for this study is the electron localization function (ELF), developed by Becke and Edgecombe [53]. More properties are derived and explained in Appendix A ELF is defined as

$$\text{ELF}(\mathbf{r}) = \frac{1}{1 + \left(\frac{D_{\tau}(\mathbf{r})}{D_{\tau}^0(\mathbf{r})}\right)^2}, \quad (4.8)$$

where

$$D_{\tau}(\mathbf{r}) = \sum_{i=1}^{\tau} (\nabla \chi_i(\mathbf{r}))^2 - \frac{1}{4} \frac{|\nabla \rho_{\tau}(\mathbf{r})|^2}{\rho_{\tau}(\mathbf{r})} \quad (4.9)$$

$$D_{\tau}^0(\mathbf{r}) = \frac{3}{5} (6\pi^2)^{2/3} \rho_{\tau}^{5/3}. \quad (4.10)$$

D_{τ} is related to the exchange hole curvature: $C_{\tau}(\mathbf{r}) = D_{\tau}(\mathbf{r})/2\rho_{\tau}(\mathbf{r})$ which quantifies the vanishing of the pair distribution for pairs of electrons of spin τ at a small inter-particle

separation [135]. Here, ρ_τ is the density restricted to spin τ . The pair distribution vanishes quadratically up to leading order, since the distribution reaches a minimum at zero interparticle distance. The curvature is then related to the number of other parallel spin electrons within a small radius. Alternatively, Eq. 4.9 is derived from the Taylor expansion of the conditional pair probability (on a shell of radius s about \mathbf{r}) [53]: $P_{\text{cond}}^{\tau\tau}(\mathbf{r}, s) \approx \frac{1}{3}D_\tau(\mathbf{r})s^2$. If the probability of finding an electron of the same spin close to another is small, then the quantity D_τ , is smaller, due to the hole being wider.

The ELF is designed to have a range from 0 to 1. Equation 4.8 shows that ELF is defined to be inversely proportional to the curvature of the exchange hole, D_τ . Also, D_τ^0 represents the uniform electron gas with spin density equal to the local value and serves as a normalization factor.

The ELF is unity in regions of perfect localization (where D_τ vanishes), while it is one-half when D_τ approaches the value of the uniform electron gas (D_τ^0). Becke and Edgecombe note that for multielectron systems in regions dominated by a single, localized, τ -electron orbital, the value of D_τ vanishes, and therefore the value of ELF approaches unity [53]. This result will become useful in the analysis of the benzene anion.

There is a wide variety of ELF studies in the literature, including studies on benzene [463, 464, 322, 165, 421, 16]. Specifically, there is work related to properties and use of ELF for radical anions, a relevant topic for this chapter. Savin *et al.* described early the shape of ELF in negative ions, such as the H^- moiety in the LiH molecule [463]. There has also been comparative work of ELF between neutral and radical anions of carbonyl and imine compounds [154], as well as the use of ELF to analyze bonding of $(\text{NO})_2$, and its radical anion and dianion [164].

4.5.4 ELF Analysis

As described in Sec. 1, the electron localization function is an illustrative tool for anionic systems. In Fig. 4.7, we represent the ELF for the α -spin system (Fig. 4.7b) and β -spin polarization (Fig. 4.7c), in free-space. The α spin polarization does not contain the excess electron, but it gives a revealing description of the σ - and π -electrons in benzene. The α -spin system does not significantly change by the addition of metallic plates, including a voltage bias (shown in Fig. 4.8).

We proceed by further analyzing the overall properties of ELF applied to benzene. We describe the ELF of neutral benzene to compare and contrast with its anion counterpart in Fig. 4.7. With the molecule parallel to the plates, we rotate the xy-plane so that, at $x = 0$ and $z = 0$, the y-axis goes through the center of four atoms (two hydrogens and two carbons). The y-coordinates of these atoms (in Å) are: $y_{\text{H}} = -2.49$, $y_{\text{C}} = -1.40$, $y_{\text{C}} = 1.40$, and $y_{\text{H}} = 2.49$. In Fig. 4.7b, as we approach $y = -4$ (always along $z = 0$) from the left, the

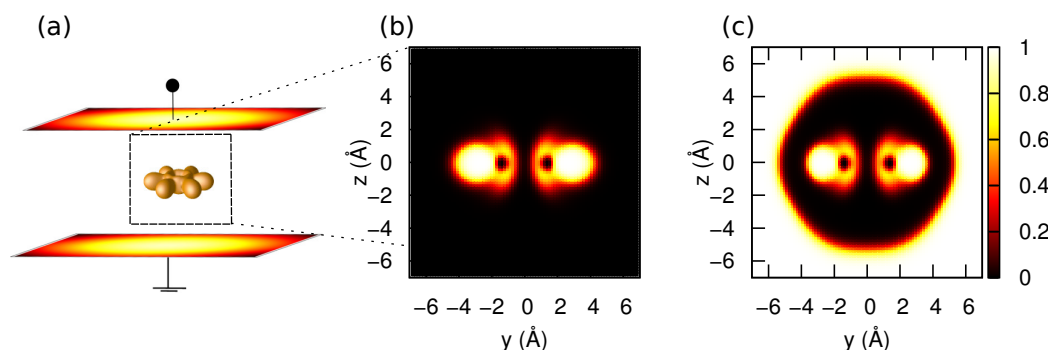


Figure 4.7: **ELF for the two spin-polarizations of benzene anion.** (a) shows a 3D representation of α -spin polarization with an isosurface values of $\text{ELF} = 0.6$. The dotted region represents the area we present the following 2D plots. Diagrams (b) and (c) show ELF of α -spin and β -spin polarization for benzene anion in free-space, respectively. The excess electron is part of the β -spin electrons. The number of α -spin electrons is the same as neutral benzene, and therefore its ELF has the same shape as neutral benzene. The β -spin electron system contain the excess electron. Close to the center of the plots, the properties of (b) and (c) are analogous. It is in the outer regions, where the excess electron dominates, that the ELF value differ.

ELF increases to show the location of a C-H σ -bond. We notice that the ELF then falls to a local minimum near $y = -1.4$, corresponding to the location of one carbon atom.

Close to this value we also observe an increase in ELF above and below the $z = 0$ line. We attribute this to the localization due to the π -electrons of benzene.

The α -spin polarization presented a clear view of the σ - and π -electrons. The β -spin polarization contains the excess electron. This gives the ELF very particular properties, as described below. We plot the ELF in Fig. 4.7c (at $x=0$).

At $y = -5, z = 0$ we find an $\text{ELF} = 0.5$ contour. It is identifiable because to the left of $y = -5$, the ELF increases rapidly to a value of one; while to the right of this point, the ELF decays to zero. This $\text{ELF} = 0.5$ contour (the ELF value for the homogeneous electron gas) is roughly circular. Inside the contour the area resembles the α -spin polarization case, and hence also describes the σ - and π -electrons.

We are interested in the region outside the contour at $y = \pm 5$. Becke and Edgecombe [53], consider the case of a single-electron system or a system dominated by a single, localized, σ -electron orbital. This is effectively the case in the region beyond $y, z = \pm 5$, where the excess electron dominates.

A positive voltage sweep (not shown) presents an ELF with similar properties, but with an inverse response with respect to the voltage bias. A similar situation arises in the case of the molecule oriented perpendicular to the plates (see Fig. 4.10).

4.5.5 Complete ELF Diagrams

The 2D-ELF diagrams (at $z = 0$) for the α -spin polarization for free-space and different voltage biases of the benzene anion oriented parallel to the plates are shown in Fig. 4.8a and Fig. 4.8b-f, respectively. As discussed in Sec. II, there is no significant change between the electron localization of the α electrons in free-space and with the metal plates.

The 2D-ELF diagrams (at $x = 0$) for the β -spin polarization for free-space and different voltage biases of the benzene anion oriented parallel to the plates are shown in Fig. 4.9a and Fig. 4.9b-f, respectively. We utilized this data to obtain ΔELF , where $\Delta\text{ELF} = \text{ELF}^{\circ} - \text{ELF}^{\ominus}$, and \circ and \ominus represent the metallic plates and free-space, respectively.

The 2D-ELF diagrams (at $x = 0$) for the β -spin polarization for free-space and different voltage biases of the benzene anion oriented perpendicular to the plates are shown in Fig. 4.10a and Fig. 4.10b-f, respectively. The description of the ELF inside the $\text{ELF}=0.5$ contour mirrors closely the explanation in Sec. II. For instance, there are six lobes corresponding to the σ -electron located close to the position of the hydrogen atoms. As the bias decreases, we once again see a depletion of the excess electron in the bottom part of the plate, as reflected by an ELF value approaching zero in this area.

4.5.6 Geometries

We work with two geometries, each of them related by a 90° rotation. The geometry of benzene parallel to the plates is presented in Table 4.1, while benzene perpendicular to the plates is shown in Table 4.2.

4.5.7 Energetic Contributions

The total energy in DFT is described below, where we label the terms shown on Tables S3-S8:

$$\begin{aligned}
 E_{\text{sys}} = & \underbrace{\sum_i \epsilon_i}_{\text{Eigenvalues}} - \underbrace{\frac{1}{2} \int d\mathbf{r} \rho_{\text{el}}(\mathbf{r}) \phi_{\text{el}}^{\parallel}(\mathbf{r})}_{\text{Hartree}} + \\
 & + \underbrace{\frac{1}{2} \int d\mathbf{r} \rho_{\text{ion}}(\mathbf{r}) \phi_{\text{ion}}^{\parallel}(\mathbf{r}) + \int d\mathbf{r} \rho_{\text{ion}} \phi^{\text{B}}(\mathbf{r})}_{\text{Nuclear}} \\
 & - \int d\mathbf{r} \phi^{\text{xc}}(\mathbf{r}) \rho_{\text{el}}(\mathbf{r}) + E^{\text{xc}}[\rho_{\text{el}}] - \underbrace{\frac{1}{2} \sum_m Q_m V_m}_{\text{Gate}} .
 \end{aligned} \tag{4.11}$$

The Hartree term is a correction of the electrostatic interaction of the electron-electron interaction since the sum over Kohn-Sham eigenvalues contains implicitly the electrostatic

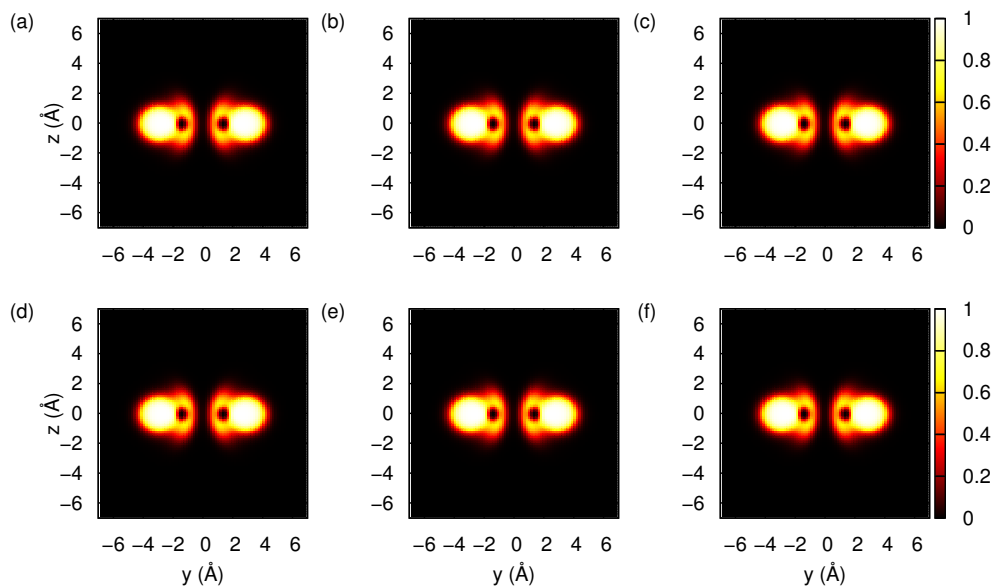


Figure 4.8: **ELF for the α -spin electrons for benzene anion in the electrostatic environment at different biases with the molecule oriented parallel to the plates.** (a) Free space (b) 0.0 V (c) -0.1 V (d) -0.2 V (e) -0.5 V (f) -1.0 V α -spin polarization does not contain the excess electron.

interaction of the electrons: $\frac{1}{2} \int d\mathbf{r} \rho_{\text{el}}(\mathbf{r}) \phi_{\text{el}}^{\parallel}(\mathbf{r}) + \int d\mathbf{r} \rho_{\text{el}}(\mathbf{r}) \phi_{\text{el}}^{\text{B}}(\mathbf{r})$.

4.5.8 Distance Dependence

We present the energetic contributions in the plate separation simulations shown in Sec. II and III, specifically in Fig. 2. The contributions when the molecule is parallel to the plates are shown on Table 4.3, while the energy terms when the molecule is perpendicular are on Table 4.4.

4.5.9 Voltage Bias

We present the energetic contributions in the plate separation simulations shown in Sec. II and III, specifically in Fig. 3. The terms of the molecule parallel to the plates are shown in for the neutral, Table 4.5, and the anion, Table 4.6. The contributions for the molecule perpendicular to the plates are presented in Table 4.7 and Table 4.8, for the neutral and anion case, respectively.

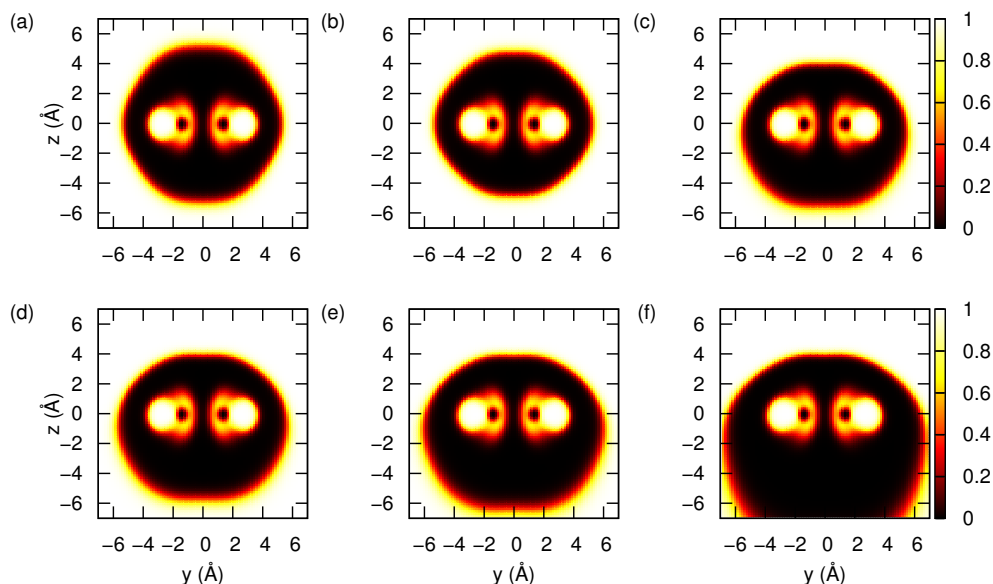


Figure 4.9: **ELF** for the β -spin electrons for benzene anion in the electrostatic environment at different biases with the molecule oriented parallel to the plates. (a) Free space; (b) 0.0 V; (c) -0.1 V; (d) -0.2 V; (e) -0.5 V; (f) -1.0 V. β -spin polarization contains the excess electron. In **a**, the zone dominated by relatively homogeneously distributed electrons (black) expands above and below $z = 0$. In **b**, the same region begins to be dominated by a value of ELF = 1 (yellow), which signifies a stronger dominance of the excess electron in the area. In **c-f**, as we decrease the bias to more negative bias, the low localization (black) starts moving further and further towards negative values of z . Thus, the excess electron is being depleted from this region of space.

Atom	x	y	z
C	1.2101359	0.6986723	0.0000000
C	1.2101359	-0.6986723	0.0000000
C	0.0000000	-1.3973446	0.0000000
C	-1.2101359	-0.6986723	0.0000000
C	0.0000000	1.3973446	0.0000000
C	-1.2101359	0.6986723	0.0000000
H	2.1556169	1.2445460	0.0000000
H	2.1556169	-1.2445460	0.0000000
H	0.0000000	-2.4890920	0.0000000
H	-2.1556169	-1.2445460	0.0000000
H	0.0000000	2.4890920	0.0000000
H	-2.1556169	1.2445460	0.0000000

Table 4.1: Benzene parallel to the metal plates

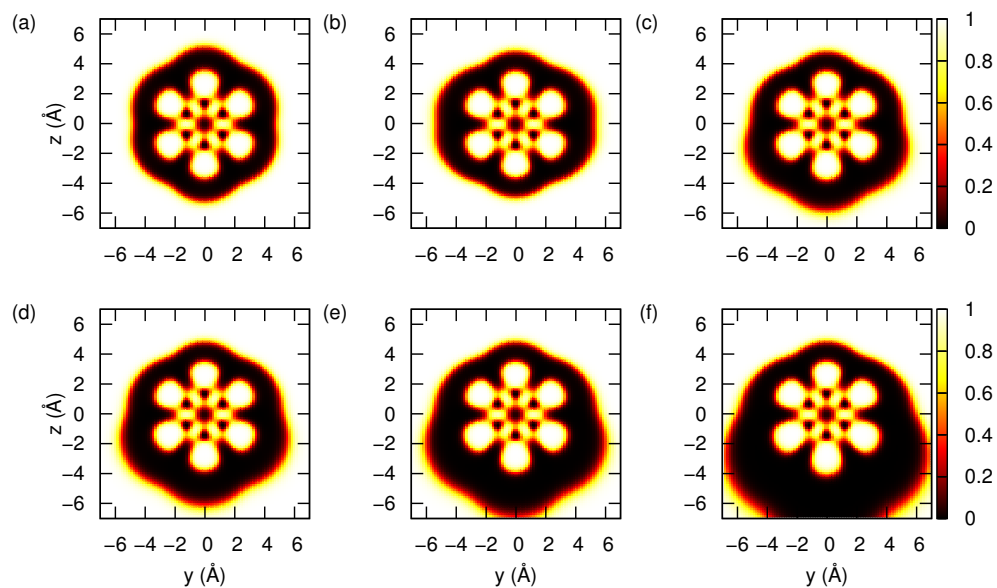


Figure 4.10: **ELF** for the β -spin electrons for benzene anion in the electrostatic environment at different biases with the molecule oriented perpendicular to the plates. (a) Free space (b) 0.0 V (c) -0.1 V (d) -0.2 V (e) -0.5 V (f) -1.0 V β -spin polarization contains the excess electron.

Atom	x	y	z
C	0.000000	1.2101359	0.6986723
C	0.000000	1.2101359	-0.6986723
C	0.000000	0.000000	-1.3973446
C	0.000000	-1.2101359	-0.6986723
C	0.000000	0.000000	1.3973446
C	0.000000	-1.2101359	0.6986723
H	0.000000	2.1556169	1.2445460
H	0.000000	2.1556169	-1.2445460
H	0.000000	0.000000	-2.4890920
H	0.000000	-2.1556169	-1.2445460
H	0.000000	0.000000	2.4890920
H	0.000000	-2.1556169	1.2445460

Table 4.2: Benzene perpendicular to the metal plates

Plate separation (Å)	Energy (eV)					$E^{\text{xc}}[\rho_{\text{el}}]$
	Total	Hartree	Nuclear	Eigenvalues	$\int dr \rho(\mathbf{r}) \phi^{\text{xc}}(\mathbf{r})$	
13.0	-1108.907742	2900.405723	2050.842485	-360.787202	-445.898614	-344.455915
15.0	-1098.503734	2987.967703	2148.691145	-360.669881	-445.898728	-344.456023
21.0	-1079.075918	3153.614461	2333.556466	-360.460605	-445.898689	-344.456006
23.0	-1074.783049	3190.154547	2374.309486	-360.380409	-445.897585	-344.455164
25.0	-1071.224008	3221.079225	2408.782662	-360.369957	-445.897982	-344.455469
28.0	-1066.779173	3259.633061	2451.751778	-360.340335	-445.897705	-344.455260
30.0	-1064.269194	3281.415070	2476.015246	-360.311886	-445.897994	-344.455479
33.0	-1061.064047	3309.753977	2507.593889	-360.346342	-445.897417	-344.455033
35.0	-1059.116002	3326.435182	2526.176324	-360.299583	-445.897667	-344.455228
40.0	-1055.093639	3362.716324	2566.586883	-360.406809	-445.898396	-344.455785
50.0	-1048.233460	3421.978148	2632.605214	-360.302794	-445.896925	-344.454656

Table 4.3: Benzene total energy (eV) and its relevant contributions with respect to plate separation (Å). The molecule lies parallel to the plate. The plate voltages are set to zero, therefore there is no energy contribution for the plate energy term.

Plate separation (Å)	Energy (eV)					
	Total	Hartree	Nuclear	Eigenvalues	$\int dr \rho(\mathbf{r}) \phi^{\text{xc}}(\mathbf{r})$	$E^{\text{xc}}[\rho_{\text{el}}]$
13.0	-1112.193234	2879.012849	2025.375474	-359.998440	-445.898187	-344.455606
15.0	-1100.618895	2973.935312	2132.032364	-360.158243	-445.897045	-344.454750
21.0	-1079.898520	3148.382826	2327.363360	-360.321588	-445.898118	-344.455584
23.0	-1075.414835	3186.129628	2369.548296	-360.275920	-445.897630	-344.455212
25.0	-1071.692542	3217.896768	2405.028106	-360.266064	-445.896622	-344.454438
28.0	-1067.129302	3257.300254	2449.015767	-360.286876	-445.896069	-344.454007
30.0	-1064.534772	3279.471752	2473.736366	-360.241024	-445.893939	-344.452300
33.0	-1061.351457	3308.236551	2505.806376	-360.363519	-445.896827	-344.454591
35.0	-1059.384183	3325.117029	2524.623355	-360.332830	-445.897201	-344.454880
40.0	-1055.118329	3361.712745	2565.418378	-360.266105	-445.896436	-344.454294
50.0	-1048.323627	3421.271246	2631.772089	-360.266617	-445.896445	-344.454299

Table 4.4: Benzene total energy (eV) and its relevant contributions with respect to plate separation (Å). The molecule lies perpendicular to the plate. The plate voltages are set to zero, therefore there is no energy contribution for the plate energy term.

Voltage (V)	Energy (eV)							$\int dr \rho(\mathbf{r}) \phi^{xc}(\mathbf{r})$	$E^{xc}[\rho_{el}]$
	Total	Hartree	Gate	Nuclear	Eigenvalues				
-1.0	-1066.732563	3178.531438	0.570599	2386.968751	-376.229204	-446.661015	-345.031088		
-0.9	-1066.624011	3178.532142	0.462184	2385.468751	-374.728387	-446.661118	-345.031167		
-0.8	-1066.526897	3178.532779	0.365183	2383.968751	-373.227658	-446.661210	-345.031237		
-0.7	-1066.441226	3178.533344	0.279593	2382.468750	-371.727030	-446.661291	-345.031299		
-0.6	-1066.367019	3178.533841	0.205416	2380.968750	-370.226520	-446.661362	-345.031354		
-0.5	-1066.304012	3178.534230	0.142650	2379.468750	-368.725902	-446.661419	-345.031398		
-0.4	-1066.252839	3178.534658	0.091286	2377.968750	-367.225678	-446.661470	-345.031437		
-0.3	-1066.212784	3178.534834	0.051353	2376.468749	-365.725387	-446.661506	-345.031465		
-0.2	-1066.185172	3178.536001	0.022802	2374.968749	-364.225165	-446.661532	-345.031485		
-0.1	-1066.165191	3178.539432	0.005665	2373.468749	-362.718887	-446.661520	-345.031475		
0.0	-1066.156551	3178.536250	0.000000	2371.968749	-361.219026	-446.661200	-345.031223		
0.1	-1066.174463	3178.533070	0.005689	2370.468749	-359.734513	-446.661587	-345.031527		
0.2	-1066.183638	3178.534502	0.022810	2368.968748	-358.225122	-446.661532	-345.031485		
0.3	-1066.213618	3178.534844	0.051353	2367.468748	-356.726211	-446.661505	-345.031464		
0.4	-1066.252759	3178.534577	0.091293	2365.968748	-355.225670	-446.661468	-345.031435		
0.5	-1066.304114	3178.534240	0.142649	2364.468748	-353.725993	-446.661418	-345.031397		
0.6	-1066.366969	3178.533815	0.205415	2362.968748	-352.226493	-446.661358	-345.031351		
0.7	-1066.441232	3178.533337	0.279591	2361.468748	-350.727043	-446.661288	-345.031297		
0.8	-1066.526882	3178.532780	0.365170	2359.968747	-349.227651	-446.661206	-345.031234		
0.9	-1066.623992	3178.532147	0.462178	2358.468747	-347.728365	-446.661112	-345.031162		
1.0	-1066.732472	3178.531427	0.570578	2356.968747	-346.229141	-446.661009	-345.031083		
1.1	-1066.852382	3178.530613	0.690425	2355.468747	-344.729990	-446.660893	-345.030994		
1.2	-1066.983779	3178.529755	0.821663	2353.968747	-343.230978	-446.660769	-345.030899		
1.3	-1067.126577	3178.528830	0.964303	2352.468747	-341.732030	-446.660633	-345.030794		
1.4	-1067.280764	3178.527803	1.118371	2350.968747	-340.233141	-446.660487	-345.030682		
1.5	-1067.446333	3178.526715	1.283840	2349.468747	-338.734292	-446.660328	-345.030560		
1.6	-1067.623426	3178.525536	1.460735	2347.968746	-337.235630	-446.660159	-345.030430		
1.7	-1067.811900	3178.524292	1.649032	2346.468746	-335.737008	-446.659979	-345.030292		
1.8	-1068.011799	3178.522991	1.848743	2344.968746	-334.238454	-446.659791	-345.030148		
1.9	-1068.223107	3178.521644	2.059813	2343.468746	-332.739993	-446.659588	-345.029992		
2.0	-1068.445835	3178.520118	2.282398	2341.968746	-331.241612	-446.659376	-345.029829		

Table 4.5: Neutral benzene total energy (eV) and its relevant contributions with respect to voltage bias (V). The molecule lies parallel to the plate.

Voltage (V)	Energy (eV)					$\int dr \rho(\mathbf{r}) \phi^{\text{xc}}(\mathbf{r})$	$E^{\text{xc}}[\rho_{\text{el}}]$
	Total	Hartree	Gate	Nuclear	Eigenvalues		
-1.0	-1068.228252	3204.409711	0.952983	2386.968751	-351.840815	-448.401397	-346.394890
-0.9	-1068.008886	3205.193975	0.803415	2385.468751	-349.484150	-448.389751	-346.385848
-0.8	-1067.798120	3206.020186	0.665626	2383.968751	-347.082078	-448.377707	-346.376688
-0.7	-1067.604078	3206.943619	0.539668	2382.468750	-344.587774	-448.366613	-346.368381
-0.6	-1067.397041	3207.904357	0.425721	2380.968750	-342.030984	-448.355754	-346.360483
-0.5	-1067.241034	3208.924361	0.323691	2379.468750	-339.453595	-448.343554	-346.351691
-0.4	-1067.080169	3209.996556	0.233935	2377.968750	-336.807135	-448.333109	-346.344400
-0.3	-1066.926907	3211.148726	0.156394	2376.468749	-334.075662	-448.321325	-346.336198
-0.2	-1066.782122	3212.425148	0.091265	2374.968749	-331.215883	-448.309293	-346.327869
-0.1	-1066.660944	3213.892996	0.038856	2373.468749	-328.174940	-448.294950	-346.317852
0.0	-1066.564643	3217.824587	0.000000	2371.968749	-322.671073	-448.235118	-346.272850
0.1	-1066.512224	3213.901935	-0.011595	2370.468749	-325.067572	-448.294296	-346.317356
0.2	-1066.497037	3212.428065	-0.009505	2368.968748	-325.028656	-448.309473	-346.328042
0.3	-1066.475929	3211.153247	0.005164	2367.468748	-324.771328	-448.321086	-346.336025
0.4	-1066.463596	3209.999109	0.032251	2365.968748	-324.389435	-448.331899	-346.343448
0.5	-1066.477328	3208.921585	0.071706	2364.468748	-323.944755	-448.344053	-346.352084
0.6	-1066.503861	3207.882905	0.123309	2362.968748	-323.461606	-448.355476	-346.360265
0.7	-1066.541469	3206.910726	0.186866	2361.468748	-322.910649	-448.365758	-346.367734
0.8	-1066.599837	3206.006039	0.262442	2359.968747	-322.301137	-448.377742	-346.376709
0.9	-1066.671374	3205.184127	0.349825	2358.468747	-321.610073	-448.389778	-346.385875
1.0	-1066.725560	3204.422974	0.448970	2356.968747	-320.828948	-448.401724	-346.395139
1.1	-1066.810461	3203.762399	0.559656	2355.468747	-319.966189	-448.412766	-346.403730
1.2	-1066.910967	3203.184232	0.681861	2353.968747	-319.024840	-448.422755	-346.411535
1.3	-1067.033781	3202.666385	0.815861	2352.468747	-318.034074	-448.434773	-346.420980
1.4	-1067.150090	3202.221962	0.961153	2350.968747	-316.951586	-448.444363	-346.428498
1.5	-1067.282289	3201.819027	1.118042	2349.468747	-315.831886	-448.454056	-346.436137
1.6	-1067.439398	3201.467616	1.286401	2347.968746	-314.674087	-448.463578	-346.443617
1.7	-1067.589971	3201.132076	1.466274	2346.468746	-313.482097	-448.471928	-346.450198
1.8	-1067.757899	3200.854307	1.657609	2344.968746	-312.238391	-448.481063	-346.457400
1.9	-1067.937065	3200.572244	1.860503	2343.468746	-310.998507	-448.489517	-346.464074
2.0	-1068.150162	3200.323973	2.074968	2341.968746	-309.747239	-448.498276	-346.471004

Table 4.6: Benzene anion total energy (eV) and its relevant contributions with respect to voltage bias (V). The molecule lies parallel to the plate.

Voltage (V)	Energy (eV)					$\int dr \rho(\mathbf{r}) \phi^{\text{xc}}(\mathbf{r})$	$E^{\text{xc}}[\rho_{\text{el}}]$
	Total	Hartree	Gate	Nuclear	Eigenvalues		
-1.0	-1067.650864	3165.508362	0.571061	2372.019260	-375.169579	-446.431075	-344.852197
-0.9	-1067.542167	3165.509045	0.462555	2370.519260	-373.668725	-446.431160	-344.852261
-0.8	-1067.444919	3165.509642	0.365471	2369.019260	-372.167982	-446.431229	-344.852314
-0.7	-1067.359218	3165.510183	0.279820	2367.519260	-370.667404	-446.431285	-344.852357
-0.6	-1067.285104	3165.510663	0.205569	2366.019260	-369.167072	-446.431334	-344.852394
-0.5	-1067.222696	3165.511026	0.142759	2364.519260	-367.667120	-446.431374	-344.852424
-0.4	-1067.172158	3165.511331	0.091368	2363.019260	-366.167673	-446.431394	-344.852440
-0.3	-1067.133194	3165.511529	0.051395	2361.519259	-364.668476	-446.431364	-344.852416
-0.2	-1067.106244	3165.512640	0.022841	2360.019259	-363.169019	-446.431600	-344.852603
-0.1	-1067.086239	3165.517500	0.005685	2358.519259	-361.661437	-446.432191	-344.853067
0.0	-1067.082484	3165.511445	0.000000	2357.019259	-360.169413	-446.432168	-344.853052
0.1	-1067.090000	3165.514338	0.005710	2355.519259	-358.668330	-446.432170	-344.853051
0.2	-1067.106444	3165.509701	0.022793	2354.019258	-357.172212	-446.431626	-344.852623
0.3	-1067.131967	3165.509147	0.051327	2352.519258	-355.669699	-446.431363	-344.852415
0.4	-1067.172113	3165.511335	0.091369	2351.019258	-354.167621	-446.431393	-344.852439
0.5	-1067.222717	3165.511021	0.142765	2349.519258	-352.667137	-446.431373	-344.852423
0.6	-1067.286078	3165.510578	0.205559	2348.019258	-351.168140	-446.431340	-344.852398
0.7	-1067.359211	3165.510181	0.279820	2346.519258	-349.667396	-446.431286	-344.852357
0.8	-1067.444951	3165.509659	0.365477	2345.019257	-348.167986	-446.431229	-344.852314
0.9	-1067.542180	3165.509052	0.462560	2343.519257	-346.668723	-446.431159	-344.852261
1.0	-1067.650840	3165.508351	0.571062	2342.019257	-345.169563	-446.431075	-344.852196
1.1	-1067.771034	3165.507575	0.690981	2340.519256	-343.670590	-446.430977	-344.852122
1.2	-1067.902613	3165.506698	0.822312	2339.019257	-342.171687	-446.430862	-344.852034
1.3	-1068.045660	3165.505682	0.965094	2337.519257	-340.672938	-446.430734	-344.851936
1.4	-1068.200103	3165.504582	1.119281	2336.019257	-339.174260	-446.430590	-344.851825
1.5	-1068.365851	3165.503353	1.284889	2334.519256	-337.675591	-446.430428	-344.851702
1.6	-1068.543170	3165.502059	1.461916	2333.019255	-336.177137	-446.430257	-344.851570
1.7	-1068.731793	3165.500635	1.650371	2331.519255	-334.678684	-446.430069	-344.851427
1.8	-1068.931803	3165.499107	1.850244	2330.019255	-333.180304	-446.429868	-344.851273
1.9	-1069.143190	3165.497480	2.061534	2328.519256	-331.681978	-446.429656	-344.851110
2.0	-1069.366016	3165.495759	2.284252	2327.019255	-330.183753	-446.429432	-344.850939

Table 4.7: Neutral benzene total energy (eV) and its relevant contributions with respect to voltage bias (V). The molecule lies perpendicular to the plate.

Voltage (V)	Energy (eV)					$\int d\mathbf{r}\rho(\mathbf{r})\phi^{\text{xc}}(\mathbf{r})$	$E^{\text{xc}}[\rho_{\text{el}}]$
	Total	Hartree	Gate	Nuclear	Eigenvalues		
-1.0	-1069.179004	3194.008396	0.955727	2372.019260	-348.223359	-448.318937	-346.329720
-0.9	-1068.957184	3194.508171	0.806886	2370.519260	-346.149194	-448.313475	-346.325669
-0.8	-1068.742692	3195.028703	0.669766	2369.019260	-344.049103	-448.304679	-346.319060
-0.7	-1068.539339	3195.602124	0.544305	2367.519260	-341.895979	-448.298007	-346.314197
-0.6	-1068.354033	3196.245754	0.430557	2366.019260	-339.678639	-448.290252	-346.308595
-0.5	-1068.176996	3196.947058	0.328611	2364.519260	-337.399788	-448.281783	-346.302581
-0.4	-1068.012491	3197.691054	0.238566	2363.019260	-335.078479	-448.272147	-346.295800
-0.3	-1067.866363	3198.529170	0.160472	2361.519259	-332.669168	-448.262100	-346.288912
-0.2	-1067.723989	3199.472861	0.094509	2360.019259	-330.145305	-448.250233	-346.280806
-0.1	-1067.589768	3200.560123	0.040859	2358.519259	-327.472915	-448.236239	-346.271368
0.0	-1067.486196	3205.329853	0.000000	2357.019259	-321.118088	-448.163553	-346.221067
0.1	-1067.463266	3200.553329	-0.009546	2355.519259	-324.403558	-448.235966	-346.271150
0.2	-1067.436360	3199.478749	-0.006345	2354.019258	-323.952670	-448.250373	-346.280917
0.3	-1067.407402	3198.521885	0.009172	2352.519258	-323.368775	-448.261990	-346.288817
0.4	-1067.418476	3197.725108	0.036904	2351.019258	-322.652608	-448.274718	-346.297832
0.5	-1067.420139	3196.933645	0.076593	2349.519258	-321.908443	-448.282195	-346.302911
0.6	-1067.444332	3196.245924	0.128131	2348.019258	-321.071074	-448.289730	-346.308189
0.7	-1067.489625	3195.609810	0.191489	2346.519258	-320.191396	-448.298118	-346.314305
0.8	-1067.535046	3195.047619	0.266534	2345.019257	-319.226233	-448.306813	-346.320731
0.9	-1067.594732	3194.496107	0.353306	2343.519257	-318.252241	-448.312805	-346.325140
1.0	-1067.675185	3194.012605	0.451671	2342.019257	-317.219328	-448.318655	-346.329492
1.1	-1067.761425	3193.548285	0.561736	2340.519256	-316.161570	-448.325868	-346.334959
1.2	-1067.860714	3193.146503	0.683379	2339.019257	-315.042751	-448.333364	-346.340702
1.3	-1067.974613	3192.726402	0.816668	2337.519257	-313.944823	-448.339165	-346.345141
1.4	-1068.097763	3192.329024	0.961533	2336.019257	-312.821635	-448.344156	-346.348984
1.5	-1068.229009	3191.982316	1.117942	2334.519256	-311.644564	-448.350227	-346.353671
1.6	-1068.376424	3191.643424	1.285983	2333.019255	-310.464449	-448.357584	-346.359406
1.7	-1068.532828	3191.303054	1.465520	2331.519255	-309.282577	-448.361664	-346.362597
1.8	-1068.700798	3191.011075	1.656623	2330.019255	-308.052951	-448.368639	-346.368042
1.9	-1068.887770	3190.716485	1.859314	2328.519256	-306.833102	-448.374642	-346.372766
2.0	-1069.077503	3190.427350	2.073465	2327.019255	-305.598821	-448.379369	-346.376491

Table 4.8: Benzene anion total energy (eV) and its relevant contributions with respect to voltage bias (V). The molecule lies perpendicular to the plate.

Chapter 5

Electronic structure calculations in arbitrary electrostatic environments

5.1 Introduction

Tremendous progress in the development and implementation of quantum chemistry methods has enabled *ab initio* calculations of electronic structure, properties, and even dynamics, to be performed on large-scale molecular systems containing many thousands of atoms. Despite these exciting developments in basic theory, fast numerical algorithms, and novel hardware utilization [552, 538, 540, 393, 567], it is not yet possible to *routinely* simulate such large systems using readily-available computer resources. However, emerging nano-scale simulation challenges involving, for example, large biomolecular aggregates or nanotechnology devices, are increasing the demand for first-principles methods that can deliver this performance. On the other hand, many of the problems of interest are inherently multi-scale and there is often no *need* to model all parts of the system at the full *ab initio* level of theory.

In this chapter we present the theory, implementation, and application of a simple, electrostatics-based approach for a specific class of multi-scale problems involving molecules at metallic interfaces of arbitrary shape. These systems are particularly relevant to the simulation of molecular nano-scale devices [469, 336, 43]. Since molecular dimensions are in the range of 0.1–1 nm, thus at least two orders of magnitude smaller than typical nanoparticles, we can identify the molecule as the *system*, while the nanoparticle is considered the *environment*. By treating only the system at the atomistic level of theory, we can recover the most important physics at a significantly reduced computational cost. Our goal is to provide a framework for describing interactions of molecules with complex nano-scale environments. This framework will be useful for studying interface phenomena that determine the properties and function of nano-scale devices, both in the absence and in the presence of an external bias. Our particular interest is in modeling surface-enhanced spectroscopies

[269, 29, 294], especially surface-enhanced Raman scattering (SERS) [269, 294, 498, 88]. The last decade has seen surface-enhanced analytical methods become very useful tools for molecular detection as well as important probes into surface properties of metallic nanoparticles. Furthermore, the study of molecular properties under an external bias provided within the proposed framework is naturally connected to electron transport in nanostructures [409, 259, 420]. Understanding of electron transport on the nano-scale is a crucial prerequisite for molecular electronics. Other applications where molecules interact non-trivially with a metallic surface also include surface-enhanced fluorescence [283] and single-molecule DNA sequencing [536].

The idea of partitioning a large system into subsystems to aid computation or understanding stretches back to the early works of Löwdin [317] and McWeeny [342], where they introduced a rigorous mathematical framework for separating (localized) degrees of freedom in large-scale electronic structure calculations. Recently, there has been considerable interest in a practical, simplified version of these ideas known as the fragment molecular orbital (FMO) method [263, 184, 390, 159] which starts with the assumption that there are localized groups of electrons which interact with the other groups (to first order) only classically. A cluster expansion is used to correct for the many-body interaction energies after the fragment wavefunctions have converged. However, all fragments are treated at the same level of theory, so the method does not reflect the multi-scale nature of many interesting problems.

In contrast, the most common methods to treat very large chemical systems over the past two decades have focused on models where there is a natural division into typically two components, a system and an environment, treated at *different* levels of approximation. These models have a strong physical motivation and are often more heuristic in nature. Typically, these models aim to describe the effects of a complex environment on a localized chemical process; for example, solvation effects on molecular properties, or the mechanisms of enzyme activity. In practice, there are essentially two schools of thought: the continuum models and the discrete models. The former are exemplified by the polarizable continuum model (PCM) [532, 531] and conductor-like screening model (COSMO) [265, 264]. In these models, solvation is described by a single bulk component, characterized by a dielectric or screened conductor, rather than explicit solvent molecules. The discrete approach maintains an explicit treatment of the environment, but simplifies the calculation by avoiding the full treatment of all electronic degrees of freedom. The combined quantum-mechanical and molecular mechanics (QM/MM) models exemplify this approach [565, 148, 476]. A fundamental issue with all of these methods, including the FMO, is how to treat the junctions between the components, especially when they cleave chemical bonds. Attempts have been made to put this on a more mathematical footing, but the pragmatic, more *ad hoc*

approaches, remain most popular.

Interactions between molecules and metallic surfaces include both an electromagnetic (EM) component [468, 360, 499] and contributions from chemical bonding [398, 616, 358, 456]. The traditional approach to these systems has employed classical electrodynamics, in particular finite-difference time-domain (FDTD) methods [598, 514], which can treat the strong, inhomogeneous electric fields present in nanostructures. The plasmonic properties of the metallic material are represented by its dielectric function. The metal–molecule interaction then amounts to the polarization of the molecule in the near-field of the nanostructure, while the back-polarization of the metal is neglected. Recent developments aim to integrate molecular electronic structure with an atomistic model of the plasmonic material [334, 335, 339, 340, 97]. On the other end of the method spectrum, continuum solvation models have found application to molecular electronic structure on metallic surfaces [116, 117]. Here, the metal–molecule interaction is derived from the mutual polarization of the neutral metallic surface and the electron density of the molecule.

As we show in detail below, the model proposed in this chapter encompasses both the strong-field and the zero-field, solvation-like regime as limiting cases and effectively interpolates between them. It is based on an electrostatic model, in which the metallic surface acts as a boundary condition for the electrostatic interactions within the molecule. As a consequence, we have to restrict our focus to situations where there is a clear system component that has minimal overlap with the environment, and for which there is a natural specification of the electrostatic potential at the system–environment interface. We argue that this is approximately the case in many nano-electronic devices. Recently, our group published a parallel paper [392] where we used the same model, implemented inside the `octopus` [93] code, to study the stabilization of the benzene anion between two charged plates. Our intentions in this paper are therefore threefold: first, to describe the theoretical background of the model in more detail; second, to explore a systematic set of test applications; and third, to meet the technical challenge of implementing the framework as a simple library that can be used in conjunction with conventional electronic structure codes, which expand the wavefunction or electron density in a Gaussian-type basis set. Gaussians give an extremely compact representation of the all-electron density, while allowing for the efficient analytical evaluation of two-electron Coulomb integrals. In contrast, `octopus` is a time-dependent density-functional theory (DFT) code which represents the electron density on a real-space grid. It computes the Hartree potential using a finite-difference Poisson solver, but this approach is rather computationally expensive for all-electron calculations. We therefore propose an algorithm for Hartree-Fock or DFT calculations which computes only a *correction* to the Fock or Kohn-Sham matrices, resulting from the interaction with the environment. The matrix elements for an isolated system are built using a standard

Gaussian-based code in the usual way, and our library adds on contributions describing the environmental effects.

The paper is therefore organized as follows: in Sec. 5.2, we characterize our physical model in detail, and provide a detailed derivation of the working equations for a DFT implementation, including a discussion of how we obtain the interaction potential and the associated matrix elements in an efficient manner. In Sec. 5.3, we apply the method to study environment effects on the electronic structure of molecules both between grounded metal plates and under external bias. The effects of the external field and of the mutual polarization are explored for a neutral quadrupolar molecule (benzene), a neutral dipolar molecule (glycine zwitterion), and a charged molecule (benzene anion). Finally, we end with our conclusions and outlook for future work in Sec. 5.4.

5.2 Theory and implementation

5.2.1 Background

To establish notation and to summarize connections to previous work, we begin by describing the electronic structure problem for systems in external electric fields, as well as in cavities within dielectric or metallic materials. Let us first consider the simple case of a molecular system subject to a time-independent external electric field,

$$\mathbf{E} = -\nabla\Phi(\mathbf{r}) \quad (5.1)$$

where $\Phi(\mathbf{r})$ is the electric scalar potential. In the special case of uniform fields,

$$\Phi(\mathbf{r}) = -\mathbf{E} \cdot \mathbf{r} \quad (5.2)$$

where the potential origin is chosen to coincide with the coordinate origin. Thus the non-relativistic molecular electronic Hamiltonian for a system in a time-independent uniform electric field with Cartesian components F_α can be written as

$$\hat{H}_e = \hat{H}_e^{(0)} - \sum_\alpha \hat{\mu}_\alpha F_\alpha \quad (5.3)$$

where $\hat{H}_e^{(0)}$ is the unperturbed electronic Hamiltonian. The dipole moment operator, $\hat{\mu}$, is defined in the usual way,

$$\hat{\mu}_\alpha \equiv - \sum_i^N r_{i\alpha} \quad (5.4)$$

where the sum is over the N electrons. More generally, for non-uniform fields, the perturbed Hamiltonian takes the form,

$$\hat{H}_e = \hat{H}_e^{(0)} - \sum_i^N \Phi(\mathbf{r}_i) + C \quad (5.5)$$

where C is an arbitrary constant depending on the choice of origin of the potential field, $\Phi(\mathbf{r})$. Of course, a change in C does nothing more than shift the zero of energy, and has no effect on the electronic structure.

Many established quantum chemistry codes allow the treatment of Hamiltonians of one, or both, of these forms. Such functionality is relevant if one wants to find the electronic structure of a system embedded in an electrostatic environment, where the scalar potential, $\Phi(\mathbf{r})$, is explicitly known or easily computable. This is the case in the QM/MM and FDTD approaches, for example. On the other hand, an explicit model of the environment, even within an electrostatic approximation, may not always be available, or even desirable if the precise details of the surroundings are unimportant. This is the case for continuum solvation models such as PCM or COSMO, where the solute system is treated as a finite cavity (containing a molecule) within a bulk dielectric medium. In the PCM approach, the perturbing potential is defined implicitly in terms of the electrostatic boundary condition at the cavity–solvent interface, rather than by explicitly defined bulk ‘solvent’ charges.

More concretely, in the *apparent surface charge* (ASC) formulation of the PCM [532, 531] a charge distribution, $\sigma(\mathbf{s})$, is identified at the dielectric interface, \mathbf{s} , which is produced by a discontinuity of the electric field across the boundary,

$$\frac{\partial\Phi_{\text{in}}}{\partial\mathbf{n}} = \epsilon \frac{\partial\Phi_{\text{out}}}{\partial\mathbf{n}} \quad (5.6)$$

Here, ϵ is the dielectric constant of the solvent (the cavity is modelled *in vacuo*) and \mathbf{n} denotes the outward unit normal from the cavity. According to elementary electrostatics for homogeneous linear dielectric media, $\sigma(\mathbf{s})$ is given by

$$\sigma(\mathbf{s}) = \frac{\epsilon - 1}{4\pi\epsilon} \left[\frac{\partial\Phi_{\text{sys}}}{\partial\mathbf{n}} + \frac{\partial\Phi_{\sigma}}{\partial\mathbf{n}} \right] \quad (5.7)$$

where the total potential inside the cavity has been decomposed into two components: $\Phi_{\sigma}(\mathbf{r})$ is the potential due to the surface charge,

$$\Phi_{\sigma}(\mathbf{r}) = \int \frac{\sigma(\mathbf{s})}{|\mathbf{r} - \mathbf{s}|} d\mathbf{s} \quad (5.8)$$

and $\Phi_{\text{sys}}(\mathbf{r})$ is the solute potential,

$$\Phi_{\text{sys}}(\mathbf{r}) = \int \frac{\rho_{\text{sys}}(\mathbf{r}')}{|\mathbf{r} - \mathbf{r}'|} d\mathbf{r}' \quad (5.9)$$

where $\rho_{\text{sys}}(\mathbf{r})$ is the total (electronic and nuclear) charge density of the molecular system,

$$\rho_{\text{sys}}(\mathbf{r}) = \rho_{\text{sys}}^{\text{nuc}}(\mathbf{r}) - \rho_{\text{sys}}^{\text{elec}}(\mathbf{r}) \quad (5.10)$$

and we have introduced a minus sign for the electron charge. Self-consistent solution of Eqs. 5.7–5.8 with respect to $\sigma(\mathbf{s})$ and $\Phi_{\sigma}(\mathbf{r})$ for a given $\Phi_{\text{sys}}(\mathbf{r})$ is the central task in the ASC method. In turn, $\Phi_{\text{sys}}(\mathbf{r})$ may be obtained self-consistently with $\Phi_{\sigma}(\mathbf{r})$ from a quantum mechanical solution of the perturbed Hamiltonian,

$$\hat{H}_e = \hat{H}_e^{(0)} - \sum_i^N \Phi_{\sigma}(\mathbf{r}_i) \quad (5.11)$$

In this way, the PCM approach models the electrostatic effect of the environment in a simple way without recourse to detailed atomistic knowledge of the solvent composition.

The technical challenge in the PCM/ASC approach stems from the fact that neither $\sigma(\mathbf{s})$ nor $\Phi_{\sigma}(\mathbf{s})$ are known *a priori*, and are only implicitly defined by the condition of self-consistency in Eqs. 5.7–5.8. The boundary conditions are considerably simplified, however, when the solvent is modelled as a conductor (i.e. in the limit $\epsilon \rightarrow \infty$). In this case, the total potential at the solute/solvent interface must be a constant; indeed it must be zero if the solvent extends to infinity. Then $\Phi_{\sigma}(\mathbf{r})$ is explicitly defined as a solution of Laplace’s equation inside the cavity under Dirichlet boundary conditions,

$$\begin{aligned} \nabla^2 \Phi_{\sigma}(\mathbf{r}) &= 0 \quad \forall \mathbf{r} \in \text{cavity} \\ \Phi_{\sigma}(\mathbf{s}) &= -\Phi_{\text{sys}}(\mathbf{s}) \end{aligned} \quad (5.12)$$

Unlike in the PCM/ASC algorithm, $\Phi_{\sigma}(\mathbf{r})$ can now be computed directly without any knowledge of $\sigma(\mathbf{s})$. Moreover, a good approximation to the true potential produced by (large) finite ϵ can also be obtained by rescaling $\Phi_{\sigma}(\mathbf{r})$ by a simple constant, $(\epsilon - 1)/\epsilon$. This simplification forms the basis of a well-known approximation to the PCM, known as COSMO [265]. PCM models have been previously applied to study electronic structure of molecules at metallic surfaces [116, 117]. In the following, we draw on all of these ideas to develop our model.

5.2.2 The CheESE Model

In this chapter, we appeal to the above system–environment models with a different application focus in mind: namely, the simulation of molecules in electrostatic nano-environments where there is a natural and simple specification of the boundary conditions. We refer to our model as CheESE (chemistry in electrostatic environments). An implementation of the CheESE scheme in a real-space density functional code `octopus` was presented

in a parallel paper [392]. The new code presented here is implemented as a stand-alone library that can be easily interfaced to quantum chemistry packages employing Gaussian-type basis sets (see more details below). As in the PCM, we partition our problem into two components, analogous to solute and solvent, which we call *system* and *environment*, respectively. We then propose an effective electronic Hamiltonian for the system which includes an additional one-electron operator to describe the electrostatic effects of the environment. Thus our model has 3 key assumptions:

1. We assume that system and environment degrees of freedom are uncoupled beyond the classical electrostatic interaction.
2. The system charge density is completely enclosed in the system volume, Ω_{sys} ; more precisely, there is an exponentially small overlap with the environment charge density.
3. The physics of the application provides a natural specification of the total electrostatic potential, $\Phi_{\text{fixed}}(\mathbf{s})$, on the system/environment interface, \mathbf{s} , which is known *a priori*.

Our model therefore differs from the solvation models discussed above in some important ways, even though they share the common physics of including only electrostatic effects of the environment. Specifically, we make no explicit appeal to the physical form of the environment, such as the assumption of a linear dielectric or conductor etc. Instead, we simply model the environment as a sea of charges that can be rearranged without any self-energy penalty such as to satisfy the boundary condition, $\Phi_{\text{fixed}}(\mathbf{s})$, which is known from the outset.

More formally, we can write down an effective Hamiltonian for the system, \hat{H}^{eff} , as a sum of two operators: the non-relativistic Hamiltonian of the isolated system, $\hat{H}^{(0)}$, and an environment potential, $\Phi_{\text{env}}(\mathbf{r})$,

$$\hat{H}^{\text{eff}} = \hat{H}^{(0)} - \sum_i^N \Phi_{\text{env}}(\mathbf{r}_i) + \sum_k^M Z_k \Phi_{\text{env}}(\mathbf{R}_k) \quad (5.13)$$

Here, $\{\mathbf{r}_i\}$ and $\{\mathbf{R}_k\}$ are the coordinates of the system's N electrons and M nuclei (with charges Z_k), respectively. Formally, we have

$$\Phi_{\text{env}}(\mathbf{r}) = \int \frac{\rho_{\text{env}}(\mathbf{r}')}{|\mathbf{r} - \mathbf{r}'|} d\mathbf{r}' \quad (5.14)$$

in terms of the unknown environment charge density, $\rho_{\text{env}}(\mathbf{r})$, but according to assumptions 2 and 3 of the CheESE model it follows that the potential, $\Phi_{\text{env}}(\mathbf{r})$, *inside* the system volume is also a solution of Laplace's equation,

$$\nabla^2 \Phi_{\text{env}}(\mathbf{r}) = 0 \quad \forall \mathbf{r} \in \Omega_{\text{sys}} \quad (5.15)$$

under the Dirichlet boundary condition,

$$\Phi_{\text{env}}(\mathbf{s}) = \Phi_{\text{fixed}}(\mathbf{s}) - \Phi_{\text{sys}}(\mathbf{s}) \quad (5.16)$$

Note that $\Phi_{\text{sys}}(\mathbf{r})$ is the total potential due to the system's electrons *and* nuclei, as in Eqs. 5.9–5.10. For a given $\Phi_{\text{sys}}(\mathbf{r})$ and specified $\Phi_{\text{fixed}}(\mathbf{r})$, this boundary condition is known, and hence $\Phi_{\text{env}}(\mathbf{r})$ can be determined directly and uniquely without any explicit knowledge of $\rho_{\text{env}}(\mathbf{r})$. Our model implies that changes in $\rho_{\text{sys}}(\mathbf{r})$ will induce changes in $\rho_{\text{env}}(\mathbf{r})$ in order to maintain the constraint in Eq. 5.16, but physically we are not concerned with how this is achieved in detail.

Therefore, within the usual Born-Oppenheimer approximation, we define our model in terms of the ground state solution to the time-independent electronic Schrödinger equation,

$$\hat{H}_e^{\text{eff}} \Psi(\{\mathbf{r}_i\}; \{\mathbf{R}_k\}) = E(\{\mathbf{R}_k\}) \Psi(\{\mathbf{r}_i\}; \{\mathbf{R}_k\}) \quad (5.17)$$

where \hat{H}_e^{eff} is given by

$$\begin{aligned} \hat{H}_e^{\text{eff}} &= \sum_i^N -\frac{1}{2} \nabla_i^2 + \sum_{i>j}^N \frac{1}{|\mathbf{r}_i - \mathbf{r}_j|} \\ &- \sum_i^N v_{\text{nuc}}(\mathbf{r}_i) - \sum_i^N \Phi_{\text{env}}(\mathbf{r}_i) \end{aligned} \quad (5.18)$$

Here, we have used atomic units and $v_{\text{nuc}}(\mathbf{r})$ is the external potential due to the system's nuclei, defined in the usual way. We stress here that $\Phi_{\text{env}}(\mathbf{r})$ is itself an implicit function of the charge density of the system (which is an issue we shall return to). Throughout the results section, the energies we quote will be approximations to the total system energy defined by

$$E_{\text{tot}}^{\text{sys}} = \langle \Psi | \hat{H}_e^{\text{eff}} | \Psi \rangle + \int \rho_{\text{sys}}^{\text{nuc}}(\mathbf{r}) \Phi_{\text{env}}(\mathbf{r}) d\mathbf{r} + U_{\text{NN}} \quad (5.19)$$

where we have included the interaction of the nuclear charge density, $\rho_{\text{sys}}^{\text{nuc}}(\mathbf{r})$, with the environment, in addition to the usual nuclear self-repulsion energy of an isolated system,

$$U_{\text{NN}} = \sum_{k>k'}^M \frac{Z_k Z_{k'}}{|\mathbf{R}_k - \mathbf{R}_{k'}|} \quad (5.20)$$

Ultimately, one may ask what is physically being lost when we employ this model compared to a full *ab initio* calculation of the supersystem. The assumption that the system and environment have negligible overlap, however, makes the electrostatic approximation less dramatic than otherwise. For example, at the mean-field Hartree-Fock level of theory,

there are no exchange interactions between non-overlapping subsystems, and the classical Coulomb interaction between subsystems suffices. In the case of generalized-gradient approximation density-functional theory, there are neither exchange nor correlation contributions between the system and environment, if non-overlapping. However, higher-order correlations obtained in wavefunction methods beyond Hartree-Fock exchange, such as dispersion, could be significant and our model of course neglects these. Nevertheless, such contributions can be expected to be much smaller than the dominant electrostatic interactions.

We mention one final issue in passing; namely, that we are neglecting any energy changes associated with the rearrangement of charge in the environment. In our parallel paper [392], where we also explore the stability of the benzene anion between two metallic plates, we estimate the energy required to charge the plates with induced charge. However, this energy is computed after the system’s electron density has converged and does not influence the solution of the system Hamiltonian. A consideration of such effects could be included in further studies.

5.2.3 Interpreting the environment potential

We have found it useful when interpreting our results to conceptually partition the environment potential into two components,

$$\Phi_{\text{env}}(\mathbf{r}) = \Phi_{\text{image}}(\mathbf{r}) + \Phi_{\text{static}}(\mathbf{r}) \quad (5.21)$$

where the linearity of the Laplace equation allows us to define each component individually,

$$\nabla^2 \Phi_{\text{image}}(\mathbf{r}) = 0 \quad ; \quad \Phi_{\text{image}}(\mathbf{s}) = -\Phi_{\text{sys}}(\mathbf{s}) \quad (5.22)$$

$$\nabla^2 \Phi_{\text{static}}(\mathbf{r}) = 0 \quad ; \quad \Phi_{\text{static}}(\mathbf{s}) = \Phi_{\text{fixed}}(\mathbf{s}) \quad (5.23)$$

In this way, we can identify a component, $\Phi_{\text{static}}(\mathbf{r})$, which is *static* in the sense that it represents an external potential that is completely independent of the molecule and exists solely to satisfy the fixed boundary condition, $\Phi_{\text{fixed}}(\mathbf{r})$. The remaining component, $\Phi_{\text{image}}(\mathbf{r})$, is seen to act like the potential of the induced charge (or *image* charge) on a grounded conductor. That is, it reflects the potential of the molecule, and adjusts such that the total potential, $\Phi_{\text{sys}}(\mathbf{s}) + \Phi_{\text{image}}(\mathbf{s})$, vanishes on the boundary. In fact, $\Phi_{\text{image}}(\mathbf{r})$ is precisely the potential one would obtain in the COSMO solvation model summarized above, neglecting the final scaling by $(\epsilon - 1)/\epsilon$ and assuming the same cavity geometry.

Below, we shall report our test applications with this decomposition in mind. In particular, we define the energy,

$$E_{\text{static}} = E_{\text{tot}}^{\text{sys}}[\Phi_{\text{image}} \equiv 0] - E_{\text{tot}}^{\text{sys}}[\Phi_{\text{env}} \equiv 0] \quad (5.24)$$

as the SCF energy difference between the isolated system and the SCF energy when applying a static field with no image charge effects included (i.e. a regular finite-field calculation). In turn, we also define,

$$E_{\text{image}} = E_{\text{tot}}^{\text{sys}} - E_{\text{tot}}^{\text{sys}}[\Phi_{\text{image}} \equiv 0] \quad (5.25)$$

as the SCF energy difference between a full CheESE calculation and a simple static field calculation. Note that E_{image} is not the same as $\int \rho_{\text{sys}}(\mathbf{r})\Phi_{\text{image}}(\mathbf{r})d\mathbf{r}$, as extracted from a full CheESE calculation, since the image charges will perturb the system's electronic charge density away from the static field solution.

5.2.4 Solving the non-linear Schrödinger equation

Having defined our model in terms of an effective Hamiltonian, we now discuss how to solve the associated Schrödinger equation (Eq. 5.17). In contrast to the usual case for an isolated system, the equation is now formally non-linear because the environment potential, $\Phi_{\text{env}}(\mathbf{r})$, is a function of $\rho_{\text{sys}}(\mathbf{r})$ due to the constraint in Eq. 5.16. An intuitive way to proceed, however, is to make a comparison with the well-known Hartree-Fock (HF) or Kohn-Sham (KS) density-functional theory (DFT) approximations. For isolated systems, both of these approaches construct an approximate solution to the many-body problem with the explicit solution of only one-electron equations. One price to be paid for this great simplification is the sacrifice of linearity for non-linearity. That is, the HF or KS equations are non-linear and the iterative procedure usually employed to solve them self-consistently is very familiar.

In exactly the same way, we can consider a self-consistent procedure for the solution of the Schrödinger equation with the CheESE Hamiltonian. That is, we start by making an initial guess for the ground state density, $\rho_{\text{sys}}^{(0)}(\mathbf{r})$, and solve the Laplace equation 5.15–5.16 for $\Phi_{\text{env}}^{(0)}(\mathbf{r})$, where $\Phi_{\text{sys}}^{(0)}(\mathbf{s})$ on the boundary is computed from $\rho_{\text{sys}}^{(0)}(\mathbf{r})$. We may then construct the CheESE many-body Hamiltonian, \hat{H}_e^{eff} , from $\Phi_{\text{env}}^{(0)}(\mathbf{r})$ in a manner completely analogous to the construction of the Fock or Kohn-Sham matrix at each iterative cycle. Next, we can solve the Schrödinger equation with any approximate method we choose to obtain an improved ground state density and potential. The cycle is repeated with a new $\rho_{\text{sys}}^{(k)}(\mathbf{r})$, $\Phi_{\text{sys}}^{(k)}(\mathbf{r})$ and $\Phi_{\text{env}}^{(k)}(\mathbf{r})$ at the k -th iteration, and continued until self-consistency.

Although the above algorithm is general for any electronic structure method, we only use KS-DFT for our calculations here. Thus at the k -th iteration, we have a density, $\rho_{\text{sys}}^{(k)}(\mathbf{r})$, a potential, $\Phi_{\text{env}}^{(k)}(\mathbf{r})$, and the KS equations take the form

$$\hat{f}\phi_i(\mathbf{r}) = \epsilon_i\phi_i(\mathbf{r}) \quad (5.26)$$

where the modified KS operator is simply

$$\hat{f}(\mathbf{r}) = \hat{f}^{(0)}(\mathbf{r}) - \Phi_{\text{env}}^{(k)}(\mathbf{r}) \quad (5.27)$$

and $\hat{f}^{(0)}(\mathbf{r})$ is the conventional operator for the isolated system. (Note that we have dropped any k -iteration suffices on the \hat{f} operators.) On solving the KS equations, the total energy of the system is given by

$$E_{\text{tot},(k+1)}^{\text{sys}} = E_{0,(k+1)}^{\text{DFT}} + \int \rho_{\text{sys}}^{(k+1)}(\mathbf{r}) \Phi_{\text{env}}^{(k)}(\mathbf{r}) d\mathbf{r} + U_{\text{NN}} \quad (5.28)$$

where $E_{0,(k+1)}^{\text{DFT}}$ is the usual DFT energy functional for the isolated system. When changes in $E_{\text{tot}}^{\text{sys}}$ between two successive k -iterations are less than a specified threshold, we may assume the supersystem is converged, otherwise another iteration should be performed.

So far, we have assumed that the many-body problem is solved completely at each k -iteration (within an approximate method) for a given $\Phi_{\text{env}}^{(k)}(\mathbf{r})$. In KS-DFT, however, the KS equations themselves are solved iteratively in a self-consistent field (SCF) approach, implying that the above algorithm has two, nested, iterative cycles, differentiated by the point at which $\Phi_{\text{env}}(\mathbf{r})$ is updated. This raises the possibility of updating $\Phi_{\text{env}}(\mathbf{r})$ at *each KS iteration*, instead of after the KS solution has converged, thus effectively merging the two iterative cycles. Aside for issues of numerical stability, at convergence of $\Phi_{\text{env}}(\mathbf{r})$ and $\rho_{\text{sys}}(\mathbf{r})$ the final result should be the same. In fact, in our CheESE implementation, we do update $\Phi_{\text{env}}(\mathbf{r})$ at each KS iteration within the DIIS-accelerated [427] KS-SCF. It is not actually obvious whether it is more efficient to (perhaps partially) converge $\rho_{\text{sys}}(\mathbf{r})$ within the KS cycle before updating $\Phi_{\text{env}}(\mathbf{r})$, or to update both $\rho_{\text{sys}}(\mathbf{r})$ and $\Phi_{\text{env}}(\mathbf{r})$ at each KS iteration. The answer probably depends on the relative cost of updating the CheESE potential compared to a regular KS iteration, as well as how the numerical stability affects the number of iterations. Here, we have chosen to update both at each KS iteration and have observed good convergence, but the efficiency question is left open for a future study.

On a technical point, we mention that the CheESE non-linearity implies that the expectation value of the effective Hamiltonian, \hat{H}_e^{eff} , is not minimized in general by the (normalized) ground-state wavefunction (eigenfunction of \hat{H}_e^{eff}), except in the special case that $\Phi_{\text{env}}(\mathbf{r})$ is independent of $\rho_{\text{sys}}(\mathbf{r})$. In turn, this implies that care needs to be taken when deriving the Hartree-Fock or KS equations, which are based on a variational condition. In fact, we side-step the issue here, when we define $\Phi_{\text{env}}^{(k)}(\mathbf{r})$ to be independent of $\rho(\mathbf{r})$ at each k -iteration, and hence obtain the modified KS operator in Eq. 5.27 quite trivially. However, it turns out that we can write down an alternative variational functional, which *is* minimized by the ground-state density, and also yields the same KS equations when taking the functional derivative. More details are given in Appendix A.

5.2.5 Obtaining the environment potential

We now discuss our implementation for computing the environment potential $\Phi_{\text{env}}(\mathbf{r})$ and the matrix elements of the modified Kohn-Sham operator Eq. 5.27 in a Gaussian basis set. First, we emphasize that we have chosen to compute the effect of the environment as a correction term to the isolated system Hamiltonian. However, we could alternatively define a KS operator,

$$\hat{f}(\mathbf{r}) = -\frac{1}{2}\nabla^2 + v_{\text{xc}}(\mathbf{r}) - \Phi_{\text{es}}(\mathbf{r}) \quad (5.29)$$

where $v_{\text{xc}}(\mathbf{r})$ is the DFT exchange-correlation potential and $\Phi_{\text{es}}(\mathbf{r})$ collects all the electrostatic effects,

$$\Phi_{\text{es}}(\mathbf{r}) = v_{\text{nuc}}(\mathbf{r}) - \int \frac{\rho_{\text{sys}}^{\text{elec}}(\mathbf{r}')}{|\mathbf{r} - \mathbf{r}'|} d\mathbf{r}' + \Phi_{\text{env}}(\mathbf{r}) \quad (5.30)$$

Formally, $\Phi_{\text{es}}(\mathbf{r})$ can be obtained in one shot from Poisson's equation,

$$\nabla^2 \Phi_{\text{es}}(\mathbf{r}) = -4\pi\rho_{\text{sys}}(\mathbf{r}) \quad \forall \mathbf{r} \in \Omega_s \quad (5.31)$$

subject to the specified boundary condition

$$\Phi_{\text{es}}(\mathbf{s}) = \Phi_{\text{fixed}}(\mathbf{s}) \quad (5.32)$$

This is the formalism used in the `octopus` implementation, as described in our parallel paper [392]. However, the full potential, $\Phi_{\text{es}}(\mathbf{r})$, has many undesirable properties from an algorithmic perspective. In particular, even if we subtract out $v_{\text{nuc}}(\mathbf{r})$, the potential is still highly ‘spiked’ near the nuclei and is therefore very difficult to represent accurately and efficiently using a grid-based numerical solver. Instead, we exploit the properties of Gaussian basis functions to compute matrix elements over these ‘spiked’ operators analytically, and thus only deal with the correction term, $\Phi_{\text{env}}(\mathbf{r})$, by numerical solution. Compared to the other potentials, $\Phi_{\text{env}}(\mathbf{r})$ must be smooth by virtue of being a solution to Laplace's equation, which makes this approach much more attractive computationally.

More specifically, we base our Laplace solver for Eqs. 5.15–5.16 on a uniform finite-element discretization, following our previous work in Ref. [568]. The starting point is to expand the potential as

$$\Phi_{\text{env}}(\mathbf{r}) = \sum_i c_i \xi_i(\mathbf{r}) \quad (5.33)$$

where $\xi_i(\mathbf{r})$ is a three-dimensional tensor product of n -th order one-dimensional piecewise Lagrange interpolating polynomials assigned to the i th grid point. In the N th finite element

(FE), the function assigned to the i th point is given by

$$\xi_{klm}(\mathbf{r}) = \begin{cases} L_k(x - X_N) \cdot L_l(y - Y_N) \cdot L_m(z - Z_N) \\ 0 \sim (\text{the } i\text{th grid point}) \notin (\text{the } N\text{th FE}) \end{cases}$$

where we define

$$L_k(x) = \prod_{j=0, j \neq k}^n \frac{x - j\lambda}{(k - j)\lambda} \quad ; \quad \begin{array}{l} (0 \leq k \leq n) \\ (0 \leq x \leq n \cdot \lambda) \end{array} \quad (5.34)$$

and (k, l, m) is the local index of the i th grid point in the N th finite element; (X_N, Y_N, Z_N) is the origin of the N th finite element; and $n \cdot \lambda$ is the width of the finite elements. In all of our calculations, we use 3rd order polynomials. It is easy to see that the value of the potential at the i th grid point is given by c_i . Substituting the expansion (5.33) into the Laplace equation and enforcing the appropriate boundary condition leads to a set of linear equations of the form

$$\mathbf{A} \cdot \mathbf{c} = \mathbf{b} \quad (5.35)$$

where

$$A_{ij} = \int \nabla \xi_i(\mathbf{r}) \nabla \xi_j(\mathbf{r}) d\mathbf{r} \quad (5.36)$$

and the vector \mathbf{b} describes the boundary condition. It is important to realize that the matrix A_{ij} is extremely sparse and composed of relatively small, identical, overlapping sub-blocks with $O(n^6)$ elements, where n is the order of the polynomials. (Note that we have enforced continuity of the potential across element boundaries.) Exploiting this property, the full set of coefficients may be efficiently determined with an amount of work that scales linearly with the physical size of the solution domain for a given grid spacing. Here, we solve Eq. 5.35 iteratively using the conjugate gradient method.

To impose the boundary conditions in practice, we require an efficient method for evaluating $\Phi_{\text{sys}}(\mathbf{s})$ due to the system's electrons and nuclei. We achieve this using a multipole approximation previously given in detail in Ref. [568], which exploits the low scaling properties of the fast multipole method. Having obtained an explicit representation of the potential, the final task is to compute the matrix elements over Gaussian basis functions, and to update the free-space Kohn-Sham matrix. Fortunately, we can again exploit the properties of Gaussian functions and the polynomial form of the finite elements to do this in an analytical and simple way. Specifically, we use a modified form of the McMurchie-Davidson [341, 568] algorithm, which we have implemented for finite elements of arbitrary order.

Our code is designed as a stand-alone library, and in particular, the interface is extremely simple. The only information it requires is a description of the Gaussian basis set $\{\alpha\}$, nuclear charges and positions, the current atomic orbital density matrix, $D_{\alpha\beta}^i$, the fixed potential $\Phi_{\text{fixed}}(\mathbf{s})$, and of course the geometry of the solution domain, Ω_{sys} . In return, the library will update the Kohn-Sham matrix elements, $F_{\alpha\beta}^i$, at each SCF cycle. Interfacing with an existing electronic structure code is therefore quite straightforward and requires only three calls to the CheESE library: (a) an initialization call, `CheESE_init`; (b) a call to update the Kohn-Sham matrix, `CheESE_update`; (c) a final call to free the memory, `CheESE_free`. We summarize the structure of the code in Algorithm 1. For our prototype implementation we have used the DALTON 2.0 package [121]. Additional integration into other chemistry codes is encouraged and we expect to release the library on our group’s website soon with a permissive LGPL license ¹.

Algorithm 1 Structure of CheESE implementation.

- 1: Call `CheESE_init`($\{Z_k, \mathbf{R}_k\}, \Omega_{\text{sys}}, \{\alpha\}, \Phi_{\text{fixed}}(\mathbf{s})$)
 - 2: Initialize $D_{\alpha\beta}^0$
 - 3: **for** KS iterations, i **do**
 - 4: Build free-space $F_{\alpha\beta}^i$
 - 5: $F_{\alpha\beta}^i = F_{\alpha\beta}^i + \text{CheESE_update}(D_{\alpha\beta}^i)$
 - 6: Diagonalize $F_{\alpha\beta}^i$, update $D_{\alpha\beta}^{i+1}$
 - 7: Test convergence; exit if converged
 - 8: **end for**
 - 9: Call `CheESE_final`()
-

5.3 Benchmarks and applications

5.3.1 Computational details

Our prototype code is restricted to the simple case of a cuboid-shaped system volume, Ω_{sys} , with an arbitrary boundary potential, $\Phi_{\text{fixed}}(\mathbf{s})$. However, we have decided to choose a specific application focus: namely the simulation of a nano-electronic device where we can imagine a molecule placed between two parallel electrodes or plates, held at fixed potentials, as shown in Fig. 5.1. This is similar to the studies we performed in our previous paper [392]. Our intention is that the open-source library can be extended to other relevant geometries as required.

We describe in the next subsection the precise geometries and potential functions we chose for $\Phi_{\text{fixed}}(\mathbf{s})$. In the finite-element Laplace solver, we used a value of 1.0 bohr for

¹<http://www.gnu.org/copyleft/lesser.html>

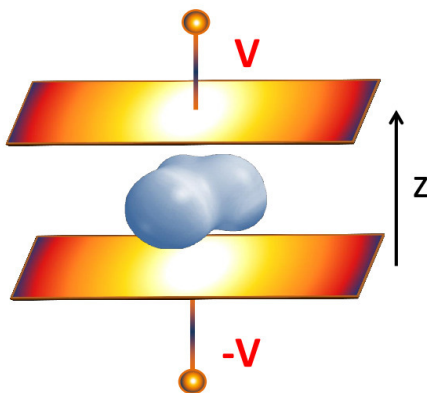


Figure 5.1: Geometry of the CheESE model showing the direction of the applied potential, $\pm V$. We use a cuboid box, with the xy -planes representing the electrodes of a nano-device. The coordinate origin is equidistant from the two plates.

the spacing, λ , in Eq. 5.34 for all the calculations in Sec. 5.3.3, and 2.0 bohr for all the other calculations with non-zero $\Phi_{\text{fixed}}(\mathbf{s})$. We found that these values were sufficient to converge the results to the precision presented in all the figures. Note that the choice of λ reflects the smoothness of the potential, $\Phi_{\text{env}}(\mathbf{r})$. Here we are able to use a relatively large λ , which results in a modest computational cost in the Laplace solver, especially for the smaller system volumes. Some example timings are given below.

All the calculations have been achieved by combining our library with the DALTON 2.0 quantum chemistry suite [121]. As explained above, it is relatively simple to interface our code with any program using Gaussian-type basis sets. We have restricted our focus to DFT calculations using the popular B3LYP exchange-correlation functional [51]. In addition, to avoid a detailed study of basis set effects, we elected to use the standard aug-cc-pVDZ basis for all calculations. This should be a reasonable choice for the level of accuracy we are expecting in this chapter, with the diffuse functions providing some flexibility for any spatial redistribution of the electron cloud under potential bias.

We have chosen to study the CheESE effect on three molecules with a similar size and number of electrons, but different symmetries: namely, (1) benzene (neutral, quadrupolar ground state), (2) benzene anion (charged, monopolar ground state), (3) glycine zwitterion (neutral, dipolar ground state). The benzene and benzene anion geometries were optimized at the B3LYP/aug-cc-pVDZ level using DALTON. In all calculations, the benzene rings were placed in the xy -plane, with the centre of mass at the coordinate origin. The glycine geometry was taken from reference [252]. The molecule was placed such that the amine group was at a positive z -coordinate, and rotated such that the electric dipole moment

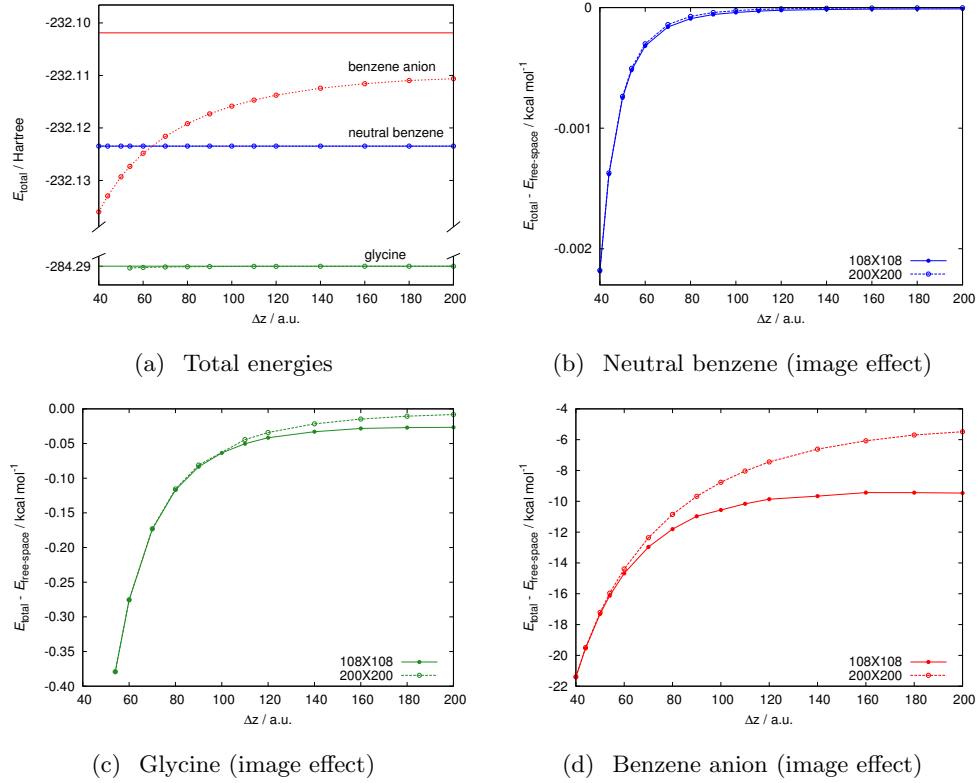


Figure 5.2: Stabilization of the benzene (blue lines), benzene anion (red lines), and glycine (green lines) molecules due to CheESE image charges in the case $\Phi_{\text{fixed}}(\mathbf{s}) = 0$ with varying Δz . Part (a) compares the total energies, $E_{\text{tot}}^{\text{sys}}$, shown as dotted lines, with the reference free-space energies, shown as solid lines, for an xy -plate area of 200×200 bohr². Parts (b)–(d) highlight the CheESE effect as the difference, $\int \rho_{\text{sys}}(\mathbf{r})\Phi_{\text{image}}(\mathbf{r})d\mathbf{r}$, between $E_{\text{tot}}^{\text{sys}}$ and the free-space energy for (b) benzene, (c) glycine, and (d) benzene anion, with two choices of plate area.

(with no external field) was parallel to the z -axis. The centre of mass was also placed at the origin.

5.3.2 Specification of the boundary conditions

As stated above, our intention is to model a molecule in a cuboid cavity representing a nano-device, with a potential bias applied across two surfaces. For our test calculations, we have therefore chosen a very simple form for the fixed boundary potential, defined as

$$\Phi_{\text{fixed}}(z_{\text{max}}) = V \quad (5.37)$$

$$\Phi_{\text{fixed}}(z_{\text{min}}) = -V \quad (5.38)$$

$$\Phi_{\text{fixed}}(\mathbf{s}) = \frac{z}{z_{\text{max}}} V \quad (5.39)$$

on the six sides of the cavity, which linearly interpolates the potential, V , from the top plate to the bottom plate. In all cases, the box is positioned in space such that the plates sit in the xy -plane and are equidistant from the coordinate origin and the centre of the cavity is at the coordinate origin; see Figure 5.1. (i.e. $z_{\max} = |z_{\min}|$.) In the following, we shall refer to Δz as the plate separation,

$$\Delta z \equiv z_{\max} - z_{\min} \quad (5.40)$$

In most of the calculations, we chose plate dimensions of 108×108 bohr², but in some cases given below, a larger area of 200×200 bohr² was studied. As for the plate separation, we studied values of Δz ranging from 40 bohr to 200 bohr.

For all the calculations, we applied boundary potentials of no more than 1 a.u. in magnitude, which corresponds to approximately 27.2 V. Thus for a plate separation of 54 bohr (which is typical in our calculations), this amounts to an electric field of approximately 2 \AA^{-1} when the plates are held at ± 1 a.u. This magnitude is similar to the field strengths previously studied by Choi *et al.* in their work on molecular orbital tuning [102, 260], but is larger than the field strengths we explored in our previous paper [392].

We note that this choice of fixed potential makes the calculation of $\Phi_{\text{static}}(\mathbf{r})$ rather trivial. Of course, this is the potential associated with a uniform electric field parallel to the z -axis, of magnitude V/z_{\max} . Indeed, $\Phi_{\text{static}}(\mathbf{r})$ can be accurately captured with only a single finite element in this case. Moreover, DALTON 2.0 already has the capability to compute Kohn-Sham matrix elements under such a uniform field. Therefore, the most interesting part of the calculation is the contribution of $\Phi_{\text{image}}(\mathbf{r})$ and this is the area we will focus on. Nevertheless, our code can already handle more complicated $\Phi_{\text{static}}(\mathbf{r})$, so future applications will be aimed towards exploring this functionality in addition to the image-charge effects.

Finally, we emphasize that the CheESE model requires negligible overlap of electron density between the system and environment. This was enforced in practice by simply choosing a geometry which ensured that no basis function tail had a significant value ($> 10^{-10}$) in the boundary region. This is a conservative constraint; a consideration of the density itself would be favourable in future work if a boundary closer to the molecular system was desired.

5.3.3 Energy calculations with $\Phi_{\text{fixed}}(\mathbf{s}) = 0$

For our test applications, we first explore the case where $\Phi_{\text{fixed}}(\mathbf{s}) = 0$; that is, $\Phi_{\text{static}}(\mathbf{s}) = 0$ so the Hamiltonian is only modified by the image charge effects contained in $\Phi_{\text{image}}(\mathbf{r})$. The image charge potential is given by Eq. 5.22 and hence depends explicitly on the total potential of the system at the boundary, $\Phi_{\text{sys}}(\mathbf{s})$. We can therefore expect

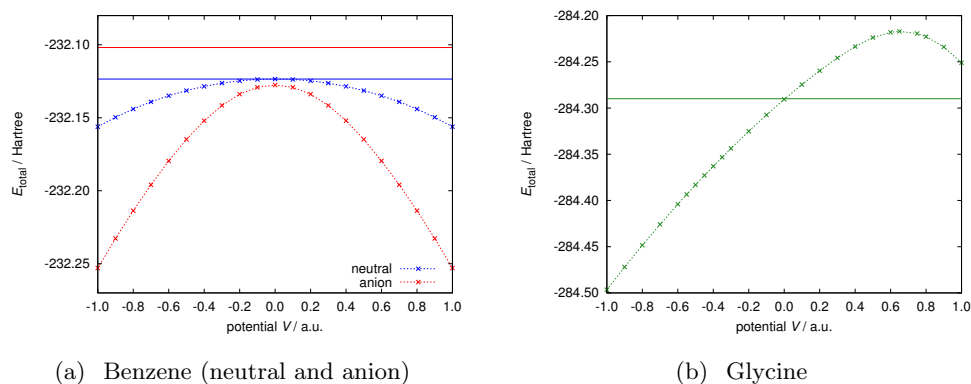


Figure 5.3: Energies of neutral benzene (blue lines), benzene anion (red lines), and glycine (green lines), with an applied potential, V , as given in Eq. 5.39, an xy -plate area of 108×108 bohr², and $\Delta z = 54$ bohr. The total CheESE energies, $E_{\text{tot}}^{\text{SYS}}$, are shown as dashed lines, and the reference free-space energies are shown as solid lines.

quite different effects for our three molecules, reflecting the decay properties of $\Phi_{\text{sys}}(\mathbf{r})$ at long range. In Fig. 5.2, we show how the total energy, $E_{\text{tot}}^{\text{SYS}}$ in Eq. 5.28, of the three test molecules changes as a function of the plate separation, Δz , compared to the free-space energies. In Fig. 5.2(a), we compare the total energies for all three molecules with a plate area of 200×200 bohr² and varying Δz , while in Figs. 5.2(b)–(d), we highlight the stabilization energy due to the image effects for each molecule individually, also including results for a smaller plate size of 108×108 bohr².

In these calculations, the stabilization energy reduces to $\Delta E = \int \rho_{\text{sys}}(\mathbf{r})\Phi_{\text{image}}(\mathbf{r})d\mathbf{r}$ since there is no static field, and $\Phi_{\text{image}}(\mathbf{r})$ is given by Eq. 5.22, so it will be larger if $\Phi_{\text{sys}}(\mathbf{s})$ is larger. Indeed, if $\Phi_{\text{sys}}(\mathbf{s})$ is a constant, this will be the uniform value of $\Phi_{\text{image}}(\mathbf{r})$ inside the cavity. However, note that even if $\Phi_{\text{image}}(\mathbf{r})$ is large, ΔE will vanish for charge-neutral molecules if $\Phi_{\text{image}}(\mathbf{r})$ is uniform because the electronic and nuclear contributions will exactly cancel. Therefore, especially for the charge-neutral systems, the size of ΔE depends not only on the magnitude of $\Phi_{\text{sys}}(\mathbf{s})$ but also on its inhomogeneity. The latter is a function of both the cavity geometry and the symmetry of the system’s charge distribution.

Looking at Fig. 5.2, the first point to note is that all the systems are stabilized by the boundary effect. We can attempt to interpret these results by appealing to an image charge picture, and this is readily done for the benzene anion. In this case, the system generates a negative potential on the boundary. Hence, the boundary condition Eq. 5.22 implies that the anion must induce a distribution of *positive* image charge in the environment such that the total potential vanishes on the cavity surface. Naturally, this positive charge stabilizes the negative charge of the anion. However, there is a sensitive cancellation of electronic

and nuclear contributions. For example, with $\Delta z = 54$ bohr and the smaller (108×108) plates, the nuclear contribution, $\int \rho_{\text{sys}}^{\text{nuc}}(\mathbf{r})\Phi_{\text{image}}(\mathbf{r})d\mathbf{r}$, is positive (679 kcal/mol), and is only just outweighed by its electronic counterpart, $\int \rho_{\text{sys}}^{\text{elec}}(\mathbf{r})\Phi_{\text{image}}(\mathbf{r})d\mathbf{r}$, which is negative (-695 kcal/mol), leading to a net stabilization.

The stabilization energies of the glycine and neutral benzene systems are much smaller, however. Specifically, while the anion is stabilized by as much as 21 kcal/mol, depending on Δz , the stabilization energy for the glycine zwitterion is about 50 times smaller, and for neutral benzene it's about four orders of magnitude smaller. This is not very surprising. To a good approximation, the cavity boundary sees the anion as a monopole, the glycine as a dipole, and the neutral benzene as a quadrupole source at the origin. The image charges in the environment therefore reflect these symmetries. As a result, ΔE is dominated by charge-charge interactions in the anion case, but only dipole-dipole interactions in the glycine case, for example. Since the latter decay more quickly with distance, it is not surprising that the stabilization energy is much smaller. More specifically, in the neutral benzene case, again for $\Delta z = 54$ bohr and the smaller (108×108) plate size, the nuclear contribution to ΔE is only 1.6368 kcal/mol and the electronic component is -1.6373 kcal/mol. Overall, there is a net stabilization energy, but it is much smaller than for the anion. As a result, for plate separations less than about 65 bohr, we find that the anion is actually *more* stable than neutral benzene, which is stabilized much less by the image effect. (In free-space, we find that the anion is about 14 kcal/mol less stable than the anion. The experimental result is about 26 kcal/mol [67, 444]. Other examples of image stabilization from electrons interacting with their environments have been studied experimentally by the group of Harris; see, for example, Ref. [348] and references therein.) In the glycine case, under the same conditions, the nuclear contribution is -2.5 kcal/mol, and the electronic contribution is 2.1 kcal/mol, giving a net stabilization which is much larger than in neutral benzene, even though the individual terms have the same order of magnitude. In fact, the balance of nuclear and electronic terms is subtle; for example, in glycine and neutral benzene, the nuclear term changes sign for some plate separations.

To further understand the relative values of ΔE , we can also examine the size of $\Phi_{\text{sys}}(\mathbf{s})$, which directly reflects the magnitude of the resulting $\Phi_{\text{env}}(\mathbf{r})$. For example, in the case $\Delta z = 60$ bohr and the smaller plate size, we observe $\Phi_{\text{sys}}(\mathbf{s}) / \text{a.u.}$ at the far corner of the system volume, (54.0, 54.0, 30.0), to be 3.1×10^{-6} , 2.3×10^{-4} , and -1.2×10^{-2} for the neutral benzene, glycine, and anion, respectively. Consistent with the size of ΔE , we see that the anion potential is about four orders of magnitude larger than the neutral benzene potential.

It is also interesting to consider the decay behaviour of ΔE with plate separation, Δz . It is generally true that as the cavity, Ω_{sys} , gets larger, $\Phi_{\text{sys}}(\mathbf{s})$ gets smaller, and the image

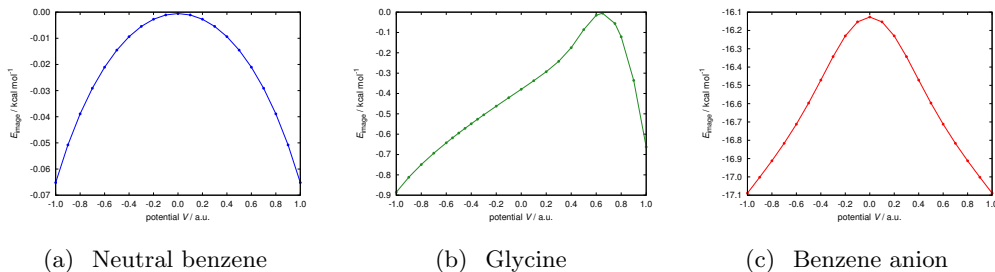


Figure 5.4: Energy changes for different applied potentials when including image charge effects in addition to a static field. E_{image} , as given by Eq. 5.25, is shown for (a) neutral benzene, (b) glycine, and (c) benzene anion, using an xy -plate area of 108×108 bohr², and $\Delta z = 54$ bohr.

charge effect is reduced. In the limit of an infinitely large cavity, ΔE is of course zero and the CheESE energy converges to the free-space energy. This effect is very clear for all the molecules in the figure, but we can also see that ΔE decays relatively more slowly for the anion than glycine, and neutral benzene shows the most rapid decay as Δz increases. Again, this is due to the different multipole characteristics of the molecules and the decay rate of $\Phi_{\text{sys}}(\mathbf{s})$ with Δz . We have also shown the difference when using smaller or larger xy -plates, which is particularly significant for the anion. In this case, to a good approximation, $\Phi_{\text{sys}}(\mathbf{s})$ is spherically symmetric about the origin. Hence, when using the smaller (108×108) plates, the ‘edge effect’ due to the finite plate areas, and the the potential on the sides of the box (i.e. xz and yz planes) becomes the limiting boundary condition as Δz exceeds about 100 bohr. This difference is less pronounced in the glycine and neutral benzene cases due to the different charge distributions. With glycine, for example, the dipole is aligned along the z -axis, and we find that $\Phi_{\text{sys}}(\mathbf{s})$ on the xy -plates is approximately two orders of magnitude larger than on the xz and yz planes at equal distance; hence changes in stabilization as Δz varies are less affected by changes in the plate size.

5.3.4 Energy calculations with $\Phi_{\text{fixed}}(\mathbf{s}) \neq 0$

Here we explore the situation with non-zero static field, $\Phi_{\text{static}}(\mathbf{r})$, in addition to the image charge effects. In particular, $\Phi_{\text{fixed}}(\mathbf{s})$ is given by Eq. 5.39, which describes a uniform external field applied along the z -axis. As before, we study the same three test molecules, and examine the change in $E_{\text{tot}}^{\text{sys}}$ as a function of the applied bias V . The results are presented in Figs. 5.3 and 5.4, where we have chosen to use the smaller 108×108 bohr² xy -plates and a z -spacing of 54 bohr throughout. This implies an external field strength of approximately 2 V \AA^{-1} when $V = \pm 1.0$ a.u. The behaviour of molecules under static

V	C_6H_6		glycine		C_6H_6^-	
	E_{static}	E_{image}	E_{static}	E_{image}	E_{static}	E_{image}
-1.0	-20.44	-0.065	-128.74	-0.89	-77.72	-17.09
-0.5	-4.94	-0.015	-57.87	-0.59	-22.89	-16.60
-0.1	-0.20	-0.001	-10.54	-0.42	-0.95	-16.15
0.1	-0.20	-0.001	9.97	-0.34	-0.95	-16.15
0.5	-4.94	-0.015	41.61	-0.09	-22.89	-16.60
1.0	-20.44	-0.065	25.08	-0.66	-77.72	-17.09

Table 5.1: Energy differences in kcal/mol, according to Eqs. 5.24–5.25, giving the change, E_{static} , to the total energy on applying a static field with potential $V/\text{a.u.}$, and the additional cheese image charge contribution, E_{image} .

external fields has been thoroughly studied in the literature, so the main purpose of this discussion is to examine the significance of the image charge effects. However, we will briefly summarize the main points of Fig. 5.3 first, which reports the total CheESE energy, $E_{\text{tot}}^{\text{sys}}$, with varying V , and mostly reflects the static field effect.

Due to the choice of the applied potential, $\Phi_{\text{fixed}}(\mathbf{s})$, and choice of geometries, the neutral and anionic benzene results are symmetric with respect to sign changes in V , and in both cases the molecules are stabilized, with negative energy contributions from both the static field interaction and the image charge effects discussed in Sec. 5.3.3. As the field increases, the static field induces a larger electronic dipole and the stabilization increases, while the image charge contribution is only moderately increased. In contrast, the glycine molecule is not symmetric along the z -axis and we observe different energies for positive and negative V . In fact, for positive V , the static field has an unfavourable direction with respect to the molecule’s net dipole moment and the system is destabilized by the static field, even though the image charge contribution actually remains negative. (Recall that the amine group is nearest the positive- z plate.) However, as the field gets stronger, the electron density is sufficiently distorted towards the upper plate that the dipole changes sign (at approximately $V = 0.65$ a.u.) and we observe a turning point in the total energy curve.

The static field effects are therefore clearly important, but here we are most interested in the image charge contributions. Therefore, in Table 5.1 and Fig. 5.4, we highlight the individual contributions of the static and image charge potentials, E_{static} and E_{image} , as defined in Eqs. 5.24–5.25. Looking at these results, it is clear that for neutral benzene and glycine the static field effect is much more significant than the image charge stabilization. Even for the smaller static field strengths ($\sim 0.2 \text{ V\AA}^{-1}$), E_{static} is greater than E_{image} by at least an order of magnitude in glycine, and two orders of magnitude in neutral benzene. For the benzene anion, however, the situation is different. In fact, for a field strength

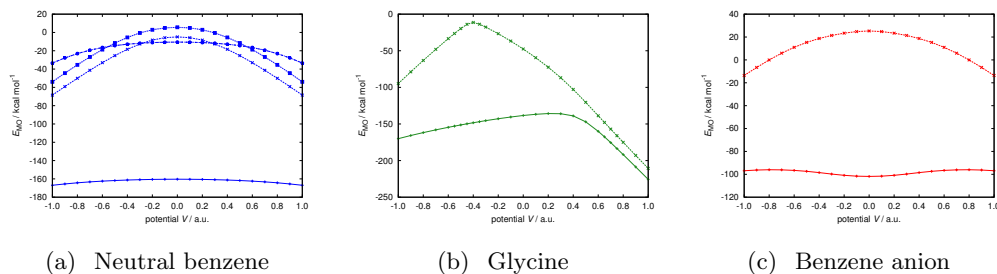


Figure 5.5: Energy profiles of the lowest lying molecular orbitals of (a) neutral benzene, (b) glycine, and (c) benzene anion, with an applied potential, V , an xy -plate area of 108×108 bohr², and $\Delta z = 54$ bohr. Since there are no relevant orbital crossings, only the HOMO and LUMO are shown for the anion and glycine.

of $1 \text{ V}\text{\AA}^{-1}$, the image and static contributions are comparable. Moreover, in the weaker field, $\sim 0.2 \text{ V}\text{\AA}^{-1}$, the image charge stabilization is approximately 16 kcal/mol, while the stabilization due to the static field is less than 1 kcal/mol: an order of magnitude smaller!

In addition to comparing the relative sizes of E_{static} and E_{image} , it is also interesting to observe how E_{image} depends on the applied potential, V . Looking at Fig. 5.4, we can see the expected symmetrical results for the benzene systems. Moreover, as V increases, E_{image} increases in magnitude. At zero V , the results are the same as shown in Fig. 5.2. As the bias is applied, the electron cloud is distorted and the image charge distribution changes from its approximate spherical symmetry. In fact, the change in the image charges is such as to reinforce the bias, V , which is already stabilizing the system. In the anion, however, the change in E_{image} due to increased bias is less than 1% across the range of V we study. In glycine, we see a non-symmetric change with V . Moreover, while E_{static} is positive for $V > 0$, E_{image} is negative for all V , although in all cases it is quite small: less than 1 kcal/mol in magnitude. Note that the turning point in E_{image} occurs at the same bias potential as the turning point in E_{static} , when the molecular dipole goes to zero. From our discussion in Sec. 5.3.3, this is perhaps not surprising. We know that the image charge potential depends on $\Phi_{\text{sys}}(\mathbf{s})$, and as the dipole tends to zero, we can expect this boundary potential to decrease as it depends on more rapidly-decaying higher-order moments. Indeed, this is what we observe in the calculations.

5.3.5 Molecular orbital tuning

So far, we have looked at total molecular energies. However, as already mentioned, it is possible to shift the total energy without making any interesting changes to the electronic structure of the system. Indeed, the addition of a constant potential to the Kohn-Sham operator will shift all the orbital energies by that same constant, but leave the molecular

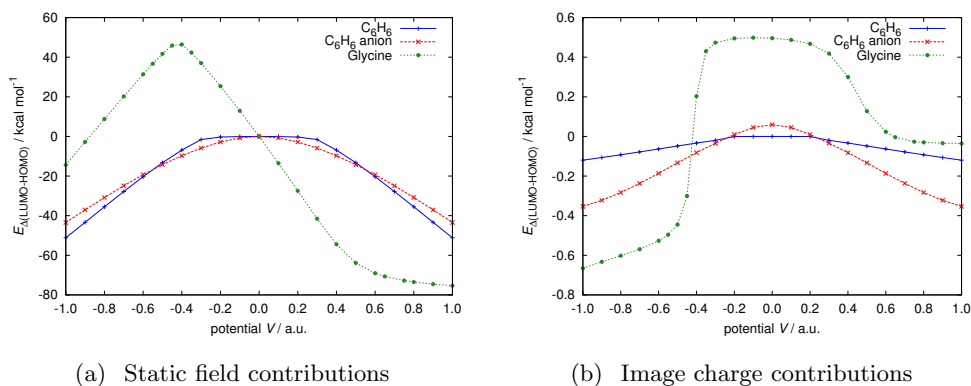


Figure 5.6: Static field and image charge contributions (see main text for definitions) to the HOMO–LUMO gap for neutral benzene (blue line), glycine (green line), and benzene anion (red line) with varying applied potential, V , an xy -plate area of 108×108 bohr², and $\Delta z = 54$ bohr.

orbitals themselves unchanged. In other words, it is important to observe if the orbital energies change in different ways. For example, the HOMO (highest occupied molecular orbital) and LUMO (lowest unoccupied MO) orbital energies are significant in nano-electronic or electron transport studies. [409, 259, 420, 260] Above all, the HOMO–LUMO gap is an important property, and if the orbital energies are simply shifted by a constant, then the gap will obviously not change.

In Figs. 5.5–5.6, we therefore plot how the HOMO, LUMO and HOMO–LUMO gap change when we apply the CheESE model. Fig. 5.5 gives the energy profiles of the HOMO and LUMO with varying V for the three molecules, including all the image effects. Since the LUMO changes character as the orbitals cross in the neutral benzene case, we have shown the three lowest lying orbitals. This explains the kinks in the neutral benzene curves in Fig. 5.6. More precisely, Fig. 5.6(a) plots the difference between the HOMO–LUMO gap in an isolated system and when applying only a static field. Fig. 5.6(b) plots the difference between the HOMO–LUMO gap computed by a full CheESE calculation (with bias potential V) and a calculation with only the static field.

The main message in Fig. 5.5 is that the orbital energies change significantly with applied field, thereby allowing the possibility of orbital ‘tuning’. Moreover, due to greater changes in the LUMO compared to the HOMO, we see changes to the HOMO–LUMO gap of as much as 75 kcal/mol (e.g. glycine at large positive V) compared to free-space. Indeed, the glycine HOMO–LUMO gap reduces dramatically when the field is large and directed against the (free-space) dipole moment. The figure does not make clear the static and image charge contributions, but the details are somewhat complex. For example, in the benzene anion, the static field stabilizes the LUMO, but actually destabilizes the HOMO,

while the (large, but fairly constant) image charge effect stabilizes both orbitals. In glycine, the static field stabilizes both HOMO and LUMO for all V , while the (small, but variable) image charge effect can either stabilize or destabilize the orbitals, depending on V .

On the other hand, we are often most interested in the gap, rather than the precise orbital energies. Fig. 5.6 distinguishes the image charge and static contributions in this case. As expected, we see that the static field effect is generally more important than the image effect. In some cases, the energy change is two orders of magnitude more than that due to the image effect. Nevertheless, the image effect is not completely negligible, and modifies the gap by almost 1 kcal/mol in the glycine case when $V = -1.0$ a.u. Moreover, with zero static field, only the image charges produce a change, and in the glycine case the gap is increased by approximately 0.5 kcal/mol when $V = 0$. Interestingly, when considering the gap, the image charge effects are most significant for glycine, not the benzene anion. Even though the anion orbitals are shifted more by the image potential, the effect is quite similar on both the HOMO and LUMO, so the gap changes little compared to glycine for most values of V . It is also interesting that the benzene curves have very similar shapes in both figures, regardless of the anion charge. In contrast, the glycine curve has a much more complex structure, reflecting the subtle changes in the electronic structure as both the static field and image charge potential change.

5.4 Conclusion

We have presented a new model and computer implementation for the treatment of molecular systems in arbitrary electrostatic environments. Our work is inspired by the continuum solvent models, but has a very different application focus in mind; for example, the simulation of molecules in nano-electronic devices. More precisely, our approach defines a system–environment model in which the effect of the environment is completely determined by the specification of a fixed electrostatic potential on the boundary interface, which is known *a priori*. In this way, the environment field must be solved self-consistently with the molecular system.

We have systematically explored the behaviour of our model in a number of controlled tests, making a detailed comparison with the simpler picture of a static external field, which is not solved self-consistently. The difference, which we term ‘the image charge effect’, is found to strongly depend on the multipole character of the system’s total charge distribution. Thus, it is quite small in the charge-neutral, quadrupolar, benzene system, but somewhat larger in the dipolar (zwitterionic) glycine case. Similarly, it is quite significant in the charged benzene anion, where it modifies the total molecular energy by between 1 and 20 kcal/mol, which is comparable in size to the changes induced by a static field of

strength 1 V\AA^{-1} . As a result, we found that the benzene anion can actually be stabilized relative to neutral benzene when confined inside a grounded cavity.

In addition to total energies, we also explored the effect on orbital energy levels and the HOMO–LUMO gap, which reflects more subtle changes to the molecular orbitals than a constant energy shift. In this case, the image charge effect was similar in magnitude for all the molecules, modifying the gap by approximately 0.1–0.5 kcal/mol, even at zero applied field. Nevertheless, this change is somewhat overwhelmed by the effect of a non-zero static bias. For example, a field strength of about 1 V\AA^{-1} adjusts the gap by two orders of magnitude more than the image charge effect.

We conclude that image charge effects are often subtle, but in special cases (such as charged systems) or in very accurate work, a careful inclusion of their contributions can be important. Since electron transport properties are known to be rather sensitive to changes in molecular orbitals and their energy levels, it would be interesting to test the CheESE model in such cases as a future study.

5.5 Appendix: A variational scheme for electrostatic environment effects

In Sec. 5.2.4, we described an iterative scheme for obtaining the CheESE ground state from the time-independent Schrödinger equation, where $\Phi_{\text{env}}(\mathbf{r})$ is fixed at each iteration and then updated according to the new ground state. In the DFT case, the derivation of the KS equations for the calculation at each iteration is therefore analogous to the conventional one. In particular, the functional derivative of $E_{\text{tot}}^{\text{sys}}$ in Eq. 5.28 with respect to the system density recovers the KS operator in the usual variational way, since $\Phi_{\text{env}}(\mathbf{r})$ is density-independent at each iteration.

On the other hand, it is also possible to consider a non-iterative algorithm, in which $\Phi_{\text{env}}(\mathbf{r})$ is not held fixed, and therefore explicitly depends on $\rho_{\text{sys}}(\mathbf{r})$. In this case, we cannot obtain the ground state density by simply minimizing the energy in Eq. 5.28; for example, in the DFT case, the functional derivative with respect to the system density would now introduce a spurious factor of two in the KS operator (see below). Instead, following Sanhueza *et al.* [462], the ground state solution of the time-independent Schrödinger equation with a non-linear Hamiltonian, \hat{H}_e^{eff} , may be found by minimizing an alternative energy-like functional,

$$J = \langle \tilde{\Psi} | \hat{H}_e^{\text{eff}} + \hat{G} | \tilde{\Psi} \rangle \quad (5.41)$$

with respect to a complete set of trial wavefunctions, $\tilde{\Psi}$, where \hat{G} depends on the form of the non-linearity.

To obtain the form of \hat{G} in the case of the CheESE Hamiltonian, we may first recognize, using a Green's function formalism, that $\Phi_{\text{image}}(\mathbf{r})$ depends *linearly* on the system density,

$$\Phi_{\text{image}}(\mathbf{r}) = - \int \rho_{\text{sys}}(\mathbf{r}') F(\mathbf{r}, \mathbf{r}') d\mathbf{r}' \quad (5.42)$$

where $F(\mathbf{r}, \mathbf{r}')$ depends only on the geometry of the system boundary, Ω_{sys} ; the precise form of $F(\mathbf{r}, \mathbf{r}')$ does not concern us here. More specifically, we can decompose $\Phi_{\text{image}}(\mathbf{r})$ into electronic and nuclear contributions,

$$\Phi_{\text{image}}^{\text{elec}}(\mathbf{r}) = \int \rho_{\text{sys}}^{\text{elec}}(\mathbf{r}') F(\mathbf{r}, \mathbf{r}') d\mathbf{r}' \quad (5.43)$$

$$\Phi_{\text{image}}^{\text{nuc}}(\mathbf{r}) = - \int \rho_{\text{sys}}^{\text{nuc}}(\mathbf{r}') F(\mathbf{r}, \mathbf{r}') d\mathbf{r}' \quad (5.44)$$

According to Sanhueza *et al.* [462], non-linearities of this form are associated with an operator \hat{G} , given by

$$\hat{G} = \frac{1}{2} \sum_i^N \Phi_{\text{image}}^{\text{elec}}(\mathbf{r}_i) \quad (5.45)$$

Note that we are not concerned with minimizing over the nuclear degrees of freedom.

In the DFT case, the electronic energy is given by,

$$E_{\text{elec}}^{\text{sys}} = E_0^{\text{DFT}} - \int \rho_{\text{sys}}^{\text{elec}}(\mathbf{r}) \Phi_{\text{env}}(\mathbf{r}) d\mathbf{r}$$

but using the above approach, we can see, in comparison, that J is given by

$$J = E_0^{\text{DFT}} - \int \rho_{\text{sys}}^{\text{elec}}(\mathbf{r}) \left[\Phi_{\text{static}} + \Phi_{\text{image}}^{\text{nuc}} + \frac{1}{2} \Phi_{\text{image}}^{\text{elec}} \right] d\mathbf{r}$$

Now, the functional derivative of J with respect to $\rho_{\text{sys}}^{\text{elec}}(\mathbf{r})$, using Eq. 5.43, returns the expected KS operator given in Eq. 5.27. However, the minimum J does not equal the CheESE ground state electronic energy. Instead, if the density which minimizes J is denoted $\rho_{\text{sys}}^*(\mathbf{r})$, then $E_{\text{elec}}^{\text{sys}}[\rho_{\text{sys}}^*]$ is the correct ground state energy, in the sense of being an (approximate) eigenvalue of the electronic Schrödinger equation (Eq. 5.17). It should be stressed that this is the reason we quote all our results in terms of $E_{\text{tot}}^{\text{sys}}$, even though it is not a minimum (in general) for the ground state density!

Part II

The Harvard Clean Energy Project

Chapter 6

Large-scale computational screening and design of organic photovoltaic materials

6.1 Introduction

The sun is an abundant source of energy and its input on earth exceeds the global consumption by 4 orders of magnitude. It is hence an obvious alternative to fossil or nuclear energy supplies and will play an important role in safely and sustainably covering the rising demands of the future [584, 112, 627, 239]. The current cost of electricity from commercial silicon-based solar cells is unfortunately still around 10 times higher than that of utility-scale electrical power generation [302, 71]. These traditional inorganic photovoltaics come with further shortcomings, such as a complicated and energy-intensive manufacturing process which leads to high production costs. They can also contain rare or hazardous elements, and the devices tend to be heavy, bulky, rigid, and fragile.

Carbon-based solar cells have emerged as one of the interesting alternatives to this conventional technology [74, 75, 509]. Organic photovoltaics (OPVs) range from crystalline small molecule approaches [516, 46, 442] and certain dye-sensitized Grätzel cells [250] to amorphous polymers (plastics) [277, 401]. OPVs have great potential in two important areas: they promise simple, low-cost, and high-volume production [189] as well as the prospect of merging the unique flexibility and versatility of plastics with electronic features. OPVs can be processed via roll-to-roll printing [167, 278]; there is active research in sprayable and paintable materials [542, 190, 497, 395]; OPVs can be semi-transparent [36], variously colored [111], they are light-weight [277], and can essentially be molded into any shape [400]. These properties make OPVs a promising candidate to achieve the ubiquitous harvesting of solar energy [217, 152], with building-integrated [327, 224, 529] and ultra-portable applications [473, 72, 54] as primary targets. The Equinox Summit international committee, for example, recently suggested the use of OPVs for the basic electrification of 2.5 billion people in rural areas without access to the power grid [235].

There are, however, still significant issues to overcome in order to make plastic solar cells a viable technology for the future. The cardinal problems are their relatively low efficiency and limited lifetime [483, 419]: the power conversion record has only reached 9.2% [478] and current materials still degrade when exposed to the environment [447, 326, 57, 58]. An increase in efficiency to about 10-15% in combination with lifetimes of over 10 years (for production materials) could push the power generation costs of OPVs below that of other currently available energy sources [170, 479].

In 2008, we started the Harvard Clean Energy Project (CEP) [107] to help find such high-efficiency OPV materials. This chapter gives a general overview of CEP and provides the context for a series of detailed technical and result-oriented papers to follow. In Sec. 6.2 we introduce the motivation and overall setup of the project, followed by a presentation of its different components: Sec. 6.2.1 discusses our OPV candidates library, Sec. 6.2.2 the use of cheminformatics descriptors to rapidly assess the potential of these candidates, and Sec. 6.2.3 is focused on the high-level calculation hierarchy in CEP. Sec. 6.2.4 is concerned with the calibration of the obtained results. The CEP database is introduced in Sec. 6.2.5 and the World Community Grid (WCG) – our primary computational resource – in Sec. 6.2.6. Throughout Sec. 6.2 we also indicate the next stages and extensions to the current setup. We summarize our discussion in Sec. 6.3.

6.2 The Harvard Clean Energy Project

The key parameters for the improvement of OPVs are essentially known, however, engineering materials which combine all these features is a hard problem [78, 225, 98, 470, 68]. Traditional experimental development is largely based on empirical intuition or experience within a certain family of systems, and only a few examples can be studied per year due to long turnaround times of synthesis and characterization [63]. Theoretical work is usually also restricted to a small set of candidates for which different aspects of the photovoltaic process are modeled [372, 622, 560].

The Clean Energy Project stands out from other computational materials science approaches as it combines conventional modeling with strategies from modern drug discovery [256, 40, 338, 193, 28, 183, 141, 182]: CEP features an automated, high-throughput infrastructure for a systematic screening of millions of OPV candidates at a *first-principles* electronic structure level.¹ It also adopts techniques from cheminformatics [41, 173] and heavily

¹The authors are aware of and acknowledge related work by Geoffrey Hutchison (University of Pittsburgh), Michel Côté (University of Montreal), and Josef Michl (University of Colorado). Their respective research efforts each have a certain degree of overlap with CEP.

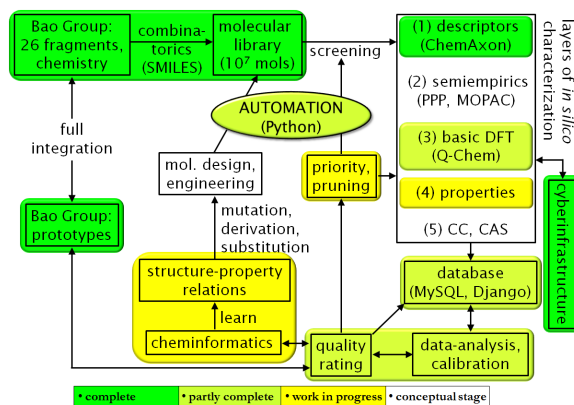


Figure 6.1: Structure and workflow of CEP.

relies on data mining [166, 195]. Pioneering work on cheminformatics-type approaches and massive electronic structure calculations was, e.g., performed by Rajan *et al.* [430, 507, 506] and Ceder *et al.* [242], respectively, in the context of inorganic solids. An *in silico* study combining the scale and level of theory found in CEP is, however, unprecedented.

As the starting point for CEP we have chosen to investigate the molecular motifs at the heart of OPV materials [78, 110]. A suitable motif is a *necessary* condition for a successful OPV development. Only a limited number of structural patterns have been explored so far, while the endless possibilities may well hold the key to overcoming the current material issues. We emphasize that a promising molecular structure is not a *sufficient* condition though, as condensed matter and device considerations have to be addressed as well. CEP is set up with a calculation hierarchy in which we will successively characterize relevant electronic structure aspects of our OPV candidates. Eventually, we will go beyond single molecule, gas-phase studies and consider intermolecular and bulk phase problems.

In addition to the search for specific structures with a desired set of properties, we also try to arrive at a systematic understanding of structure-property relationships [609, 307, 101, 312]. Learning about underlying design principles is the key to moving from a screening effort towards an active engineering of novel organic electronics [351, 45].

While its centerpiece is the *in silico* study of OPV candidates, we point out that an overarching theme of CEP is also the tight integration of experimental and theoretical work. The project is in part guided by inputs from experimentalist collaborators (in particular the Bao Group at Stanford University), and our most promising candidates are subject to in-depth studies in their laboratories [491]. CEP is designed as a community tool and we invite and welcome joint ventures.

Fig. 6.1 summarizes the overall structure and workflow of CEP, and in the following

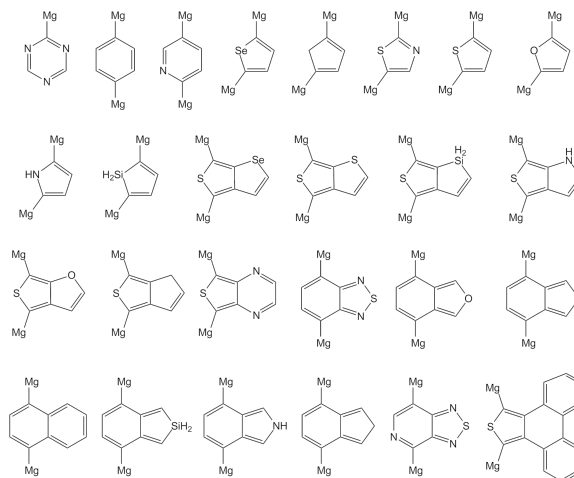


Figure 6.2: The 26 building blocks used for generating the CEP molecular library. The Mg atoms represent chemical handles, i.e., the reactive sites in the generation process. We introduce simple links between two moieties (by means of substituting two Mg for a single C-C-bond) as well as the fusion of two rings.

sections we discuss its various components.

6.2.1 Molecular candidate libraries

The molecular structure of essentially all organic electronic materials features a conjugated π -backbone [143]. Modern semiconducting compounds are often composed of linked or fused (hetero-)aromatic scaffolds [426].

We have developed a combinatorial molecule generator to build the primary CEP library. It contains $\sim 10,000,000$ molecular motifs of potential interest ($\sim 3,600,000$ distinct connectivities, each with a set of conformers) which cover small molecule OPVs and oligomer sequences for polymeric materials. They are based on 26 building blocks and bonding rules (see Fig. 6.2) which were chosen following advice from our experimental collaborators considering promise and feasibility. The fragments were linked and fused up to a length of 4-5 units according to the given rules. The generator is graph-based and employs a SMILES (simplified molecular input line entry specification) [574] string representation of the molecules as well as SMARTS (SMILES arbitrary target specification) in its engine. It is built around Marvin Reactor [95], and the Corina code [454] provides force-field optimized 3-dimensional structures. A detailed description of the library generator is in preparation.

The construction of the primary library was tailored towards OPV donor candidates, but the obtained structures are of interest for organic electronics in general [144, 343]. Our generator approach is flexible and can readily produce additional libraries (e.g., geared

towards acceptor materials or Grätzel cell dyes) by using a different set of fragments and connection rules. Substituents can be incorporated in a similar fashion. Combinatorial libraries allow for an exhaustive and systematic exploration of well defined chemical spaces, but the number of generated molecules grows exponentially. At a later stage we plan to use a genetic algorithm [406, 31, 178, 332, 288] as a complement to the current approach. The fitness function will be based on the information gathered from the screening of the primary library. Finally, CEP also provides the facility (e.g., to collaborators) to manually add structures to the screening pool.

6.2.2 Cheminformatics descriptors

While the main objective of CEP is the *first-principles* characterization of OPV candidates, we also explore the use of cheminformatics descriptors [530, 512] and ideas from machine learning [352, 595], pattern recognition [61, 160], and drug discovery [173, 338, 256] to rapidly gauge their quality. We have devised descriptor models for parameters such as the short-circuit current density (J_{sc}), the open-circuit voltage (V_{oc}), and the power conversion efficiency (PCE). Our models are the first step in a successive ladder of approximations for these key quantities associated with photovoltaic performance.

The basic strategy behind this approach is to identify and exploit correlations between certain physicochemical or topological descriptors and the properties of interest. Suitable descriptors are combined into models which are then empirically parametrized using a training set of experimentally well-characterized reference systems. As descriptors are easily computed, we can quickly (i.e., within a few days on a single workstation) obtain an initial assessment and preliminary ranking of the entire molecular library.

In Fig. 6.3 we present the linear regression model for V_{oc} along with the histogram of the calculated values for the molecular library. We note that our model for V_{oc} shows a very good correlation. This can be rationalized considering the principle dependence of V_{oc} on intramolecular properties which are apparently well reflected in the employed molecular descriptors. The J_{sc} model behaves similarly well although J_{sc} is also linked to bulk effects. For the fill factor – a quantity primarily determined by morphology and device characteristics – we could in contrast only obtain poor models.

The early stages of this work [391] utilized descriptors from the Marvin code by ChemAxon [95] and for the modeling we employed the R statistics package [429]. Recently, we started using the more comprehensive descriptor set from Dragon [515] and the specialized modeling code StarDrop [396]. A focus of our current work is to utilize the quantum chemical results discussed in the following section as a descriptor basis in our models.

As in biomedical applications of cheminformatics, we do not expect quantitative results,

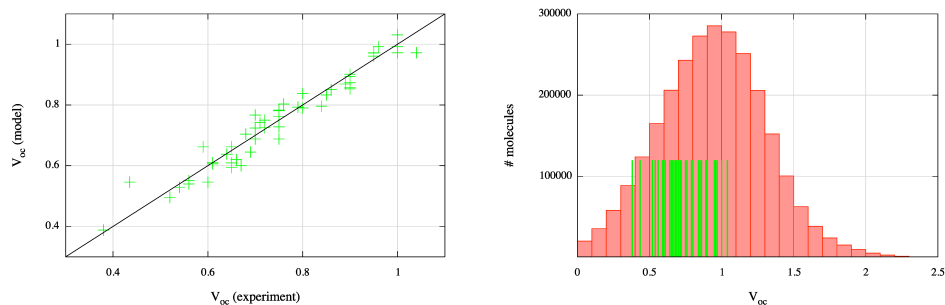


Figure 6.3: Left: Linear regression model for V_{oc} with the training set data. Right: Histogram of the projected V_{oc} values in the molecular library with the position of the training set marked in green (with arbitrary height). See Ref. [391] for details.

but this technique can yield valuable trends which we use to prioritize and prune the high-level screening and to uncover molecular motifs of particular interest. In Ref. [391] we give an introduction to this approach with a detailed discussion of the systematic construction and optimization of descriptor models.

6.2.3 First-principles screening hierarchy

Electronic structure theory offers a way to probe the properties of OPV materials and the photophysical processes in organic solar cells [25, 446]. The complexity of these problems, however, poses severe methodological challenges. Multi-scale simulations have improved considerably in recent years [372, 559], but in practice we still commonly choose to model, approximate, or deduce the different aspects of the problem separately. CEP adopts such a divide-and-conquer approach and combines it with a calculation hierarchy to screen for promising material candidates. This multi-level setup is designed to successively address the relevant issues in OPVs and provide results at an increasing level of theory. At each stage, the candidates are rated with respect to the investigated parameters. The scoring is freely customizable to reflect different research priorities. The most promising candidates and related structures from the library receive priority in the CEP hierarchy and their characterization is expedited. On the other hand, if a candidate is unfit with respect to a tested criterium and hence unlikely to be successful overall, it has lower priority and may be characterized in less detail.

The early CEP stages concentrate on various molecular properties of our material candidates and are hence most useful to assess macroscopic quantities which primarily depend on them, such as the V_{oc} . The later stages will shift the focus to intermolecular and condensed phase characteristics. The latter are central to, e.g., exciton and charge

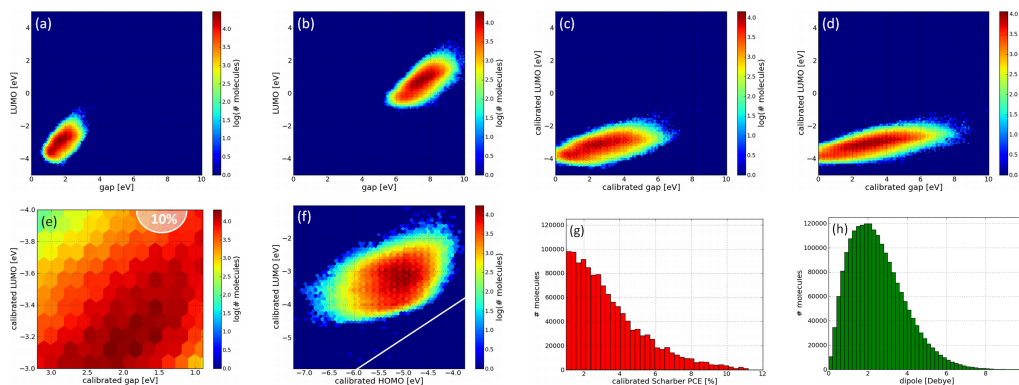


Figure 6.4: (a-e) Distribution of CEP hits in the gap-LUMO plane suggested by Scharber *et al.* [467]. Note that the density plots are on a logarithmic scale, and the red entries correspond to $\mathcal{O}(10,000)$ compounds and $\mathcal{O}(150,000)$ individual electronic structure calculations; (a) and (b) show the raw data from BP86/def2-SVP and BP86/def2-SVP//HF/def2-SVP (i.e., calculations which incorporate 0% vs. 100% exact exchange), respectively; (c) and (d) display the corresponding data after preliminary calibration; (e) shows the OPV relevant parameter space with the 10% PCE region (with respect to a PCBM acceptor). About 0.3% of the screened compounds fall in this high-efficiency region; (f) indicates the dynamic gap range, i.e., the range of available LUMO energies given a particular HOMO and vice versa; (g) displays the PCE histogram according to the Scharber model, and (h) the dipole moment histogram; (e-h) are all at BP86/def2-SVP//PBE0/def2-TZVP level of theory (calibrated).

transport processes [56, 191, 225, 589, 372, 622], for which molecular properties alone are clearly of limited value. Bulk structure considerations impact quantities like the external quantum efficiency and thus J_{sc} as well as the overall PCE. Since the cost and complexity of such studies increase significantly, they can only be performed for a subset of highest rated candidates.

In the first CEP phase, we perform a set of density functional theory (DFT) calculations [405, 271] employing the BP86 [50, 413], B3LYP [50, 296, 51], PBE0 [412, 414, 517, 416, 3], BH&HLYP [50, 296, 52], and M06-2X [618, 617] functionals as well as Hartree-Fock (HF) theory in combination with the single- ζ STO-6G [220, 219], double- ζ def2-SVP, and triple- ζ def2-TZVP [571] basis sets. We test and compare both restricted and spin-polarized settings. Our selection of functionals covers both generalized gradient approximation (GGA) and hybrid designs with a progression in the amount of exact exchange [51] (BP86 and HF can be seen as the limiting cases). The latter has a systematic influence on orbital localization and thus eigenvalues [610]. The GGA BP86 is a cost effective way to obtain good geometries, B3LYP is arguably the most widely used functional in molecular quantum mechanics, PBE0 has shown favorable performance in a variety of areas, as has the highly parameterized M06-

2X. (We will further test meta-GGAs like TPSS [517] and double-hybrids like B2PLYP [194] when they become available for CEP.) This range of model chemistries was chosen to put our analysis on a broader footing, but also to assess the performance of the different theoretical methods [271]. In total, each molecule is characterized by a BP86/def2-SVP geometry optimization and 14 single-point ground state calculations. We obtain geometries, total energies (including their decomposition into different contributions), molecular orbitals (MOs) and their energy eigenvalues, electron and spin densities, electrostatic potentials, multipole moments, Mulliken [366, 579] and natural populations [437, 439], as well as natural atomic, localized molecular, and bond orbital analysis [438, 153, 436] for the different model chemistries [151].

These basic electronic quantities can be used as a first approximation to the following points. The MO energies and their differences can be related to ionization potentials, electron affinities, gaps, and partial density of states (we note that the application of Koopmans' theorem is problematic in DFT) [505, 204, 103, 320, 610, 608, 34]. The electronic levels have to be tuned for an efficient light absorption, for the necessary interplay between donor, acceptor, and lead materials, as well as for atmospheric stability [78]. The delocalization of the frontier orbitals can be associated with (intramolecular) exciton and charge carrier mobility [484, 472, 243, 272, 422]. Their spatial overlap indicates the transition character and probability of the corresponding excitation [324, 407, 142]. Excess spin densities reflect the inadequacy of simple closed-shell solutions and can also point to a complex and potentially unstable electronic situation [200]. Charge maps can identify chemically unstable sites in these highly unsaturated molecules as well as patterns which may have an impact on their packing in the condensed phase. The molecular multipole moments can correspondingly be correlated to the organization in the bulk structure and also to transport properties [137, 581, 70, 599]. The wavefunction analysis techniques are of interest for the study of structure-property relations. The obtained data can furthermore be utilized as quantum chemical descriptors for the models described in Sec. 6.2.2. The results of a consecutive oligomer series can be used to extrapolate to the polymer limit [604, 174, 603, 287].

One example for how this basic information can be employed is the model developed by Scharber *et al.* in Ref. [467]. The authors assume (based on observations on actual OPV materials) that condensed matter aspects in such systems can be tuned to a certain viable level (i.e., a fill factor and external quantum efficiency of each 65% can be achieved). If that is the case, their PCE can be approximated using only gap and lowest unoccupied molecular orbital (LUMO) energy values. This model can readily be applied to the current CEP data as shown in Fig. 6.4. Our preliminary analysis reveals that only about 0.3% of the screened compounds (i.e., presently resulting in $\sim 3,000$ - $5,000$ distinct structures, depending on the model chemistry) have the necessary energetic levels to realize OPVs with 10% or

higher efficiency. This underscores the importance of carefully selecting the compounds to be synthesised and tested, and at the same time the value of the fast theoretical characterization and extensive search that CEP can provide towards this task. An unaided search has only a small chance of success, while CEP finds several thousand suitable structures. Fig. 6.4 also displays the dynamic gap range and dipole moment distribution of the screened candidates as examples for the wide range of electronic properties found in the CEP library. This versatility will be vital to a successful discovery of materials with specifically adjusted features (e.g., for different acceptors or tandem devices [17]).

We again emphasize that this first phase of CEP only addresses a subset of the important material issues [221] and has the inherent accuracy of the employed model chemistries and calibrations, if taken at face value. There are, however, four factors that add considerable value to these calculations: i) we correlate the computed results to actual experimental quantities to provide insights into their relationship; ii) we use the electronic structure data as a source for new cheminformatics descriptors, which will put our modeling efforts on a more physical foundation; iii) the analysis of the aggregated data from millions of molecules in combination with structural similarity measures can reveal guiding trends, even if the absolute result for an individual candidate might be inaccurate due to a particular limitation of its electronic structure; iv) by employing a variety of different model chemistries, we compensate for the chance of such a failure in any particular method. We do not rely on any single result but use a composite scoring with many contributions.

The calculations allow for the elimination of unfit candidates and provide a first set of predictions for promising structural trends. For these we can carry out the subsequent levels of increasingly more sophisticated calculations which are planned as following: we will calculate i) vibrational spectra and partition functions to gauge phonon-scattering and trapping in vibrational modes [534, 77]; ii) anionic/cationic states for improved electron affinity/ionization potential values; a Dyson orbital analysis [59] can improve our insights into the charge transfer processes [487]; iii) optimized geometries in the ionic states to deduce the reorganization during charge migration [77]; iv) triplet states and gaps to indicate potential for singlet fission processes [490]; v) linear response properties to assess the charge mobility [229, 481]; vi) excited states employing the maximum overlap method [175] and/or (range-separated) time-dependent DFT [240, 292] with an electron attachment/detachment density [215] and natural transition orbital analysis [329] for a more sound description of the absorption process. Each higher level result can be used to assess the interpretations at the lower levels. Further studies could involve the calculation of transfer integrals between oligomer pairs [77], packing and interactions in the bulk phase, as well as the use of high-level wavefunction theory for more reliable results in complicated bonding situations. We also want to consider the opposite approach, i.e., how well simple semiempirical and model

Hamiltonian calculations (which are popular in other communities) perform compared to *first-principles* DFT [25, 231]. Possible stages of the CEP hierarchy were recently vetted in a successful proof-of-principle study: we predicted exceptional charge mobility in a novel organic semiconductor and this prediction could be confirmed experimentally [491]. We also used quantum chemical calculations in an earlier study to explain the observed mobility values in another system [458].

6.2.4 Empirical result calibration

To bridge the gap between theory and experiment, we have introduced an empirical calibration of the computational results. Such a calibration is a pragmatic way to approximately account and correct for differences in experimental and theoretical property definitions, as well as *in vacuo* vs. bulk, and oligomer vs. polymer results.

We have established the organic electronics 2011 (OE11) training set of experimentally well-characterized organic electronic materials for the calibration and aligned the theoretical findings with the corresponding data from experiment. The current calibration is largely based on data from bulk-heterojunction setups with PCBM as acceptor and introduces a corresponding bias. A different focus can be chosen provided appropriate reference data. The use of training sets is a common technique in other areas of quantum chemistry [120, 618]. The details of this work will be presented elsewhere. A preliminary calibration of the current CEP results was used in the analysis shown in Fig. 6.4, and panels (a-d) in particular demonstrate the success of this approach.

6.2.5 Database and data mining

The results of all calculations are used to build up a reference database — the Clean Energy Project Database (CEPDB). This data collection is comparable to the more general but much smaller NIST Computational Chemistry Comparison and Benchmark Database (CCCBDB) [377]. As mentioned before, the information accumulated in CEPDB is not only relevant to OPVs but to organic electronics in general. It is also designed to provide benchmarks for the performance of various theoretical methods in this family of systems as well as a parameter repository for other calculations (e.g., for model Hamiltonians [100, 457, 549] or custom force fields [533]). It will be available to the public by 2012.

The primary purpose of CEPDB is to store and provide access to the CEP data. Candidates with a certain set of desired parameters can readily be identified. CEPDB also serves as the hub for all data mining, analysis, and scoring operations to facilitate the study of global trends, correlations, and OPV design rules. Finally, CEPDB is also responsible for bookkeeping, archiving the raw data (including the binary MO eigenvectors for subsequent

to be automated to keep it feasible, efficient, and reduce human error. We created the necessary facilities using the Python scripting language [47, 290].

6.3 Conclusions

This initial presentation of the Harvard Clean Energy Project outlined its overall architecture, the machinery we put in place, and upcoming extensions. We pointed to first results and more detailed reports on the various aspects of the project – tied together by this chapter – will be given in subsequent publications.

CEP applies a modern cyberinfrastructure paradigm to computational materials science and in particular to renewable energy research. Engineering successful OPV materials is a complex challenge as a number of optical and electronic requirements have to be met. We showed that CEP with its large-scale screening is well equipped for a knowledge-based search of systems with suitable features. It provides a unique access to data for a wide array of potential compounds with diverse electronic structures and it is ideally suited to identify highly promising donor or acceptor candidates in the infinite space of organic electronics. Our work can thus complement and accelerate traditional research approaches, and it can help develop an understanding of structure-property relationships to facilitate the rational design of new materials. We hope that joint efforts with experimental collaborators can contribute to overcoming the current limitations of OPV materials in order to provide a clean source of electricity which can compete with conventional power production.

Chapter 7

Accelerated computational discovery of organic photovoltaic materials by means of cheminformatics

7.1 Introduction

Current human consumption of energy amounts to 550 EJ per year, which corresponds to 260 million barrels of oil equivalent (MBOE) per day. If the world economy keeps growing at rates close to what has been observed in the last hundred years, human consumption of energy will reach 360 MBOE per day by 2035 [113]. To maintain a supply for this growing demand is a challenge, primarily because of the decreasing energy return on investments. At the same time, the continuing use of fossil fuels will increase the impact of global climate change. Almost 87% of the energy consumed by humanity is currently derived from fossil fuels [80] and all renewable energy sources will be needed in order to satisfy the present and future demand for clean energy.

Solar power is a prominent source for renewable energy, in particular for the production of electricity without greenhouse gas emissions. Solar cells are made of thin layers of photovoltaic materials which can harness sunlight for conversion into electricity. Crystalline silicon-based solar cells have dominated the field of commercial photovoltaics, but drawbacks in the manufacturing process as well as high production cost have precluded them from widespread use [169]. Thin-film technologies have led to the development of solar cells based on other inorganic materials such as CdTe [488], as well as the development of dye-sensitized solar cells [397]. Although none of these technologies have reached a higher efficiency than crystalline silicon at 25% [615], they allow for the possibility of cheaper fabrication and a favorable efficiency/cost ratio, as their production process is less energy-intensive.

Organic photovoltaic (OPV) cells represent another thin-film approach which has drawn

a lot of attention and has shown significant progress in recent years [218]. OPVs are particularly promising due to the abundance of their main constituents, their low cost, scalability, and versatility of their installation. Moreover, the potential of rational design to improve the performance of the solar cells has driven recent progress in OPVs. The record power conversion efficiencies of OPVs have improved considerably in the last years: from 1% in 1985 [516]; 4% in 2002; 6% in 2009; and up to 9.2% in 2011 [478]. If power conversion efficiencies of 10-15% in combination with a lifetime of more than 10 years can be achieved in production materials, OPVs could compete with inorganic-based photovoltaics and become a commercially viable alternative for harnessing electricity from sunlight in a wide range of applications.

Organic-optoelectronic materials span a vast chemical space due to the structural versatility of their carbon-based framework. The prospect of exploring this space has interesting implications for materials design considerations. Due to challenges in the synthesis and experimental characterization of these systems, usually only a modest number of compounds can be studied as candidates for active materials in OPVs [63, 458]. Approaches that involve the *in silico* screening of potential organic semiconductors for OPV applications can aid in accelerating the discovery of high-efficiency materials [386, 491, 201].

In this chapter, we review the recent progress of semiconductor polymers for plastic solar cells, and later present the basic ideas of cheminformatics (chemical informatics) for the search of novel organic photovoltaic materials. We adopt the use of physicochemical and topological descriptors, which are commonly known and employed in drug discovery, for the identification of promising organic semiconductors with desired current-voltage characteristics and high power conversion efficiencies. In this context we discuss the systematic construction and optimization of the descriptor models. This technique is employed as part of the Harvard Clean Energy Project [107, 201], a high-throughput *in silico* screening and design effort to develop novel high-performance materials for OPVs. The cheminformatics investigation presented here is a valuable complement to the much more time consuming first-principles electronic structure calculations performed in other parts of this project.

7.2 Bulk-heterojunction solar cells

The state-of-the-art of OPVs are based on a bulk-heterojunction (BHJ) architectures of two semiconductor compounds: one acting as a electron donor (typically a polymer, or a small molecule) and the other acting as an electron acceptor (a high electron affinity molecule) [600]. Fig. 7.1 shows a schematic illustration of a BHJ solar cell. The photovoltaic process begins with light absorption and ends with charge transport to the electrodes. It occurs through the following steps: i) optical absorption and exciton formation, ii) exciton

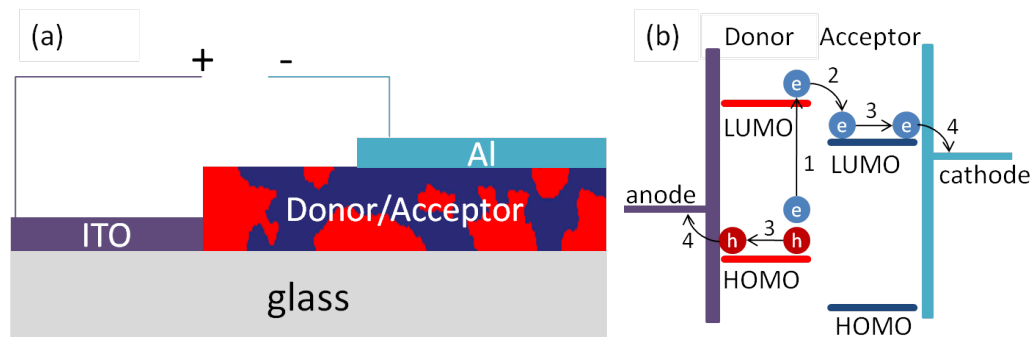


Figure 7.1: (a) Device architecture of a bulk-heterojunction solar cell. Light is incident upon the glass substrate. (b) Bulk-heterojunction photophysics: 1) a photon excites an electron to form an exciton, which migrates to the donor/acceptor interface; 2) a difference between the LUMO levels of the donor and acceptor (typically of the order of 300 meV or greater) causes the exciton to dissociate; 3) electrons and holes are transported towards the cathode and anode, respectively; 4) charge is collected at the electrodes, thus transforming light into current.

migration, iii) exciton dissociation at the donor-acceptor interface, iv) charge carrier migration to the electrodes, and v) charge collection at the electrodes. These five steps are summarized in Fig. 7.1(b). This mechanism naturally carries potential losses at each stage, mainly stemming from inefficient absorption in the beginning and exciton recombination at the intermediate steps. Further details of these elementary processes and their limiting factors have been described extensively in the literature [78, 262, 68].

The parameters which determine the overall efficiency of the energy conversion process in a solar cell are examined in terms of its current-voltage (*i. e.*, power) characteristics [521, 75]. The power conversion efficiency (PCE) is defined as the percentage of the ratio of power output (P_{out}), to power input (P_{in}). P_{out} is the maximum (m) obtainable electric power: the product of current, J_m , and voltage, V_m . It is also possible to define P_{out} as depending linearly on the product of the short circuit current density (J_{sc}), the open circuit voltage, (V_{oc}), and the fill factor (FF). The fill factor is the ratio of the maximum power, $J_m V_m$, to the product of J_{sc} and V_{oc} . The product $J_m V_m$ represents the potential power available under the ideal conditions imposed by $J_{\text{sc}} V_{\text{oc}}$ [509]. The FF then becomes a parameter that measures the capacity of the device to obtain the most power available. Losses depend on the parasitic resistance of the device and other inefficiencies, which are related to the cell morphology [370, 258]. Thus, the formula to compute power conversion efficiency can be written as:

$$\% \text{PCE} = \frac{\text{FF} \cdot J_{\text{sc}} \cdot V_{\text{oc}}}{P_{\text{in}}} \times 100. \quad (7.1)$$

J_{sc} and V_{oc} are quantities that can easily be determined under device illumination and largely depend on the molecular properties of the donor and acceptor moieties.

As detailed by Brabec [75], V_{oc} is related to exciton dissociation, which leads to the charge separation process (step iii, above). V_{oc} scales linearly with respect to the energy difference between the highest occupied molecular orbital (HOMO) of the donor and the lowest unoccupied molecular orbital (LUMO) of the acceptor [73]. J_{sc} , on the other hand, largely depends on the charge mobility and the bandgap of the donor, which determines the spectral overlap: the smaller the bandgap, the higher the spectral overlap. The theoretical understanding of the important parameters for high photovoltaic efficiency has led to models that predict the efficiency of a donor material with respect to a given acceptor, commonly PCBM, ¹ as a function of their energy levels [467, 275]. In particular, the model of Scharber *et al.*, Ref. [467], has been instructive for this purpose due to its simplicity.

The first generation of OPV architectures involved a structure in which donor and acceptor layers of $O(100\text{nm})$ were spin-cast. These original designs for donor-acceptor bilayers are limited by the intrinsic exciton diffusion length, as the excitons formed in the donor layer have to reach the interface with the acceptor for the exciton to dissociate [109]. BHJ devices involve blends of donor and acceptor materials which mix at the nanometer scale, creating connected domains of $O(10\text{ nm})$ of donor and acceptor materials that facilitate exciton diffusion to the interface before recombination takes place [601, 202, 600]. A challenge for theoretical methods for materials discovery is that the ultimate efficiency of BHJ materials depends on annealing conditions and co-solvents, also known as additives [410]. The general complexity and multiscale nature of the device morphology is very hard to model with electronic structure theory.

Recent developments in device architecture that go beyond simple BHJ designs are numerous. They include textured substrates for increased light path lengths [368], the addition of a titanium oxide (TiO_x) layer on top of the BHJ layer as an optical spacer which has internal quantum efficiencies of 100% [257, 403] and other improvements such as plasmonic concentrators [32].

7.3 Organic photovoltaic materials

In this section, we provide a brief overview on the evolution of the different design approaches for novel OPV materials. The sequence of developments will be relevant to the discussion of our computational approach in the following sections, as the results from the cheminformatics screening should correspond to the experimentally observed trends. We

¹1-(3-methoxycarbonyl)propyl-1-phenyl-[6,6]C₆₁






Generation	Motif	Name	Maximum PCE (experimental)	No. top 1000 $V_{oc}J_{sc}$ (predicted)
PPV		MDMO-PPV [76]	3.3%	—
P3HT		P3HT [257]	5.0%	0
DADA		PCPDTBT [410]	5.2%	17
DTAT		PBnDT-DTfBT [621]	7.2%	13
QUINO		PBDTTT-CF [96]	7.7%	117

Table 7.1: A non exhaustive overview of OPV development. Successive generations of OPV based on monomers and co-monomers: We show record PCE achieved and the number of molecules predicted in the present study corresponding to a particular design concept. Fragment key: circle, PPV; pentagon, P3HT; square, donor; triangle, acceptor; cross, quino-line. Color Key: Color schematically indicates bandgap size; except gray, which indicates a fragment with good hole mobility.

show a (by no means exhaustive) overview of the OPV milestones in Table 7.1.

Many of the initial donor materials for BHJ devices derived from MDMO-PPV,² Fig. 7.2. These donors are combined with PCBM as the acceptor. PCBM has been extensively used as a solar cell acceptor material, along with its C₇₀ analogue [600, 230, 125], and all reported values in this chapter (*e.g.*, V_{oc} , J_{sc} , the FF and PCE) use these molecules as acceptors. MDMO-PPV has a low-lying HOMO of -5.4 eV. For the junction, a V_{oc} of 0.82 V and a J_{sc} of 5–6 mA/cm² was measured. The small J_{sc} value can be explained by the large donor bandgap, and it ultimately limits the PCE to 3.3% [76, 218].

Regioregular poly-(3-hexylthiophene) (rr-P3HT Fig. 7.2) with a 1.9 eV bandgap emerged as a predominant donor due to its higher J_{sc} , and refined morphological characteristics that lead to a presumably higher exciton mobility than found in MDMO-PPV. This advantage results in efficiencies of over 5% [257, 125]. A high lying donor HOMO precludes this molecule from having a larger PCE, despite the improvements in J_{sc} and morphology.

Recent searches for donor materials have focused on improving either V_{oc} or J_{sc} , while Eq. 7.1 clearly suggests the need to optimize both. However, there seems to be a trade-off between J_{sc} and V_{oc} that can partially be attributed to the relatively high LUMO of the fullerene-based acceptors and their interaction with the frontier molecular orbitals of the donor. To improve upon this, a new generation of co-monomer based materials was introduced, in which an electron-donor and an electron-acceptor motif are coupled to form

²poly-[2-methoxy-5-(3',7'-dimethyloctyloxy)-1,4-phenylene vinylene]

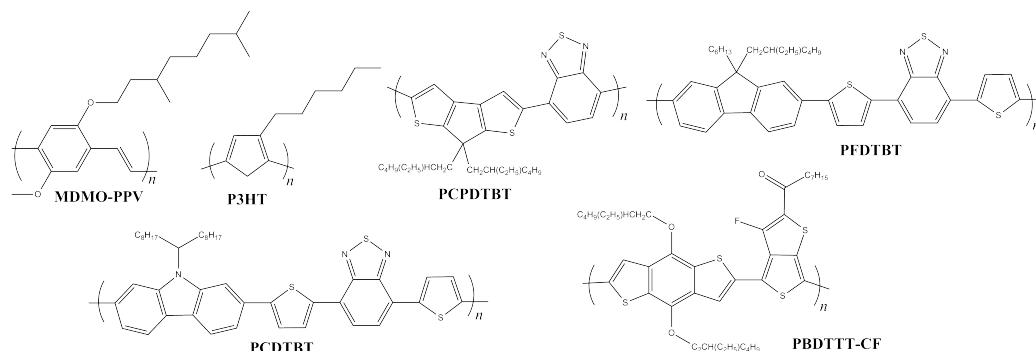


Figure 7.2: Chemical structures highlighted in Sec. 7.3. MDMO-PPV was one of the first donor materials used. P3HT is a prevalent donor which has shown higher J_{sc} , and refined morphological characteristics. PFDTBT and PCDTBT are co-monomers, in which the donor-acceptor polymer strategy was applied to obtain higher PCE. PBDTTT-CF is a co-monomer, which features quinoidal stabilization and with the aid of the fluorine group has yielded an efficiency of 7.7%.

the “monomer” of the polymer unit.

Donor-acceptor designs— One strategy, first proposed by Havinga, Zhang and others [212, 611, 548], involves improving the donor polymer properties by using a set of alternating electron-rich (*i.e.*, donor) and electron-deficient (*i.e.*, acceptor) moieties to form co-monomers. This approach results in a smaller bandgap for the donor via the hybridization of the energy levels between the donor (typically with high HOMO) and the acceptor (low LUMO) fragments in the co-monomer [548, 81]. It also improves the intramolecular charge-transfer [449, 245, 450]. This technique is thus labeled “donor-acceptor polymer” approach (DADA in Table 7.1). For example, Mühlbacher *et al.* synthesized PCPDTBT,³ Fig. 7.2, which shows a low bandgap (1.7 eV) and also absorption activity in the infrared region, with an overall efficiency of 3.2% [365]. Morphological improvements via the co-solvent approach mentioned above, led to an improved efficiency of 5.5% [410].

Incorporation of high-mobility inducing fragments— Further improvements have been achieved by adding a moiety which promotes the charge-carrier mobility. The co-monomer PFDTBT,⁴ Fig. 7.2 [511, 234] has three components: thiophene (T), as a donor; benzothiadiazole (BT), as an acceptor; and fluorene (F), as the high-mobility fragment; it is represented as DTAT in Table 7.1. The fluorene moiety is known to absorb at short wave-

³poly-[2,6-(4,4-bis-(2-ethylhexyl)-4H-cyclopenta[2,1-b;3,4-b']-dithiophene)-alt-4,7-(2,1,3-benzothiadiazole)]

⁴poly-[2,7-(9-(2'-ethylhexyl)-9-hexyl-fluorene)-alt-5,5-(4',7')-di-2-thienyl-2',1',3'-benzothiadiazole]

lengths, but the mixture with thienyl fragments red-shifts the absorption. The thiophene moiety has in addition good hole-transport properties, increases planarity, and is used as the fragment on which alkyl chains are typically fastened for improved processing. An initial success with this design was demonstrated by an improved V_{oc} of 1.05 V. However, the J_{sc} remained low at 3.65 mA/cm². The PCE of PFDTBT was estimated to be 1.7%, but modifying the R groups in fluorene pushed the PCE to 2.1% [511, 234].

Blouin *et al.* concentrated on finding better acceptor units in the co-monomer. They substituted the fluorene moiety for carbazole, a fully aromatic system, to obtain PCDTBT,⁵ Fig. 7.2. A considerable increase of the J_{sc} to 6 mA/cm² was achieved, albeit with a slightly lower V_{oc} of 0.9 V. This resulted in an overall PCE of 3.6% [64]. Following a similar technique, Wang *et al.* replaced the fluorene moiety with silafluorene (SiF), and obtained a PCE of 5.4% [558]. The higher efficiency is a result of the broader absorption spectrum of silafluorene, which allows for a J_{sc} of 9.5 mA/cm².

Blouin *et al.* continued to optimize their PCDTBT co-monomer to focus on the acceptor fragments [63]. Despite the HOMO and LUMO levels being ideally tuned in some cases, they were unable to improve their reported PCE of 3.6% [64]. Recently, Park *et al.* were able to obtain 6.1% efficiency using PCDTBT and adding a titanium oxide (TiO_x) layer on top of the BHJ layer as an optical spacer [403]; an example of optimization via modifying the device architecture. This improvement brings PCDTBT efficiency close to the PCE limit predicted by the Scharber model [467].

Chen and Cao reviewed and analyzed donor-acceptor polymer materials which contained either benzothiadiazole, thiophene, thienopyrazine or quinoxaline for a total of 39 co-monomers [98]. Their analysis revealed that systems with a lower bandgap resulted in higher PCE values. The authors argue that although there is a linear trend between the HOMO position and the V_{oc} [73], there is significant scatter in the data to conclude that other effects influence the open-circuit voltage. Furthermore, Yang *et al.* [592] have studied the effect of alkyl chains on the V_{oc} and J_{sc} for a given backbone. They found that there is a significant change with respect to length and shape of the R-groups, which argues in favor of strong dependence on morphology. The relationship between these changes are attributed to the strength of intermolecular interactions between the polymer and PCBM blend.

Weak donor, strong-acceptor motifs— Zhou and Price *et al.* have extended the donor-acceptor polymer approach by introducing the concept of *weak*-donors and *strong*-acceptors [620, 619, 621, 425, 424]. Co-monomers are built similar to PFDTBT: donor, thiophene,

⁵poly-[N-9'-heptadecanyl-2,7-carbazole-alt-5,5-(4',7'-di-2-thienyl-2',1',3'-benzothiadiazole)]

acceptor, thiophene (DTAT in Table 7.1). Once again, thiophene moieties are present to increase planarity and as a location to add the R-groups. Zhou *et al.* generate a *weak*-donor moiety by starting from a strong (*i.e.*, electron-rich) component like thiophene and then fusing it with benzene, a less electron-rich moiety [620]. In the case of *strong*-acceptors, it is important for the moiety to be π -electron deficient: the benzene moiety in the benzothiadiazole unit can for instance be substituted with pyridine, to generate thiadiazolo[3,4-*c*]pyridine [619]. Power conversion efficiencies following this design have reached up to 6.3%. Further work revealed an explicit dependence between the donor HOMO and the acceptor LUMO of this co-monomer layout. Recent findings by these authors have concentrated on optimizing these co-monomers using different acceptors (including fluorinated moieties) and resulted in a PCE of over 7% [621, 424].

Quinoidal structures— A successful technique to reduce the bandgap was based on using alternating thieno[3,4-*b*]thiophene (TTP) and benzodithiophene (BDT) units [308, 309, 96, 306]. The reduction of the bandgap is due to the stabilization of the quinoidal structure of TTP. BDT experiences quinoidal stabilization as well, but it also provides rigidity to the backbone (represented as QUINO in Table 7.1. Liang, Chen *et al.* have also explored the use of alkoxy sidechains to yield further improvements. In particular, PBDTTT-CF, ⁶ Fig. 7.2 has the TTP unit alkoxyated and fluorinated in positions 2 and 3, respectively. PBDTTT-CF results in a maximum PCE of 7.7% [96], which is one of the best efficiencies to date.

The fluorine moiety shifts the donor HOMO and LUMO values which leads to a greater V_{oc} , without affecting the J_{sc} . Further work based on the quinoidal strategy has met with mixed results since the control of the bandgap becomes more difficult when there are no explicit acceptors and donors in the polymer [266].

Improved acceptor materials— The development of acceptor materials has been dominated by functionalized fullerene derivatives, such as PCBM. PCBM has been extensively employed as a solar cell acceptor material since it was first reported in 1995 [600, 230, 125]. Although the HOMO and LUMO levels of these systems are not ideal for the known donor polymers, no better candidates have been found [467]. C_{60} and C_{70} -based molecules exhibit a high electron mobility and affinity, which is highly isotropic due to their spherical shape. Functionalizing them with the ester moiety provides for good solubility, as well as a higher LUMO level, which reduces its work function [274]. Due to the relative success of PCBM, the search for better organic photovoltaic materials has primarily become a pursuit for finding ideal donor properties constrained by the energy levels of fullerene-based acceptors.

⁶poly-[4,8-bis(2-ethylhexyloxy)-benzo[1,2-*b*:4,5-*b'*]dithiophene-2,6-diyl-alt-(4-octanoyl-5-fluoro-thieno[3,4-*b*]thiophene-2-carboxylate)-2,6-diyl]

Recent reviews on acceptor materials include those by Anthony on organic-based non-fullerene molecules [27] and by Xu and Qiao on inorganic-based systems [590]. We refer to the recent work by Gendron and Leclerc for other classes of donor polymers [171]. As outlined in this section, a series of compound-design strategies for donors and acceptors and their rationalization has resulted in a systematic increase of reported efficiencies. In the following section we will explore how computational approaches based on cheminformatics can provide guidance towards innovation and the next generation of OPV materials.

7.4 Cheminformatics modelling

The rational design of donor and acceptor molecules ⁷ for OPVs can be pursued by computational studies of potential candidates. Electronic structure calculations represent a valuable tool to characterize optoelectronic features and processes central to the performance of organic semiconductors [231, 459]. Current calculation schemes allow the prediction of electronic properties such as HOMO, LUMO and optical bandgap, as well as other molecular properties that are considered to ultimately be related to the OPV efficiency, such as partial charges, intramolecular interactions, and geometries. These calculations are, however, still time consuming and computationally demanding. The Harvard Clean Energy Project (CEP) [107, 201] has been set up for an automated, large scale *in silico* characterization of millions of molecules. Based on computational resources provided by distributed volunteer computing in collaboration with IBM's World Community Grid [586], CEP is currently performing a systematic screening of millions of candidate molecules using electronic structure theory. Cheminformatics methods allow the "transformation of data into information and information into knowledge" [82] and they are being employed as a complementary approach to the quantum chemical work within CEP.

To date, cheminformatics has primarily been designed to provide a fast way of screening large libraries of potential compounds, mostly for pharmaceutical applications. This discipline has been described as "all the information resources that a scientist needs to optimize the properties of a ligand to become a drug" [83]. However, the tools developed in this field, and closely related techniques in machine learning and pattern recognition, can in principle be applied to other materials discovery endeavors. Developments in cheminformatics have been driven by the combination of experimental high-throughput screening (the assay and analysis of more than a million chemical reactions) and with the ability to computationally predict physicochemical parameters (called descriptors). The basic strategy of this approach is to obtain these descriptors for candidate molecules, often obtained

⁷In the following we will collectively use the term 'molecules' for monomers, oligomers, and actual molecules.

from designated candidate libraries [301, 176, 471, 146, 561, 254, 285, 286, 199], to score their fitness with respect to a desired set of properties.

One of the most important methods is the identification of quantitative structure-property relationships (QSPR) [39, 207, 591, 295, 99, 168]. This technique has focused intensely in the search for molecules to be experimentally screened as potential drugs, or as drug leads [550]. More recently, QSPR were employed in the study of certain molecules for an understanding of the fundamental processes of cellular and organismic biology [310, 134]. In similar fashion to QSPR, quantitative structure-activity relationships (QSAR) are used to study the biological activity of such problems. We note that the complexities faced in the interactions between organic molecules in biological systems are greater than in those found in organic electronic materials. Despite these challenges, cheminformatics has been successful in several areas on the interface between chemistry and biology [8]. For instance, it is possible to analyze the conformation of drug candidates to evaluate their docking potential to a particular biomolecular target and for a prediction of its use as a pharmacophore.

QSPR have been developed for a wide variety of applications, which include single-molecule, intermolecular and reactive properties. The success of this approach has stimulated its use in recent years, as can be seen in several reviews [550, 253]. The materials science community has just begun to utilize machine-learning methods, which encompass cheminformatics and QSPR. Work in this area has led to the prediction of crystal structures of inorganic molecules [149, 430, 211, 42], as well as the development of methods for visualizing and identifying potential porous materials [208, 520].

The simplest QSPR approaches are based on linear regression models, but more sophisticated forms which incorporate genetic algorithms, artificial neural networks, and the Gaussian processes technique have been developed in recent years [519, 85, 387, 386]. Several other techniques in cheminformatics have been used for the identification of leads not related to regression models. These include statistical tools used in machine learning such as principal component analysis, linear discriminants, and decision trees [138, 39, 295, 261].

QSAR and QSPR largely rely on the calculation of molecular properties called descriptors, which we will discuss in Sec. 7.4.1. Descriptors include physical, chemical and topological properties. Descriptors can be classified as either one-, two- or three-dimensional, depending on whether they describe bulk properties, connectivities or conformation dependent properties, respectively [591, 530]. The use of descriptors in cheminformatics has provided simple rules to evaluate druglikeness, as in the case of Lipinski's Rule of Five which analyzes molecules using a set of structural descriptors: molecular mass, hydrogen bond donors, hydrogen bond acceptors, partition coefficient, and number of rotatable bonds [311]. These rules have been very useful for the development of drug leads. Therefore, there have been

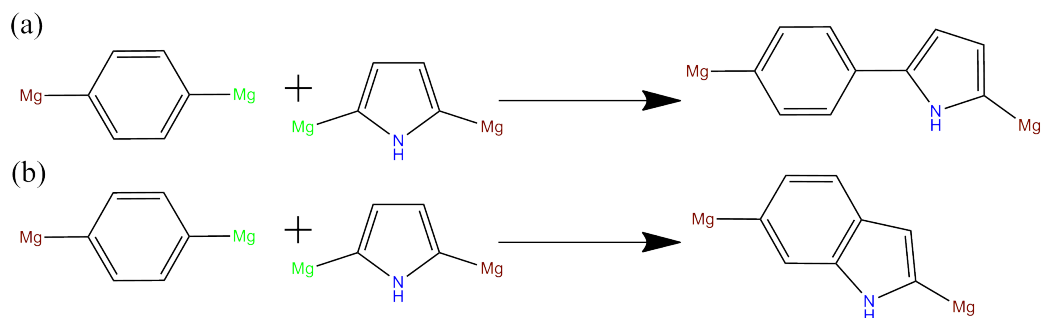


Figure 7.3: A reaction-based approach for enumerating a molecular library. (a) Linking reaction: Benzene molecule with Mg chemical handles in the *para* position reacts with pyrrole with Mg chemical handles at the 2,5-position. One set of Mg (green) react to form a linked co-monomer of these moieties. (b) Fusion reaction: Benzene molecule with Mg chemical handles in the *para* position reacts with pyrrole with Mg chemical handles at the 2,5-position to form benzopyrrole. In both cases, a second set of Mg handles (red) is present so that this product can be used as a reagent and enable the generation of co-monomers of greater size.

active efforts to develop computer codes that allow the rapid evaluation of hundreds of such descriptors [95, 396, 515].

7.4.1 The molecular library and physicochemical molecular descriptors

In order to search for donor molecules that have the best combination of electronic properties, we built a molecular library of approximately 2.6 million conjugated molecules. The molecular library employed is built via a combinatorial molecule generation scheme starting from a set of 30 molecular building blocks (in Sec. 7.6). The fragments include the most prevalent molecular motifs used in the experimental design of OPVs to date and are chosen with input from experimentalist collaborators from the group of Zhenan Bao at Stanford University to ensure synthetic feasibility [356]. As discussed in Sec. 7.3, R-groups play an important role in OPV materials but for the present work we chose to focus only on the molecular backbone.

We enumerate the library using a virtual reaction-based approach by either *linking* or *fusing* the fragments together, as shown in Fig. 7.3. We also extend the size of the co-monomers by properly adding molecular handles, so they can be *further* linked or fused. Complete details of the molecular library generation will be presented in a separate publication [394].

We use the previously introduced descriptors for an initial characterization of our molecular library. We employ the Marvin code by ChemAxon [95]. ChemAxon provides a set

of over 200 descriptors that are relevant for drug design applications, but they nonetheless proved useful in the application for OPV donor materials. We selected descriptors corresponding to elemental analysis, charge, geometry, and electronic states based on Hückel theory for the study of monomers for use as donor in OPVs. For atomic-based properties, we assessed the maximum, minimum and average value in the molecule. There are a total of 33 descriptors in our model, their classes are listed in Table 7.5. These can be easily computed for the whole library within a few days on a single workstation.

A specific example of a descriptor that displayed statistically significant correlation is the electrophilic localization energy, $L(+)$, which is an atom-centered property based on the Hückel method: the simplest semiempirical approach for obtaining quantum-mechanical properties of conjugated molecules [237]. $L(+)$ is the energy related to removing an atom from conjugation, effectively donating two π -electrons to the electrophile. The lower the value of $L(+)$, the more reactive the compound. Therefore, a small value of electrophilic localization energy means that the atom contributes little to the overall conjugation of the molecule. The effect is shown in Fig. 7.4.

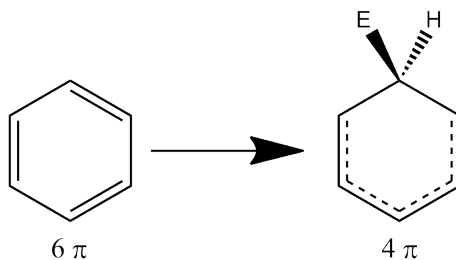


Figure 7.4: The electrophilic localization energy, $L(+)$. The energy related to the bond formation at a conjugated center, which will remove that center from conjugation, effectively taking away two π -electrons from the conjugated backbone. The lower the value of $L(+)$, the more reactive the compound, meaning that the atom contributes little to conjugation.

7.4.2 Descriptor model and training set results

We have chosen a simple linear regression model for this initial investigation. The descriptors chosen above are assembled accordingly and the resulting model is parametrized using a training set of organic monomers with experimentally known current-voltage characteristics. We selected a set of 50 training molecules compiled from the literature [365, 441, 489, 558, 355, 344, 23, 22, 389, 63, 522, 325, 140, 98]. These molecules include aliphatic side chains used to control packing structures. The current chapter is concerned with donor materials of BHJ design, but this method can naturally be applied to other device architectures and materials given the appropriate training set.

Property	R ² (all desc.)	Descriptors	R ²
V_{oc}	0.9580	20	0.9455
J_{sc}	0.9202	18	0.8989
%PCE	0.8937	15	0.8409
FF	0.6567	20	0.6170
$V_{oc}J_{sc}$	0.9025	20	0.8809

Table 7.2: Summary of linear fitting results for each of the properties we study. We compare the coefficients of determination (R^2) using all 33 descriptors (all desc.) and the statistically significant ones. The number of significant descriptors ranges from 15–20, but the R^2 is not largely affected in all cases.

As mentioned in Sec. 7.1, we focus on the four most relevant parameters for the performance characteristics of a solar cell. These are PCE, and its components as expressed in Eq. 7.1: the FF, V_{oc} and J_{sc} . Note that V_{oc} and J_{sc} largely depend on properties intrinsic to the donor and acceptor. FF broadly depends on the morphology and the specific device architectures. We can therefore expect that the molecular descriptors used and the experimental values will show a better correlation for the first two than for the latter. The expression to determine PCE includes all three parameters and its correlation should thus fit in between the others.

The multiple linear regression for the descriptor models with respect to these four parameters was performed using the R code [429]. The correlation, as obtained by the use of the 33 descriptors, varied from very good ($R_{V_{oc}}^2 = 0.96$, $R_{J_{sc}}^2 = 0.92$) or good ($R_{PCE}^2 = 0.89$) to poor ($R_{FF}^2 = 0.66$). We performed a significance test on the descriptors and eliminated the least significant ones which only slightly reduced the precision of the fit (shown in Sec. 7.6). The significance of the descriptors was obtained from a two-sided t-statistics test. The p-value for each descriptor ranged from 10^{-3} to 10^{-1} .

In order to mitigate the difficulty of predicting the FF from a purely cheminformatics approach, we also built a model for the product $V_{oc}J_{sc}$, which is proportional to PCE but only contains parameters well represented in our cheminformatics approach. We summarize the results related to the coefficients of determination (R^2) of the fitting in Table 7.2. We also present the results of the predicted properties against the measured ones in Fig. 7.5. As stressed above, it is not unexpected that the parameters which depend on the material properties, V_{oc} and J_{sc} , result in a much better fit than the FF.

The fit resulted in families of significant descriptors that were different for each of the experimental parameters. The best description included 20 descriptors for V_{oc} and $V_{oc}J_{sc}$, 18 for J_{sc} and 15 for PCE. Four descriptors are present in the models of each four parameters. We group estimates of these descriptors in Table 7.3. We notice that each descriptor in this subset has either a positive or a negative correlation for all four values.

Descriptor	Estimates			
	V_{oc}	J_{sc}	%PCE	$V_{oc}J_{sc}$
Rotatable bond count	+0.2375	+2.3886	+0.8393	+1.9484
Electron density (lowest)	-0.8403	-24.1885	-11.3297	-20.9617
Orbital electronegativity (σ) (average)	-1.4448	-38.4895	-15.5656	-23.4284
Orbital electronegativity (π) (highest)	+0.2317	+2.5199	+1.7823	+3.0837

Table 7.3: Estimates for the four prevalent descriptors for the V_{oc} (20 descriptors), J_{sc} (18 descriptors), PCE (15 descriptors), and the product $V_{oc}J_{sc}$ (20 descriptors). The estimate for each of these descriptors are all within two orders of magnitude and have the same sign.

	V_{oc} (V)	J_{sc} (mA/cm ²)	$V_{oc}J_{sc}$ (mAV/cm ²)	%PCE
Max. value (experimental)	1.04	15.0	8.63	5.32
Max. value (predicted)	2.97	41.5	23.61	10.36
% molecules above highest experimental	43.6	37.2	43.4	1.5
% molecules with negative value (predicted)	0.8	8.3	8.0	19.7

Table 7.4: Best current-voltage characteristics predicted from molecular descriptors in the molecular library as compared with experimentally measured for the training set. The highest efficiency predicted is 95% above than the best experimental value. The percentage of molecules predicted to have parameters exceeding the highest experimental value is above 37% for the better fits. Also shown is the percentage of molecules showing (unrealistic) negative values of the parameters.

The separation between estimates is never larger than two orders of magnitude. Therefore, these descriptors form a tight set of estimates that affect each of the parameters in a similar fashion.

As in most machine learning approaches, it is a complicated task to uniquely specify the role of all of individual descriptors for a specific property. Ultimately the combination of all the descriptors in the model is what makes the fit have a relatively good R^2 value of the fits.

7.4.3 Predictions from cheminformatics

We now apply the models created in the previous section to the 2.6 million molecules of the candidate library and summarize our findings. The histograms of the obtained results are shown in Fig. 7.6. In the cases of V_{oc} and J_{sc} (and therefore in $V_{oc}J_{sc}$) there are a considerable number of molecules with predicted values well above the largest observed

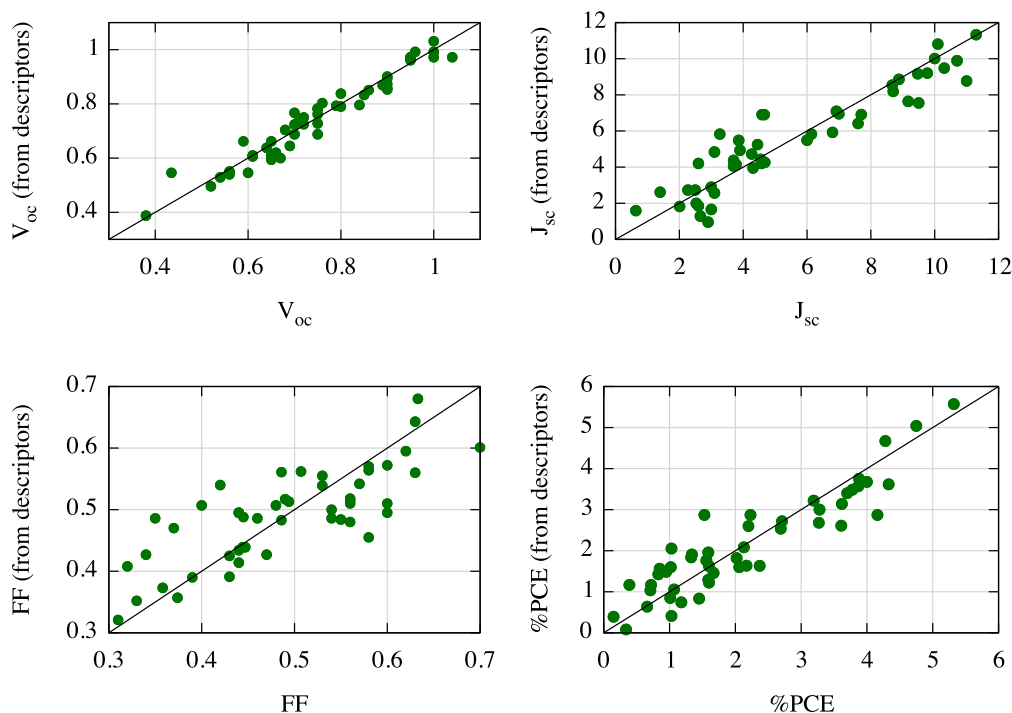


Figure 7.5: Results for the multiple linear regression of the four models and the values of the training set. The predicted value from fitted descriptors is compared to the experimental value originally used for fitting. Units are mA/cm^2 for J_{sc} , and V for V_{oc} .

to date. These molecules constitute the most promising candidates for BHJ donor OPV materials within the presented cheminformatics approach. Some molecules are predicted to have an unrealistic negative value. The fraction of molecules in this situation is small for all parameters except for the FF, which can easily be explained by its relatively poor model. Being mindful of the limitations of the extrapolation, we find that for V_{oc} nearly half of the molecules are predicted to have a value higher than the best of the experimental molecules (1.04 V), and only 0.8% have a negative value; for J_{sc} , 41.5% of the molecules have a value higher than the best experimental, and 8.3% have a negative value; only 1.5% of the molecules have a predicted value of PCE higher than the highest experimental, and the highest value is 10.4%, but there are 43.4% of molecules with a value of the product $V_{oc}J_{sc}$ higher than the highest experimental; these molecules, combined with an appropriate value of the FF (which is not predicted well by these descriptors) could have values of PCE above current records. These results are summarized in Table 7.4.

We further investigate which of the highest rated molecules have the best value for each of the three current-voltage parameters considered (V_{oc} , J_{sc} , $V_{oc}J_{sc}$). We test if a promising

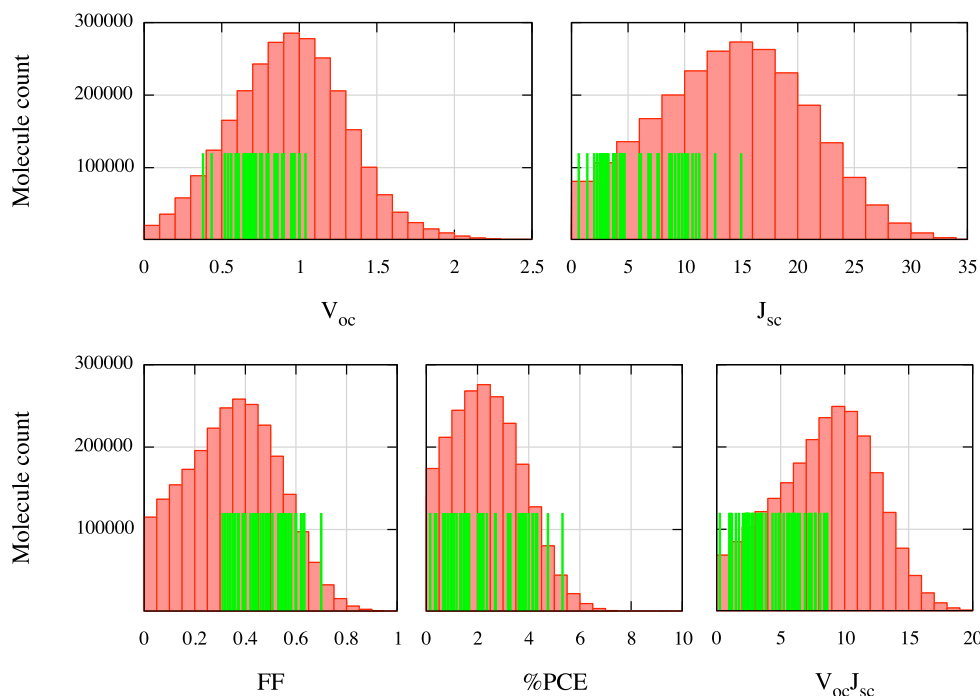


Figure 7.6: Histograms of the predicted current-voltage parameters (open circuit voltage (V_{oc}), short circuit current density (J_{sc}), fill factor (FF), power conversion efficiency (PCE), and the product $V_{oc}J_{sc}$) for the screening of 2,671,405 molecules. Units are mA/cm^2 for J_{sc} , and V for V_{oc} . The vertical lines correspond to the experimental values of the molecules in the training set (*i.e.*, independent of the y -axis value). Note that the predicted values are larger than the best experimental ones, especially for V_{oc} and J_{sc} , their product, and PCE.

molecule for V_{oc} is also a good candidate for J_{sc} and $V_{oc}J_{sc}$. We selected the top 10% from each group and compared them. We find that molecules predicted to have a high value of V_{oc} only rarely have also a high value of J_{sc} , and *vice versa*. Fig. 7.7 shows the position in the predicted V_{oc} vs. J_{sc} space of the top 10% of molecules from each group: V_{oc} , J_{sc} , and $V_{oc}J_{sc}$. We observe that molecules predicted to have the highest values of the product $V_{oc}J_{sc}$ have mostly a high value of J_{sc} and an average value of V_{oc} , *i.e.* they have a higher overlap with the top values of J_{sc} . This suggests that the search for high efficiency monomers, is particularly promising with molecules based on motifs present in both the J_{sc} and $V_{oc}J_{sc}$ optimization.

For a more detailed analysis of the results we focus on the top thousand molecules (all following quantities are taken w.r.t. to the top 1000) with the best current-voltage characteristics. For V_{oc} , we notice that these have at least one silicon atom and are built

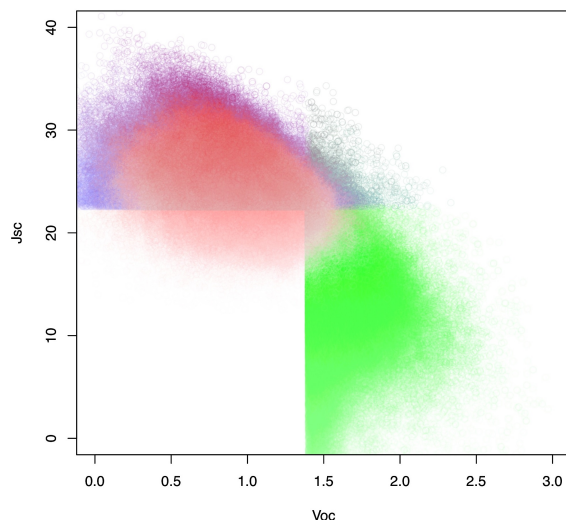


Figure 7.7: Top 10% molecules with highest predicted values of V_{oc} (green), J_{sc} (blue), and $V_{oc}J_{sc}$ (red). The intensity of the point corresponding to a given molecule is coded according to the value of the product $V_{oc}J_{sc}$. The best molecules, according to the present study, are located in the upper left region of the figure. Units are mA/cm^2 for J_{sc} , and V for V_{oc} .

mostly by both linking and fusing the 30 basic fragments. A typical molecule from this set is shown in Fig. 7.8a. For J_{sc} , silicon atoms are not as common (161 molecules have at least one) but instead selenium-containing heteroatoms are more frequent (313 molecules have at least one) and the thienopyrrole motif is present in 822 molecules. The molecules of this set have a predominantly linked rather than fused backbone. Fig. 7.8b shows a typical molecule from this set.

Again, the best expected co-monomers for application in heterojunction OPVs correspond, according to this QSPR analysis, to the ones with the highest value of $V_{oc}J_{sc}$, for which the set of the best thousand have molecules with silicon atoms (375), selenium atoms (131), silicon and selenium atoms (53) and come mostly from linking the basic units (890). The benzothiadiazole or pyridinethiadiazole motifs are prevalent in this set of candidates (see Fig. 7.9), present in 463 molecules. Similarly, units that can potentially have quinoid stabilization are prominent in this set. Specifically, 117 present the thienothiophene moiety. This suggests that the search for monomers with high efficiency as OPV's, should start with molecules based in the motifs presented in Fig. 7.9, as well with those with potential quinoidal stabilization. We currently work on a cross-validation of the present predictions with the ones from the quantum chemical studies within the Harvard Clean Energy Project which will be presented in the near future.

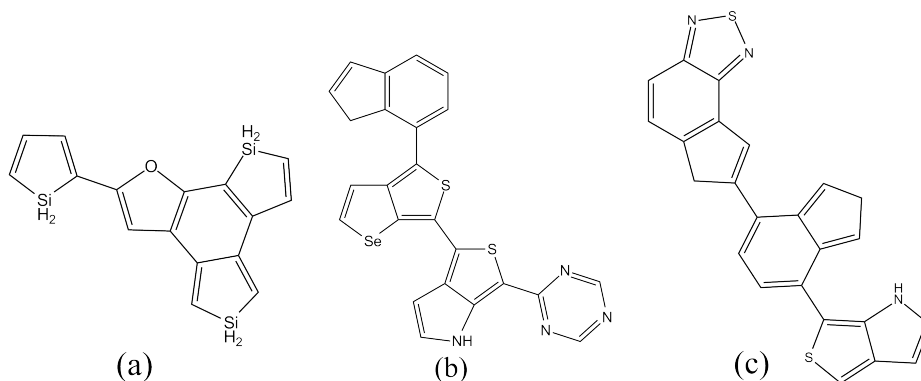


Figure 7.8: Typical molecules from the set of cheminformatics predictions for highest (a) V_{oc} (note the mixed linked and fused heterocyclic units with silicon), (b) J_{sc} (note the linked backbone, the selenium atoms and the thienopyrrole motif), (c) $V_{oc}J_{sc}$ (note the mixed linked and fused structure and the benzothiadiazole and thienopyrrole motifs).

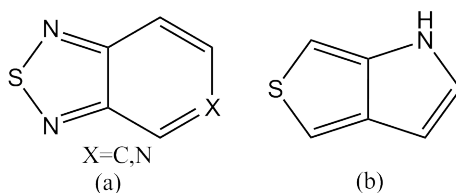


Figure 7.9: Ubiquitous motifs present in many of the most promising molecules according to the predicted $V_{oc}J_{sc}$ parameter: a) benzothiadiazole or pyridinethiadiazole motif, b) thienopyrrole motif

7.5 Discussion and conclusions

In the present chapter we introduced a cheminformatics based approach for the discovery of promising OPV donor materials. We calculated the current-voltage properties of 2.6 million molecular motifs using linear regression descriptor models. These allowed us to identify candidates with a favorable set of performance related parameters, which – according to our QSPR analysis – have the prospect of being suitable as high-efficiency BHJ solar cell materials. The molecules with the most promising predictions feature a variety of structural designs, but three motifs appear repeatedly in our top candidates: benzothiadiazole, pyridinethiadiazole and thienopyrrole, shown in Fig. 7.9.

As summarized in Table 7.1, the evolution of OPV donor materials has followed different design strategies, including the donor-acceptor polymer approach and the quinoidal stabilization. The last column of Table 7.1 shows the number of molecules, from our top

1000 selection, which are part of each design “generation”. We note that PPV-like molecules were not included in our study, and P3HT was not predicted to be in the top 1000. However, there were 17 molecules that followed the donor-acceptor approach. We obtained 13 molecules with the design specified as DTAT, although in our case these systems only had one thiophene scaffold. Finally, molecules with quinoidal stabilization (*i.e.*, containing thienothiophene) numbered 117. A significant fraction of our top molecules hence belongs to the latest generation of OPVs.

Despite the limitations of this simple approach, we can conclude that the use of QSPR and cheminformatics-type approaches can be a valuable guide for the design of lead molecules for solar cell materials. Current efforts to improve upon the presented here include the use of more sophisticated and flexible models, extended and improved training sets, as well as a new generation of descriptors specifically designed for organic semiconductors. The latter can be derived from higher level quantum-chemical studies carried out in the Harvard Clean Energy Project [107, 201].

7.6 Appendix

7.6.1 Molecular Library Generation

In Fig. 7.10, we show the set of building blocks. These are used to generate the molecular library. Further details of the molecular library generation will be detailed in a separate publication [394].

7.6.2 Descriptors

We selected a subset of descriptors available through ChemAxon. The subset selected is shown in Table 7.6. These descriptors were coded in a program and applied to our huge set of molecules.

It should be noted that many descriptors are calculated for each atom of the molecule. In these cases we selected the lowest, the highest and the average value to be used in the calibration and in the prediction.

7.6.3 Calibration molecules

We selected a set of 50 molecules which have been studied experimentally and results are available.

We built molecular formulae from the original papers. For these calculations, aliphatic chains were stripped from the molecular formula. The set of molecules with efficiency

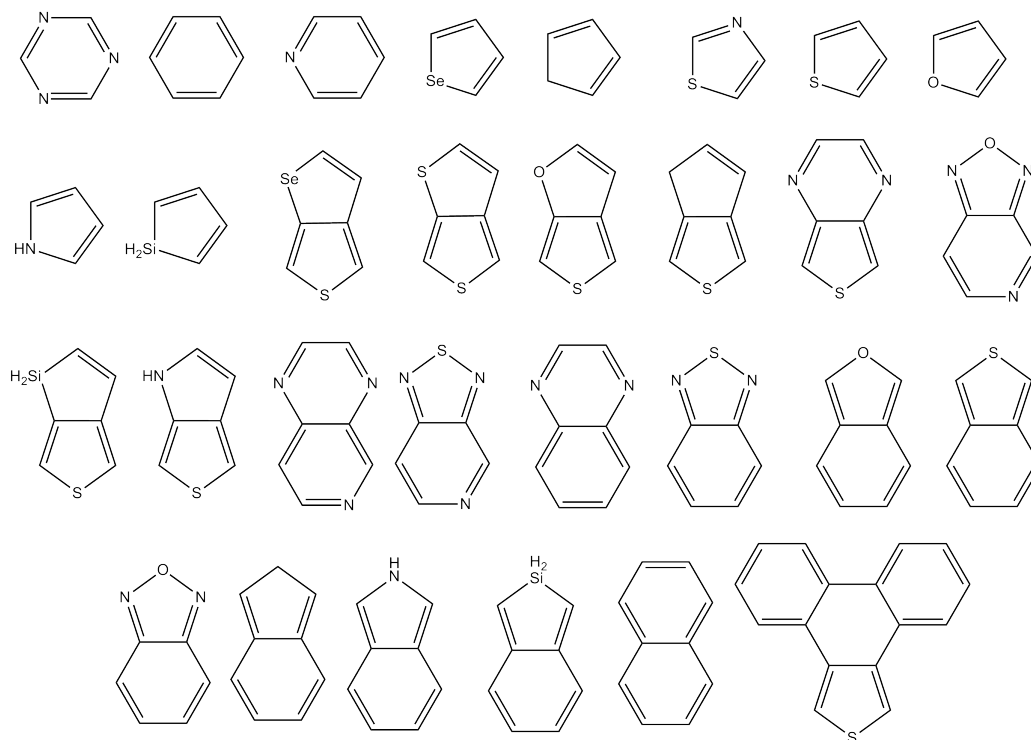


Figure 7.10: The thirty basic heterocyclic units used in this study are shown with their Mg chemical handles at the 2,5- or para- position of the five-membered and six-membered ring, respectively.

parameters measured experimentally, thus used in this study, is shown in Fig. 7.11 and Fig. 7.12.

7.6.4 Selection of descriptors and results for the calibration molecules

Figures 7.13, 7.14 and 7.15 show plots of V_{oc} versus each one of the 33 descriptors, none of them showing an obvious correlation. We used R to perform a multiple linear regression. As could have been expected, 50 experimental data with 33 descriptors make for a very good fit with R-squared of 0.9580. Some of the descriptors are not statistically significant, so we removed the less significant descriptors and ended up with a fitting from 20 descriptors (with R-squared of 0.9455) all of them significant. Table 7.7 show results of the fitting.

Next, we used the same technique for J_{sc} . Table 7.8 show results of the fitting. In this case, 18 significant descriptors fit the experimental values with R-squared of 0.8989.

Table 7.9 show results of the fitting of PCE. In this case, 15 significant descriptors fit the experimental values with R-squared of 0.8409.

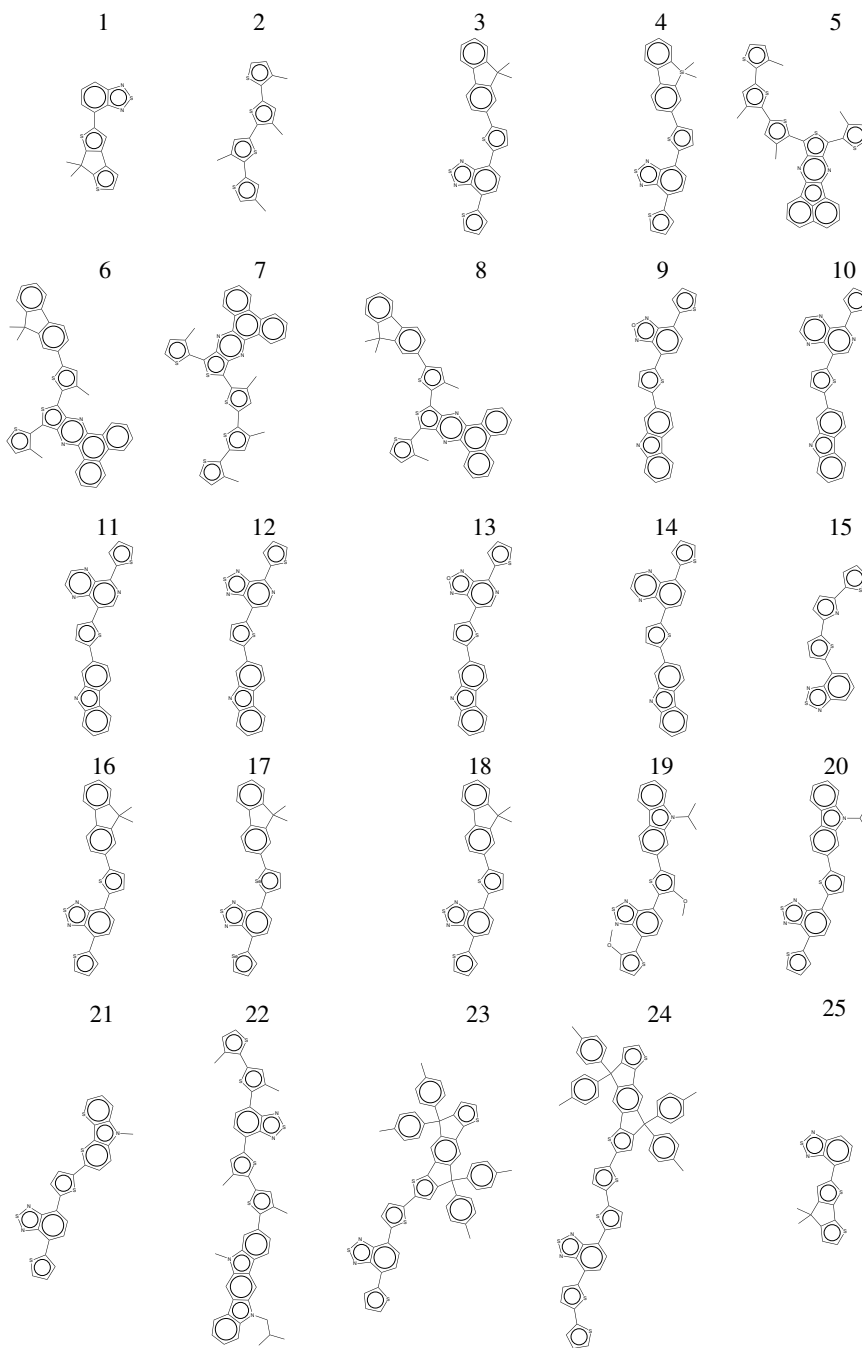


Figure 7.11: First set of the fifty experimentally characterized molecules (shown here without aliphatic side chains). Once stripped of the aliphatic tails, several molecules are equivalent (6 and 8; 3, 16 and 18; and 48 and 50), but all are retained in the training set.

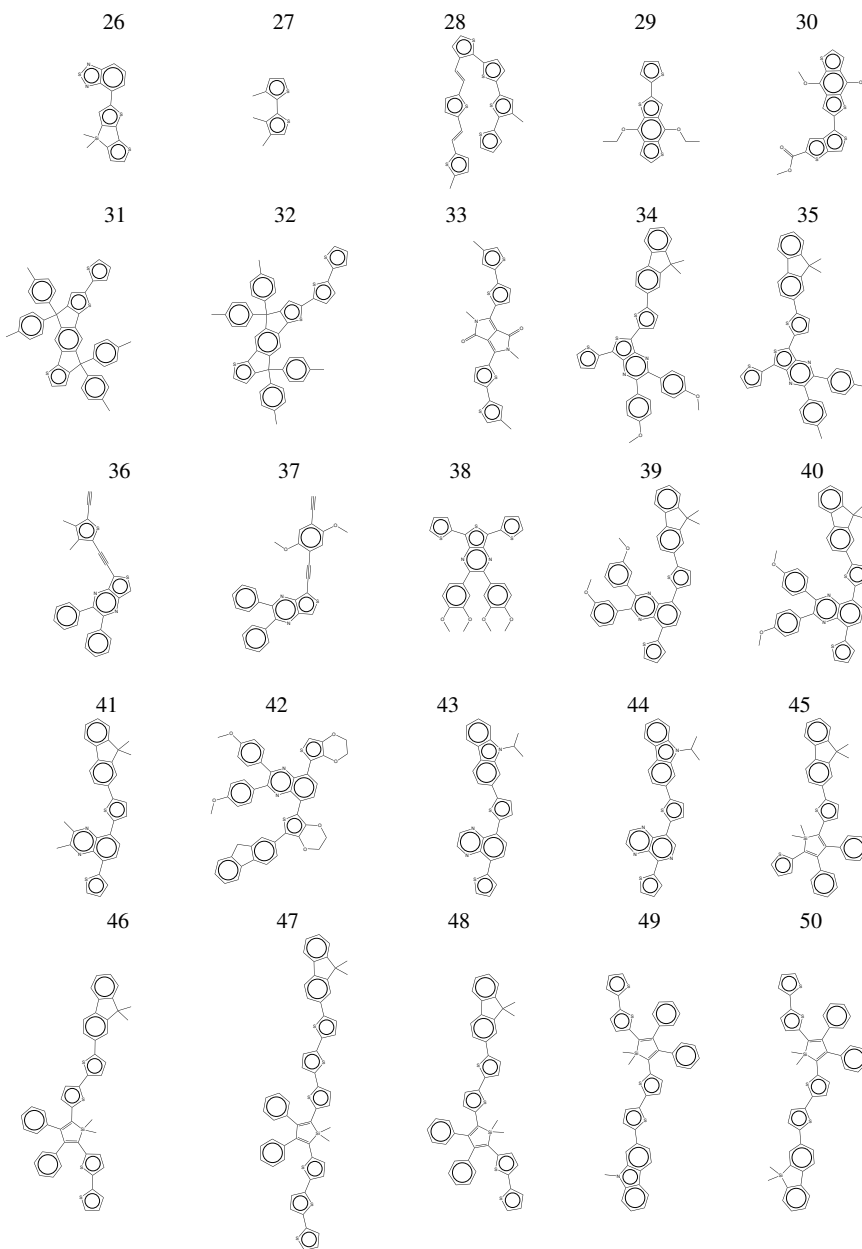


Figure 7.12: Second set of the fifty experimentally characterized molecules (shown here without aliphatic side chains). Once stripped of the aliphatic tails, several molecules are equivalent (6 and 8; 3, 16 and 18; and 48 and 50), but all are retained in the training set.

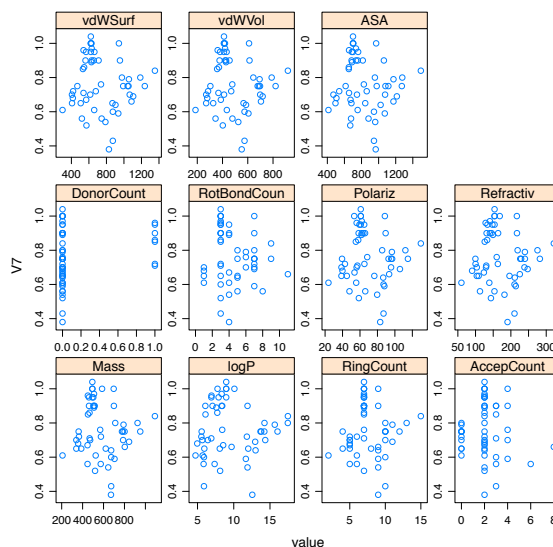


Figure 7.13: Experimental values of V_{oc} versus a set of 33 descriptors obtained from ChemAxon for the set of 50 calibration molecules stripped of their aliphatic tails.

Table 7.10 show results of the fitting of FF. In this case, 20 significant descriptors fit the experimental values with R-squared of 0.6170; not all of them are significant but one has to go to only 12 descriptors to get them all significant and then R-squared drops to 0.4757. This is interpreted as meaning that the fitting for FF is not credible at all, as it may be expected for this morphology based experimental parameter.

Table 7.11 show results of the fitting of the product $V_{oc}J_{sc}$. The fitting is good with R-squared of 0.8809 and all 20 descriptors are significant.

A common test of the calibration of the training set to the descriptors is the leave “1/3 out” technique. The whole set of calibration molecules is randomly divided in three subsets: A (17 molecules in this case), B (17 molecules), and C (16 molecules). For V_{oc} , the set of 20 descriptors previously selected is used to fit separately to the subsets AB (34 molecules), AC (33 molecules) and BC (33 molecules). The coefficients thus obtained are used to predict J_{sc} for the set not used in the fitting (C for AB, for instance). Results are shown in Fig. 7.16. As can be seen, the prediction of excluded molecules is consistent.

We performed the same analysis for J_{sc} —results are shown in Fig. 7.17— and for the product $V_{oc}J_{sc}$ —results shown in Fig. 7.18.

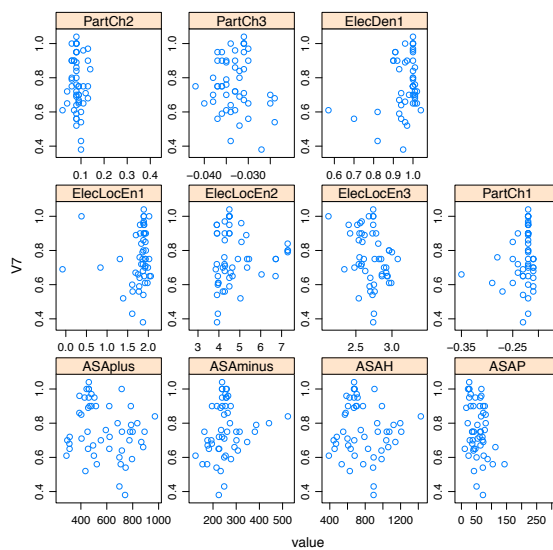


Figure 7.14: Experimental values of V_{oc} versus a set of 33 descriptors obtained from ChemAxon for the set of 50 calibration molecules stripped of their aliphatic tails.

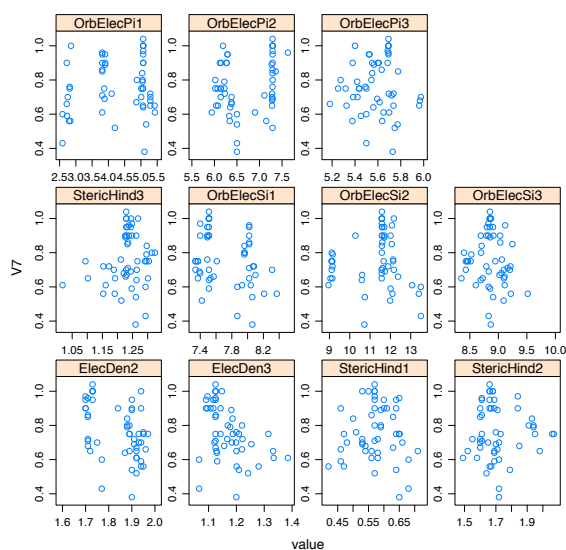


Figure 7.15: Experimental values of V_{oc} versus a set of 33 descriptors obtained from ChemAxon for the set of 50 calibration molecules stripped of their aliphatic tails.

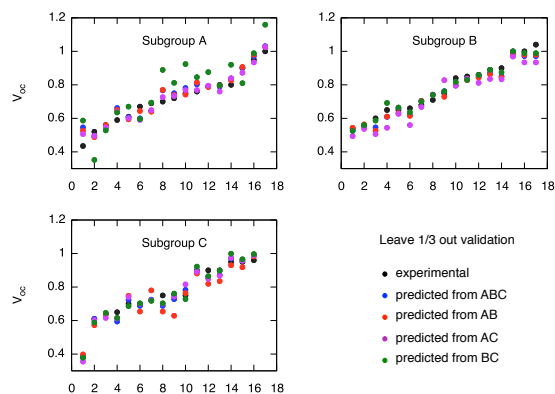


Figure 7.16: Results of the “leave 1/3 out” correlation test for V_{oc} .

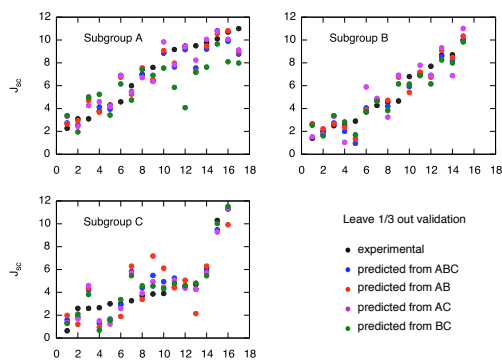


Figure 7.17: Results of the “leave 1/3 out” correlation test for J_{sc} .

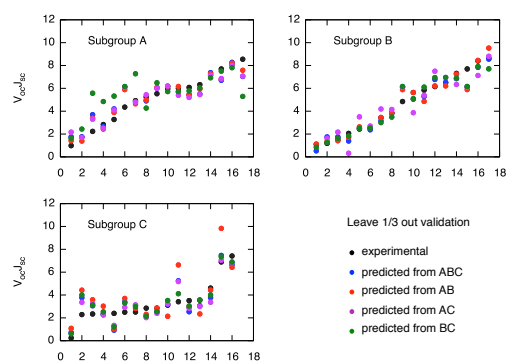


Figure 7.18: Results of the "leave 1/3 out" correlation test for $V_{oc}J_{sc}$.

Descriptor	Description
Molecular mass	Molecular mass
logP	Octanol-water partition coefficient, a measure of hydrophobicity based on group contributions from a set of basic fragments fitted to experimental values [268]
Ring count	Number of rings in the molecule
Hydrogen bond acceptor count	Number of hydrogen bond acceptor atoms
Hydrogen bond donor count	Number of hydrogen bond donor atoms
Rotatable bond count	Excludes bonds connecting hydrogens and terminal atoms
Molecular polarizability	Empirical calculation based on a dipole interaction model from atomic polarizabilities, experimental and <i>ab initio</i> values [546, 349]
Refractivity	Empirical calculation of atomic refractivity; related to London dispersion forces [551]
van der Waals surface area	Molecular surface area as defined by van der Waals radii
van der Waals volume	Molecular surface volume as defined by van der Waals radii
Water accessible area	Water accessible surface area based on atomic properties
Electronic localization energy*	Energy related to removing an atom from conjugation [431, 237]
Partial charge*	Partial atomic charges for π systems and electronegativity-based calculation for the σ network [133]
Electron density*	Based on occupancy of atomic-centered orbitals [431, 237]
Steric hindrance	Steric hindrance of an atom calculated from the covalent radii values
σ orbital electronegativity*	Mulliken atomic orbital electronegativity from σ orbitals [133]
π orbital electronegativity*	Mulliken atomic orbital electronegativity from π orbitals [133]

Table 7.5: Classes of physicochemical and topological descriptors employed in the presented models. We note that these 17 descriptor classes amount to 33 individual descriptors. An asterisk denotes the descriptor is based on semiempirical Hückel model calculations.

-
-
1. Molecular mass
 2. logP partition constant octanol/water
 3. Ring count
 4. Hydrogen bond acceptor atom count in molecule
 5. Hydrogen bond donor atom count in molecule
 6. Rotatable bond count
 7. Molecular polarizability
 8. Refractivity
 9. van der Waals surface area
 10. van der Waals volume
 11. Water accesible area calculation (ASA)
 12. Water accesible area calculation of all atoms with positive partial charge (ASA+)
 13. Water accesible area calculation of all atoms with negative partial charge (ASA-)
 14. Water accesible area calculation of all hydrophobic ($|q_i| < 0.125$) atoms (ASA_H)
 15. Water accesible area calculation of all polar ($|q_i| \geq 0.125$) atoms (ASA_P)
 16. Electrophilic localization energy (lowest)
 17. Electrophilic localization energy (highest)
 18. Electrophilic localization energy (average)
 19. Partial charge calculation (lowest)
 20. Partial charge calculation (highest)
 21. Partial charge calculation (average)
 22. Electron density (lowest)
 23. Electron density (highest)
 24. Electron density (average)
 25. Steric hindrance (lowest)
 26. Steric hindrance (highest)
 27. Steric hindrance (average)
 28. Orbital electronegativity (sigma) (lowest)
 29. Orbital electronegativity (sigma) (highest)
 30. Orbital electronegativity (sigma) (average)
 31. Orbital electronegativity (pi) (lowest)
 32. Orbital electronegativity (pi) (highest)
 33. Orbital electronegativity (pi) (average)
-
-

Table 7.6: The set of descriptors calculated using ChemAxon.

	Estimate	Std. Error	t value	Pr(> t)	
(Intercept)	17.0788482	1.9956354	8.558	1.99e-09	***
logP	-0.1328980	0.0155249	-8.560	1.98e-09	***
RingCount	0.2204759	0.0279730	7.882	1.08e-08	***
AcceptorCount	-0.0996894	0.0139580	-7.142	7.35e-08	***
RotBondCount	0.2374734	0.0240348	9.880	8.67e-11	***
Refractivity	-0.0075611	0.0017250	-4.383	0.00014	***
VdWArea	0.0063744	0.0009059	7.036	9.72e-08	***
VdWVolume	-0.0083368	0.0013763	-6.057	1.36e-06	***
ASA	-0.0037351	0.0010949	-3.411	0.00192	**
ASAH	0.0024702	0.0010328	2.392	0.02347	*
ElecLocEn(lo)	0.0371339	0.0157293	2.361	0.02517	*
PartialCh(lo)	-1.6637886	0.4416521	-3.767	0.00075	***
PartialCh(hi)	-3.3145356	0.5805118	-5.710	3.54e-06	***
PartialCh(avg)	50.3586495	6.6593831	7.562	2.46e-08	***
ElecDen(lo)	-0.8402735	0.2704179	-3.107	0.00420	**
ElecDen(avg)	-2.3826616	0.2394278	-9.951	7.37e-11	***
StericHind(hi)	-0.8950969	0.1545381	-5.792	2.82e-06	***
σ ElecNeg(lo)	0.1993522	0.0588838	3.386	0.00206	**
σ ElecNeg(hi)	0.0448449	0.0190354	2.356	0.02545	*
σ ElecNeg(avg)	-1.4447603	0.2073776	-6.967	1.17e-07	***
π ElecNeg(hi)	0.2316545	0.0345617	6.703	2.36e-07	***

Signif. codes: 0 '***' 0.001 '**' 0.01 '*' 0.05 '.' 0.1 ' ' 1

Residual standard error: 0.04702 on 29 degrees of freedom
(8 observations deleted due to missingness)

Multiple R-squared: 0.9455, Adjusted R-squared: 0.9079
F-statistic: 25.15 on 20 and 29 DF, p-value: 4.09e-13

Table 7.7: Results for the fitting of V_{oc} to 20 descriptors

	Estimate	Std. Error	t value	Pr(> t)	
(Intercept)	241.2144	34.5775	6.976	7.91e-08	***
logP	1.5085	0.4307	3.502	0.001424	**
AcceptorCount	1.6288	0.4314	3.776	0.000678	***
DonorCount	6.0441	1.6055	3.765	0.000700	***
RotBondCount	2.3886	0.3408	7.008	7.24e-08	***
MolPolarizability	-0.3654	0.1033	-3.537	0.001297	**
ASA+	-174.9657	43.9844	-3.978	0.000388	***
ASA-	-174.9481	43.9840	-3.978	0.000389	***
ASAH	174.9342	43.9859	3.977	0.000389	***
ASAP	175.0909	43.9871	3.981	0.000386	***
ElecLocEn(lo)	-24.2310	3.4067	-7.113	5.42e-08	***
ElecLocEn(avg)	15.4843	2.4773	6.250	6.03e-07	***
ElecDen(lo)	-24.1885	6.1314	-3.945	0.000426	***
StericHind(hi)	16.6785	2.8987	5.754	2.48e-06	***
σ ElecNeg(lo)	-6.2720	1.4874	-4.217	0.000199	***
σ ElecNeg(hi)	1.1994	0.5035	2.382	0.023531	*
σ ElecNeg(avg)	-38.4895	5.5345	-6.954	8.40e-08	***
π ElecNeg(hi)	2.5199	0.9816	2.567	0.015305	*
π ElecNeg(avg)	23.4035	3.7781	6.195	7.06e-07	***

Signif. codes: 0 '***' 0.001 '**' 0.01 '*' 0.05 '.' 0.1 ' ' 1

Residual standard error: 1.356 on 31 degrees of freedom
(8 observations deleted due to missingness)

Multiple R-squared: 0.8989, Adjusted R-squared: 0.8402

F-statistic: 15.31 on 18 and 31 DF, p-value: 1.016e-10

Table 7.8: Results for the fitting of J_{sc} to 18 descriptors

	Estimate	Std. Error	t value	Pr(> t)	
(Intercept)	121.834817	22.037026	5.529	3.87e-06	***
RotBondCount	0.839267	0.162001	5.181	1.08e-05	***
Refractivity	-0.043604	0.014191	-3.073	0.004234	**
VdWArea	0.019545	0.006214	3.145	0.003503	**
ASA+	-89.561436	20.122423	-4.451	9.21e-05	***
ASA-	-89.554274	20.122510	-4.450	9.22e-05	***
ASAH	89.537003	20.122831	4.450	9.24e-05	***
ASAP	89.592594	20.123894	4.452	9.18e-05	***
ElecLocEn(hi)	0.570364	0.165122	3.454	0.001535	**
PartCharge(avg)	164.421493	82.195338	2.000	0.053744	.
ElecDen(lo)	-11.329732	2.569477	-4.409	0.000104	***
StericHind(lo)	-7.596139	2.418105	-3.141	0.003539	**
σ ElecNeg(hi)	0.523366	0.216473	2.418	0.021304	*
σ ElecNeg(avg)	-15.565577	1.935828	-8.041	2.81e-09	***
π ElecNeg(hi)	1.782254	0.462344	3.855	0.000507	***
π ElecNeg(avg)	4.212309	1.925005	2.188	0.035839	*

Signif. codes: 0 '***' 0.001 '**' 0.01 '*' 0.05 '.' 0.1 ' ' 1

Residual standard error: 0.6436 on 33 degrees of freedom
(9 observations deleted due to missingness)

Multiple R-squared: 0.8409, Adjusted R-squared: 0.7686

F-statistic: 11.63 on 15 and 33 DF, p-value: 3.784e-09

Table 7.9: Results for the fitting of %PCE to 15 descriptors

	Estimate	Std. Error	t value	Pr(> t)	
(Intercept)	0.179217	0.937496	0.191	0.84978	
MolecMass	0.003691	0.001849	1.997	0.05568	.
RingCount	-0.335110	0.105620	-3.173	0.00365	**
DonorCount	-0.260610	0.097487	-2.673	0.01239	*
RotBondCount	-0.107250	0.038108	-2.814	0.00884	**
MolPolarizability	0.058696	0.018165	3.231	0.00315	**
VdWVolume	-0.005359	0.003037	-1.765	0.08854	.
ASA	7.987770	3.732320	2.140	0.04119	*
ASA+	-7.988750	3.732284	-2.140	0.04117	*
ASA-	-7.988540	3.732144	-2.140	0.04117	*
ASAP	0.001865	0.001394	1.338	0.19150	
ElecLocEn(lo)	0.478993	0.161497	2.966	0.00611	**
ElecLocEn(hi)	0.234037	0.068207	3.431	0.00188	**
ElecLocEn(avg)	-0.582206	0.201671	-2.887	0.00742	**
PartialCharge(lo)	-1.450116	1.032790	-1.404	0.17129	
PartialCharge(avg)	-14.432399	8.624697	-1.673	0.10539	
ElecDen(hi)	-1.170898	0.404904	-2.892	0.00733	**
ElecDen(avg)	1.407407	0.386459	3.642	0.00109	**
σ ElecNeg(hi)	0.077231	0.030475	2.534	0.01715	*
π ElecNeg(lo)	-0.046796	0.041594	-1.125	0.27011	
π ElecNeg(hi)	-0.133699	0.070364	-1.900	0.06776	.

Signif. codes: 0 '***' 0.001 '**' 0.01 '*' 0.05 '.' 0.1 ' ' 1
Residual standard error: 0.07763 on 28 degrees of freedom
(9 observations deleted due to missingness)
Multiple R-squared: 0.6170, Adjusted R-squared: 0.3434
F-statistic: 2.255 on 20 and 28 DF, p-value: 0.02361

Table 7.10: Results for the fitting of FF to 20 descriptors. Note that not all of them are significant.

	Estimate	Std. Error	t value	Pr(> t)	
(Intercept)	171.92666	30.65770	5.608	4.69e-06	***
MolMass	0.03479	0.01458	2.386	0.023758	*
logP	0.96304	0.28544	3.374	0.002120	**
AcceptorCount	1.11779	0.31584	3.539	0.001375	**
DonorCount	3.49484	1.37146	2.548	0.016383	*
RotBondCount	1.94840	0.28063	6.943	1.25e-07	***
Refractivity	-0.16140	0.03961	-4.075	0.000327	***
ASA	134.93698	47.32570	2.851	0.007942	**
ASA+	-134.97116	47.32624	-2.852	0.007929	**
ASA-	-134.95525	47.32343	-2.852	0.007932	**
ASAP	0.07088	0.02203	3.218	0.003167	**
ElecLocEn(lo)	-12.30036	2.60418	-4.723	5.47e-05	***
ElecLocEn(avg)	11.63824	2.18073	5.337	9.95e-06	***
PartCharge(hi)	-46.00685	12.68492	-3.627	0.001090	**
ElecDen(lo)	-20.96171	5.18290	-4.044	0.000355	***
ElecDen(avg)	-9.95094	5.09448	-1.953	0.060495	.
StericHind(hi)	11.98562	2.77777	4.315	0.000169	***
σ ElecNeg(lo)	-5.57994	1.35516	-4.118	0.000290	***
σ ElecNeg(avg)	-23.42843	3.95824	-5.919	1.99e-06	***
π ElecNeg(hi)	3.08369	0.75953	4.060	0.000340	***
π ElecNeg(avg)	13.62962	2.72602	5.000	2.54e-05	***

Signif. codes: 0 '***' 0.001 '**' 0.01 '*' 0.05 '.' 0.1 ' ' 1

Residual standard error: 1.042 on 29 degrees of freedom
(8 observations deleted due to missingness)

Multiple R-squared: 0.8809, Adjusted R-squared: 0.7988

F-statistic: 10.73 on 20 and 29 DF, p-value: 1.427e-08

Table 7.11: Results for the fitting of $V_{oc}J_{sc}$ to 20 descriptors

Part III

Accelerating quantum chemistry algorithms using graphics processing units

Chapter 8

Accelerating resolution-of-the-identity second order Møller-Plesset calculations with graphical processing units

8.1 Introduction

Optimizing computational chemistry codes for central processing units (CPUs) running both in serial and in parallel has been the main focus of software developers in the scientific-computing community, especially for massively parallel high-performance computing systems. However, the increasing demand for sophisticated graphics for video games, computer-aided design (CAD), animation, and other applications is driving the development of more and more powerful graphical processing units (GPUs), which take advantage of data parallelism to render graphics at high speeds. While video cards have been traditionally used only for graphics-intensive applications, they have also been recently leveraged towards scientific-computing problems, such as finite-difference time-domain algorithms [276], sorting algorithms for large databases [186], n-body problems [203], and quantum Monte Carlo methods for chemical applications [19]. In these cases, programmers were required to construct GPU algorithms using a limited set of operations originally intended for computer graphics applications; however, the recent release of graphics card manufacturer NVIDIA's compute unified device architecture (CUDA) development toolkit for some of their high-end graphics cards allows developers to code algorithms in a C-like language [384]. CUDA greatly eases the transition from using CPUs to general-purpose computing on GPUs (GPGPU), as evidenced by the application of CUDA-implemented algorithms to n-body problems in astrophysics [55] and two-electron integrals in electronic structure problems [597]. Additionally, recent abstracts have indicated speedups using CUDA-implemented algorithms for Coulomb integral evaluations [331] and molecular dynamics [501].

Along with CUDA, NVIDIA also released compute unified basic linear algebra subprograms (CUBLAS) as a linear algebra library for cards that support CUDA [382]. In this chapter, we explore using GPGPU computing for electronic structure applications by executing matrix-matrix multiplication operations using CUBLAS. In particular, we focus on reducing computational time of the resolution-of-the-identity second order Møller-Plesset perturbation theory (RI-MP2) [147, 572, 576, 333] as implemented in Q-Chem 3.1 [480, 132]. One of the widely used correlation treatments for electronic structure calculations, MP2 evaluates two-electron repulsion integrals of the form [216]

$$(\mu\nu|\lambda\sigma) = \int \int \phi_\mu(r_1)\phi_\nu(r_1)r_{12}^{-1}\phi_\lambda(r_2)\phi_\sigma(r_2)dr_1dr_2, \quad (8.1)$$

where μ, ν, λ and σ are orbital basis function(ϕ) indices. The calculation of the energy (E) is dependent on

$$E^{(2)} = \sum_{ijab} \frac{(ia|jb)^2 + \frac{1}{2}[(ia|jb) - (ib|ja)]^2}{\epsilon_i + \epsilon_j - \epsilon_a - \epsilon_b},$$

$$(ia|jb) = \sum_{\mu\nu\lambda\sigma} C_{\mu i}C_{\nu a}C_{\lambda b}C_{\sigma b}(\mu\nu|\lambda\sigma),$$

where i, j (a, b) are occupied (virtual) molecular orbitals which are Fock operator eigenfunctions with eigenvalues ϵ_i, ϵ_j (ϵ_a, ϵ_b), and C is the molecular orbital coefficient matrix.

In RI-MP2, the evaluation time is reduced compared to traditional MP2 calculations [147, 572]. This technique involves approximating the costly four-center two-electron integrals, Eq. 8.1, with the use of two-center and three-center integrals. To evaluate the integral, products of orbital basis functions are represented as a linear combination of atom-centered auxiliary basis functions P

$$\rho_{\mu\nu}(r) = \mu(r)\nu(r) \approx \tilde{\rho}_{\mu\nu}(r) = \sum C_{\mu\nu,P}P(r).$$

By minimizing the Coulomb self-interaction of the residual density, the four-center integrals are approximated as

$$(\mu\nu|\lambda\sigma) = \sum_{P,Q} (\mu\nu|P)(P|Q)^{-1}(Q|\lambda\sigma).$$

This step is an approximate insertion of the resolution-of-the-identity,

$$I = \sum_m |m\rangle\langle m| \approx \sum_{P,Q} |P\rangle\langle P|Q\rangle\langle Q|$$

RI-MP2 is known to produce equilibrium geometries that rival density functional theory (DFT) except for transition metal compounds [155]. On the other hand, RI-MP2 is also known to capture long-range correlation effects, which are missing in many popular density functionals. So for many weakly-bound systems, where DFT results might become questionable, RI-MP2 stands as essentially the least expensive alternative [132, 573].

In Section 2, we present an overview of GPGPU computing and Section 3 contains general results of matrix-matrix multiplication times for both CPU and GPU implementations. In Section 4, we describe performance improvements achieved through the use of a GPU in RI-MP2 calculations of a series of alkanes, showing the effect of changing the number of electrons and the quality of the basis set used in the computation. Finally, in Section 5, we conclude with our resulting RI-MP2 speedup and the potential impact that GPGPU computing can have on electronic structure calculations.

8.2 General-purpose computing on graphical processing units

Graphical processors are able to outperform CPUs for certain applications because of intrinsic parallelization within the device. Multi-core and parallel CPU architectures, while able to run many instructions simultaneously, require computational threads to be explicitly coded to make optimal use of the available resources. Whereas a single-core CPU can only execute a single instruction at a time (although several instructions may be in the pipeline), a GPU can execute a single instruction on many pieces of data at the same time, using a single instruction, multiple data (SIMD) paradigm. This inherent parallelization is a result of hardware architecture; graphics cards are composed of an array of multiprocessors, each of which has its own section of pipeline bandwidth. The graphics card used in this study has 16 multiprocessors, with each multiprocessor containing eight processors and able to handle up to 768 threads concurrently [384]. At any given clock cycle, each multiprocessor executes the same thread on all eight processors, although each processor operates on different data. The threads are periodically switched to minimize the chance that a thread is waiting for the appropriate data to be available. For problems that exhibit high levels of data parallelism, GPUs can provide considerable computational speedup since this hardware design allows multiple computational threads to execute quickly on a block of data that is reused. This approach is ideal for rendering graphical data, but some scientific-computing applications can also be adapted for use on these powerful video cards.

Until recently, a major hurdle in developing general-purpose applications for GPUs was the difficulty of programming for them. The only access to the device was either through graphics packages like OpenGL or by using a special assembly language made for the card. Graphics packages provide the wrong abstraction for non-graphical applications, making programs written with them difficult to understand, maintain and use. Writing assembly code directly for the device is a less than ideal solution because of limits on the number of instructions the card is able to process at a given time and the expertise required to write code for a particular GPU. However, due to the computational potential of GPUs for general computation, programmers were interested in implementing linear algebra routines

on GPUs, even before the release of the CUDA toolkit [281, 145]. Operations such as vector products and matrix-matrix multiplication are easily parallelizable, have high levels of data reuse, and are important building blocks for other applications. With the release of the CUBLAS library, migrating code written in C and Fortran to GPUs is now considerably easier.

Despite decades of sustained progress in state-of-the-art of quantum chemistry methodology, speeding up calculations and thereby increasing the size of tractable molecules is an ongoing activity. The use of GPUs provides an important opportunity to gain further speedups when linear algebra operations are heavily used, as in RI-MP2. For this study, we focus on the effect of carrying out matrix-matrix multiplication using a GPU since this operation is one of the more time-consuming routines for CPUs to perform. The best known matrix-matrix multiplication algorithm scales as $O(n^{2.3})$ in computational time with matrix edge length [114]. The CUBLAS matrix-matrix multiplication function scales as $O(n^3)$ [382], nevertheless the scaling prefactor is found to be considerably smaller than for comparable CPU algorithms, as discussed in Section 3.

8.3 Computational setup and matrix multiplication comparison

The hardware setup consists of a single NVIDIA Quadro FX 5600 GPU, an AMD Dual Core Opteron 170 processor, a LanParty NForce 4 motherboard, and two gigabytes of RAM. The operating system used is Ubuntu 7.04 with a Linux 2.6 kernel and the Intel Fortran Compiler v10.0. In order to characterize CUBLAS function performance, we obtained benchmarks of the speed of matrix-matrix multiplication using both the host CPU (regular BLAS function) and the GPU (CUBLAS function). Fig. 8.1a shows the average ($N=20$) computational times to multiply a pair of square matrices with 300 to 4000 elements on a side. To multiply a pair of 300 by 300 matrices, both the CPU and the GPU took only a hundredth of a second. As the size of the matrices increases, the benefit of the GPU becomes apparent. Large matrices can be multiplied about thirteen times faster on the GPU than on the host CPU, a significant gain for a moderate programming effort. We separately analyzed the times of preprocessing, actual matrix multiplication and postprocessing for the CPU and the GPU. The preprocessing and postprocessing times are due mostly to data transfer between the motherboard and the GPU memory. The scaling with matrix size is the same for a given stage in both units, but the prefactor is reduced twenty-fold for the GPU in the case of the multiplication step. This reduction in evaluation time overwhelms the modest increase in pre- and post-processing time for the GPU and the advantage of using the GPU for this function increases for larger matrices.

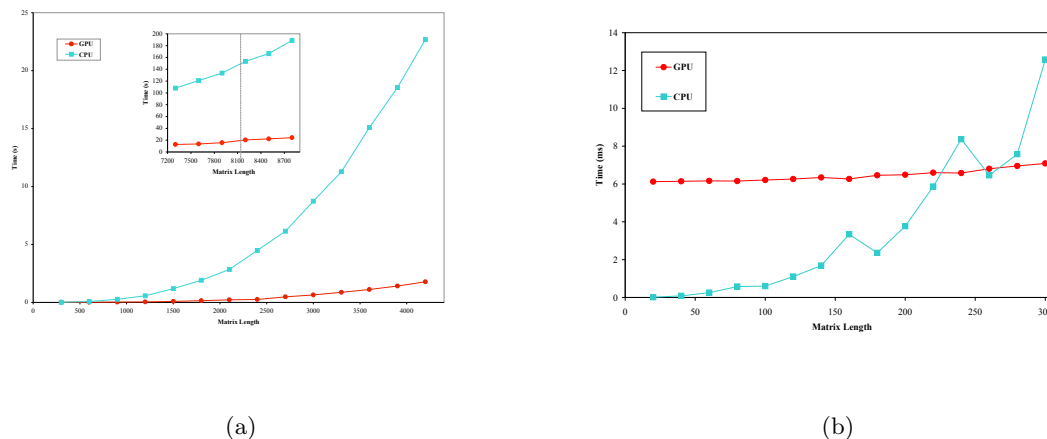


Figure 8.1: Average processing times for the multiplication of large matrices using a CPU and a GPU (as a coprocessor). Pairs of square matrices are multiplied on an AMD dual-core CPU and on an NVIDIA Quadro FX 5600 GPU. (a) For matrices as small as 750 elements per side, the GPU outperforms the CPU. For matrices with an area of a few million elements, a 13x speedup is obtained using the GPU. *Inset:* Matrices larger than 2^{13} elements on a side cannot be directly multiplied in the GPU due to memory limitations, but splitting the matrices into smaller pieces before GPU multiplication shows no appreciable difference in total time. (b) For small matrices, the data transfer overhead of the slow PCI bus makes the GPU slower than the CPU implementation.

A challenge to effectively using GPUs for linear algebra occurs when matrices become very large though. The GPU on-board memory is a finite resource which can restrict the number of matrix elements that can be passed to the card. While the Quadro FX 5600 has 1.5 gigabytes of on-board RAM, the memory required to multiply very large matrices can exceed this limit, causing the device to crash. When we attempted to multiply matrices larger than 8192 elements on a side, the memory on the device was exhausted and the CUBLAS library process stopped. To get around this memory limitation, the large matrices can be split into pieces before being sent to the GPU, multiplied there, and then put back together using the CPU. The inset of Fig. 8.1a shows the result of using this method on a hardware system consisting of a single NVIDIA Quadro FX 5600 GPU, an AMD Dual Core Athlon X2 processor, an Asus M2N32-SLI Deluxe motherboard, and four gigabytes of RAM. Data points for matrices smaller than 8192 elements on a side are multiplied using the standard library call while points for larger matrices use the method described. While a little performance is lost transferring data in the bus, multiplying these very large matrices in multiple passes on the GPU is still significantly faster than using just the CPU.

In electronic structure applications, however, many of the matrices that need to be

multiplied are much smaller than a thousand elements on a side. Fig. 8.1b shows average ($N=20$) computational times for multiplying a pair of square matrices that have only 20 to 300 elements on a side. The major bottleneck for using the GPU is revealed by this figure – the PCI bus latency. Data communication between the GPU and the CPU is conducted via a NVIDIA CK804 PCI x16 Bridge (Clock 66 MHz, Width 32 bits), which is considerably slower than typical memory access for a CPU. The time it takes to transfer data over the bus is long enough to make using a GPU for matrix multiplication on matrices smaller than two hundred elements on a side inefficient. Our approach, therefore, is to set a lower bound on when to use the graphics card processors, similar to Yasuda’s use of a threshold parameter to control integral evaluations [597]. If a resultant matrix has an area smaller than the square of a cutoff threshold, it is multiplied using the CPU and all matrices larger than the cutoff are multiplied using the GPU. Since electronic structure calculations use rectangular matrices, the optimal cutoff threshold is not obvious, as discussed in the next section.

8.4 Speedups of RI-MP2 calculations on a series of alkanes

Within Q-Chem 3.1, the RI-MP2 correlation energy is evaluated in the five steps. The steps are listed below with the following abbreviations: atomic basis functions, auxiliary basis functions, occupied and virtual orbitals have the same notation as in Section 1, N (M) is the number of atomic (auxiliary) basis functions, O (V) is the number of occupied (virtual) orbitals, and α, β, γ and η are prefactors for the estimated computational cost.

Step 1: Evaluate $(P|Q)$, which are a two-electron repulsion integrals between two auxiliary basis functions and form the square root of its inverse matrix, $(P|Q)^{-\frac{1}{2}}$. The estimated computational cost of this step is $\alpha M^2 + \beta M^3$.

Step 2: Evaluate $(\mu\nu|P)$, which are two-electron repulsion integrals between a pair of normal atomic basis functions, then transform the 3-center integrals into $(ia|P)$. The estimated computational cost of this step is $\gamma N^2 M + 2N^2 MO + 2NMOV$.

Step 3: Form $B_{ia,Q}$ via

$$B_{ia,Q} = \sum_P^{AUX} (ia|P)(P|Q)^{-\frac{1}{2}}.$$

The estimated computational cost of this step is $2M^2OV$.

Step 4: Form $(ia|jb)$ via

$$(ia|jb) \approx \sum_Q^{AUX} B_{ia,Q} B_{jb,Q}.$$

The estimated computational cost of this step is MO^2V^2 .

Step 5: Evaluate RI-MP2 energy using

$$E_{RI-MP2} = \sum_{ijab} \frac{|(ia|jb) - (ib|ja)|^2}{E_i + E_j - E_a - E_b}.$$

The estimated computational cost of this step is ηO^2V^2 .

We observe that steps 1 and 5 contribute little to the total CPU time, whereas step 2 and 3, which both scale as $O(n^4)$ with the system size, have comparable costs. Step 4, which scales as $O(n^5)$, dominates the RI-MP2 energy evaluation, and becomes our primary concern in this study. In the original code for step 4 within Q-Chem 3.1, there is a loop over (i, j) pairs, and within the loop, a matrix of size MV is multiplied to the transpose of a matrix of the same size. In this chapter, we introduce a new parameter, S , which groups S occupied orbitals together during the computation and, within each loop, results in the total matrix size of $M(SV)$. Based on speedups obtained for n-octane (which uses the smallest matrices of the series), S is set to five for all n-alkane calculations. This simple code modification stacks matrices that would otherwise be smaller than the cutoff threshold together, allowing the GPU to be used more effectively.

Fig. 8.2 shows the speedup in RI-MP2 calculations obtained simply by modifying the code as described above and using the GPU as a coprocessor to execute the matrix-matrix multiplication in step 4. Results are shown for n-octane (Fig. 8.2a) and for n-tetradecane (Fig. 8.2b), both treated with a cc-pVDZ basis set [139]. Total computational time is plotted against the threshold used to send matrices to the GPU with CPU time for each calculation shown as a reference. As seen in Fig. 8.2a, the value of the threshold must be set smaller than the maximum matrix size to ensure that matrices are sent to the GPU (around 850 for n-octane with the cc-pVDZ basis and $S = 5$). For larger systems, such as n-tetradecane (Fig. 8.2b), the maximum matrix size is greater than 1000, so a speedup is obtained for all threshold values. For the n-alkane series comparison, a threshold of 350 is used. However, it should be noted that the value of S and the cutoff threshold can be optimized to minimize the impact of bus latency discussed in Section 3. While systems as large as $C_{22}H_{46}$ with the cc-pVDZ basis set did not reach the limit of the graphics card memory, calculations as small as $C_{14}H_{34}$ with the cc-pVTZ basis set [139] cause the device to crash. Code modifications are currently underway to incorporate the method described in Section 3 into Q-Chem 3.1 to treat larger systems with more accurate basis sets.

A price to pay for the speedup achieved by using the GPU is some loss of precision (see Fig. 8.3). Current GPUs only support 32-bit single precision floating point numbers instead of the 64-bit double precision numbers used by modern CPUs; however, this is most

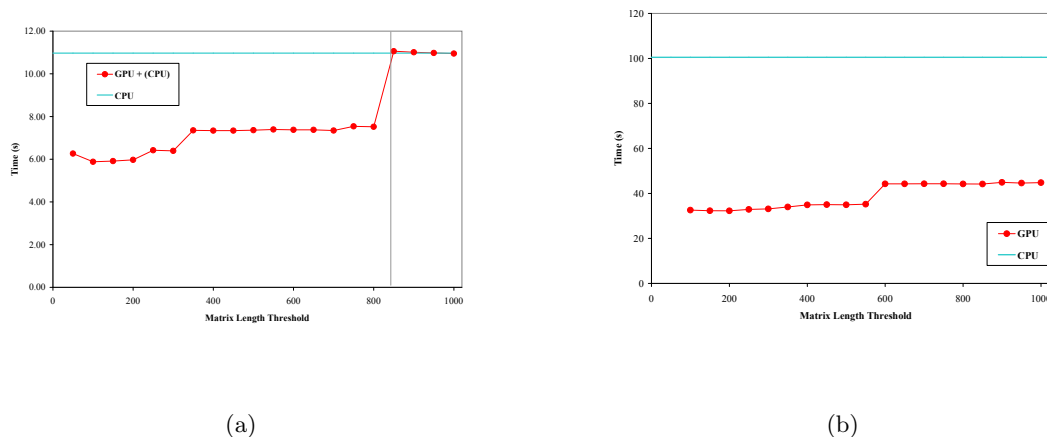


Figure 8.2: Total RI-MP2 calculation time for n-octane and n-tetradecane using a CPU and a GPU (as a coprocessor). If a matrix edge is smaller than the threshold, it is multiplied in the CPU, otherwise it is multiplied in the GPU. For both cases the matrix grouping factor S is set to five. (a) For n-octane, larger thresholds revert back to CPU timings because there are no matrices with edges larger than 850 (vertical line) when using the cc-pVDZ basis set. (b) n-tetradecane calculations are 70% faster than the CPU in the 150-500 range of thresholds.

likely a temporary setback because manufacturers have promised double precision support in future generations of GPUs. The precision degradation due to single precision is not of great concern with our RI-MP2 calculations as long as an appropriate cutoff threshold is used. In general, the energies obtained using single precision on the graphics card were only slightly different from the ones found using double precision on the CPU. As seen in Fig. 8.3, the difference of the RI-MP2 correlation energy using the GPU from that found using double precision using the CPU is on the order of 10^{-4} Hartrees for both n-octane and n-decane. Fig. 8.4 shows the total and RI-MP2 correlation energy for a series of conformers of n-octane as the torsional angle of the central bond is rotated. The average error introduced in the RI-MP2 correlation energy is only -0.08 mHartrees (Fig. 8.4b), preserving the trend of the CPU calculation.

The general picture of the speedups obtained by combining the use of the GPU and the CPU can be seen in Fig. 8.5, where we report calculations of single point energies with the RI-MP2 method for a series of linear alkanes using the cc-pVDZ basis set. Energies for alkanes with an even number of carbon atoms from octane (C_8H_{18}) to docosane ($C_{22}H_{46}$) are calculated. Speedups of 1.5x (35%) to 4.3x (77%), with an average of 2.7x (63%), are achieved throughout the series. This is a significant increase of efficiency in molecular calculations with no considerable expense of precision. Even with GPUs that only work with

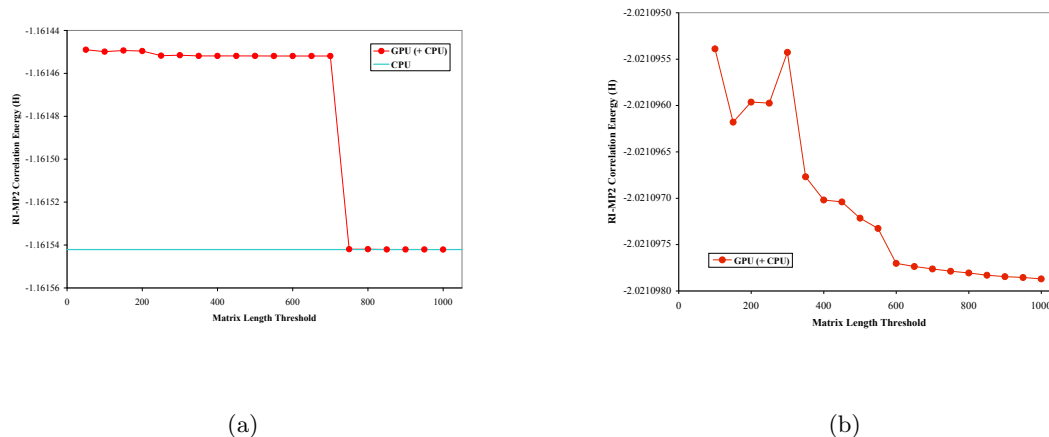


Figure 8.3: RI-MP2 correlation energy obtained for n-octane and n-tetradecane using the cc-pVDZ basis set on a CPU and a GPU (as a coprocessor). (a) For n-octane, the GPU-implemented algorithm returns an energy only 0.11 mHartrees off of the value obtained using the CPU alone. (b) For n-tetradecane, the CPU-calculated energy is -2.02124 Hartrees (not shown).

single precision arithmetic, the average error in RI-MP2 correlation energy is 0.3 mHartrees (RMSD: 0.5 mHartrees, MAD: 0.3 mHartrees). This is only 6×10^{-5} % of the average total energy.

To show the effect of using the GPU for matrix-matrix multiplication in RI-MP2 calculations, Fig. 8.6 plots the computational time required by each RI-MP2 step for the series of alkanes. For $C_{22}H_{46}$, a system with 178 electrons, the time required to evaluate step 4 of the RI-MP2 calculation on the CPU is 78% of the total (Fig. 8.6a). By using the GPU (Fig. 8.6b), the time spent on this step is reduced to 50% of the total RI-MP2 time. The next largest contribution to the calculation becomes step 2, which increases from 10% to 35% of the RI-MP2 time when using the GPU for docosane. This step involves the evaluation of three-center integrals and subsequent two-index transformations. For the evaluation of three-center integrals, in the future we can potentially adapt the approach developed by Yasuda for the evaluation of two-center integrals to approximate Coulomb integrals. We expect that by combining the two approaches, a total speedup of 6.6x can be obtained for RI-MP2 treatment of electron correlation with only a moderate programming effort.

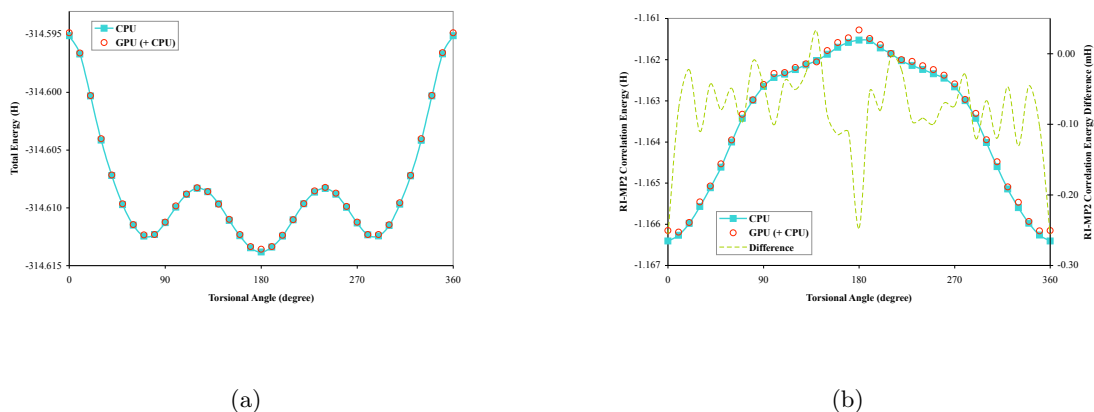


Figure 8.4: Total and RI-MP2 correlation energy obtained for n-octane conformers using the cc-pVDZ basis set on a CPU and a GPU (as a coprocessor) over a range of central bond torsional angles. (a) Total energy from single point calculations for the series of conformers. (b) RI-MP2 correlation energy for the series of conformers shows that the average random error introduced by the GPU calculations is -0.08 mHartrees (RMSD: 0.1 mHartrees, MAD: 0.05 mHartrees).

8.5 Conclusions

In this chapter, we demonstrated that simply rerouting one linear algebra routine in the evaluation of RI-MP2 correlation from a CPU to a GPU achieved a speedup of 4.3x for the calculation of the single point energy of doecicosane. To the best of our knowledge, this is the first implementation of a CUBLAS library function in electronic structure codes. The C-like language of CUDA allows easy migration of code segments to implementations using a GPU. The resulting price/performance is very competitive; the parallelization offered by graphical processors will allow scientific calculations that are usually run on clusters and special-purpose supercomputers to be evaluated at a fraction of the cost. Efforts to reduce computational time even more by implementing the two-electron repulsion integrals, as well as other linear-algebra operations in the code (matrix-vector multiplication and diagonalization routines), are underway. The recent availability of the CUBLAS library is an encouraging development for electronic structure developers. The level of abstraction allowed us to encapsulate the linear algebra calls of Q-Chem in such a way that all matrix-matrix multiplies are carried out with CUBLAS with minimal code modification. This encapsulation strategy allows for faster adoption of other novel technologies such as other types of linear algebra co-processing units as they become available. The challenge left for the electronic structure community is to restructure and adapt the current algorithms to

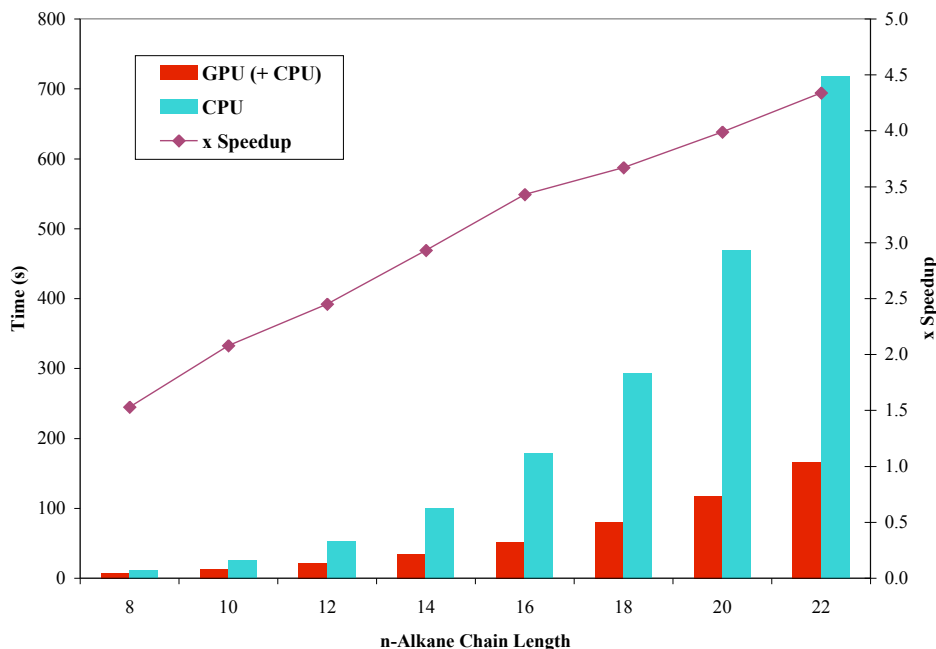


Figure 8.5: Total processing times for the calculation of RI-MP2 single point energies for a series of linear alkanes using the cc-pVDZ basis set on a CPU and a GPU (as a coprocessor). The series of linear alkanes with even numbers of carbon atoms from octane (C_8H_{18}) to doicosane ($C_{22}H_{46}$) is investigated. Speedups of 1.5x to 4.3x (average 2.7x) are achieved throughout the series with an average RI-MP2 correlation energy error of 0.3 mHartree.

environments where the linear algebra operations can be carried out expeditiously aided by GPUs or other similar devices such as field-programmable gate arrays (FPGAs).

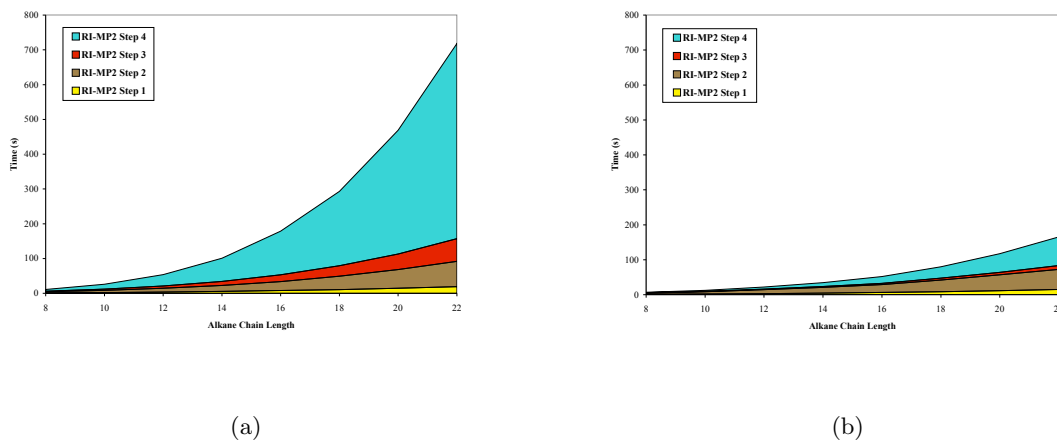


Figure 8.6: Computational time for the each step of the RI-MP2 calculation is plotted for a series of linear alkanes. The time required for step 5 is less than 1 s which is smaller than the visible scale of the graphs. (a) The breakdown of processing times for each step on the CPU shows that the matrix-matrix multiplication is 78% of the total calculation time. (b) Using the GPU as a coprocessor, the cost of step 4 is reduced to only 50% of the total computational time.

Chapter 9

Accelerating correlated quantum chemistry calculations using graphical processing units and a mixed-precision matrix multiplication library

9.1 Introduction

Ever since scientists began to solve the equations of molecular quantum mechanics using numerical methods and computational tools, the interplay between fundamental theory and application has been inextricably linked to exponential advances in hardware technology. Indeed, many influential contributions to quantum chemistry have been motivated by insights into how best to utilize the available computational resources within the same theoretical model. One example is Almlöf's appreciation of the discrepancy that had appeared between data storage capacity and raw processor speed [14]. His subsequent introduction of the Direct SCF technique transformed calculations from being memory (or disk) bound into being processor bound; previously impossible applications could be attempted by using additional processor time.

We are now witnessing yet another era in the optimization of quantum chemistry codes, following an explosion of interest in the application of coprocessors such as graphics processing units (GPUs) to general scientific computing [385]. This interest in GPUs and related massively-parallel processors is largely driven by their tremendous cost to performance ratio (in operation counts per second per unit of currency) which arises from the economies of scale in their manufacture and their great demand in numerous multimedia applications. Another key factor in their widespread uptake for scientific use is the recent release of NVIDIA's compute unified device architecture (CUDA) programming interface that allows development of algorithms for the GPU using a relatively simple extension of the standard C language [385].

A GPU is an example of a stream-processing architecture [251] and can outperform

a general-purpose central processing unit (CPU) for certain tasks because of the intrinsic parallelization within the device which uses the single instruction, multiple data (SIMD) paradigm. Typical GPUs contain multiple arithmetic units (streaming processors) which are typically arranged in groups of eight to form multiprocessors that share fast access memory and an instruction unit; all eight processors execute the same instruction thread simultaneously on different data streams. In contrast, in multiple-core or parallel CPU architectures, each thread must have an instruction explicitly coded for each piece of data. One of the most recent GPU cards, the Tesla C1060 from NVIDIA, contains 240 streaming processors, can provide up to 933 GFLOPS of single-precision computational performance, and has a cost which is approximately one order of magnitude less than an equivalent CPU cluster.

GPUs are therefore well-suited to high-performance applications with dense levels of data parallelism where very high accuracy is not required. (Although double-precision cards are available, in the case of NVIDIA GPUs, they have a peak FLOP count approximately 10 times less than single precision cards.) The challenge for scientists wanting to exploit the efficiency of the GPU is to expose the SIMD parallelism in their problem and to efficiently implement it on the new architecture. A key component of this task is a careful consideration of the memory hierarchy to efficiently hide memory access latency.

Already, GPUs have been recruited extensively by the scientific community to treat a wide range of problems, including finite-difference time-domain algorithms [276], and n -body problems in astrophysics [203]. For computational chemistry, GPUs are emerging as an extremely promising architecture for molecular dynamics simulations [501, 21], quantum Monte Carlo [19], density-functional theory and self-consistent field calculations [597, 596, 539, 538, 540, 541] and correlated quantum chemistry [552] methods. Efficiency gains of between one and three orders of magnitude using NVIDIA graphics cards have been reported compared to conventional implementations on a CPU. In this way, new domains of scientific application have become amenable to calculation where, previously, extremely expensive and rare supercomputing facilities would have been required.

As an example of the more general impact of accelerator technologies, Brown *et. al.* [84] have accelerated density-functional theory up to an order of magnitude using a Clearspeed coprocessor. The Clearspeed hardware is a proprietary compute-oriented stream architecture promising raw performance comparable to that of modern GPUs, while offering double-precision support and an extremely low power consumption. The challenges of efficiently utilizing the Clearspeed boards are similar to those of using GPUs, requiring a fine-grained parallel programming model with a large number of lightweight threads. Thus, the algorithmic changes suggested for their work and ours have a common value independently of the precise hardware used, which will of course change with time.

In the current chapter, we introduce two new techniques with general utility for the adoption of GPUs in quantum chemistry. Firstly, we propose a general approach for the efficient GPU acceleration of matrix-matrix multiplications where the matrix size is too large for the whole computation to be held in the GPU’s onboard memory, requiring the division of the original matrices into smaller pieces. This is a major issue in quantum chemical calculations where matrix sizes can be very large.

Secondly, we describe how to improve the accuracy of general matrix-matrix multiplications when using single-precision GPUs, where the 6-7 significant figures are often insufficient to achieve ‘chemical accuracy’ of 1 kcal/mol. To solve this problem, we have implemented a new algorithm within a heterogeneous computing model whereby numerically large contributions to the final result are computed and accumulated on a double-precision device (typically the CPU) and the remaining small contributions are efficiently treated by the single-precision GPU device.

We have applied these ideas in an extension of our previously published GPU-enabled implementation of resolution-of-the-identity second-order Møller-Plesset perturbation theory (RI-MP2) [147, 572, 576, 333]. Thus the paper begins in Section 9.2 with an overview of the RI-MP2 method and our previous GPU implementation. In Sections 9.3 and 9.4, we discuss our new matrix-multiplication library and its performance. In Section 9.5, we examine the accuracy and speedups achieved when applying the technology to RI-MP2 calculations on molecules with up to 168 atoms, and we end the paper with some brief conclusions.

9.2 GPU acceleration of RI-MP2

One of the most widely-used and computationally least expensive correlated treatments for electronic structure is second-order Møller-Plesset perturbation theory (MP2). MP2 is known to produce equilibrium geometries of comparable accuracy to density functional theory (DFT) [155], but unlike many popular DFT functionals is able to capture long-range correlation effects such as the dispersion interaction. For many weakly bound systems where DFT results are often questionable, MP2 is essentially the least expensive and most reliable alternative [573]. The expression for computing the MP2 correlation energy takes the form

$$E^{(2)} = \sum_{ijab} \frac{(ia|jb)^2 + \frac{1}{2} [(ia|jb) - (ib|ja)]^2}{\epsilon_i + \epsilon_j - \epsilon_a - \epsilon_b} \quad (9.1)$$

in terms of the $\{i, j\}$ occupied and $\{a, b\}$ virtual molecular orbitals (MOs) that are eigenfunctions of the Fock operator with eigenvalues $\{\epsilon\}$. The MO integrals

$$(ij|ab) = \sum_{\mu\nu\lambda\sigma} C_{\mu i} C_{\nu j} C_{\lambda a} C_{\sigma b} (\mu\nu|\lambda\sigma) \quad (9.2)$$

are obtained by contracting two-electron integrals over the (real) atomic orbital (AO) basis functions

$$(\mu\nu|\lambda\sigma) = \int \int \phi_\mu(\mathbf{r}_1)\phi_\nu(\mathbf{r}_1)\mathbf{r}_{12}^{-1}\phi_\lambda(\mathbf{r}_2)\phi_\sigma(\mathbf{r}_2)d\mathbf{r}_1d\mathbf{r}_2 \quad (9.3)$$

where \mathbf{C} is the matrix of MO coefficients describing the expansion of each MO as a linear combination of AOs. One way to considerably reduce the computational cost associated with traditional MP2 calculations (which formally scales as $O(N^5)$ with the number of basis functions) is to exploit the linear-dependence inherent in the product space of atomic orbitals. This allows one to expand products of AOs as linear combinations of atom-centered auxiliary basis functions, P ,

$$\rho_{\mu\nu}(\mathbf{r}) = \mu(\mathbf{r})\nu(\mathbf{r}) \approx \tilde{\rho}(\mathbf{r}) = \sum C_{\mu\nu,P}P(\mathbf{r}) \quad (9.4)$$

and to therefore approximate all costly four-center two-electrons in terms of only two- and three-center integrals,

$$(\widetilde{\mu\nu|\lambda\sigma}) = \sum_{P,Q} (\mu\nu|P)(P|Q)^{-1}(Q|\lambda\sigma) \quad (9.5)$$

where we have assumed that the expansion coefficients are determined by minimizing the Coulomb self-repulsion of the residual density. The result is equivalent to an approximate insertion of the resolution-of-the-identity (RI).

All our work is implemented in a development version of Q-Chem 3.1 [480], where the RI-MP2 correlation energy is evaluated in five steps, as described elsewhere [552]. Previously we showed that step 4, the formation of the approximate MO integrals, was by far the most expensive operation for medium to large-sized systems, and requires the matrix multiplication

$$(\widetilde{ia|jb}) \approx \sum_Q B_{ia,Q}B_{jb,Q} \quad (9.6)$$

where

$$B_{ia,Q} = \sum_P (ia|P)(P|Q)^{-1/2} \quad (9.7)$$

The evaluation of Eq. 9.6 is typically an order of magnitude more expensive than Eq. 9.7. We shall concentrate on these two matrix multiplications in this chapter. Consistent with our previous paper [552], we will repeatedly refer to these evaluations as step 3 (Eq. 9.7) and step 4 (Eq. 9.6) as we investigate the accuracy and efficiency of our new GPU implementation.

Included in the CUDA software development toolkit is an implementation of the BLAS linear algebra library, named CUBLAS [383]. As previously reported [552], we accelerated the matrix multiplication in Eq. 9.6 by simply replacing the BLAS `*GEMM` routines with corresponding calls to CUBLAS `SGEMM`. This initial effort achieved an overall speedup of 4.3x for the calculation of the correlation energy of the 68-atom doicosane ($C_{22}H_{46}$) molecule with a cc-pVDZ basis set using a single GPU. At this early stage in development, we used the GPU purely as an accelerator for `*GEMM` and made no effort to keep data resident on the device.

In the present chapter, we further explore the acceleration of our RI-MP2 code through the application of CUBLAS combined with two new techniques. These enable us to perform more accurate calculations on larger molecules and basis sets involving larger matrices while also mitigating the errors associated with single-precision GPUs. We discuss both techniques in the following section.

9.3 GPU acceleration of GEMM

In large-scale quantum chemistry calculations, the size of the fundamental matrices typically grows as the square of the number of atomic basis functions (even if the number of non-negligible elements is much smaller). Moreover, intermediate matrices are sometimes even larger, such as the \mathbf{B} matrices of Eq. 9.7.

A GPU can only accelerate a calculation that fits into its onboard memory. While the most modern cards designed for research can have up to 4 GiB of RAM, consumer level cards may have as little as 256 MiB (with some portion possibly devoted to the display). If we wish to run large calculations, but only have a small GPU available, then some means of dividing the calculation up and staging it through the GPU must be found.

Next, we consider the question of accuracy arising from the use of single-precision GPU cards. It turns out [540], that many operations do not require full double precision support to achieve acceptable accuracy for chemistry, but, nevertheless, single precision is not always sufficient. Double-precision (DP) capable GPUs have only become available within the past year, and so are not yet widespread. Moreover, we cannot rely on the support of DP cards by manufacturers in the future since the commercial driving force behind such processors is the wealth of multimedia applications that do not require high precision. We address this problem with the introduction of a new way to balance the desire for GPU acceleration with a need for high accuracy.

9.3.1 Cleaving GEMMs

Consider the matrix multiplication

$$C = A \cdot B \quad (9.8)$$

where A is an $(m \times k)$ matrix and B is an $(k \times n)$ matrix, making C an $(m \times n)$ matrix. We can divide A into a column vector of $r + 1$ matrices

$$A = \begin{pmatrix} A_0 \\ A_1 \\ \vdots \\ A_r \end{pmatrix} \quad (9.9)$$

where each entry A_i is a $(p_i \times k)$ matrix, and $\sum_{i=0}^r p_i = m$. In practice, all the p_i will be the same, with the possible exception of p_r , which will be an edge case. In a similar manner, we can divide B into a row vector of $s + 1$ matrices

$$B = \left(B_0 \quad B_1 \quad \cdots \quad B_s \right) \quad (9.10)$$

where each B_j is an $(k \times q_j)$ matrix and $\sum_{j=0}^s q_j = n$. Again all the q_j will be the same, with the possible exception of q_s . We then form the outer product of these two vectors

$$C = \begin{pmatrix} A_0 \\ A_1 \\ \vdots \\ A_r \end{pmatrix} \cdot \left(B_0 \quad B_1 \quad \cdots \quad B_s \right) \quad (9.11)$$

$$= \begin{pmatrix} A_0 \cdot B_0 & A_0 \cdot B_1 & \cdots & A_0 \cdot B_s \\ A_1 \cdot B_0 & A_1 \cdot B_1 & & A_1 \cdot B_s \\ \vdots & & \ddots & \\ A_r \cdot B_0 & & & A_r \cdot B_s \end{pmatrix} \quad (9.12)$$

Each individual $C_{ij} = A_i B_j$ is an $(p_i \times q_j)$ matrix, and can be computed independently of all the others. Generalizing this to a full *GEMM implementation, which includes the possibility of transposes being taken, is tedious but straightforward.

We have implemented this approach for the GPU, as a complete replacement for *GEMM. The p_i and q_j values are chosen such that each sub-multiplication fits within the currently available GPU memory. Each multiplication is staged through the GPU, and the results assembled on the CPU. This process is hidden from the user code, which simply sees a standard *GEMM call.

9.3.2 Heterogeneous computing with MGEMM

With the problem of limited memory solved, we will now demonstrate how to overcome the lack of double precision GPU hardware. Again, consider the matrix multiplication

$$C = A \cdot B \tag{9.13}$$

We can split each matrix element-wise into ‘large’ and ‘small’ components, giving

$$\begin{aligned} C &= (\mathbf{A}^{\text{large}} + \mathbf{A}^{\text{small}}) (\mathbf{B}^{\text{large}} + \mathbf{B}^{\text{small}}) \\ &= A \cdot \mathbf{B}^{\text{large}} + \mathbf{A}^{\text{large}} \cdot \mathbf{B}^{\text{small}} + \mathbf{A}^{\text{small}} \cdot \mathbf{B}^{\text{small}} \end{aligned}$$

The $\mathbf{A}^{\text{small}}\mathbf{B}^{\text{small}}$ term consists entirely of ‘small’ numbers, and can be run in single precision on the GPU (using the cleaving approach described above, if needed). The other two terms contain ‘large’ numbers, and need to be run in double precision. However, since each of the ‘large’ matrices should be sparse, these terms each consist of a dense-sparse multiplication. We only store the non-zero terms of the $\mathbf{A}^{\text{large}}$ and $\mathbf{B}^{\text{large}}$ matrices, cutting the computational complexity significantly. Consider

$$C'_{ik} = A_{ij} \mathbf{B}^{\text{large}}_{jk} \tag{9.14}$$

Only a few $\mathbf{B}^{\text{large}}_{jk}$ will be non-zero, and we consider each in turn. For a particular *scalar* $\mathbf{B}^{\text{large}}_{jk}$, only the *k*th column of C' will be non-zero, and equal to the product of $\mathbf{B}^{\text{large}}_{jk}$ and the *column vector* A_{ij} (where *j* is fixed by the particular $\mathbf{B}^{\text{large}}_{jk}$ we are considering). This non-zero column vector C'_{ik} can be added to the final result, C , and the next $\mathbf{B}^{\text{large}}_{jk}$ considered. A similar process can be applied to the $\mathbf{A}^{\text{large}}\mathbf{B}^{\text{small}}$ term (producing *row* vectors of C). Again, this approach can be generalized to a full *GEMM implementation including transposes.

The remaining question is that of splitting the matrices. We have taken the simple approach of defining a cutoff value, δ . If $|A_{ij}| > \delta$, that element is considered ‘large,’ otherwise it is considered to be ‘small.’

We have implemented our algorithm we have dubbed MGEMM, for ‘mixed-precision general matrix multiply.’ It operates similarly to the other *GEMM routines, but takes one extra argument - the value of δ .

9.4 MGEMM benchmarks

We will now discuss some benchmarks for MGEMM. Our aim is to assess the speed and accuracy of MGEMM for various matrix structures and choice of cutoff tolerance compared to a DGEMM call on the CPU. In particular, it is important to benchmark how much computational

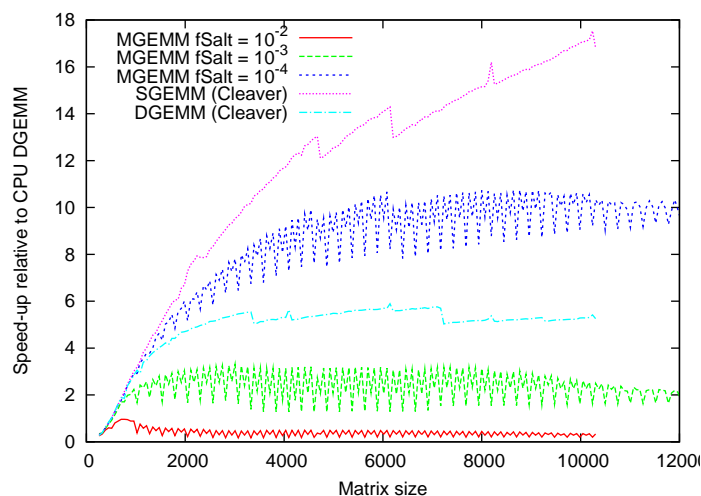


Figure 9.1: Speedup for various *GEMM calls as a function of (square) matrix size (averaged over ten runs). Most elements were in the range $[-1, 1]$, with the ‘salt’ values in the range $[90, 110]$. Times are scaled relative to running DGEMM on the CPU.

speed is gained using the mixed-precision MGEMM with the GPU as a function of the loss in accuracy compared to DGEMM. Throughout this section, CPU calculations were made using an Intel Xeon E5472 (Harpertown) processor clocked at 3.0 GHz attached to an NVIDIA Tesla C1060 (packaged into a Tesla S1070). The GPU calls were limited to 256 MiB of RAM to model a more restricted GPU in a typical BOINC (Berkeley Open Infrastructure for Network Computing) client [66, 107].

9.4.1 Using model matrices

In Fig. 9.1 we show the speedup for a variety of *GEMM calls using matrices of increasing (square) size. Three different types of matrix were considered, based on the number of randomly scattered ‘large’ elements. All the matrices were initialized with random values in the range $[-1, 1]$ forming the ‘background’, and ‘salted’ with a fraction f_{salt} of random larger values in the range $[90, 110]$. The size of the MGEMM cutoff parameter δ was chosen such that all the salted elements were considered ‘large’.

There are three MGEMM curves plotted, for different values of $f_{\text{salt}} = 10^{-2}, 10^{-3}$ and 10^{-4} . The SGEMM(cleaver) curve corresponds to doing the full matrix multiplication on the GPU using the GEMMcleaver and includes the time taken to down-convert the matrices to single precision on the CPU. The DGEMM(cleaver) curve corresponds to a full double-precision matrix multiplication on the GPU, which is possible for modern cards, and we include it for completeness. Square matrices were used in all cases, with no transpositions in

the ***GEMM** calls. All the runs were performed ten times and speedups are obtained relative to the time taken for the corresponding **DGEMM** call on the CPU.

Examining the results, we see that **SGEMM** on the GPU gives a speedup of 17.1x over running **DGEMM** on the CPU for a matrix of size 10048×10048 , and is even faster for larger matrices. This represents an upper bound for the speedups we can hope to obtain with **MGEMM** for such matrices. The speedups increase significantly as the matrices become larger due to the masking of memory access latencies and other overheads when employing the GPU for more compute-intensive processes.

Considering the **MGEMM** results, we see that the speedups are strongly dependent on the number of large elements which must be evaluated in double-precision on the CPU. For the relatively high value of $f_{\text{salt}} = 10^{-2}$, running **MGEMM** was actually slower than running **DGEMM** on the CPU alone. This is understandable when one considers the extra steps in the **MGEMM** algorithm. In addition to down-converting the matrices to single precision, the CPU has to perform cache-incoherent operations on the ‘large’ multiplications. We store our matrices column-major, so the operations performed in Eq. 9.14 are cache-coherent. However, it is easy to see that the corresponding operations for $C' = \mathbf{A}^{\text{large}}\mathbf{B}^{\text{small}}$ will be cache-incoherent for both C' and $\mathbf{B}^{\text{small}}$ (recall that $\mathbf{A}^{\text{large}}$ will be stored as individual elements). This brings a huge penalty over a standard ***GEMM** implementation which is tiled for cache-coherency.

In contrast, for $f_{\text{salt}} = 10^{-4}$, there is much less penalty to running **MGEMM** over **SGEMM** on the GPU, due to the small fraction of large elements computed on the CPU. Speedups of approximately 10x are observed for the largest matrices. For $f_{\text{salt}} = 10^{-3}$, the performance is naturally reduced, and speedups of approximately 2x relative to CPU **DGEMM** are obtained for the largest matrices. In this case **MGEMM** runs approximately 2.5 times slower than full **DGEMM** on the GPU (available in the most modern cards). We may also note that the thresholds for matrix cleaving can be discerned. They start at matrix sizes of 3344 for double precision and 4729 for single precision. These are detectable on the curves, but do not alter the times significantly.

In Fig. 9.2, we examine the accuracy of **MGEMM** for various matrix structures. Shown in the figure are the maximum absolute errors of a single element (relative to the CPU **DGEMM** result) plotted as a function of matrix size, for different fractions f_{salt} and sizes of salted values. As before, all the matrices were initialized with random values in the range $[-1, 1]$, but now the salting sizes were grouped into two ranges: $[90, 110]$ and $[9990, 10010]$. There is one curve using **SGEMM** corresponding to a fraction of salted values, $f_{\text{salt}} = 1\%$, in the range $[90, 110]$, and several **MGEMM** curves.

Looking at the figure, we see that the salted **SGEMM** calculation produces substantial errors for the largest matrices, which are of the same order of magnitude as the background elements themselves. In contrast, the errors are significantly reduced when using **MGEMM**

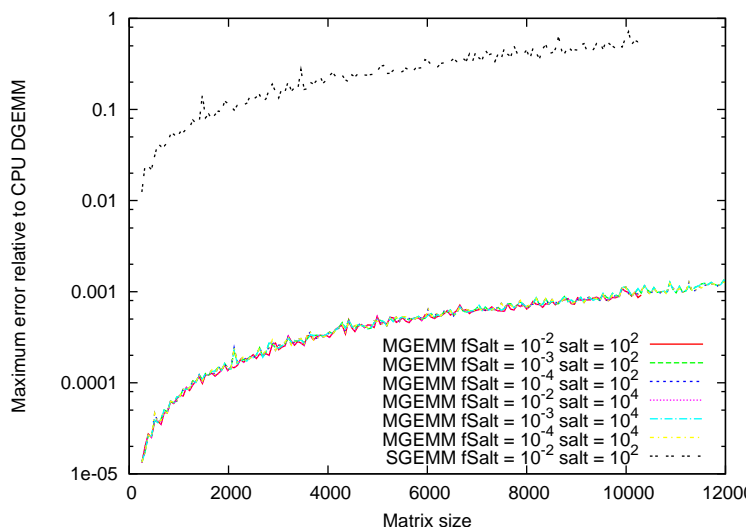


Figure 9.2: Maximum Absolute Error in a single element for various **GEMM** calls as a function of matrix (square) size. Most elements were in the range $[-1, 1]$, with the ‘salt’ values in the range $[90, 110]$ or $[9990, 10010]$. A CPU **DGEMM** call was taken as the reference calculation.

and are the same regardless of the fraction or size of the salted elements. In fact, these limiting **MGEMM** errors are the same as the errors observed when using **SGEMM** on a pair of *unsalted* random matrices. Essentially, **MGEMM** is limiting the maximum error in any element to that of the ‘background’ matrix computed in single precision since the cutoff tolerance guarantees that all the salted contributions will be computed in double precision on the CPU.

The order of magnitude of the limiting error can be rationalized from a consideration of the number of single-precision contributions per output element (approximately 1000-10000 in this case) and the expected error in each (approximately $10^{-6} - 10^{-7}$ for input matrices with a random background on $[-1, 1]$). A consequence of this observation is that an upper bound to the maximum error can be estimated from a consideration of only the matrix size and the cutoff parameter δ , although this estimate will be very conservative in cases where there is no obvious ‘constant background’, as we shall see in the following.

9.4.2 Using RI-MP2 matrices

For a more realistic assessment of **MGEMM** for quantum chemistry applications, we also ran benchmarks on two pairs of matrices taken from an RI-MP2 calculation on the taxol molecule in a cc-pVDZ basis, as described below in Section 9.5. In this case, the **MGEMM** cutoff parameter δ will no longer be dimensionless, but rather will take the same units as the

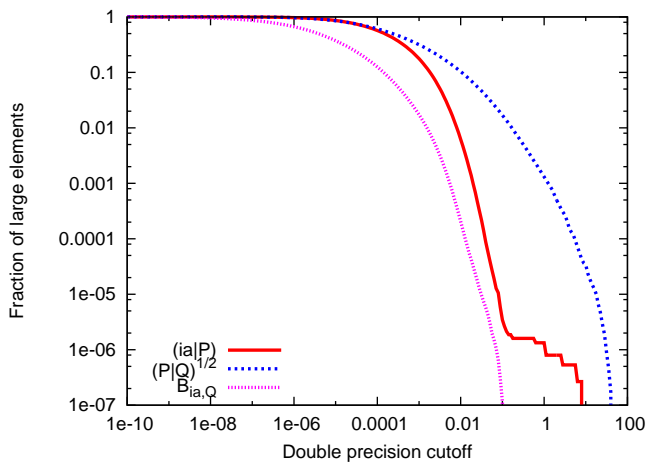


Figure 9.3: Fraction of ‘large’ elements as a function of the cutoff parameter, δ , for the taxol RI-MP2 matrices in steps 3 and 4 of the algorithm outlined in Sec. 9.2.

the input matrix elements, which, for Eqs. 9.6 and 9.7, are all computed in atomic units. For simplicity, we have dropped these units in the following discussion and assumed their implicit understanding based on the matrices that the δ -value is referring to.

As summarized in Section 9.2, our RI-MP2 implementation has two steps involving significant matrix multiplications. That is, the evaluation of Eqs. 9.6 and 9.7. As described in Sec. 9.2 and consistent with Chapter 8 [552], we shall refer to these two matrix multiplications as step 3 (Eq. 9.7) and step 4 (Eq. 9.6) throughout the following discussion. Although step 3 is typically an order of magnitude faster than step 4, we need to take care to study it since we are interested not only in speed, but also error accumulation using MGEMM.

For the case of taxol in a cc-pVDZ basis, the full $(P|Q)^{-1/2}$ matrix is of size 4186×4186 . However, in the Q-Chem implementation, the full $(ia|P)$ and $B_{ia,Q}$ matrices do not need to be explicitly constructed. Instead, it is sufficient to loop over discrete batches of i , depending on available memory. As seen above, larger matrices deliver a greater speedup when multiplied on the GPU, thus there is a motivation for choosing as large a batch size (over i) as possible in our GPU calculations. In these test benchmarks, we chose batch sizes of 1 and 7 based on the available CPU memory such that the $(ia|P)$ and $B_{ia,Q}$ matrices have dimensions of 897×4186 and 6279×4186 , respectively. We do not batch the step 3 matrices since there are only $O(N)$ multiplications taking place and the more computationally intensive process is step 4, which has order $O(N^2)$ operations.

We note that the structure of these matrices was found to be very different from the model matrices considered in the previous subsection. Specifically, the distribution of large

and small elements was structured, as described below. In the case of the $(P|Q)^{-1/2}$ matrix, involving only the auxiliary basis set, the large elements were heavily concentrated on the top left-hand corner in a diagonal fashion, while the other matrices were observed to have a striped vertical pattern of large elements. In the current implementation, the main issue affecting the efficiency of MGEMM is the ratio of large to small elements in the input matrices, but in general we can also expect the sparsity structure to impact performance. In cases where the structure is known in advance, a more specialized treatment could give worthwhile speedups, but this is beyond the scope of the current chapter.

The precise fractions of large and small elements for the taxol case are plotted in Fig. 9.3 with varying cutoff parameter δ for both the step 3 and step 4 matrices. We should note that these curves are only for one particular i -batch, as explained above, and not the full matrices. However, to ensure that the results are representative of the full matrix, we have checked the distributions from the other batches, and we chose the most conservative matrices for our plots, which had large elements across the broadest range of δ -values.

Looking at the curves, it is significant that the step 3 matrices have a greater fraction of large elements than the step 4 matrices, and specifically, the $(P|Q)^{-1/2}$ matrix has the largest elements of all. This means that for a constant δ -value, we can expect MGEMM to introduce larger errors in the step 3 matrix multiplications than in step 4. In future work, it could be advantageous to tailor the δ -value for different steps in an algorithm, or even different input matrices, but in this first study, we use a constant δ -value throughout any given calculation.

In the model matrices of the previous subsection, the distribution would have resembled a step function around $\delta = 1.0$, rapidly dropping from 1.0 to the chosen fraction of salted values for $\delta > 1.0$, and rapidly stepping again to 0 for δ -values beyond the salt size. In contrast, we see a continuous decay of element values in the real matrices across many orders of magnitude. In Fig. 9.1, MGEMM was seen to outperform DGEMM for a fraction of salts of order 10^{-4} . Comparing to Fig. 9.3, this suggests that δ should be greater than 0.01 to ensure significant MGEMM speedups when considering the $(ia|P)$ and $B_{ia,Q}$ matrices, while the fraction of large elements in the $(P|Q)^{-1/2}$ matrices only becomes this small for δ -values of order 10.

Having analyzed the distributions, we can consider their effect on the accuracy and speedups compared to the model benchmarks. On the top plots of Fig. 9.4 and Fig. 9.5, we show how the speedup for various *GEMM calls (compared to a CPU DGEMM call) varies with δ , averaged over ten calls. We see that the MGEMM performance varies continuously from being almost the same speed as CPU DGEMM to reaching the GPU SGEMM limit for sufficiently large cutoff values. As expected, for the step 4 matrices, significant speedups are only observed for δ -values greater than approximately 0.01. Similarly, for step 3, the

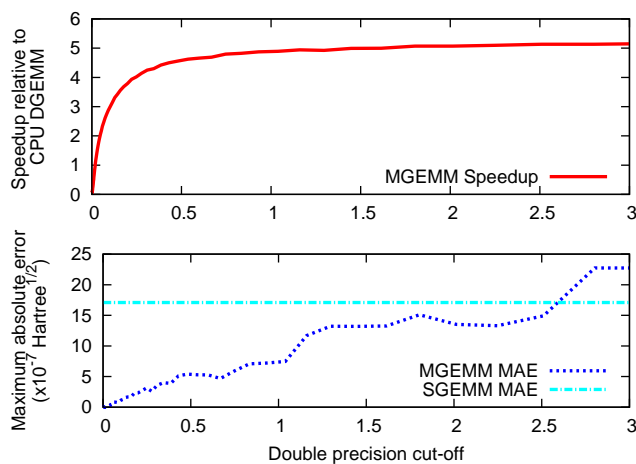


Figure 9.4: Results from the step 3 matrix multiplication in a taxol RI-MP2 calculation as a function of the cutoff variable δ . Top: MGEMM speedups relative to a CPU DGEMM calculation. Bottom: Maximum absolute error (Hartree^{1/2}) in a single element of the output matrix for MGEMM and SGEMM runs.

greatest speedups are only observed for much larger δ -values, approximately 1 to 2 orders of magnitude greater than for step 4. The limiting values for the speedups are approximately 5x and 9x for step 3 and step 4, respectively. This difference is mainly due to the different sizes of the matrices used in each benchmark, recognizing that the smaller matrices used in step 3 will give smaller speedups (c.f. Fig. 9.1).

Considering the MGEMM accuracy, the bottom plots in Fig. 9.4 and Fig. 9.5 show the maximum absolute errors of a single element (relative to the CPU DGEMM result) plotted as a function of δ . As δ increases, the MGEMM errors steadily increase as expected, with the single precision limit being approached for sufficiently large δ . Again we see significant differences between step 3 and step 4, as expected from the element distributions. Firstly, the errors in step 3 are approximately 2 orders of magnitude greater than in step 4. Moreover, in step 4, the errors reach the SGEMM limit for $\delta \sim 0.1$, while the errors in step 3 continue to increase for cutoff values an order of magnitude larger. Examining Fig. 9.3, it is expected that the relatively large fraction of elements greater than 1.0 in the $(P|Q)^{-1/2}$ matrix are responsible for these observations.

Unexpectedly, however, the errors are not seen to steadily converge to the SGEMM limit for step 3 in the same way as for step 4, with errors *larger* than SGEMM being observed for $\delta > 2.5$. We have performed additional tests to understand why this may be happening and our conclusion is that it results from error cancellation effects. To verify this idea, we repeated similar calculations replacing all matrix elements with their absolute values, so

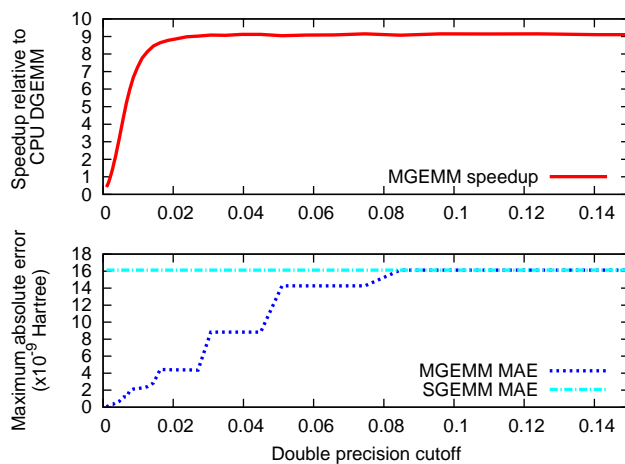


Figure 9.5: Results from the step 4 matrix multiplication in a taxol RI-MP2 calculation as a function of the cutoff variable δ . Top: MGEMM speedups relative to a CPU DGEMM calculation. Bottom: Maximum absolute error (Hartree) in a single element of the output matrix for MGEMM and SGEMM runs.

that any error cancellation would be essentially removed. The result was a monotonic curve much more similar to that observed for step 4, showing the same steady convergence to the SGEMM limit (not shown).

We may now consider the advantages of using MGEMM over SGEMM in terms of accuracy and speed. Comparing the subplots in Figs. 9.4 and 9.5 we can see that for a rather modest performance decrease from approximately 5x to 4x, and 9x to 7x, for steps 3 and 4 respectively, an order of magnitude reduction in the errors can be obtained. However, it might be noted that in all cases the maximum errors are rather small in these tests, being only of order 10^{-6} in the worst case. Considering real RI-MP2 applications, we might therefore expect the final errors in the molecular energy to be almost negligible using single precision only. However, in Sec. 9.5, the benchmarks show that for larger molecules the errors propagate such that the resulting correlation energy errors are too large to be acceptable.

Finally, from Fig. 9.2, we can estimate an upper bound on the maximum absolute error of each element for different δ -values. Since the matrix dimension is approximately 4000, the choice $\delta = 0.1$ would give a conservative error bound of approximately $4000 * 10^{-6} * 0.1$ which is of order 10^{-4} . However, because the matrices do not have a ‘constant background’ of 0.1 this estimate is very conservative, and the observed error in Fig. 9.5 is much less.

9.5 RI-MP2 acceleration benchmarks

In this section, our intention is to perform full RI-MP2 quantum chemistry calculations on real molecules and to benchmark the speedups and accuracy in the resulting molecular energy that can be obtained when using the GPU. In this case, we include in the timings all steps required to compute the RI-MP2 correlation energy (after the SCF cycle has finished) while the GPU *GEMM libraries are used to accelerate the matrix multiplications in steps 3 (Eq. 9.7) and 4 (Eq. 9.6), as described in the previous sections. As a result, the observed speedups will be reduced compared to the previous benchmarks since not all steps are accelerated.

For all these benchmarks, we used an AMD Athlon 5600+ CPU clocked at 2.8 GHz, combined with an NVIDIA Tesla C1060 GPU with 4 GiB of RAM. For some calculations, the GPU was limited to 256 MiB of RAM, as described below.

We emphasize that only the latest GPU cards have double-precision support to enable CUBLAS DGEMM, while older cards also have limited memory which significantly constrains the size of even the CUBLAS SGEMM matrix multiplications. Our previous attempts to use GPUs to accelerate RI-MP2 calculations were limited to molecular systems with less than 500 basis functions [552] due to this constraint. However, using the matrix cleaver in the (MGEMM) library, we are now able to run calculations of a size limited only by the CPU specification, independent of the GPU memory.

For our test systems we chose a set of linear alkanes (C_8H_{18} , $C_{16}H_{34}$, $C_{24}H_{50}$, $C_{32}H_{66}$, $C_{40}H_{82}$) as well as two molecules of pharmaceutical interest, taxol ($C_{47}H_{51}NO_{14}$) and valinomycin ($C_{54}H_{90}N_6O_{18}$), and we considered both the cc-pVDZ and cc-pVTZ [139] basis sets.

The matrix cleaver and MGEMM were implemented in a modified version of the Q-Chem 3.1 RI-MP2 code previously described [552]. Concerning the batching over occupied orbitals, as discussed in Section 9.4.2, only the step 4 matrices were batched. For taxol, the batch size was 7, as before. For all molecules, the batch size was chosen dynamically based on the matrix sizes and available CPU memory (for taxol, this results in a batch size of 7, as used before). However, in these benchmarks the batching issue is less important since we were limited to only 256 MiB of GPU RAM, which means that large batches would have to be cleaved by the MGEMM library in any case.

Firstly, in Table 9.1 we benchmarked the reference case of using either CUBLAS SGEMM or DGEMM for each test molecule using the double- ζ basis set. The table shows the speedup in computing the RI-MP2 correlation energy and the error relative to a standard CPU calculation (for SGEMM only). The speedups and SGEMM errors are seen to be greater for the larger molecules, as expected, with the largest speedups observed for valinomycin at

Molecule	Speedup		SGEMM energy error (kcal mol ⁻¹)
	SGEMM	DGEMM	
C ₈ H ₁₈	2.1	1.9	-0.05616
C ₁₆ H ₃₄	4.5	3.7	-0.12113
C ₂₄ H ₅₀	6.9	5.2	-0.62661
C ₃₂ H ₆₆	9.0	6.4	-0.75981
C ₄₀ H ₈₂	11.1	7.2	-1.12150
Taxol	11.3	7.1	-6.26276
Valinomycin	13.8	7.8	-9.99340

Table 9.1: Speedups using CUBLAS SGEMM and DGEMM and total energy errors relative to CPU DGEMM for various molecules in a cc-pVDZ basis.

13.8x and 7.8x, using SGEMM and DGEMM, respectively. However, while CUBLAS DGEMM gives essentially no loss of accuracy, the SGEMM error is approximately -10.0 kcal mol⁻¹, which is well beyond what is generally accepted as chemical accuracy.

The results from Table 9.1 highlight the need for MGEMM to reduce the errors when double-precision GPUs are unavailable. As an initial test of MGEMM for this purpose, we repeated the calculation of the taxol molecule in the double- ζ basis set (1123 basis functions) for various choices of cutoff value δ . Fig. 9.6 shows the speedup relative to CPU DGEMM as well as the absolute error in the energy.

As the cutoff increases, the MGEMM speedup increases rapidly to the asymptotic limit of 10.6x, which is slightly less than the SGEMM limit of 11.3x due to the MGEMM overhead. In contrast, the energy error in this range increases almost linearly towards the SGEMM limit. Recalling Figs. 9.4 and 9.5, it seems that the errors are dominated by the step 3 operations, where we form the $B_{ia,Q}$ matrices, since these errors are also seen to steadily increase over the range of cutoff values considered in Fig. 9.6. The overall speedups are also seen to have a similar shape to the step 3 speedups, but are approximately twice as large. This reflects the greater speedups in step 4, noting that step 4 on the CPU is the most expensive step in the algorithm.

To achieve a target accuracy of 1.0 kcal mol⁻¹, Fig. 9.6 shows that a cutoff value of $\delta < 2.0$ in the case of taxol in a double- ζ basis is necessary. However, trading the accuracy and speedup, a good choice of cutoff would be $\delta = 1.0$. This gives an error of 0.5 kcal mol⁻¹, which is an order of magnitude smaller than using SGEMM, with a speedup very close to the MGEMM limit and only about 7% less than the SGEMM limit.

In Table 9.2, we explore the performance of MGEMM using a constant cutoff value of $\delta=1.0$. The table shows speedups and total energy errors for each molecule in both the double- ζ and triple- ζ basis sets. In this particular case, we have limited the GPU to use only 256 MiB of RAM to mimic the capability of older cards and emphasize the use of the

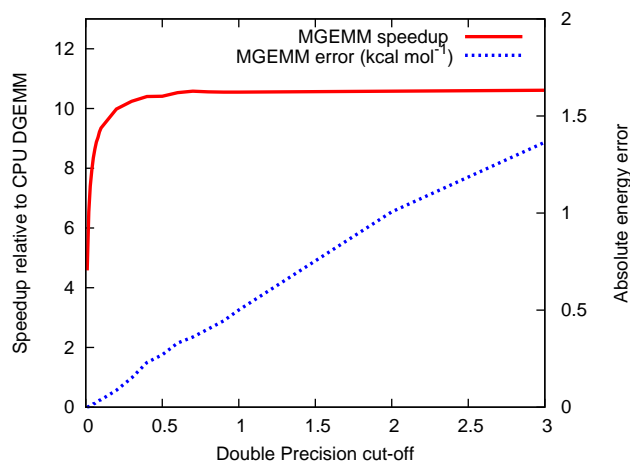


Figure 9.6: Taxol MGEMM calculation using a double- ζ basis set with respect to the double precision cutoff (δ). We plot the MGEMM speedup relative to CPU DGEMM and it shows a rapid increase with δ towards an asymptotic value of 10.6x. We also show the energy difference relative to CPU DGEMM, which is seen to increase steadily over the range of δ -values chosen, but is significantly less than the previously computed SGEMM error of 6.6276 kcal mol⁻¹.

MGEMM clever. This will naturally result in a loss of speedup compared to utilizing a larger GPU memory. In the case of taxol the reduction is approximately 20%, but obviously still much faster than a calculation using only the CPU.

Looking at Table 9.2, the trends are the same as in Table 9.1, but the MGEMM errors are seen to be approximately an order of magnitude less than the SGEMM errors (for the larger molecules). For valinomycin in the cc-pVDZ basis, the SGEMM speedup is reduced from 13.8x to 10.1x using MGEMM, but the error in the total energy is also reduced from -10.0 kcal mol⁻¹ to -1.2 kcal mol⁻¹, which is now very close to chemical accuracy. Moreover, while CUBLAS DGEMM clearly has the advantage (when available) of not introducing errors, if -1.2 kcal mol⁻¹ is an acceptable accuracy, MGEMM may even be favoured since the DGEMM speedup is only 7.8x compared to 10.1x. Moreover, since the error increases as δ is increased, there will be a substantial error cancellation when obtaining energy differences. Thus, the apparent error in MGEMM will approach the DGEMM value.

It is unsurprising that the errors are larger when using the triple- ζ basis. The manner in which the errors grow can be anticipated using the arguments mentioned in Section 9.4, where we estimate an upper bound on the maximum absolute error from MGEMM by consideration of a constant background of elements no larger than the cutoff threshold and the size of the input matrices. In practice, this upper bound can be rather conservative. Moreover,

Molecule	Speedup		Energy error (kcal mol ⁻¹)	
	Double- ζ	Triple- ζ	Double- ζ	Triple- ζ
C ₈ H ₁₈	1.9	2.7	-0.01249	-0.03488
C ₁₆ H ₃₄	3.8	5.6	-0.00704	-0.04209
C ₂₄ H ₅₀	5.8	8.2	-0.14011	-0.33553
C ₃₂ H ₆₆	7.9	9.2	-0.08111	-0.29447
C ₄₀ H ₈₂	9.4	10.0	-0.13713	-0.51186
Taxol	9.3	10.0	-0.50110	-1.80076
Valinomycin	10.1	-	-1.16363	-

Table 9.2: MGEMM speedups and total energy errors with respect to CPU DGEMM for various molecules in a cc-pVDZ and cc-pVTZ basis.

if the quantity of interest is the final energy, we must also take into account how the matrices are used *after* the application of MGEMM (e.g if they are multiplied by large numbers). Nevertheless, a topic of future study could be the search for a more sophisticated method for determining a safe and optimal δ -value for a given size of acceptable error in the final energy.

9.6 Conclusion

We have developed and implemented two new tools for the acceleration of computational chemistry codes using graphical processing units (GPUs). Firstly, we proposed a general black-box approach for the efficient GPU acceleration of matrix-matrix multiplications where the matrix size is too large for the whole computation to be held in the GPU's onboard memory. Secondly, we have shown how to improve the accuracy of matrix multiplications when using only single-precision GPU devices by proposing a heterogeneous computing model whereby both single and double precision operations are evaluated in a mixed fashion on the GPU and CPU, respectively.

This matrix cleaver and mixed-precision matrix multiplication algorithm have been combined into a general library named MGEMM [475], which may be called like a standard SGEMM function call with only one extra argument, the cutoff parameter δ , which describes the partitioning of single and double-precision work. Benchmarks of general interest have been performed to document the library's performance in terms of accuracy and speed.

Compared to a CPU DGEMM implementation, MGEMM is shown to give speedups approaching the CUBLAS SGEMM case when very few operations require double precision, corresponding to a large δ value (which is equivalent to having a large fraction of small elements in the input matrices). However, when the fraction of large elements approaches 0.1% or greater,

much less benefit is seen. Concerning accuracy, **MGEMM** restricts the maximum error in an element of the output matrix to an upper bound based on the size of the matrix and the choice of δ -value. In practice, this upper bound is usually conservative. In general, the precise performance achieved with **MGEMM** is strongly dependent on the distribution of large and small values in the input matrices, as we have shown.

To illustrate the utility of **MGEMM** for quantum chemistry, we have implemented it into the Q-Chem program package to accelerate RI-MP2 calculations. We have considered both the use of modern high-end GPU cards, with up to 4 GiB of memory and double-precision capability, as well as legacy cards with only single-precision capability and potentially only 256 MiB of RAM. Greater speedups, but also larger absolute errors in the correlation energy were observed with the larger test molecules. In particular, for the 168-atom valinomycin molecule in a cc-pVDZ basis set, we observed speedups of 13.8x, 10.1x and 7.8x, for **SGEMM**, **MGEMM** and **DGEMM**, respectively. The corresponding errors in the correlation energy were $-10.0 \text{ kcal mol}^{-1}$, $-1.2 \text{ kcal mol}^{-1}$, and essentially zero, respectively. The **MGEMM** δ -value was chosen as 1.0 for these benchmarks.

We have also suggested ways in which the size of the **MGEMM** error may be parameterized in terms of a conservative error bound. In addition, we have observed that the correlation energy error grows approximately linearly with the choice of δ -value, which may suggest a route to the *a priori* determination of the δ for a given target accuracy.

As we submit this paper for publication, we have become aware of the planned release of the next-generation GPU from NVIDIA, currently code-named Fermi. This card will have double-precision support with a peak performance only a factor of 2 less than single-precision operations. However, despite the emergence of double-precision GPU devices, it is our hope that the current chapter will provide a framework for thinking about other mixed-precision algorithms. Even with the more widespread availability of double-precision cards in the future, we have seen how **MGEMM** can run faster than CUBLAS **DGEMM** if a specified level of accuracy is tolerated. Indeed, practical calculations on GPUs are very often bound by memory bandwidth to/from the device, rather than raw operation count. In these cases, the transfer and processing of only single-precision data could effectively double the performance compared to naive double-precision calculations.

Moreover, we are interested in the use of commodity GPUs as part of a grid-computing environment, such as the BOINC network. CUDA capable GPUs are extremely common in legacy gaming devices, but most of the client machines will not host the latest high-end hardware. We therefore see a significant application for **MGEMM** in leveraging these large numbers of legacy cards to overcome their lack of RAM and double-precision arithmetic. We are therefore optimistic overall about the role **MGEMM** can play in helping to accelerate computations using GPUs in the near future.

Chapter 10

Accelerating correlated quantum chemistry calculations using graphical processing units

10.1 Introduction

With the advent of modern quantum theory a century ago, scientists quickly realized that quantum mechanics could offer a predictive theory of chemistry, revolutionizing the subject in the same way that Newton's laws had transformed the study of classical mechanics. Over the intervening decades, we have witnessed an exponential increase in available computing power. Coupled with tremendous advances in theory and algorithmic methods, as well as the painstaking development of sophisticated program suites often consisting of millions of lines of code, the scope of phenomena now amenable to the predictive techniques of quantum chemistry is large and continually growing.

Modern computational chemistry has an important role to play in many practical applications, such as the discovery of new drugs or industrial catalysts, and the development of new materials or technologies to meet global energy and environmental challenges. Its widespread application has resulted in major efforts to reduce its computational cost: accurate quantum chemistry methods consume a significant fraction of computing resources at national laboratories.

As a result, we are witnessing a new era in the optimization of quantum chemistry codes following an explosion of interest in the utilization of coprocessors such as graphical processing units (GPUs) [385]. This interest in GPUs and other accelerators is largely driven by their combination of formidable performance and relatively low cost. But another key reason for their emergence in scientific fields was the release of NVIDIA's CUDA (compute unified device architecture) toolkit that dramatically simplified the process of developing code for GPUs.

Already, GPUs have started to be used by computational chemists to treat a wide range of problems. These include molecular dynamics [501, 21], and quantum Monte Carlo simu-

lations [19], density-functional theory and self-consistent field calculations [597, 596, 539, 538, 540, 541] as well as correlated quantum chemistry applications [552, 393]. Efficiency gains of between one and three orders of magnitude have been reported compared to conventional implementations on a CPU. Thus new domains of scientific application are now possible where, previously, extremely expensive and rare supercomputing facilities would have been required.

A very important area for many scientific applications is the acceleration of linear algebra operations, which are quite well-suited for GPU architectures. Included in the CUDA software development toolkit is an implementation of the BLAS linear algebra library, named CUBLAS [383]. By simply replacing the BLAS `*GEMM` routines with corresponding CUBLAS `SGEMM` calls to accelerate key matrix multiplications, our group [552] was able to achieve a speedup of 4.3x when calculating the RI-MP2 (resolution-of-the-identity second-order Møller-Plesset perturbation theory [222, 147]) correlation energy of doecicosane ($C_{22}H_{46}$).

This initial effort was one of the first quantum chemistry applications to leverage GPUs, but it revealed several issues for future work. For example, while modern GPU cards designed for research can have up to 4 GiB of RAM, consumer level cards may have as little as 256 MiB. Without some means to overcome the memory bottleneck, our first attempts to use GPUs to accelerate RI-MP2 calculations were limited to systems with less than 600 basis functions.

Another issue is numerical precision. The vast majority of GPU cards currently in use worldwide support only single-precision arithmetic. Single precision is generally insufficient to achieve ‘chemical accuracy’ of 1 kcal/mol in calculations on anything but the smallest and simplest systems, since the errors quickly accumulate for larger molecules. An interesting topic in the computer science [304, 226] community has been the development of libraries which achieve precision beyond the hardware specification through algorithmic techniques. In this chapter, we consider this problem in detail for the special case of single-precision GPU devices and applications to quantum chemistry.

In summary, we describe our efforts to develop tools for the GPU acceleration of correlated quantum chemistry calculations [552, 393]. We address the issues of limited GPU device memory, as well as achieving higher accuracy using only single-precision GPU operations. We begin in Section 10.2 with an overview of basic quantum chemistry theory, followed by the algorithms behind our new libraries. Next we report the efficiency of our methods for general matrix multiplications and in the context of accelerating quantum chemistry calculations. We end the chapter with a brief conclusion and our future perspective.

10.2 Quantum chemistry theory

Traditional quantum chemistry strives to solve the time-independent Schrödinger equation,

$$\hat{H}(\mathbf{r}, \mathbf{R})\psi(\mathbf{r}, \mathbf{R}) = E(\mathbf{R})\psi(\mathbf{r}, \mathbf{R}) \quad (10.1)$$

where $\psi(\mathbf{r}, \mathbf{R})$ is the electronic wavefunction for a molecular system defined by the Hamiltonian $\hat{H}(\mathbf{r}, \mathbf{R})$ in terms of a set of coordinates for the electrons, \mathbf{r} , and nuclei, \mathbf{R} . The total molecular energy is given by the eigenvalue $E(\mathbf{R})$ and is often referred to as the *potential energy surface*. It is parameterized in terms of the nuclear coordinates since we have assumed the Born-Oppenheimer approximation, and is fundamental to the *ab initio* theory of chemical reaction dynamics.

The solution of Eq. 10.1 yields the electronic wavefunction for a given nuclear configuration, and in turn the probability density for finding an electron at a given point in space. Exact solution is intractable, even numerically, for all but the simplest systems due to the formidable nature of the many-body problem inherent in the form of $\hat{H}(\mathbf{r}, \mathbf{R})$, which describes not only the electronic kinetic energy, but also the complex Coulomb interactions between the electrons and nuclei. Only for one-electron systems, where there is no electron-electron coupling, are exact solutions readily available.

Nevertheless, it is a hallmark of quantum chemistry that there is a well-defined hierarchy of methods for solving Eq. 10.1 approximately. Indeed, given sufficient computational power, a solution may be improved systematically to yield a wavefunction of arbitrary numerical accuracy. The simplest method in the hierarchy is a mean-field approach known as Hartree-Fock (HF) theory.

In HF theory, we write the electronic wavefunction for an N -electron system as an antisymmetrized product of *molecular orbitals*, $\phi(\mathbf{r}_i)$, which are wavefunctions for a single electron under a one-electron Hamiltonian known as the *Fock operator*,

$$\hat{f}(\mathbf{r}, \mathbf{R}) = \hat{h}(\mathbf{r}, \mathbf{R}) + \sum_{j=1}^{N/2} \left[2\hat{J}_j(\mathbf{r}) - \hat{K}_j(\mathbf{r}) \right] \quad (10.2)$$

The one-electron, $\hat{h}(\mathbf{r})$, Coulomb, $\hat{J}_j(\mathbf{r})$, and exchange, $\hat{K}_j(\mathbf{r})$, operators are given by

$$\hat{h}(\mathbf{r}, \mathbf{R}) = -\frac{1}{2}\nabla^2 + v(\mathbf{r}, \mathbf{R}) \quad (10.3)$$

$$\hat{J}_j(\mathbf{r}) = \int \frac{\phi_j^*(\mathbf{r}')\phi_j(\mathbf{r}')}{|\mathbf{r} - \mathbf{r}'|} d\mathbf{r}' \quad (10.4)$$

$$\hat{K}_j(\mathbf{r})\phi_i(\mathbf{r}) = \int \frac{\phi_j^*(\mathbf{r}')\phi_i(\mathbf{r}')}{|\mathbf{r} - \mathbf{r}'|} d\mathbf{r}' \phi_j(\mathbf{r}) \quad (10.5)$$

where $v(\mathbf{r}, \mathbf{R})$ is the nuclear potential. The associated Hartree-Fock equations,

$$\hat{f}\phi_i(\mathbf{r}) = \epsilon_i\phi_i(\mathbf{r}) \quad (10.6)$$

permit a complete set of eigenfunctions. In the simplest case where N is even, each of the $N/2$ orbitals corresponding to the lowest eigenvalues is associated with two electrons of opposite spin. These *occupied* orbitals are used to construct the many-electron wavefunction; they are labelled by the subscripts i, j, \dots . The remaining functions form the *virtual* orbitals and are indicated by the subscripts a, b, \dots .

Although in some implementations, the Hartree-Fock equations are solved numerically, the traditional approach is to expand the molecular orbitals (MOs) in a basis of *atomic orbitals*, $\{\eta_\alpha\}$,

$$\phi_p(\mathbf{r}) = \sum_{\alpha}^{N_b} c_{\alpha p} \eta_{\alpha}(\mathbf{r}) \quad (10.7)$$

The optimized coefficients, $c_{\alpha p}$, and orbital energies, ϵ_p , are determined from the secular equations, which in matrix notation can be written as

$$\mathbf{FC} = \mathbf{SC}\epsilon \quad (10.8)$$

where \mathbf{S} is the atomic orbital (AO) overlap matrix, $\langle \eta_\alpha | \eta_\beta \rangle$, \mathbf{F} is the AO Fock matrix, $\langle \eta_\alpha | \hat{f} | \eta_\beta \rangle$, \mathbf{C} is the matrix of MO coefficients and ϵ is the diagonal matrix of MO energies. These are the celebrated Roothaan-Hall self-consistent field equations.

The Hartree-Fock solution (in a complete AO basis) generally recovers more than 99% of the exact energy, which is remarkable. The neglected energy is known as the *correlation energy*, and its accurate and efficient recovery is the central challenge in quantum chemistry. Indeed, for the purposes of predictive chemistry, we are largely interested in energy differences which are of similar magnitude to the correlation energy: about $0.04 E_h$ (100 kJ mol^{-1}) for two electrons in a doubly occupied orbital.

Currently the most popular approach for solving Eq. 10.1 including electron correlation, is density functional theory (DFT). DFT, which bypasses explicit construction of the many-body wavefunction and focuses only on the much simpler 3-dimensional electron density as the basic variable, is extremely useful due its favorable balance between accuracy and efficiency.

Instead, we examine in this chapter another approach: a widely-used and computationally efficient correlated wavefunction-based method, known as second-order Møller-Plesset perturbation theory (MP2) [222]. MP2 is known to produce equilibrium geometries of comparable accuracy to density functional theory (DFT) and in particular is able to capture long-range correlation effects such as the dispersion interaction. For many weakly bound

systems where DFT results are often questionable, MP2 is essentially the least expensive and most reliable alternative.

If HF theory can be thought of as a first-order solution to Eq. 10.1, then MP2 theory is the second-order solution within the framework of perturbation theory, where the many-electron Hamiltonian is partitioned as

$$\hat{H} = \sum_i \hat{f}(\mathbf{r}_i) + \lambda \hat{H}^{(1)} \quad (10.9)$$

We have introduced an order parameter, λ , to expand the energy and wavefunction,

$$E = E^{(0)} + \lambda E^{(1)} + \lambda^2 E^{(2)} + \dots \quad (10.10)$$

$$\Psi = \Psi_{\text{HF}} + \lambda \Psi^{(1)} + \lambda^2 \Psi^{(2)} + \dots \quad (10.11)$$

where Ψ_{HF} is the zero-order (Hartree-Fock) wavefunction, and the zero and first-order energies are given by

$$E^{(0)} = \sum_i \epsilon_i \quad (10.12)$$

$$E^{(0)} + \lambda E^{(1)} = \langle \Psi_{\text{HF}} | \hat{H} | \Psi_{\text{HF}} \rangle \quad (10.13)$$

The second-order (MP2) correlation energy takes the form

$$E^{(2)} = \sum_{ijab} \frac{(ia|jb)^2 + \frac{1}{2} [(ia|jb) - (ib|ja)]^2}{\epsilon_i + \epsilon_j - \epsilon_a - \epsilon_b} \quad (10.14)$$

where the MO integrals,

$$(ij|ab) = \sum_{\mu\nu\lambda\sigma} C_{\mu i} C_{\nu j} C_{\lambda a} C_{\sigma b} (\mu\nu|\lambda\sigma) \quad (10.15)$$

are obtained by transforming the AO integrals,

$$(\mu\nu|\lambda\sigma) = \int \int \frac{\eta_\mu(\mathbf{r}_1) \eta_\nu(\mathbf{r}_1) \eta_\lambda(\mathbf{r}_2) \eta_\sigma(\mathbf{r}_2)}{|\mathbf{r}_1 - \mathbf{r}_2|} d\mathbf{r}_1 d\mathbf{r}_2 \quad (10.16)$$

One way to considerably reduce the computational cost of MP2 calculations is to exploit the linear dependence in the product space of atomic orbitals. This allows us to expand products of AOs as linear combinations of atom-centered auxiliary basis functions, P ,

$$\rho_{\mu\nu}(\mathbf{r}) = \eta_\mu(\mathbf{r}) \eta_\nu(\mathbf{r}) \approx \tilde{\rho}_{\mu\nu}(\mathbf{r}) = \sum C_{\mu\nu,P} P(\mathbf{r}) \quad (10.17)$$

and to therefore approximate Eq. 10.16 in terms of only 2 and 3-index quantities as

$$\widetilde{(\mu\nu|\lambda\sigma)} = \sum_{P,Q} (\mu\nu|P) (P|Q)^{-1} (Q|\lambda\sigma) \quad (10.18)$$

The idea is equivalent to an approximate insertion of the resolution-of-the-identity (RI),

$$I = \sum_m |m\rangle\langle m| \approx \sum_{P,Q} |P\rangle\langle P|Q\rangle^{-1}\langle Q| \quad (10.19)$$

from which the name RI-MP2 is derived.

Our work is implemented in a development version of Q-Chem 3.1 [480], where the RI-MP2 correlation energy is evaluated in five steps, as described elsewhere [552]. Previously we showed that steps 3 and 4, the formation of the approximate MO integrals, were by far the most expensive operations for medium to large-sized systems, and require the matrix multiplications

$$\widetilde{(ia|jb)} \approx \sum_Q B_{ia,Q} B_{jb,Q} \quad (10.20)$$

and

$$B_{ia,Q} = \sum_P (ia|P) (P|Q)^{-1/2} \quad (10.21)$$

These are the two operations we will concentrate on accelerating in this chapter.

10.3 GPU acceleration of GEMM

In this section we first describe our cleaving algorithm to allow matrix multiplications of arbitrary size to be accelerated on the GPU (assuming sufficient CPU memory). Next, we propose two different algorithms for the MGEMM (‘mixed-precision general matrix multiply’) library, using two different schemes to partition the matrices into simpler components.

10.3.1 Cleaving GEMMs

Consider the matrix multiplication

$$\mathbf{C} = \mathbf{A}\mathbf{B} \quad (10.22)$$

where \mathbf{A} is an $(m \times k)$ matrix, \mathbf{B} is an $(k \times n)$ matrix, and \mathbf{C} an $(m \times n)$ matrix. We can divide \mathbf{A} into a column vector of $r + 1$ matrices

$$\mathbf{A} = \begin{pmatrix} \mathbf{A}_0 \\ \mathbf{A}_1 \\ \vdots \\ \mathbf{A}_r \end{pmatrix} \quad (10.23)$$

where each entry \mathbf{A}_i is a $(p_i \times k)$ matrix, and $\sum_i^r p_i = m$. In practice, all the p_i will be the same, with the possible exception of p_r , which will be an edge case. In a similar manner, we can divide \mathbf{B} into a row vector of $s + 1$ matrices

$$\mathbf{B} = \left(\mathbf{B}_0 \quad \mathbf{B}_1 \quad \cdots \quad \mathbf{B}_s \right) \quad (10.24)$$

where each \mathbf{B}_j is an $(k \times q_j)$ matrix and $\sum_j^s q_j = n$. Again all the q_j will be the same, with the possible exception of q_s . We then form the outer product of these two vectors

$$\mathbf{C} = \begin{pmatrix} \mathbf{A}_0 \\ \mathbf{A}_1 \\ \vdots \\ \mathbf{A}_r \end{pmatrix} \left(\mathbf{B}_0 \quad \mathbf{B}_1 \quad \cdots \quad \mathbf{B}_s \right) \quad (10.25)$$

$$= \begin{pmatrix} \mathbf{A}_0\mathbf{B}_0 & \mathbf{A}_0\mathbf{B}_1 & \cdots & \mathbf{A}_0\mathbf{B}_s \\ \mathbf{A}_1\mathbf{B}_0 & \mathbf{A}_1\mathbf{B}_1 & & \mathbf{A}_1\mathbf{B}_s \\ \vdots & & \ddots & \\ \mathbf{A}_r\mathbf{B}_0 & & & \mathbf{A}_r\mathbf{B}_s \end{pmatrix} \quad (10.26)$$

Each individual $\mathbf{C}_{ij} = \mathbf{A}_i\mathbf{B}_j$ is an $(p_i \times q_j)$ matrix, and can be computed independently of all the others. Generalizing this to a full *GEMM implementation, which includes the possibility of transposes being taken, is tedious but straightforward.

We have implemented this approach for the GPU as a complete replacement for *GEMM. The p_i and q_j values are chosen such that each sub-multiplication fits within the currently available GPU memory. Each multiplication is staged through the GPU, and the results assembled on the CPU. This process is hidden from the user code, which simply sees a standard *GEMM call. In this way, we are able to multiply matrices of arbitrary size using MGEMM regardless of the available GPU memory.

10.3.2 Bitwise MGEMM algorithm

Consider the partitioning of a double-precision (DP) floating point number, $A = m * 2^k$,

$$A \approx A^u + A^l \quad (10.27)$$

where A^u and A^l are single-precision (SP) numbers storing the uppermost n_u , and the next lowest n_l , significant bits of m , respectively. Consider next the multiplication of two scalars, A, B . Applying the bitwise partitioning, we can approximate the full DP multiplication as four SP multiplications,

$$AB \approx A^u B^u + A^u B^l + A^l B^u + A^l B^l \quad (10.28)$$

where the result of each SP multiplication is accumulated in DP. For Eq. 10.28 to be exact, n_u and n_l must now be sufficiently small such that no round-off error occurs when storing each of the four multiplications in SP.

Anticipating the performance of Eq. 10.28, we can introduce an alternative approximation, involving only three SP multiplications,

$$AB \approx A^u B^u + A^u B^l + A^l (B^u + B^l) \quad (10.29)$$

where $B^u + B^l$ is replaced by the SP cast of B . In general, we can expect the round-off error associated with $A^l B^u$ to be of the same order of magnitude, on average, as the round-off error associated with $A^l (B^u + B^l)$.

Finally, we can generalize Eq. 10.29 for the matrix multiplication,

$$\mathbf{AB} \approx \mathbf{A}^u \mathbf{B}^u + \mathbf{A}^u \mathbf{B}^l + \mathbf{A}^l (\mathbf{B}^u + \mathbf{B}^l) \quad (10.30)$$

where, for each element of $\mathbf{X} \in \{\mathbf{A}, \mathbf{B}\}$,

$$X_{ij} \approx X_{ij}^u + X_{ij}^l \quad (10.31)$$

As above, the final term may be considered as either two separate multiplications, or as a single multiplication where $\mathbf{B}^u + \mathbf{B}^l$ is pre-summed. All the multiplications may be evaluated efficiently using the CUBLAS SGEMM library routines on the GPU. The results may then be accumulated in DP on the CPU to yield the final approximation for \mathbf{AB} .

For Eq. 10.30 to be exact, in addition to the issues for scalar multiplication, we have the additional round-off errors arising from the multiply-add operations. Specifically, if \mathbf{A} is a $M \times K$ matrix and \mathbf{B} is a $K \times N$ matrix, \mathbf{AB} effectively consists of MN dot products of length K . As K increases, or as the range of magnitudes of X_{ij} becomes wider, more round-off error will occur due to the accumulation in SP. We explore these issues more in the benchmarks below.

10.3.3 Heterogeneous MGEMM algorithm

A different way to improve the precision is to consider the magnitudes of the matrix elements from the outset. That is, we decompose the matrix multiplication, $\mathbf{C} = \mathbf{AB}$, by splitting \mathbf{A} and \mathbf{B} into ‘large’ and ‘small’ components, giving

$$\begin{aligned} \mathbf{C} &= \left(\mathbf{A}^{\text{large}} + \mathbf{A}^{\text{small}} \right) \left(\mathbf{B}^{\text{large}} + \mathbf{B}^{\text{small}} \right) \\ &= \mathbf{AB}^{\text{large}} + \mathbf{A}^{\text{large}} \mathbf{B}^{\text{small}} + \mathbf{A}^{\text{small}} \mathbf{B}^{\text{small}} \end{aligned} \quad (10.32)$$

where we have taken the simple approach of introducing a cutoff value, δ , to define the split. i.e. if $|X_{ij}| > \delta$, the element is considered ‘large,’ otherwise it is considered ‘small.’

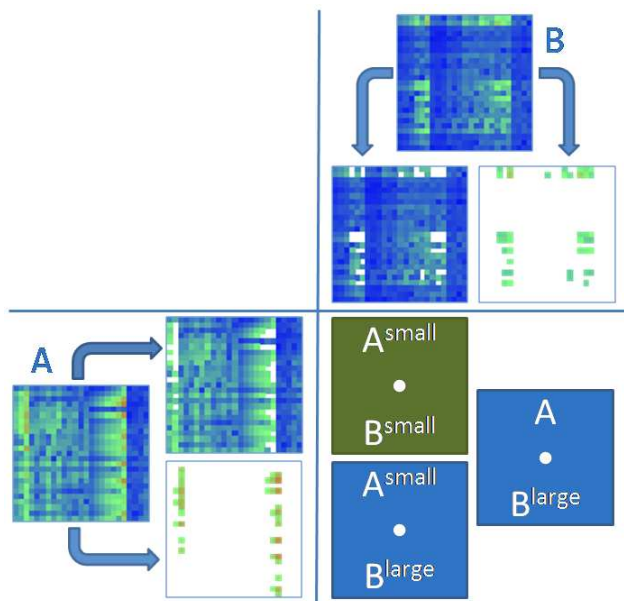


Figure 10.1: Pictorial representation of the heterogeneous MGEMM algorithm. The bottom-left and top-right panels show the \mathbf{A} and \mathbf{B} matrices and their separation into matrices with large and small elements, given a cutoff parameter δ . The right-bottom panel shows the components of the final \mathbf{AB} matrix, where the green component involves a dense matrix multiplication computed with cublas-SGEMM, while the blue components involve sparse matrix multiplications computed with a daxpy-like algorithm (explained in the text). The blocks follow the nomenclature shown on Eq. 10.32.

The $\mathbf{A}^{\text{small}}\mathbf{B}^{\text{small}}$ term consists entirely of ‘small’ numbers, and can be run with reasonable accuracy in single precision on the GPU (using the cleaving approach described above, if needed). The other two terms contain ‘large’ numbers, and need to be run in double precision to achieve greater accuracy. However, since each of the ‘large’ matrices will often be sparse, these terms each consist of a dense-sparse multiplication.

We only store the nonzero terms of the $\mathbf{A}^{\text{large}}$ and $\mathbf{B}^{\text{large}}$ matrices, cutting the computational complexity significantly. Consider

$$C'_{ik} = A_{ij}B_{jk}^{\text{large}} \quad (10.33)$$

Only a few B_{jk}^{large} will be nonzero, and we consider each in turn. For a particular scalar B_{jk}^{large} , only the k th column of \mathbf{C}' will be nonzero and is equal to the product of B_{jk}^{large} and the j th column vector of \mathbf{A} . This nonzero column vector C'_{ik} can be added to the final result, \mathbf{C} , and the next B_{jk}^{large} considered. A similar process can be applied to the $\mathbf{A}^{\text{large}}\mathbf{B}^{\text{small}}$ term (producing *row* vectors of \mathbf{C}). Again, this approach can be generalized to a full *GEMM implementation including transposes. Fig. 10.1 shows a cartoon of the

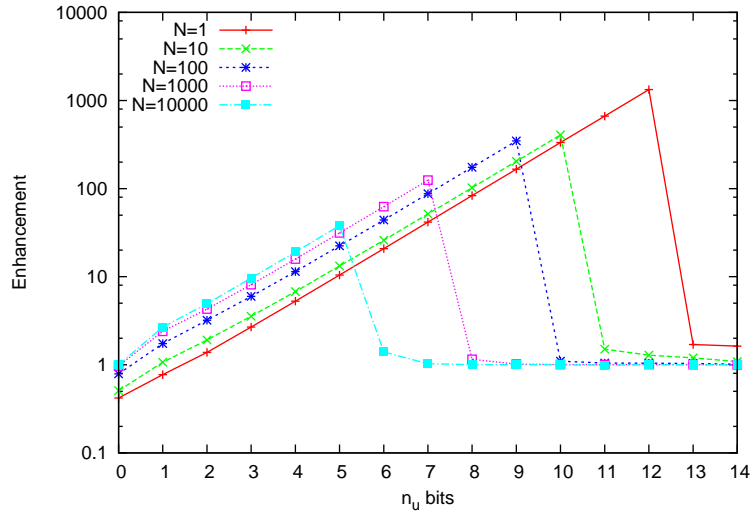


Figure 10.2: MGEMM enhancement versus the number of upper bits, n_u , (and $n_l = 23$) for $N \times N$ matrices where $N \in \{1, 10, 100, 10^3, 10^4\}$. The matrices were initialized with uniform random numbers on the range $[1, 2]$.

heterogeneous MGEMM algorithm described above.

10.4 MGEMM benchmarks

We now explore the accuracy and efficiency of the two MGEMM algorithms for various matrix structures. Clearly, the aim is to achieve greater accuracy than a simple SGEMM call on the GPU, but with minimal extra computational cost. Throughout this section, calculations were made using an Intel Xeon E5472 (Harpertown) CPU clocked at 3.0 GHz attached to an NVIDIA Tesla C1060.

10.4.1 Bitwise MGEMM benchmarks

First we examine the MGEMM algorithm described in Section 10.3.2. In the following, we chose to only benchmark the implementation using 3 multiplications, as in Eq. 10.29. Numerous test calculations showed that using 4 explicit multiplications gave no significant improvement in accuracy over the scheme with 3 multiplications. Since the latter is faster, it should obviously be favoured.

To quantify the accuracy, we found it useful to introduce a new metric which we call the *enhancement*, χ . Using DGEMM as the reference, if s and m are the root mean square (RMS) errors in a matrix element for SGEMM and MGEMM, respectively, then we define $\chi = s/m$.

Note that when multiplying two $N \times N$ matrices, the RMS errors are evaluated from N^2 data points. For the small matrices, therefore, the number of data points was insufficient to obtain reliable statistics. To remedy this, we repeated the smaller matrix multiplications (with different random numbers) to get more data points. The number of repeats was chosen to ensure that the standard error of the mean was at least two orders of magnitude smaller than the RMS error.

Fig. 10.2 shows the enhancement for the multiplication of random $N \times N$ matrices with varying number of upper bits, n_u , (and $n_l = 23$). Five curves are shown for $N \in \{1, 10, 100, 10^3, 10^4\}$. The matrices were initialized with numbers uniform in the range $[1, 2]$.

The enhancement is dominated by round-off errors in the $\mathbf{A}^u \mathbf{B}^u$ terms. On average, these errors are of the same order of magnitude as the SGEMM errors, thus MGEMM will only show an improvement when these errors vanish. We can achieve this by first remembering that a single-precision float can only store 24 significant bits in the mantissa. Therefore, if we only multiply floats with less than 12 significant bits, there will be no round-off error associated with the operation.

For $N = 1$, the effect is clear in Fig. 10.2: the enhancement suddenly decreases for $n_u > 12$. For $N > 1$, the number of bits, n_u , must be sufficiently small to also prevent round-off errors when accumulating results from many multiply-add operations. As N becomes larger, this effect is exacerbated, so the optimal n_u decreases.

Decreasing n_u , however, introduces larger errors into the other terms, such as $\mathbf{A}^u \mathbf{B}^l$. These errors are smaller than the $\mathbf{A}^u \mathbf{B}^u$ errors, but increase exponentially as n_u decreases. Decreasing n_u is therefore favourable until the $\mathbf{A}^u \mathbf{B}^u$ errors vanish, but there is no advantage to decreasing n_u further. In general, the combination of these effects means that the peak enhancement decreases with N .

Fig. 10.3 explores the peak enhancement in more detail. Each curve uses the optimal n_u values and initializes \mathbf{A} and \mathbf{B} with uniform random numbers on one of 5 intervals: $[1, W]$ where $W \in \{2, 100, 10^3, 10^4, 10^5\}$.

For $W = 2$, the enhancement decreases from $O(10^3)$ to $O(10^1)$ as N increases, for reasons discussed above. For errors corresponding to a classical random walk, we'd expect χ to decrease as \sqrt{N} , which implies a gradient of 1/2 in the log-log plot; this is approximately true for $W = 2$. For $W > 2$, however, the gradient in the log-log plot is reduced, and the enhancements are almost 2 orders of magnitude smaller for all $N > 1$. In summary, bitwise MGEMM is clearly most effective in a few special cases, such as for very small matrices, or when all the matrix elements are the same order of magnitude.

Table 10.1 highlights the issues regarding speedup when running bitwise MGEMM on the GPU compared to DGEMM on the CPU for different N . In addition, we catalogue the optimal

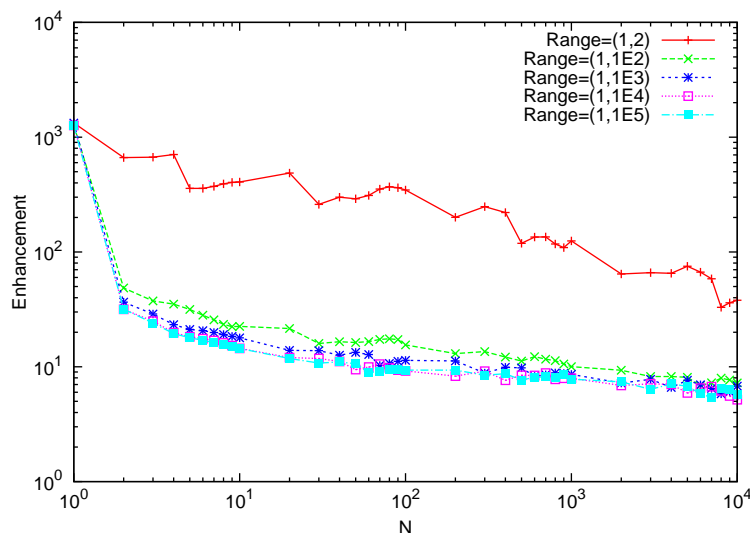


Figure 10.3: MGEMM peak enhancement versus matrix size using uniform random numbers on 5 ranges: $[1, 2]$, $[1, 100]$, $[1, 10^3]$, $[1, 10^4]$, and $[1, 10^5]$. Optimal values of n_u upper bits (and $n_l = 23$) were used for all data points.

values of n_u , as a function of N and W (the range of random numbers $[1, W]$.) As expected, the speedup increases as N increases, but unfortunately, bitwise MGEMM is only faster for the very largest matrices. The overheads of using the GPU, such as data transfer costs and memory access latencies, are well known; for $N < 1000$ the acceleration can be marginal (see also Fig. 10.4). In addition, in our simple implementation of Eq. 10.29, there is also a significant overhead from splitting and processing the \mathbf{A} and \mathbf{B} matrices. Equation 10.30 implies three matrix multiplications, which are independent of each other. Therefore, it has not escaped our attention that this scheme is parallelizable. In summary, we see up to 3 times speedup over CPU DGEMM for large N , but a slowdown for $N \leq 1000$.

10.4.2 Heterogeneous MGEMM benchmarks

We now benchmark the second MGEMM algorithm, described in Section 10.3.3. Fig. 10.4 shows the speedup for a variety of *GEMM calls on the GPU with respect to the size, N , of a $N \times N$ matrix, relative to the time taken for the corresponding DGEMM call on the CPU.

The input matrices were initialized with uniform random values in the range $[-1, 1]$ and then ‘salted’ with a fraction f_{salt} of random larger values in the range $[90, 110]$. Both SGEMM and DGEMM were timed using the GPU (the latter being possible for modern cards, and included for reference). Three MGEMM runs were tested, for $f_{\text{salt}} = 10^{-2}$, 10^{-3} and 10^{-4} . The size of the cutoff parameter δ was chosen such that all the salted elements were

N	Speedup	Optimal n_u				
		$W = 2$	$W = 100$	$W = 10^3$	$W = 10^4$	$W = 10^5$
1	0.01	12	12	12	12	12
10	0.01	10	6	6	6	6
100	0.07	9	5	4	4	4
1000	0.52	7	4	4	4	4
10000	2.87	5	3	3	3	3

Table 10.1: Speedups relative to CPU DGEMM and optimal number of upper bits, n_u , when using bitwise MGEMM for various matrix sizes with random elements on five intervals $[1, W]$.

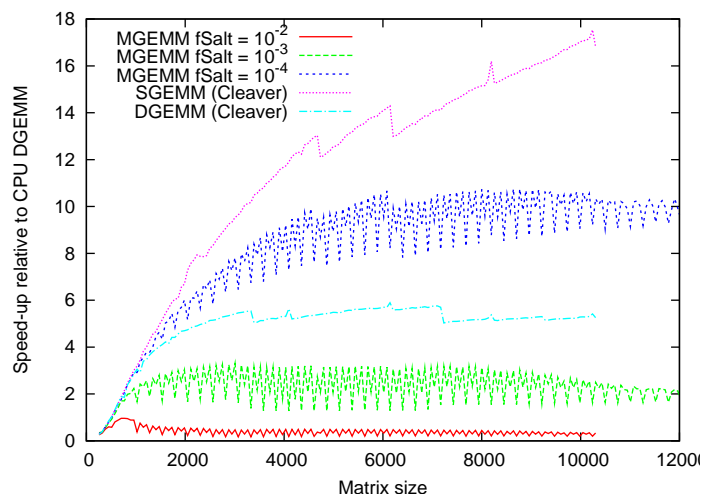


Figure 10.4: Speedup for various *GEMM calls as a function of matrix size. Most elements were in the range $[-1, 1]$, with the ‘salt’ values in the range $[90, 110]$. Times are scaled relative to running DGEMM on the CPU.

considered ‘large’. All timings were averaged over ten runs.

Running CUBLAS SGEMM is approximately 17.1 times faster than running DGEMM on the CPU for a matrix of size 10048×10048 , and is even faster for larger matrices. This represents an upper bound for the speedups we can hope to obtain with MGEMM for such matrices. Leveraging the GPU for small matrices is not effective, due to well-known overheads such as memory transfer and access latencies.

In contrast, the MGEMM speedups are strongly dependent on the fraction f_{salt} , which determines how much of the calculation is done in double-precision on the CPU. For $f_{\text{salt}} = 10^{-4}$, the speedups are approximately 10x, but for $f_{\text{salt}} = 10^{-3}$, speedups of approximately 2x relative to CPU DGEMM are observed. Indeed, for $f_{\text{salt}} = 10^{-2}$, MGEMM is actually slower than CPU DGEMM.

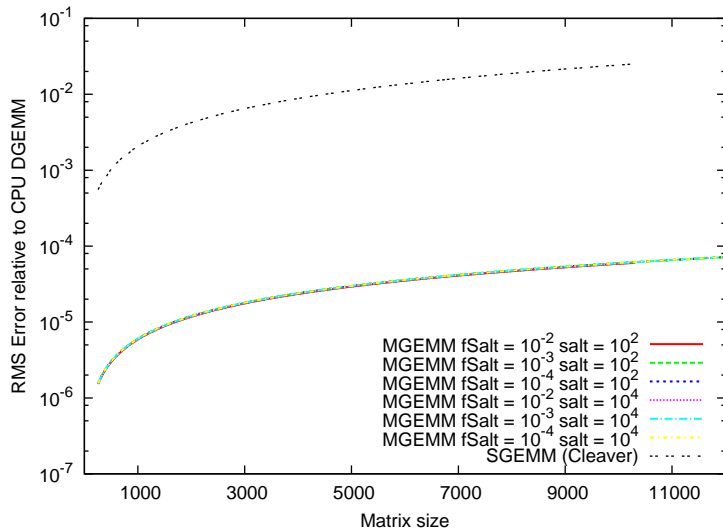


Figure 10.5: RMS error in a single element for various **GEMM** calls as a function of matrix size compared to CPU **DGEMM**. Background elements were in the range $[-1, 1]$, with the ‘salt’ values in the range $[90, 110]$ or $[9990, 10010]$.

Next we consider the accuracy enhancement when using **MGEMM** compared to **SGEMM**. In Fig. 10.5, we show the root mean square (RMS) errors of each matrix element relative to CPU **DGEMM** for different matrix sizes. As above, all the matrices were initialized with uniform random values in the range $[-1, 1]$, but now the salting sizes were grouped into two ranges: $[90, 110]$ and $[9990, 10010]$. Results are shown for **SGEMM** and **MGEMM** for various salting fractions.

As expected, **SGEMM** produces substantial errors. With a fraction of salted values, $f_{\text{salt}} = 1\%$, in the range $[90, 110]$, the errors are of $O(0.01)$ for the medium-sized matrices. In contrast, the errors are more than 2 orders of magnitude smaller when using **MGEMM**, and are the same regardless of the fraction or size of the salted elements. The limiting **MGEMM** errors are the same as the **SGEMM** errors for a pair of *unsalted* random matrices on $[-1, 1]$ because the **MGEMM** algorithm guarantees that all the salted contributions are computed on the CPU. Indeed, if the salts were larger or more numerous, the **SGEMM** errors would be even larger, but the **MGEMM** errors would be unchanged. This is in stark contrast to the behaviour of the bitwise **MGEMM** algorithm.

10.4.3 Comparison of **MGEMM** schemes

The behaviour of the two **MGEMM** algorithms is very different. First, the speed of the bitwise **MGEMM** depends only on the size of N , not on the elements of **A** or **B**. Moreover,

it is only 3 times faster than CPU DGEMM in the best case. In contrast, the speed of the heterogeneous MGEMM algorithm strongly depends on the fraction of ‘large’ elements. While it is up to 10 times faster than CPU DGEMM for a 0.01% fraction of large elements, for a 1.0% fraction, it is actually slower.

Concerning the accuracy of the two algorithms, consider the following cases. First, suppose the elements of \mathbf{A} and \mathbf{B} are random numbers on the interval $[1, 2]$. Mean errors produced by bitwise MGEMM are approximately 2 to 3 orders of magnitude smaller than SGEMM, depending on the matrix size (c.f. Fig. 10.2). In contrast, it is obvious that no value of δ can be chosen to make the heterogeneous MGEMM useful. At the other extreme, consider two matrices with a vast majority of elements in the range $[0, 1]$, and a small minority of scattered elements of unlimited size. Now, the heterogeneous MGEMM will be extremely useful, while the bitwise algorithm is likely to be quite ineffective due to the problems previously explained.

For this research, we are interested in accelerating quantum chemistry. It turns out that the relevant \mathbf{A} and \mathbf{B} for the RI-MP2 method have large N and very large W , suggesting that the heterogeneous algorithm should be the method of choice.

10.5 RI-MP2 acceleration benchmarks

We now show how the tools described above can accelerate full RI-MP2 quantum chemistry calculations on real molecules. To achieve this, we accelerate the evaluation of Eq. 10.20 and Eq. 10.21 using MGEMM running on a GPU. We compare to the use of standard DGEMM BLAS on the CPU, and CUBLAS SGEMM on the GPU. For all these benchmarks, we used an AMD Athlon 5600+ CPU clocked at 2.8 GHz, combined with an NVIDIA Tesla C1060 GPU with 4 GiB of RAM. The matrix cleaver and MGEMM were implemented in a modified version of the Q-Chem 3.1 RI-MP2 code described elsewhere [552].

As anticipated in the previous section, the bitwise MGEMM library does not give useful improvements compared to a standard CPU DGEMM. In the evaluation of Eq. 10.20, we observed no significant improvement in accuracy using bitwise MGEMM, and an enhancement of only 2.5 for Eq. 10.21. Thus we decided not to study the use of bitwise MGEMM further here. The results of applying the heterogeneous MGEMM algorithm (just MGEMM, from now on) were much more encouraging.

For our test systems we chose a set of linear alkanes (C_8H_{18} , $\text{C}_{16}\text{H}_{34}$, $\text{C}_{24}\text{H}_{50}$, $\text{C}_{32}\text{H}_{66}$, $\text{C}_{40}\text{H}_{82}$) as well as two molecules of pharmaceutical interest, the anti-cancer drugs taxol ($\text{C}_{47}\text{H}_{51}\text{NO}_{14}$) and valinomycin ($\text{C}_{54}\text{H}_{90}\text{N}_6\text{O}_{18}$). We used the cc-pVDZ and cc-pVTZ [139] atomic orbital basis sets throughout.

First, in Table 10.2 we benchmark the reference case of using either CUBLAS SGEMM

Molecule	Speedup		SGEMM energy error (kcal mol ⁻¹)
	SGEMM	DGEMM	
C ₈ H ₁₈	2.1	1.9	-0.05616
C ₁₆ H ₃₄	4.5	3.7	-0.12113
C ₂₄ H ₅₀	6.9	5.2	-0.62661
C ₃₂ H ₆₆	9.0	6.4	-0.75981
C ₄₀ H ₈₂	11.1	7.2	-1.12150
Taxol	11.3	7.1	-6.26276
Valinomycin	13.8	7.8	-9.99340

Table 10.2: Speedups using CUBLAS SGEMM and DGEMM and total energy errors relative to CPU DGEMM for various molecules in a cc-pVDZ basis.

or DGEMM for each test molecule using the double- ζ basis set. The table shows the speedup in computing the RI-MP2 correlation energy and the error relative to a standard CPU calculation (the DGEMM errors are negligible). The speedups and SGEMM errors are greater for the larger molecules, with the largest speedups observed for valinomycin: 13.8x and 7.8x, using SGEMM and DGEMM, respectively. However, while CUBLAS DGEMM gives essentially no loss of accuracy, the SGEMM error is approximately -10.0 kcal mol⁻¹, which is well beyond what is generally accepted as chemical accuracy.

Quantum chemistry generally aims to achieve a target accuracy of 1.0 kcal mol⁻¹. In Table 10.3, we explore the performance of MGEMM using a constant cutoff value of $\delta=1.0$ to try and reduce the SGEMM errors in Table 10.2. The results show speedups and total energy errors for each molecule in both the double- ζ and triple- ζ basis sets. In this particular case, we have limited the GPU to use only 256 MiB of RAM to mimic the capability of older cards and emphasize the use of the MGEMM cleaver. This will naturally result in a loss of speedup compared to utilizing a larger GPU memory. In the case of taxol the reduction is approximately 20%.

Molecule	Speedup		Energy error(kcal mol ⁻¹)	
	Double- ζ	Triple- ζ	Double- ζ	Triple- ζ
C ₈ H ₁₈	1.9	2.7	-0.01249	-0.03488
C ₁₆ H ₃₄	3.8	5.6	-0.00704	-0.04209
C ₂₄ H ₅₀	5.8	8.2	-0.14011	-0.33553
C ₃₂ H ₆₆	7.9	9.2	-0.08111	-0.29447
C ₄₀ H ₈₂	9.4	10.0	-0.13713	-0.51186
Taxol	9.3	10.0	-0.50110	-1.80076
Valinomycin	10.1	-	-1.16363	-

Table 10.3: MGEMM speedups and total energy errors with respect to CPU DGEMM for various molecules in a cc-pVDZ and cc-pVTZ basis.

Looking at Table 10.3, the trends are the same as in Table 10.2, but the **MGEMM** errors are approximately an order of magnitude less than the **SGEMM** errors (for the larger molecules). For valinomycin in the cc-pVDZ basis, the **SGEMM** speedup is reduced from 13.8x to 10.1x using **MGEMM**, but the error in the total energy is also reduced from $-10.0 \text{ kcal mol}^{-1}$ to $-1.2 \text{ kcal mol}^{-1}$, which is now very close to chemical accuracy. Moreover, while CUBLAS **DGEMM** clearly has the advantage (when available) of high accuracy, if $-1.2 \text{ kcal mol}^{-1}$ is deemed an acceptable accuracy, **MGEMM** could be favoured since the **DGEMM** speedup is only 7.8x compared to 10.1x. Note that the errors are larger for the triple- ζ basis simply because it requires more computation, which leads to greater error accumulation; this is a general issue not only for higher quality basis sets, but also for larger molecules using lower quality basis sets.

10.6 Conclusion

We have demonstrated how computational quantum chemistry can benefit from leveraging the power of graphical processing units in a very simple way. Our new tools are easy to incorporate into existing legacy codes where matrix multiplications involve a substantial fraction of the overall computational cost. Clearly, more efficient use of the GPU can be achieved in special cases by devoting time to rewriting and redesigning the algorithms for GPU architectures. However, this is often not a feasible option in practice, especially for a mature discipline such as quantum chemistry where we typically employ large program suites representing years or decades of coding effort.

In summary, our contribution has been the development, testing and benchmarking of a general black-box approach for the efficient GPU acceleration of matrix-matrix multiplications. In particular, our new library, which we call **MGEMM** [475], works for matrices of arbitrary size, even if too large for the whole computation to be held in the GPU's onboard memory. Moreover, while assuming only single-precision operations to be available on the GPU, we have demonstrated two algorithms whereby orders of magnitude greater accuracy can be achieved within the context of a mixed-precision approach.

To illustrate the utility of **MGEMM** for quantum chemistry, we combined it with the Q-Chem 3.1 [480] program package and computed the MP2 correlation energy of the 168-atom valinomycin molecule in a cc-pVDZ basis set. Using **SGEMM**, **MGEMM** and (GPU) **DGEMM**, we observed speedups of 13.8x, 10.1x and 7.8x, respectively, while **MGEMM** was an order of magnitude more accurate than **SGEMM**, thus achieving 'chemical accuracy'.

Traditionally, GPUs have only had single-precision (SP) support and it remains true that the vast majority of GPU cards worldwide currently do not have double precision (DP) capability. Indeed, we are interested in using commodity GPUs within a grid-computing

environment, such as that promoted by the Berkeley Open Infrastructure for Network Computing (BOINC) [66]. GPUs in a typical BOINC client do not have DP support, yet comprise a formidable resource worldwide.

Nevertheless, DP devices and co-processors are now available. Moreover, the trend seems to be towards the release of more advanced DP support in the future, such as the next-generation GPU from NVIDIA, currently code-named Fermi. Fermi will reportedly have a DP peak performance which is only a factor of 2 less than the SP performance. (For NVIDIA's C1060, the ratio is approximately 12).

It is therefore valid to question the potential of mixed-precision algorithms for next-generation GPU architectures. We believe this is an open issue. For example, practical calculations on GPUs are very often bound by memory bandwidth, rather than raw operation count. While DP cards are getting faster, this I/O bottleneck is likely to remain. In these cases, the transfer and processing of only SP data could effectively double the performance compared to naive DP calculations. Overall, we believe that mixed-precision algorithms could remain important for applications where the highest performance is a priority.

Part IV

Conclusions and future directions

Chapter 11

Conclusions and future directions

We have developed methods to study the response of molecules in nanoscale environments. In the case of SERS, the analyte is surrounded by nanostructured environments in the form of particles or surfaces. This causes a change in terms of the Raman response of the molecule with respect to the incident field. In the case of materials for organic photovoltaic applications, the molecular environment involves other molecules of a similar type (*e.g.*, a donor) and its counterpart (*e.g.*, the acceptor). The interaction between these two components is essential for enabling energy transfer processes. In both cases, the development of quantum chemistry methods has aided to understand phenomena present in spectroscopy and solar energy harvesting. As a third rail, the development and use of new hardware technologies has permitted the study of high-throughput approach in quantum chemistry, while GPUs have permitted an order of magnitude or more acceleration in post Hartree-Fock methods.

We have contributed to an understanding of the local effects of the metal–molecule interactions in SERS. Specifically, we have shown that there are both static and dynamic effects present in the chemical enhancement effect. To show this, we studied the immediate environment of the molecule by way of approximating the metal nanoparticle as a metal cluster. This work led us to propose a potential additional enhancement by means of adding a transition metal overlayer on top of a typical plasmonic substrate. We posited that the improved metal–molecule interactions would provide a *lending* effect. This effect was proven experimentally to yield an overall analytical enhancement.

We also developed a set of algorithms that we chose to name CheESE: Chemistry in Electrostatic Environments¹. This involved studying the effect of a molecule when inside a metallic environment by modifying the system’s boundary conditions such that they could

¹Quantum chemists should also enjoy the delight of naming their methods after something pronounceable, after all the NMR community has been doing this for some time, as they name their methods GRAPE or CORPSE. Why does our community like acronyms like B3LYP/6-31G*?

simulate a perfect metallic conductor. Our model system was studying benzene and how an excess electron could in fact be stabilized due to image charge effects. These methods were developed both for real-space and basis-set based quantum chemistry codes.

Our motivation for developing CheESE was to approximate the metallic environment to study SERS. In this way, we could go beyond local effects, prevalent in the cluster models, and account for image-charge and plasmon phenomena present in the metal nanoparticles of arbitrary shape. In fact, this implementation became a set of initial steps to consider the SERS effect in a truly multiscale fashion. To account for plasmon resonances, methods must be developed to go beyond simple Drude-like phenomenology of the plasmon effect. As mentioned in Chapter 1, it is perhaps useful to consider 2D jellium-like models for the metallic surfaces. Ultimately, the study of SERS must be motivated by experimental results, and therefore attempting to reproduce the nanoscale conditions will become of prime importance; especially when these conditions are very hard to elicit experimentally.

The massive search for new materials for organic photovoltaics has brought about a serious change of thinking for the analysis of quantum chemistry calculations. A researcher typically deals with tens or perhaps hundreds of results. The CEP, by means of distributed computing, has currently obtained tens of millions of results. We began developing and applying cheminformatics methods to complement those of quantum chemistry in the search for molecules. In a way, this was a necessary step to propose a molecular library of potential candidates. However, we went a step ahead and started investigating whether machine learning methods, prevalent in drug discovery and pattern recognition, will be useful to find better materials.

Although the material parameters that are important for organic solar cells are known, they are not always simple to calculate and much less easy to predict. The search for structure-property characteristics using machine learning then becomes increasingly important. We have begun this research with a relatively simple regression, however work left in progress promises the use of more complex machinery including classification tools and non-linear methods that rely on Bayesian statistics. At the same time, it is important to emphasize that machine learning is no substitute to theoretical methods. Rather, these methods should be used to enhance the properties that quantum chemistry methods yield. For instance, we are beginning to use ground state results to train a set with mixed topological and quantum chemistry values, leading to the smallest root-mean-square deviations we have yet found for any model.

We have also contributed to the field of accelerating quantum chemistry codes using heterogeneous architectures, namely GPUs. As this provided us with a different kind of computational resources, we strived to obtain a balance between implementing code for the new hardware, while keeping sections of code that were not necessary to port. As the GPU

field in chemistry was just blossoming, it was necessary to develop new tools and borrow and improve old ones, such as mixed-precision approaches. Our strategy to use GPUs for only certain parts of the calculations eased its implementation with Q-Chem, one of the more popular quantum chemistry programs. Its most current release contains the GPU acceleration of RIMP2, which we covered in Chapters 8–10.

The field of general purpose applications to GPUs matured in under five years. This has led to GPUs to become semi-ubiquitous in the newest supercomputer designs as well as in most or if not all modern workstations. In order to progress with the work presented in this dissertation, it is important to continue integrating all the different areas. Methods development under new setups and architectures is essential for enabling the research. Similarly, high-throughput methods used in computer science and other fields will become increasingly important to assess underlying correlations, which cannot always be extracted using current theories. The study of molecules under nanoscale environments must have feedback from different areas, even if they seem as disparate as SERS and organic photovoltaic generation. This means the development of a true multiscale implementation where molecular and nanometer-sized effects are considered will fuel quantum chemistry research in the years to come.

Appendix A

On the electron localization function

A.1 Motivation

The electron localization function (ELF) has become a useful tool to characterize the electronic structure of the system [53, 463, 464, 485]. ELF is designed to be inversely proportional to the probability of finding an electron of the same spin close to another, and to have a range from 0 to 1. The properties of the ELF have been widely understood. For instance, the ELF shines light on bonding, such that one can interpret regions where σ - or π -bonds dominate. This function has been used for several applications ranging from understanding reactivity such as electrophilic aromatic substitutions [165], electrophilic aminations [16], and even iron chalcogenide clusters [448].

In this appendix, we will begin by reviewing the concept of curvature, and then apply it to the Fermi hole, in Secs. A.3 and A.4. Finally, we will develop the formulas of ELF in Sec. A.5.

A.2 Curvature

For a set of Cartesian parametric equation $x = x(t)$, $y = y(t)$, where t is shown in Fig. A.1. The curvature is defined as [267]:

$$K = \frac{\partial\theta}{\partial s} \tag{A.1}$$

In turn, we can define these as the set of parametric equations:

$$K = \frac{\partial\theta/\partial t}{\partial s/\partial t} = \frac{\partial\theta/\partial t}{\sqrt{\left(\frac{\partial x}{\partial t}\right)^2 + \left(\frac{\partial y}{\partial t}\right)^2}} \tag{A.2}$$

We are able to obtain Eq. A.2 by noticing that ∂s can be represented by its x and y components, as seen in Fig. A.1. To get the curvature, we are left to find out what is $\partial\theta/\partial t$.

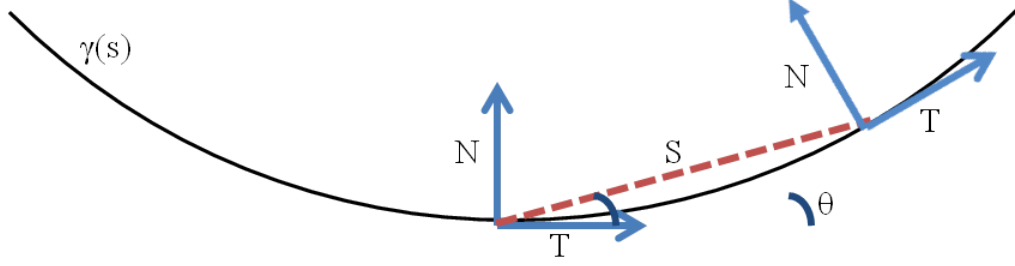


Figure A.1: Schematic representation of the curvature of a function $\gamma(s)$. s is the arc length; θ is the tangential angle; t is the tangent; N is the unit normal vector.

We begin by relating $\tan \theta$ with its derivative:

$$\tan \theta = \frac{\partial y}{\partial x} = \frac{\partial y / \partial t}{\partial x / \partial t} = \frac{y'}{x'} \implies \frac{\partial}{\partial t} \left(\frac{\partial y / \partial t}{\partial x / \partial t} \right) = \frac{x' - y'' - x'' - y'}{x'^2} \quad (\text{A.3})$$

$$= \sec^2 \theta \frac{\partial \theta}{\partial t} \quad (\text{A.4})$$

And so,

$$\sec^2 \theta = \frac{1}{\cos^2 \theta} = \frac{\left(\sqrt{\left(\frac{\partial x}{\partial t} \right)^2 + \left(\frac{\partial y}{\partial t} \right)^2} \right)^2}{\left(\frac{\partial x}{\partial t} \right)^2} = \frac{x'^2 + y'^2}{x'^2} \quad (\text{A.5})$$

So after combining Eqs. A.3– A.5 we obtain:

$$\frac{\partial \theta}{\partial t} = \frac{1}{\sec^2 \theta} \cdot \frac{x' - y'' - x'' - y'}{x'^2} = \frac{x' - y'' - x'' - y'}{x'^2 + y'^2} \quad (\text{A.6})$$

And finally, we get the curvature as:

$$K = \frac{x' - y'' - x'' - y'}{(x'^2 + y'^2)^{3/2}} \quad (\text{A.7})$$

Therefore, for a 2D plot in the form $y = f(x)$, the curvature will then be:

$$K = \frac{1y'' - 0}{(1 + y'^2)^{3/2}} = \frac{y''}{(1 + y'^2)^{3/2}} \quad (\text{A.8})$$

A.2.1 Interpretation

Returning to Fig. A.1, one can also understand the curvature as the acceleration, or rather, the derivative of the tangent T . Therefore, $K(s) = \|\Gamma''(s)\|$, where naturally the first derivative of the curve is the tangent T . Physically, the curvature measures how fast the vector is rotating. In this sense, if we could map the curvature to a circle (or sphere), the curvature will be the reciprocal of its radius.

A.3 The Fermi hole and its curvature

The pair density of a N -fermion system can be described by a many-body wavefunction, as derived by Dobson [135]:

$$n_2(\mathbf{r}_1, \sigma_1; \mathbf{r}_2, \sigma_2) = N(N-1) \sum_{\sigma_3 \dots \sigma_N} \int d^3\mathbf{r}_3 \dots \int d^3\mathbf{r}_N |\phi(\mathbf{r}_1, \sigma_1; \mathbf{r}_2, \sigma_2; \dots, \mathbf{r}_N, \sigma_N)|^2 \quad (\text{A.9})$$

$$= 2\Gamma(x_1, x_2 | x_1, x_2) \quad (\text{A.10})$$

$$= 2\Gamma_{2\sigma_1\sigma_2}(\mathbf{r}_1, \mathbf{r}_2) \quad (\text{A.11})$$

Notice that Γ is a pair density matrix. Becke uses Eq. A.11 to express n_2 . n_2 can be interpreted as the probability density of finding one particle at position \mathbf{r}_1 with spin projection σ_1 and simultaneously a second particle at \mathbf{r}_2 with spin projection σ_2 . The departure of n_2 from a product of spin densities: $n(\mathbf{r}_1, \sigma_1)n(\mathbf{r}_2, \sigma_2)$ is termed a ‘‘hole’’. This quantity has also been explored by Löwdin [318], and he expressed it originally as in Eq. A.10. We notice that for antiparallel spins, the hole is due to interparticle repulsion. Therefore, it is termed as the Coulomb hole. The hole for parallel spins has been termed the Fermi hole [318], due to the Fermi statistics that must be obeyed. The antisymmetry of the wavefunction implies that for $\sigma_1 = \sigma_2$ and $\mathbf{r}_1 = \mathbf{r}_2$, $\Gamma = 0$. Löwdin further derived that Γ behaves quadratically in the limit as $\mathbf{r}_{12} \rightarrow 0$, where $\mathbf{r}_{12} = |\mathbf{r}_1 - \mathbf{r}_2|$. This means that the gradient vanishes at $\mathbf{r}_{12} = 0$ as well.

The curvature of the hole, then becomes an interesting quantity in order to shed light on particle-particle interactions. In Sec. A.2, we derived the interesting properties for a 1D curvature in Sec. A.2. Briefly, for a 1D system, the curvature of any plot $y(x)$ is given by: $y''(1+y'^2)^{-3/2}$, but as we mentioned, the gradient goes to zero. Therefore, at $\mathbf{r}_{12} = 0$ the curvature depends on the second derivative and on the direction of approach. We can use the Laplacian to define the curvature at point \mathbf{r} :

$$C(\mathbf{r}, \sigma) = [\nabla'^2 n_2(\mathbf{r}, \sigma; \mathbf{r}', \sigma')]_{\mathbf{r}'=\mathbf{r}} \quad (\text{A.12})$$

What Dobson [135] finds for a Hartree-Fock system the curvature is related to a quantity D_s , such that:

$$\begin{aligned} C_{\text{HF}} &= 2n(\mathbf{r}, \sigma) \left[\tau(\mathbf{r}, \sigma) - \frac{1}{4} \frac{|\nabla n(\mathbf{r}, \sigma)|^2}{n(\mathbf{r}, \sigma)} \right] \\ &= 2n(\mathbf{r}, \sigma) D_\sigma \end{aligned} \quad (\text{A.13})$$

where D_σ is:

$$D_\sigma = \tau(\mathbf{r}, \sigma) - \frac{1}{4} \frac{|\nabla n(\mathbf{r}, \sigma)|^2}{n(\mathbf{r}, \sigma)}, \quad (\text{A.14})$$

and $\tau(\mathbf{r}, \sigma)$ is given by the sum of the square of the gradient of the occupied wavefunctions:

$$\tau(\mathbf{r}, \sigma) = \sum_{i, \text{occ}} |\nabla \phi_i(\mathbf{r}, \sigma)|^2 \quad (\text{A.15})$$

A.4 Laplacian of the pair density matrix

Becke and Edgecombe's work [53] uses the gradient of Eq. A.11, but their derivation is motivated by taking a spherically-averaged Taylor-expansion around the conditional pair probability, which also leaves a Laplacian term, and so the curvature will be related to the leading elements of the Taylor expansion. This will be developed in Sec. A.4 below.

Similar to Dobson, albeit in a more detailed way, we aim to understand what is the curvature of Eq. A.11. In order to reach this for the ELF formalism [53], Becke uses the negative of the Fermi hole density: the exchange charge density $n_{x\uparrow}$ [49]. After showing the Laplacian (and hence the curvature) of this function, we can go ahead and obtain it for Eq. A.11.

From Eq. A.11, we recall that the 2-body probability density for like spin pairs (*i.e.*, $\sigma = \uparrow$) is for two electrons at \mathbf{r} and $\mathbf{r} + \mathbf{s}$, respectively [49]:

$$\Gamma_{2\uparrow\uparrow}(\mathbf{r}, \mathbf{r} + \mathbf{s}) = n_{\uparrow}(\mathbf{r})n_{\uparrow}(\mathbf{r} + \mathbf{s}) - |n_{1\uparrow}(\mathbf{r}, \mathbf{r} + \mathbf{s})|^2, \quad (\text{A.16})$$

where $n_{1\uparrow}(\mathbf{r}, \mathbf{r} + \mathbf{s})$ is the exchange charge density and is given by:

$$n_{1\uparrow}(\mathbf{r}, \mathbf{r} + \mathbf{s}) = \sum_i^{\sigma=\uparrow} \phi_i^*(\mathbf{r})\phi_i(\mathbf{r} + \mathbf{s}). \quad (\text{A.17})$$

In this case, the summation is restricted to orbitals of $\sigma = \uparrow$ spin only.

The exchange energy can be given as the integral over \mathbf{r}_1 and \mathbf{r}_2 over \mathbf{r}_{12} . However, if one changes the variables to $\mathbf{r} = \mathbf{r}_1$ and $\mathbf{s} = \mathbf{r}_1 - \mathbf{r}_2$, and multiply and divide by $n_{\uparrow}(\mathbf{r})$:

$$E_{x\uparrow} = -\frac{1}{2} \int \int_{\mathbf{r}_{12}} \frac{1}{\mathbf{r}_{12}} n_{1\uparrow}(\mathbf{r}_1, \mathbf{r}_2) d\mathbf{r}_1 d\mathbf{r}_2 = -\frac{1}{2} \int \int \mathbf{s}^{-1} n_{\uparrow}(\mathbf{r}) n_{x\uparrow}(\mathbf{r}, \mathbf{r} + \mathbf{s}) d\mathbf{r} d\mathbf{s},$$

where $n_{x\uparrow}$ is the exchange charge density and is given as:

$$n_{x\uparrow}(\mathbf{r}, \mathbf{r} + \mathbf{s}) = \frac{|n_{1\uparrow}(\mathbf{r}, \mathbf{r} + \mathbf{s})|^2}{n_{\uparrow}(\mathbf{r})} \quad (\text{A.18})$$

Equation A.18 is also referred as the conditional probability of a finding a second σ_{\uparrow} electron at position $\mathbf{r} + \mathbf{s}$, when a first σ_{\uparrow} spin electron is located with certainty at position \mathbf{r} [53]. $n_{x\uparrow}$ must fulfill certain properties that are detailed elsewhere [49, 53]. As mentioned in Sec. A.3, one of the most important points is the small- \mathbf{s} behavior of $\Gamma_{2\uparrow\uparrow}$ near the reference point \mathbf{r} [48]. Löwdin showed that it scales quadratically as $\mathbf{s} = 0$ (*i.e.*, $r_{12} = 0$). Thus one can take a spherically-averaged Taylor expansion of $\Gamma_{2\uparrow\uparrow}$ to see its curvature [49].

A.4.1 Study of the short-range behavior of \mathbf{s}

Since we are interested in the region of small \mathbf{s} , we take the Taylor expansion of $n_{x\uparrow}(\mathbf{r}, \mathbf{r} + \mathbf{s})$ of \mathbf{s} around the reference point \mathbf{r} :

$$\begin{aligned} n_{x\uparrow}(\mathbf{r}, \mathbf{r} + \mathbf{s}) &= \sum_{n=0}^{\infty} \frac{1}{n!} (\mathbf{r} + \mathbf{s} - \mathbf{r})^n \frac{\partial}{\partial \mathbf{s}} n_{x\uparrow}(\mathbf{r}, \mathbf{r}_1) \Big|_{\mathbf{r}_1=\mathbf{r}'} \\ &= \sum_{n=0}^{\infty} \frac{s^n}{n!} \frac{\partial}{\partial \mathbf{s}} n_{x\uparrow}(\mathbf{r}, \mathbf{r}_1) \Big|_{\mathbf{r}_1=\mathbf{r}'} \\ &= e^{\mathbf{s} \cdot \nabla_1} n_{x\uparrow}(\mathbf{r}, \mathbf{r}_1) \Big|_{\mathbf{r}_1=\mathbf{r}'} \end{aligned} \quad (\text{A.19})$$

The spherical average of the Taylor expansion is developed in Sec. A.6. It shows that:

$$\langle e^{\mathbf{s} \cdot \nabla_1} \rangle = \left(1 + \frac{1}{3!} s^2 \nabla_1^2 + \dots \right) n_{x\uparrow}(\mathbf{r}, \mathbf{r}_1) \Big|_{\mathbf{r}_1=\mathbf{r}'} \quad (\text{A.20})$$

Going through the derivation, when we take the Laplacian of $n_{x\uparrow}(\mathbf{r}, \mathbf{r}_1) \Big|_{\mathbf{r}_1=\mathbf{r}'}$:

$$\nabla_1^2 n_{x\uparrow}(\mathbf{r}, \mathbf{r}_1) \Big|_{\mathbf{r}_1=\mathbf{r}'} = \nabla_1^2 \frac{|n_{1\uparrow}(\mathbf{r}, \mathbf{r}_1)|^2}{n_{\uparrow}(\mathbf{r})} = \frac{1}{n_{\uparrow}(\mathbf{r})} \nabla_1^2 |n_{1\uparrow}(\mathbf{r}, \mathbf{r}_1)|^2. \quad (\text{A.21})$$

Taking the Laplacian of the last term in Eq. A.21 yields Eq. A.22:

$$\begin{aligned} \nabla_1^2 |n_{1\uparrow}(\mathbf{r}, \mathbf{r}_1)|^2 &= \nabla_1^2 \sum_{ij} \phi_i(\mathbf{r}) \phi_i^*(\mathbf{r}_1) \phi_j^*(\mathbf{r}) \phi_j(\mathbf{r}_1) \Big|_{\mathbf{r}=\mathbf{r}_1} \\ &= \sum_{ij} \phi_i(\mathbf{r}) \nabla_1^2 (\phi_i^*(\mathbf{r}_1) \phi_j^*(\mathbf{r}) \phi_j(\mathbf{r}_1)) = \sum_{ij} \phi_i(\mathbf{r}) \phi_j^*(\mathbf{r}) \nabla_1^2 (\phi_i^*(\mathbf{r}_1) \phi_j(\mathbf{r}_1)) \\ &= \sum_{ij} \phi_i(\mathbf{r}) \phi_j^*(\mathbf{r}) [(\nabla_1^2 \phi_i^*(\mathbf{r}_1)) \phi_j(\mathbf{r}_1) + \phi_i^*(\mathbf{r}_1) \nabla_1^2 \phi_j(\mathbf{r}_1) + 2(\nabla \phi_i^*(\mathbf{r}_1) \cdot \nabla \phi_j(\mathbf{r}_1))] \Big|_{\mathbf{r}=\mathbf{r}_1} \\ &= \underbrace{\sum_j \phi_j^*(\mathbf{r}) \phi_j(\mathbf{r}_1)}_{n_{\uparrow}} \sum_i (\nabla_1^2 \phi_i^*(\mathbf{r}_1)) \phi_i(\mathbf{r}) + \underbrace{\sum_i \phi_i^*(\mathbf{r}_1) \phi_i(\mathbf{r})}_{n_{\uparrow}} \sum_j \phi_j^*(\mathbf{r}) \nabla_1^2 \phi_j(\mathbf{r}_1) + \\ &+ 2 \sum_i (\nabla \phi_i^*(\mathbf{r}_1)) \phi_i(\mathbf{r}) \cdot \sum_j (\nabla \phi_j(\mathbf{r}_1)) \phi_j^*(\mathbf{r}) \end{aligned} \quad (\text{A.22})$$

Afterwards, we go ahead and divide by $n_{\uparrow}(\mathbf{r})$, and evaluate $\mathbf{r} = \mathbf{r}_1$. At this limit, $n_{x\uparrow}(\mathbf{r}, \mathbf{r}) = n_{\uparrow}(\mathbf{r})$. We can cancel out the terms present in Eq. A.22:

$$\begin{aligned} \nabla_1^2 n_{x\uparrow}(\mathbf{r}, \mathbf{r}_1) \Big|_{\mathbf{r}_1=\mathbf{r}'} &= \sum_i \nabla^2 \phi_i^*(\mathbf{r}) \phi_i(\mathbf{r}) + \sum_i \phi_i^*(\mathbf{r}) \phi_i(\mathbf{r}) + \\ &+ \frac{2}{n_{\uparrow}(\mathbf{r})} \sum_i (\nabla \phi_i^*(\mathbf{r})) \phi_i(\mathbf{r}) \cdot \sum_j (\nabla \phi_j(\mathbf{r})) \phi_j^*(\mathbf{r}) \\ &= \nabla^2 n_{\uparrow}(\mathbf{r}) - 2\tau_{\uparrow}(\mathbf{r}) + \frac{2}{n_{\uparrow}(\mathbf{r})} \sum_i (\nabla \phi_i^*(\mathbf{r})) \phi_i(\mathbf{r}) \cdot \sum_j (\nabla \phi_j(\mathbf{r})) \phi_j^*(\mathbf{r}). \end{aligned} \quad (\text{A.23})$$

The last step is reached by using Eq. A.15 and by noting that at this limit,

$$\nabla^2 n_\uparrow = \nabla^2 \sum_i (\phi_i^* \phi_i) = \sum_i (\nabla^2 \phi_i^*) \phi_i + \sum_i \nabla^2 \phi_i^* (\phi_i) + 2 \sum_i (\nabla \phi_i^*) (\nabla \phi_i).$$

By considering ϕ to be real,

$$\nabla n_\uparrow = \nabla \sum_i \phi_i^* \phi_i = \sum_i (\nabla \phi_i^*) \phi_i + \sum_i \phi_i^* \nabla \phi_i = 2 \sum_i (\nabla \phi_i) \phi_i.$$

Therefore, under this assumption, the last term in Eq. A.23 is

$$\sum_i (\nabla \phi_i^*(\mathbf{r})) \phi_i(\mathbf{r}) \cdot \sum_j (\nabla \phi_j(\mathbf{r})) \phi_j^*(\mathbf{r}) = \left(\frac{1}{2} \nabla n_\uparrow \right) \cdot \left(\frac{1}{2} \nabla n_\uparrow \right).$$

Finally, Eq. A.23 yields:

$$\nabla_1^2 n_{x\uparrow}(\mathbf{r}, \mathbf{r}_1) |_{\mathbf{r}_1=\mathbf{r}'} = \nabla^2 n_\uparrow(\mathbf{r}) - 2\tau_\uparrow(\mathbf{r}) + \frac{1}{2} \frac{(\nabla n_\uparrow(\mathbf{r}))^2}{n_\uparrow(\mathbf{r})} \quad (\text{A.24})$$

The short-range behavior of the exchange charge density up to second order in \mathbf{s} is:

$$\langle n_{x\uparrow}(\mathbf{s}) \rangle = n_\uparrow + \frac{1}{6} \left(\nabla^2 n_\uparrow - 2\tau_\uparrow + \frac{1}{2} \frac{(\nabla n_\uparrow)^2}{n_\uparrow} \right) s^2.$$

We can do the same analysis, but with Eq. A.11, in the form of Eq. A.16:

$$\begin{aligned} \Gamma_{2\uparrow\uparrow}(\mathbf{r}, \mathbf{r}_1) |_{\mathbf{r}=\mathbf{r}_1} &= \nabla_1^2 \left(n_\uparrow(\mathbf{r}) n_\uparrow(\mathbf{r}_1) - |n_{1\uparrow}(\mathbf{r}, \mathbf{r} + \mathbf{s})|^2 \right) \\ &= n_\uparrow(\mathbf{r}) \nabla_1^2 n_\uparrow(\mathbf{r}) - \left(\nabla^2(\mathbf{r}) n_\uparrow(\mathbf{r}) - 2\tau_\uparrow(\mathbf{r}) + \frac{1}{2} \frac{(\nabla n_\uparrow(\mathbf{r}))^2}{n_\uparrow(\mathbf{r})} \right) n_\uparrow(\mathbf{r}) \\ \Gamma_{2\uparrow\uparrow}(\mathbf{r}, \mathbf{r}_1) |_{\mathbf{r}=\mathbf{r}_1} &= 2n_\uparrow(\mathbf{r}) \left(\tau_\uparrow(\mathbf{r}) - \frac{1}{4} \frac{(\nabla n_\uparrow(\mathbf{r}))^2}{n_\uparrow(\mathbf{r})} \right) \end{aligned} \quad (\text{A.25})$$

We reach Eq. A.25 by noticing that we have solved for the Laplacian in the last term of Eq. A.16 in Eq. A.24, but in this case the $1/n_\uparrow$ term does not appear, so that only affects the evaluation part. We notice that the inside part of Eq. A.25 is D_σ , derived in Eq. A.13. In fact, this is the quantity used by Becke and Edgecombe to define the electron localization function, which we will further develop in the next section.

A.5 The electron localization function

Once we have established the origin of D_σ , and its relation to the curvature of the Fermi hole, we can go ahead and see if it has any issue in chemistry. In fact, it turns out that the electron localization and D_σ are inversely related. If D_σ is large, this means that

the exchange hole curvature changes rapidly and thus, there is a small localization of the second electron, since the Fermi hole will be very deep. In the case of finite systems, for example, D_σ should decay to zero meaning that all the electrons are fully localized [53].

However, since D_σ is not bound from above, we need to use this quantity in a smarter way. Therefore, Becke and Edgecombe [53] proposed the following definition for ELF:

$$\text{ELF} = \frac{1}{1 + \chi_\sigma^2}, \quad (\text{A.26})$$

where $\chi_\sigma = D_\sigma/D_\sigma^0$, where D_σ^0 is the D-value of the uniform-density electron gas, which is used as reference:

$$D_\sigma^0 = \frac{3}{5} (6\pi)^{2/3} \rho_\sigma^{5/3}. \quad (\text{A.27})$$

What Eq. A.27 does is give a bound to the ELF in Eq. A.26. The range of ELF goes as $0 \leq \text{ELF} \leq 1$. $\text{ELF}=1$ corresponds to perfect localization, just as in the case of high D_σ , and $\text{ELF}=1/2$ corresponds to electron-gas-like probability of localization, as we are using the bound. Lastly, Becke and Edgecombe note that for multielectron systems in regions dominated by a single, localized, τ -electron orbital, the value of D_τ vanishes, and therefore the value of ELF approaches unity [53]. These tools are all what is necessary for ELF to give an understanding of bonding and electron pairs.

A.6 Solution of a spherically-averaged Taylor expansion

We take the spherical average of the Taylor expansion ¹, as used by Becke [48]:

$$\begin{aligned} \langle e^{s \cdot \nabla_1} \rangle &= \frac{1}{4\pi} \int_0^{2\pi} d\phi \int_{-1}^1 d \cos \theta e^{s \cdot \nabla_1 \cos \theta} = \frac{1}{2} \frac{e^{s \cdot \nabla_1 \cos \theta}}{s \cdot \nabla_1} \Big|_{-1}^1 \\ &= \frac{1}{2} \frac{e^{s \cdot \nabla_1} - e^{-s \cdot \nabla_1}}{s \cdot \nabla_1} = \frac{\sinh(s \cdot \nabla_1)}{s \cdot \nabla_1} \\ \langle e^{s \cdot \nabla_1} \rangle &= \frac{1}{4\pi} \int e^{s \cdot \nabla_1} d\Omega = \frac{\sinh(s \cdot \Omega_1)}{(s \cdot \nabla_1)} = \left(1 + \frac{1}{3!} s^2 \nabla_1^2 + \frac{1}{5!} s^4 \nabla_1^4 + \dots \right) \end{aligned} \quad (\text{A.28})$$

¹It is helpful to use a $f(r)$ term so that the solution of the integral is more evident

Appendix B

Resolution of the identity approximation

We have implemented a heterogeneous version of the resolution-of-the identity second order Møller-Plesset perturbation theory (RIMP2) [147, 572, 576, 333]. In the following, we provide a derivation of the RI approximation, which we used in Chapters 8–10. Moreover, we rely on the derivation presented by Hättig [210], though we will be consistent with the notation developed in the chapters mentioned above.

The electron repulsion integrals using atomic orbitals (AOs) η_α are obtained by solving the following four-index, two-electron integral:

$$(\mu\nu|\lambda\sigma) = \int \int \frac{\eta_\mu(\mathbf{r}_1)\eta_\nu(\mathbf{r}_1)\eta_\lambda(\mathbf{r}_2)\eta_\sigma(\mathbf{r}_2)}{|\mathbf{r}_1 - \mathbf{r}_2|} d\mathbf{r}_1 d\mathbf{r}_2. \quad (\text{B.1})$$

We exploit the linear dependence in the product space of atomic orbitals. This allows us to expand the products of the AOs as linear combinations of atom-centered auxiliary basis functions, P ,

$$\eta_\mu(\mathbf{r})\eta_\nu(\mathbf{r}) \approx \sum_P C_{\mu\nu,P} P(\mathbf{r}) \quad (\text{B.2})$$

The advantage of this approach is that the dimensionality is much smaller. The coefficients $C_{\mu\nu,P}$ can be determined through a least squares procedure. We define the error in the expansion of an orbital pair:

$$R_{\mu\nu}(\mathbf{r}_1) = \eta_\mu(\mathbf{r}_1)\eta_\nu(\mathbf{r}_1) - \sum_P C_{\mu\nu,P} P(\mathbf{r}_1). \quad (\text{B.3})$$

We can express the quadratic error in the Coulomb repulsion integrals $(\mu\nu|\lambda\sigma)$ as:

$$(R_{\mu\nu}|R_{\lambda\sigma}) = \int \int \frac{R_{\mu\nu}(\mathbf{r}_1)R_{\lambda\sigma}(\mathbf{r}_2)}{|\mathbf{r}_1 - \mathbf{r}_2|} d\mathbf{r}_1 d\mathbf{r}_2.$$

The integrals must fulfill the Schwartz inequality. Minimizing $(R_{\mu\nu}|R_{\lambda\sigma})$ with respect to the expansion coefficients C leads to the following conditions:

$$\frac{d}{dC_{\mu\nu,P}} (R_{\mu\nu}|R_{\lambda\sigma}) = 0 \Leftrightarrow (R_{\mu\nu}|P) = 0 \Leftrightarrow (\mu\nu|Q) - \sum_P C_{\mu\nu,P} (P|Q) = 0. \quad (\text{B.4})$$

We notice $(P|Q)$ is a 2-index, 2-electron quantity, while $(\mu\nu|Q)$ is a 3-index, 2-electron one:

$$\begin{aligned}(P|Q) &= \int \int \frac{P(\mathbf{r}_1)Q(\mathbf{r}_2)}{|\mathbf{r}_1 - \mathbf{r}_2|} d\mathbf{r}_1 d\mathbf{r}_2; \\ (\mu\nu|Q) &= \int \int \frac{\eta_\mu(\mathbf{r}_1)\eta_\nu(\mathbf{r}_1)Q(\mathbf{r}_2)}{|\mathbf{r}_1 - \mathbf{r}_2|} d\mathbf{r}_1 d\mathbf{r}_2.\end{aligned}$$

From Eq. B.4, we can obtain the coefficients $C_{\mu\nu,P}$. It is straightforward to obtain this by converting the equations into matrix form:

$$(\mu\nu|Q) - \sum_P C_{\mu\nu,P} (P|Q) = 0 \rightarrow \mathbf{D} - \mathbf{C}\mathbf{V} = 0 \rightarrow \mathbf{C} = \mathbf{D}\mathbf{V}^{-1},$$

where $\mathbf{D} = (\mu\nu|Q)$; \mathbf{C} are the matrix elements $C_{\mu\nu,P}$; and, $\mathbf{V} = (P|Q)$. Therefore, the coefficients are given by:

$$C_{\mu\nu,P} = \sum_Q (\mu\nu|Q) (Q|P)^{-1}, \quad (\text{B.5})$$

and we can express Eq. B.1 in terms of only 2 and 3-index quantities as:

$$(\widetilde{\mu\nu|\lambda\sigma}) = \sum_{P,Q} (\mu\nu|P) (P|Q)^{-1} (Q|\lambda\sigma). \quad (\text{B.6})$$

Finally, this idea is equivalent to an approximate insertion of the resolution-of-the-identity (RI),

$$I = \sum_m |m\rangle\langle m| \approx \sum_{P,Q} |P\rangle\langle P| (P|Q)^{-1} \langle Q| \quad (\text{B.7})$$

from which the name RI-MP2 is derived.

References

- [1] M. E. Abdelsalam, S. Mahajan, P. N. Bartlett, J. J. Baumberg, and A. E. Russell. Sers at structured palladium and platinum surfaces. *J. Am. Chem. Soc.*, **129**, 7399 (2007).
- [2] M. Abdi. Bonferroni and Sidak corrections for multiple comparisons. In N. Salkind, editor, *Encyclopedia of Measurement and Statistics*, pages 103–107. Sage, Thousand Oaks (CA), 2007.
- [3] C. Adamo and V. Barone. Toward reliable density functional methods without adjustable parameters: The PBE0 model. *J. Chem. Phys.*, **110**, 6158 (1999).
- [4] C. Adamo, M. Cossi, G. Scalmani, and V. Barone. Accurate static polarizabilities by density functional theory: Assessment of the PBE0 model. *Chem. Phys. Lett.*, **307**, 265 (1999).
- [5] C. Adamo, G. E. Scuseria, and V. Barone. Accurate excitation energies from time-dependent density functional theory: Assessing the PBE0 model. *J. Chem. Phys.*, **111**, 2889 (1999).
- [6] F. J. Adrian. Charge transfer effects in surface-enhanced Raman scattering. *J. Chem. Phys.*, **77**, 5302 (1982).
- [7] R. L. Aggarwal, L. W. Farrar, E. D. Diebold, and D. L. Polla. Measurement of the absolute Raman scattering cross section of the 1584 cm^{-1} band of benzenethiol and the surface-enhanced Raman scattering cross section enhancement factor for femtosecond laser-nanostructured substrates. *J. Raman Spectrosc.*, **40**, 1331 (2009).
- [8] D. Agrafiotis, D. Bandyopadhyay, J. Wegner, and H. Van Vlijmen. Recent advances in chemoinformatics. *J. Chem. Inf. Model.*, **47**, 1279 (2007).
- [9] R. Ahlrichs, M. Bär, M. Häser, H. Horn, and C. Kölmel. Electronic structure calculations on workstation computers: The program system TURBOMOLE. *Chem. Phys. Lett.*, **162**, 165 (1989). For current version see <http://www.turbomole.com>.
- [10] J. Ahrens, B. Hendrickson, G. Long, S. Miller, R. Ross, and D. Williams. Data-intensive science in the US DOE: Case studies and future challenges. *Comput. Sci. Eng.*, **13**, 14 (2011).

- [11] C. M. Aikens and G. C. Schatz. TDDFT studies of absorption and SERS spectra of pyridine interacting with Au₂₀. *J. Phys. Chem. A*, **110**, 13317 (2006).
- [12] A. C. Albrecht. On the theory of Raman intensities. *J. Chem. Phys.*, **34**, 1476 (1961).
- [13] M. G. Albrecht and J. A. Creighton. Anomalously intense Raman spectra of pyridine at a silver electrode. *J. Am. Chem. Soc.*, **99**, 5215 (1977).
- [14] J. Almlöf and P. R. Taylor. Computational aspects of direct SCF and MCSCF methods. In C. Dykstra, editor, *Advanced Theories and Computational Approaches to the Electronic Structure of Molecules*, pages 107–125. D. Reidel, Dordrecht, 1984.
- [15] R. A. Álvarez Puebla and L. M. Liz-Marzán. Environmental applications of plasmon assisted Raman scattering. *Energy Environ. Sci.*, **3**, 1011 (2010).
- [16] C. Amador-Bedolla, R. Salomón-Ferrer, W. A. Lester, J. A. Vázquez-Martínez, and A. Aspuru-Guzik. Reagents for electrophilic amination: A quantum Monte Carlo study. *J. Chem. Phys.*, **126**, 204308 (2007).
- [17] T. Ameri, G. Dennler, C. Lungenschmied, and C. J. Brabec. Organic tandem solar cells: A review. *Energy Environ. Sci.*, **2**, 347 (2009).
- [18] G. Anderegg and H. Wanner. Pyridine derivatives as complexing agents. xiii. the stability of the palladium(ii) complexes with pyridine, 2,2'-bipyridyl, and 1,10-phenanthroline. *Inorg. Chim. Acta*, **113**, 101 (1986).
- [19] A. G. Anderson, W. A. Goddard-III, and P. Schröder. Quantum Monte Carlo on graphical processing units. *Comput. Phys. Commun.*, **177**, 298 (2007).
- [20] D. P. Anderson. BOINC: A system for public-resource computing and storage. In *Proceedings of the 5th IEEE/ACM International Workshop on Grid Computing*, GRID '04, pages 4–10, Washington, DC, 2004. IEEE Computer Society.
- [21] J. A. Anderson, C. D. Lorenz, and A. Travesset. General purpose molecular dynamics simulations fully implemented on graphics processing units. *J. Comput. Phys.*, **227**, 5342 (2008).
- [22] S. Ando, R. Murakami, J. Nishida, H. Tada, Y. Inoue, S. Tokito, and Y. Yamashita. n-Type organic field-effect transistors with very high electron mobility based on thiazole oligomers with trifluoromethylphenyl groups. *J. Am. Chem. Soc.*, **127**, 14996 (2005).
- [23] S. Ando, J. Nishida, H. Tada, Y. Inoue, S. Tokito, and Y. Yamashita. High performance n-type organic field-effect transistors based on π -electronic systems with trifluoromethylphenyl groups. *J. Am. Chem. Soc.*, **127**, 5336 (2005).
- [24] D. Andrae, U. Häußermann, M. Dolg, H. Stoll, and H. Preuß. Energy-adjusted ab initio pseudopotentials for the second and third row transition elements. *Theor. Chim. Acta*, **77**, 123 (1990).

- [25] J.-M. André, J. Delhalle, and J.-L. Brédas. *Quantum Chemistry Aided Design of Organic Polymers: An Introduction to the Quantum Chemistry of Polymers and Its Applications*. World Scientific, Singapore, 1991.
- [26] J. N. Anker, W. P. Hall, O. Lyandres, N. C. Shah, J. Zhao, and R. P. Van Duyne. Biosensing with plasmonic nanosensors. *Nature Mater.*, **7**, 442 (2008).
- [27] J. Anthony. Small-molecule, nonfullerene acceptors for polymer bulk heterojunction organic photovoltaics. *Chem. Mater.*, **23**, 583 (2011).
- [28] K. Appell, J. J. Baldwin, and W. J. Egan. Combinatorial chemistry and high-throughput screening in drug discovery and development. In S. Ahuja and S. Scypinski, editors, *Handbook of Modern Pharmaceutical Analysis*, volume 3 of *Separation Science and Technology*, pages 23–56. Academic Press, San Diego, 2001.
- [29] R. F. Aroca. *Surface Enhanced Vibrational Spectroscopy*. Wiley, Chichester, 2006.
- [30] R. F. Aroca, R. E. Clavijo, M. D. Halls, and H. B. Schlegel. Surface-enhanced Raman spectra of phthalimide. interpretation of the sers spectra of the surface complex formed on silver islands and colloids. *J. Phys. Chem. A*, **104**, 9500 (2000).
- [31] V. Arora and A. Bakhshi. Molecular designing of novel ternary copolymers of donor-acceptor polymers using genetic algorithm. *Chem. Phys.*, **373**, 307 (2010).
- [32] H. A. Atwater and A. Polman. Plasmonics for improved photovoltaic devices. *Nature Mater.*, **9**, 205 (2010).
- [33] M. D. Austin, H. Ge, W. Wu, M. Li, Z. Yu, D. Wasserman, S. A. Lyon, and S. Y. Chou. Fabrication of 5 nm linewidth and 14 nm pitch features by nanoimprint lithography. *Appl. Phys. Lett.*, **84**, 5299 (2004).
- [34] P. Ayers and J. Melin. Computing the Fukui function from ab initio quantum chemistry: Approaches based on the extended Koopmans' theorem. *Theor. Chem. Acc.*, **117**, 371 (2007).
- [35] B. Azzopardi, C. J. M. Emmott, A. Urbina, F. C. Krebs, J. Mutale, and J. Nelson. Economic assessment of solar electricity production from organic-based photovoltaic modules in a domestic environment. *Energy Environ. Sci.*, **4**, 3741 (2011).
- [36] R. F. Bailey-Salzman, B. P. Rand, and S. R. Forrest. Semitransparent organic photovoltaic cells. *Appl. Phys. Lett.*, **88**, 233502 (2006).
- [37] C. D. Bain, E. B. Troughton, Y. T. Tao, J. Evall, G. M. Whitesides, and R. G. Nuzzo. Formation of monolayer films by the spontaneous assembly of organic thiols from solution onto gold. *J. Am. Chem. Soc.*, **111**, 321 (1989).
- [38] K. Baishya, J. C. Idrobo, S. Ögüt, M. Yang, K. Jackson, and J. Jellinek. Optical absorption spectra of intermediate-size silver clusters from first principles. *Phys. Rev. B*, **78**, 075439 (2008).

- [39] J. Bajorath. Selected concepts and investigations in compound classification, molecular descriptor analysis, and virtual screening. *J. Chem. Inf. Comput. Sci.*, **41**, 233 (2001).
- [40] J. Bajorath. Integration of virtual and high-throughput screening. *Nat. Rev. Drug Discovery*, **1**, 882 (2002).
- [41] J. Bajorath. *Cheminformatics: Concepts, Methods, and Tools for Drug Discovery*. Humana Press, Totowa, NJ, 2010.
- [42] P. V. Balachandran, S. R. Broderick, and K. Rajan. Identifying the ‘inorganic gene’ for high-temperature piezoelectric perovskites through statistical learning. *Proc. R. Soc. A* (2011).
- [43] P. B. Balbuena and J. M. Seminario, editors. *Nanomaterials: Design and Simulation*, volume 18 of *Theoretical and Computational Chemistry*. Elsevier, Amsterdam, 2007.
- [44] R. Bauernschmitt and R. Ahlrichs. Treatment of electronic excitations within the adiabatic approximation of time dependent density functional theory. *Chem. Phys. Lett.*, **256**, 454 (1996).
- [45] P. M. Beaujuge, C. M. Amb, and J. R. Reynolds. Spectral engineering in π -conjugated polymers with intramolecular donor-acceptor interactions. *Acc. Chem. Res.*, **43**, 1396 (2010).
- [46] N. Beaumont, I. Hancox, P. Sullivan, R. A. Hatton, and T. S. Jones. Increased efficiency in small molecule organic photovoltaic cells through electrode modification with self-assembled monolayers. *Energy Environ. Sci.*, **4**, 1708 (2011).
- [47] D. M. Beazley. *Python Essential Reference*. Addison-Wesley, Upper Saddle River, NJ, 4th edition, 2009.
- [48] A. D. Becke. Hartree-Fock exchange energy of an inhomogeneous electron gas. *Int. J. Quantum Chem.*, **23**, 1915 (1983).
- [49] A. D. Becke. Local exchange-correlation approximations and first-row molecular dissociation energies. *Int. J. Quantum Chem.*, **27**, 585 (1985).
- [50] A. D. Becke. Density-functional exchange-energy approximation with correct asymptotic behavior. *Phys. Rev. A*, **38**, 3098 (1988).
- [51] A. D. Becke. Density-functional thermochemistry. III. The role of exact exchange. *J. Chem. Phys.*, **98**, 5648 (1993).
- [52] A. D. Becke. A new mixing of Hartree-Fock and local density-functional theories. *J. Chem. Phys.*, **98**, 1372 (1993).
- [53] A. D. Becke and K. E. Edgecombe. A simple measure of electron localization in atomic and molecular systems. *J. Chem. Phys.*, **92**, 5397 (1990).

- [54] A. Bedeloglu, A. Demir, Y. Bozkurt, and N. S. Sariciftci. A flexible textile structure based on polymeric photovoltaics using transparent cathode. *Synth. Met.*, **159**, 2043 (2009).
- [55] R. G. Belleman, J. Bédorf, and S. F. P. Zwart. High performance direct gravitational N-body simulations on graphics processing units II: An implementation in CUDA. *New Astronomy*, **13**, 103 (2008).
- [56] T. Benanti and D. Venkataraman. Organic solar cells: An overview focusing on active layer morphology. *Photosynth. Res.*, **87**, 73 (2006).
- [57] S. Bertho, I. Haeldermans, A. Swinnen, W. Moons, T. Martens, L. Lutsen, D. Vanderzande, J. Manca, A. Senes, and A. Bonfiglio. Influence of thermal ageing on the stability of polymer bulk heterojunction solar cells. *Sol. Energy Mater. Sol. Cells*, **91**, 385 (2007).
- [58] S. Bertho, G. Janssen, T. J. Cleij, B. Conings, W. Moons, A. Gadisa, J. D'Haen, E. Goovaerts, L. Lutsen, J. Manca, and D. Vanderzande. Effect of temperature on the morphological and photovoltaic stability of bulk heterojunction polymer: Fullerene solar cells. *Sol. Energy Mater. Sol. Cells*, **92**, 753 (2008).
- [59] H. A. Bethe and E. E. Salpeter. *Quantum Mechanics of One and Two Electron Atoms*. Plenum, New York, 1977.
- [60] K. B. Biggs, J. P. Camden, J. N. Anker, and R. P. V. Duyne. Surface-enhanced Raman spectroscopy of benzenethiol adsorbed from the gas phase onto silver film over nanosphere surfaces: Determination of the sticking probability and detection limit time. *J. Phys. Chem. A*, **113**, 4581 (2009).
- [61] C. M. Bishop. *Pattern Recognition and Machine Learning*. Springer, Berlin, 2nd edition, 2007.
- [62] C. M. Bishop. *Pattern Recognition and Machine Learning (Information Science and Statistics)*. Springer, 2007.
- [63] N. Blouin, A. Michaud, D. Gendron, S. Wakim, E. Blair, R. Neagu-Plesu, M. Belletête, G. Durocher, Y. Tao, and M. Leclerc. Toward a rational design of poly(2,7-carbazole) derivatives for solar cells. *J. Am. Chem. Soc.*, **130**, 732 (2008).
- [64] N. Blouin, A. Michaud, and M. Leclerc. A low-bandgap poly(2,7-carbazole) derivative for use in high-performance solar cells. *Adv. Mater.*, **19**, 2295 (2007).
- [65] R. Bohacek, C. Marin, and W. Guida. The art and practice of structure-based drug design: A molecular modeling perspective. *Med. Res. Rev.*, **16**, 3 (1996).
- [66] J. Bohannon. Grassroots supercomputing. *Science*, **308**, 310 (2005).
- [67] M. Boness, I. Larkin, J. Hasted, and L. Moore. Virtual negative ion spectra of hydrocarbons. *Chem. Phys. Lett.*, **1**, 292 (1967).

- [68] H. Borchert. Elementary processes and limiting factors in hybrid polymer/nanoparticle solar cells. *Energy Environ. Sci.*, **3**, 1682 (2010).
- [69] M. Born and R. Oppenheimer. Zur quantentheorie der molekeln. *Ann. Phys.*, **389**, 457 (1927).
- [70] P. M. Borsenberger and J. J. Fitzgerald. Effects of the dipole moment on charge transport in disordered molecular solids. *J. Phys. Chem.*, **97**, 4815 (1993).
- [71] M. Boxwell. *Solar Electricity Handbook – 2011 Edition*. Greenstream Publishing, Ryton on Dunsmore, UK, 4th edition, 2011.
- [72] C. J. Brabec. Organic photovoltaics: Technology and market. *Sol. Energy Mater. Sol. Cells*, **83**, 273 (2004).
- [73] C. J. Brabec, A. Cravino, D. Meissner, N. Sariciftci, T. Fromherz, M. Rispens, L. Sanchez, and J. Hummelen. Origin of the open circuit voltage of plastic solar cells. *Adv. Funct. Mater.*, **11**, 374 (2001).
- [74] C. J. Brabec, V. Dyakonov, J. Parisi, and N. S. Sariciftci. *Organic Photovoltaics: Concepts and Realization*. Springer, Berlin, 2010.
- [75] C. J. Brabec, V. Dyakonov, and U. Scherf. *Organic Photovoltaics: Materials, Device Physics, and Manufacturing Technologies*. Wiley-VCH, Weinheim, 2008.
- [76] C. J. Brabec, S. E. Shaheen, C. Winder, N. S. Sariciftci, and P. Denk. Effect of LiF/metal electrodes on the performance of plastic solar cells. *Appl. Phys. Lett.*, **80**, 1288 (2002).
- [77] J.-L. Brédas, D. Beljonne, V. Coropceanu, and J. Cornil. Charge-transfer and energy-transfer processes in π -conjugated oligomers and polymers: A molecular picture. *Chem. Rev.*, **104**, 4971 (2004).
- [78] J.-L. Brédas, J. E. Norton, J. Cornil, and V. Coropceanu. Molecular understanding of organic solar cells: The challenges. *Acc. Chem. Res.*, **42**, 1691 (2009).
- [79] H.-P. Breuer and F. Petruccione. *The Theory of Open Quantum Systems*. Oxford University Press, USA, 2002.
- [80] British Petroleum. BP Statistical Review of World Energy. <http://bp.com/statisticalreview>, 2011.
- [81] G. Brocks and A. Tol. Small band gap semiconducting polymers made from dye molecules: Polysquaraines. *J. Phys. Chem.*, **100**, 1838 (1996).
- [82] F. Brown. Chemoinformatics — a ten year update. *Curr. Opin. Drug Discov. Devel.*, **8**, 298 (2005).
- [83] F. K. Brown. Chemoinformatics: What is it and how does it impact drug discovery. In J. A. Bristol, editor, *Annual Reports in Medicinal Chemistry*, volume 33, pages 375 – 384. Academic Press, 1998.

- [84] P. Brown, C. Woods, S. McIntosh-Smith, and F. R. Manby. Massively multicore parallelization of Kohn-Sham Theory. *J. Chem. Theory Comput.*, **4**, 1620 (2008).
- [85] F. R. Burden. Quantitative structure-activity relationship studies using Gaussian processes. *J. Chem. Inf. Comput. Sci.*, **41**, 830 (2001).
- [86] W. B. Cai, B. Ren, X. Q. Li, C. X. She, F. M. Liu, X. W. Cai, and Z. Q. Tian. Investigation of surface-enhanced Raman scattering from platinum electrodes using a confocal Raman microscope: Dependence of surface roughening pretreatment. *Surf. Sci.*, **406**, 9 (1998).
- [87] J. P. Camden, J. A. Dieringer, J. Zhao, and R. P. Van Duyne. Controlled plasmonic nanostructures for surface-enhanced spectroscopy and sensing. *Acc. Chem. Res.*, **41**, 1653 (2008).
- [88] A. Campion and P. Kambhampati. Surface-enhanced Raman scattering. *Chem. Soc. Rev.*, **27**, 241 (1998).
- [89] G. Cao and Y. Wang. *Nanostructures and Nanomaterials: Synthesis, Properties, and Applications*. World Scientific series in nanoscience and nanotechnology. World Scientific, Singapore, 2010.
- [90] F. Capasso, J. N. Munday, D. Iannuzzi, and H. B. Chan. Casimir forces and quantum electrodynamic torques: Physics and nanomechanics. *IEEE J. Sel. Top. Quantum Electron.*, **13**, 400 (2007).
- [91] K. T. Carron and L. G. Hurley. Axial and azimuthal angle determination with surface-enhanced Raman spectroscopy: Thiophenol on copper, silver, and gold metal surfaces. *J. Chem. Phys.*, **95**, 9979 (1991).
- [92] M. E. Casida. Time-dependent density-functional response theory for molecules. In D. P. Chong, editor, *Recent Advances in Density Functional Methods, Part I*, pages 155–192. World Scientific, Singapore, 1995.
- [93] A. Castro, H. Appel, M. Oliveira, C. A. Rozzi, X. Andrade, F. Lorenzen, M. A. L. Marques, E. K. U. Gross, and A. Rubio. octopus: A tool for the application of time-dependent density functional theory. *Phys. Status Solidi B*, **243**, 2465 (2006).
- [94] C. Catlett et al. Teragrid: Analysis of organization, system architecture, and middle-ware enabling new types of applications. *Adv. Parallel Comput.*, **16**, 225 (2008).
- [95] ChemAxon. Marvin 5.3.2, 2011, <http://www.chemaxon.com>.
- [96] H. Chen, J. Hou, S. Zhang, Y. Liang, G. Yang, Y. Yang, L. Yu, Y. Wu, and G. Li. Polymer solar cells with enhanced open-circuit voltage and efficiency. *Nature Photon.*, **3**, 649 (2009).
- [97] H. Chen, J. M. McMahon, M. A. Ratner, and G. C. Schatz. Classical electrodynamics coupled to quantum mechanics for calculation of molecular optical properties: A RT-TDDFT/FDTD approach. *The Journal of Physical Chemistry C*, **114**, 14384 (2010).

- [98] J. Chen and Y. Cao. Development of novel conjugated donor polymers for high-efficiency bulk-heterojunction photovoltaic devices. *Acc. Chem. Res.*, **42**, 1709 (2009).
- [99] W. L. Chen. Chemoinformatics: Past, present, and future. *J. Chem. Inf. Model.*, **46**, 2230 (2006).
- [100] D. L. Cheung and A. Troisi. Modelling charge transport in organic semiconductors: From quantum dynamics to soft matter. *Phys. Chem. Chem. Phys.*, **10**, 5941 (2008).
- [101] C. L. Chochos and S. A. Choulis. How the structural deviations on the backbone of conjugated polymers influence their optoelectronic properties and photovoltaic performance. *Prog. Polym. Sci.*, **36**, 1326 (2011).
- [102] Y. C. Choi, W. Y. Kim, K.-S. Park, P. Tarakeshwar, K. S. Kim, T.-S. Kim, and J. Y. Lee. Role of molecular orbitals of the benzene in electronic nanodevices. *J. Chem. Phys.*, **122**, 094706 (2005).
- [103] D. P. Chong, O. V. Gritsenko, and E. J. Baerends. Interpretation of the Kohn-Sham orbital energies as approximate vertical ionization potentials. *J. Chem. Phys.*, **116**, 1760 (2002).
- [104] Y. Chu, M. G. Banaee, and K. B. Crozier. Double-resonance plasmon substrates for surface-enhanced Raman scattering with enhancement at excitation and Stokes frequencies. *ACS Nano*, **4**, 2804 (2010).
- [105] Y. Chu, E. Schonbrun, T. Yang, and K. B. Crozier. Experimental observation of narrow surface plasmon resonances in gold nanoparticle arrays. *Appl. Phys. Lett.*, **93**, 181108 (2008).
- [106] Y. Chu, D. Wang, W. Zhu, and K. B. Crozier. Double resonance surface enhanced Raman scattering substrates: An intuitive coupled oscillator model. *Opt. Express*, **19**, 14919 (2011).
- [107] Clean Energy Project. <http://cleanenergy.harvard.edu> (accessed august 10, 2011).
- [108] D. Clery. IBM offers free number crunching for humanitarian research projects. *Science*, **308**, 773 (2005).
- [109] K. M. Coakley and M. D. McGehee. Conjugated polymer photovoltaic cells. *Chem. Mater.*, **16**, 4533 (2004).
- [110] S. Colella, M. Mazzeo, R. Grisorio, E. Fabiano, G. Melcarne, S. Carallo, M. D. Angione, L. Torsi, G. P. Suranna, F. della Sala, P. Mastrorilli, and G. Gigli. Monodispersed molecular donors for bulk hetero-junction solar cells: From molecular properties to device performances. *Chem. Commun.*, **46**, 6273 (2010).
- [111] A. Colsmann, A. Puetz, A. Bauer, J. Hanisch, E. Ahlswede, and U. Lemmer. Efficient semi-transparent organic solar cells with good transparency color perception and rendering properties. *Adv. Energy Mater.*, **1**, 599 (2011).

- [112] J. J. Conti, P. D. Holtberg, J. A. Beamon, A. M. Schaal, J. C. Ayoub, and J. T. Turnure. *Annual Energy Outlook 2011*. U.S. Energy Information Administration, Washington, DC, 2011.
- [113] J. J. Conti, P. D. Holtberg, J. A. Beamon, A. M. Schaal, G. E. Sweetnam, and A. S. Kydes. *Annual Energy Outlook 2010*. National Energy Information Center, U. S. Energy Information Administration, 2010.
- [114] D. Coppersmith and S. Winograd. Matrix multiplication via arithmetic progressions. *J. Symbolic Comput.*, **9**, 251 (1990).
- [115] S. Corni and J. Tomasi. Enhanced response properties of a chromophore physisorbed on a metal particle. *J. Chem. Phys.*, **114**, 3739 (2001).
- [116] S. Corni and J. Tomasi. Surface enhanced Raman scattering from a single molecule adsorbed on a metal particle aggregate: A theoretical study. *J. Chem. Phys.*, **116**, 1156 (2002).
- [117] S. Corni and J. Tomasi. From metal nanoparticles and nanoparticles aggregates with continuum models. *Top. Appl. Phys.*, **124**, 105 (2006).
- [118] A. Cravino. Origin of the open circuit voltage of donor-acceptor solar cells: Do polaronic energy levels play a role? *Appl. Phys. Lett.*, **91**, 243502 (2007).
- [119] J. A. Creighton. Surface Raman electromagnetic enhancement factors for molecules at the surface of small isolated metal spheres: The determination of adsorbate orientation from SERS relative intensities. *Surf. Sci.*, **124**, 209 (1983).
- [120] L. A. Curtiss, K. Raghavachari, P. C. Redfern, and J. A. Pople. Assessment of Gaussian-2 and density functional theories for the computation of enthalpies of formation. *J. Chem. Phys.*, **106**, 1063 (1997).
- [121] DALTON. A molecular electronic structure program (2011), see <http://www.daltonprogram.org>.
- [122] W. W. Daniel. *Bioestadística: Base para el Análisis de las Ciencias de la Salud*. Editorial Limusa, 2006.
- [123] P. Deglmann, F. Furche, and R. Ahlrichs. An efficient implementation of second analytical derivatives for density functional methods. *Chem. Phys. Lett.*, **362**, 511 (2002).
- [124] M. Dell'Angela, G. Kladnik, A. Cossaro, A. Verdini, M. Kamenetska, I. Tamblyn, S. Y. Quek, J. B. Neaton, D. Cvetko, A. Morgante, and L. Venkataraman. Relating energy level alignment and amine-linked single molecule junction conductance. *Nano Lett.*, **10**, 2470 (2010).
- [125] G. Dennler, M. C. Scharber, and C. J. Brabec. Polymer-fullerene bulk-heterojunction solar cells. *Adv. Mater.*, **21**, 1323 (2009).

- [126] A. E. DePrince and J. R. Hammond. Coupled Cluster Theory on Graphics Processing Units I. The Coupled Cluster Doubles Method. *J. Chem. Theory Comput.*, **7**, 1287 (2011).
- [127] E. D. Diebold, N. H. Mack, S. K. Doorn, and E. Mazur. Femtosecond laser-nanostructured substrates for surface-enhanced Raman scattering. *Langmuir*, **25**, 1790 (2009).
- [128] E. D. Diebold, P. Peng, and E. Mazur. Isolating surface-enhanced Raman scattering hot spots using multiphoton lithography. *J. Am. Chem. Soc.*, **131**, 16356 (2009).
- [129] J. A. Dieringer, A. D. McFarland, N. C. Shah, D. A. Stuart, A. V. Whitney, C. R. Yonzon, M. A. Young, X. Zhang, and R. P. Van Duyne. Surface enhanced Raman spectroscopy: New materials, concepts, characterization tools, and applications. *Faraday Discuss.*, **132**, 9 (2006).
- [130] J. A. Dieringer, K. L. Wustholz, D. J. Masiello, J. P. Camden, S. L. Kleinman, G. C. Schatz, and R. P. Van Duyne. Surface-enhanced Raman excitation spectroscopy of a single rhodamine 6G molecule. *J. Am. Chem. Soc.*, **131**, 849 (2009).
- [131] P. A. M. Dirac. Quantum mechanics of many-electron systems. *Proc. R. Soc. London, Ser. A*, **123**, 714 (1929).
- [132] R. A. Distasio, R. P. Steele, Y. M. Rhee, Y. Shao, and M. Head-Gordon. An improved algorithm for analytical gradient evaluation in resolution-of-the-identity second-order Møller-Plesset perturbation theory: Application to alanine tetrapeptide conformational analysis. *J. Comput. Chem.*, **28**, 839 (2007).
- [133] S. L. Dixon and P. C. Jurs. Atomic charge calculations for quantitative structure—property relationships. *J. Comput. Chem.*, **13**, 492 (1992).
- [134] C. M. Dobson. Chemical space and biology. *Nature*, **432**, 824 (2004).
- [135] J. F. Dobson. Interpretation of the Fermi hole curvature. *J. Chem. Phys.*, **94**, 4328 (1991).
- [136] J. D. Driskell, S. Shanmukh, Y. Liu, S. B. Chaney, X.-J. Tang, Y.-P. Zhao, and R. A. Dluhy. The use of aligned silver nanorod arrays prepared by oblique angle deposition as surface enhanced Raman scattering substrates. *J. Phys. Chem. C*, **112**, 895 (2008).
- [137] J. D. Dunitz and A. Gavezzotti. How molecules stick together in organic crystals: Weak intermolecular interactions. *Chem. Soc. Rev.*, **38**, 2622 (2009).
- [138] W. Dunn III, D. Scott, and W. Glen. Principal components analysis and partial least squares regression. *Tetrahedron Comput. Methodol.*, **2**, 349 (1989).
- [139] T. Dunning Jr. Gaussian basis sets for use in correlated molecular calculations. I. The atoms boron through neon and hydrogen. *J. Chem. Phys.*, **90**, 1007 (1989).

- [140] H. Ebata, E. Miyazaki, T. Yamamoto, and K. Takimiya. Synthesis, properties, and structures of benzo[1,2-b:4,5-b']bis[b]benzothiophene and benzo[1,2-b:4,5-b']bis[b]benzoselenophene. *Org. Lett.*, **9**, 4499 (2007).
- [141] J. A. Ellman. Design, synthesis, and evaluation of small-molecule libraries. *Acc. Chem. Res.*, **29**, 132 (1996).
- [142] J. Fabian, M. Mann, and M. Petiau. The origin of the color of 1,2-dithiins - interpretation by Kohn-Sham orbitals. *J. Mol. Model.*, **6**, 177 (2000).
- [143] A. Facchetti. π -conjugated polymers for organic electronics and photovoltaic cell applications. *Chem. Mater.*, **23**, 733 (2011).
- [144] R. Farchioni and G. Grosso. *Organic Electronic Materials: Conjugated Polymers and Low Molecular Weight Organic Solids*. Springer, Berlin, 2001.
- [145] K. Fatahalian, J. Sugerman, and P. Hanrahan. Understanding the efficiency of gpu algorithms for matrix-matrix multiplication. In *Proceedings of the ACM SIGGRAPH/EUROGRAPHICS conference on Graphics hardware*, page 133, Grenoble, France, 2004. ACM.
- [146] U. Fechner and G. Schneider. Flux (1): A virtual synthesis scheme for fragment-based *de novo* design. *J. Chem. Inf. Model.*, **46**, 699 (2006).
- [147] M. Feyereisen, G. Fitzgerald, and A. Komornicki. Use of approximate integrals in ab initio theory. An application in MP2 energy calculations. *Chem. Phys. Lett.*, **208**, 359 (1993).
- [148] M. J. Field, P. A. Bash, and M. Karplus. A combined quantum mechanical and molecular mechanical potential for molecular dynamics simulations. *J. Comput. Chem.*, **11**, 700 (1990).
- [149] C. C. Fischer, K. J. Tibbetts, D. Morgan, and G. Ceder. Predicting crystal structure by merging data mining with quantum mechanics. *Nature Mater.*, **5**, 641 (2006).
- [150] M. Fleischmann, P. J. Hendra, and A. J. McQuillan. Raman spectra of pyridine adsorbed at a silver electrode. *Chem. Phys. Lett.*, **26**, 163 (1974).
- [151] J. B. Foresman and A. Frisch. *Exploring Chemistry With Electronic Structure Methods*. Gaussian Inc., Pittsburgh, PA, 2nd edition, 1996.
- [152] S. R. Forrest. The path to ubiquitous and low-cost organic electronic appliances on plastic. *Nature*, **428**, 911 (2004).
- [153] J. P. Foster and F. Weinhold. Natural hybrid orbitals. *J. Am. Chem. Soc.*, **102**, 7211 (1980).
- [154] I. Fourré, B. Silvi, P. Chaquin, and A. Electron localization function comparative study of ground state, triplet state, radical anion, and cation in model carbonyl and imine compounds. *J. Comput. Chem.*, **20**, 897 (1999).

- [155] G. Frenking, I. Antes, M. Böhme, S. Dapprich, A. W. Ehlers, V. Jonas, A. Neuhaus, M. Otto, R. Stegmann, A. Veldkamp, and S. F. Vyboishchikov. Pseudopotential calculations of transition metal compounds: Scope and limitations. In K. B. Lipkowitz and D. B. Boyd, editors, *Reviews in Computational Chemistry*, volume 8, pages 63–144. VCH, New York, 1996.
- [156] M. S. Friedrichs, P. Eastman, V. Vaidyanathan, M. Houston, S. Legrand, A. L. Beberg, D. L. Ensign, C. M. Bruns, and V. S. Pande. Accelerating molecular dynamic simulation on graphics processing units. *J. Comput. Chem.*, **30**, 864 (2009).
- [157] D. P. Fromm, A. Sundaramurthy, A. Kinkhabwala, P. J. Schuck, G. S. Kino, and W. E. Moerner. Exploring the chemical enhancement for surface-enhanced Raman scattering with Au bowtie nanoantennas. *J. Chem. Phys.*, **124**, 61101 (2006).
- [158] R. R. Frontiera, A.-I. Henry, N. L. Gruenke, and R. P. Van Duyne. Surface-enhanced femtosecond stimulated Raman spectroscopy. *J. Phys. Chem. Lett.*, **2**, 1199 (2011).
- [159] T. Fujita, T. Nakano, and S. Tanaka. Fragment molecular orbital calculations under periodic boundary condition. *Chem. Phys. Lett.*, **506**, 112 (2011).
- [160] K. Fukunaga. *Introduction to Statistical Pattern Recognition*. Academic Press, San Diego, 2nd edition, 1990.
- [161] R. Furche and D. Rappoport. Density functional methods for excited states: Equilibrium structure and electronic spectra. In M. Olivucci, editor, *Computational Photochemistry*, pages 93–128. Elsevier, Amsterdam, 2005.
- [162] T. E. Furtak and D. Roy. Nature of the active site in surface-enhanced Raman scattering. *Phys. Rev. Lett.*, **50**, 1301 (1983).
- [163] T. E. Furtak and D. Roy. The short-range mechanism of surface enhanced Raman scattering. *Surf. Sci.*, **158**, 126 (1985).
- [164] F. Fuster, C. Dézarnaud-Dandine, H. Chevreau, and A. Sevin. A theoretical study of the bonding in NO, (NO)₂, (NO)₂⁻ and (NO)₂⁻² using a topological analysis of the electron localization function. *Phys. Chem. Chem. Phys.*, **6**, 3228 (2004).
- [165] F. Fuster, A. Sevin, and B. Silvi. Topological analysis of the electron localization function (ELF) applied to the electrophilic aromatic substitution. *J. Phys. Chem. A*, **104**, 852 (2000).
- [166] M. M. Gaber. *Scientific Data Mining and Knowledge Discovery: Principles and Foundations*. Springer, Berlin, 2009.
- [167] Y. Galagan, I. G. de Vries, A. P. Langen, R. Andriessen, W. J. Verhees, S. C. Veenstra, and J. M. Kroon. Technology development for roll-to-roll production of organic photovoltaics. *Chem. Eng. Process.*, **50**, 454 (2011).
- [168] J. Gasteiger. Chemoinformatics: A new field with a long tradition. *Anal. Bioanal. Chem.*, **384**, 57 (2006).

- [169] R. Gaudiana. Third-generation photovoltaic technology — the potential for low-cost solar energy conversion. *J. Phys. Chem. Lett.*, **1**, 1288 (2010).
- [170] R. Gaudiana and C. Brabec. Organic materials: Fantastic plastic. *Nat. Photonics*, **2**, 287 (2008).
- [171] D. Gendron and M. Leclerc. New conjugated polymers for plastic solar cells. *Energy Environ. Sci.*, **4**, 1225 (2011).
- [172] J. Gersten and A. Nitzan. Electromagnetic theory of enhanced Raman scattering by molecules adsorbed on rough surfaces. *J. Chem. Phys.*, **73**, 3023 (1980).
- [173] A. K. Ghose, T. Herbertz, J. M. Salvino, and J. P. Mallamo. Knowledge-based chemoinformatic approaches to drug discovery. *Drug Discovery Today*, **11**, 1107 (2006).
- [174] J. Gierschner, J. Cornil, and H.-J. Egelhaaf. Optical bandgaps of π -conjugated organic materials at the polymer limit: Experiment and theory. *Adv. Mater.*, **19**, 173 (2007).
- [175] A. T. B. Gilbert, N. A. Besley, and P. M. W. Gill. Self-consistent field calculations of excited states using the maximum overlap method (MOM). *J. Phys. Chem. A*, **112**, 13164 (2008).
- [176] V. J. Gillet. Designing combinatorial libraries optimized on multiple objectives. *Methods Mol. Biol.*, **275**, 335 (2004).
- [177] G. Giri, E. Verploegen, S. C. B. Mannsfeld, S. Atahan-Evrenk, D. H. Kim, S. Y. Lee, H. A. Becerril, A. Aspuru-Guzik, M. F. Toney, and Z. Bao. Tuning charge transport in solution-sheared organic semiconductors using lattice strain. *Nature*, **480**, 504 (2011).
- [178] R. Giro, M. Cyrillo, and D. S. Galvão. Designing conducting polymers using genetic algorithms. *Chem. Phys. Lett.*, **366**, 170 (2002).
- [179] M. Gokhale, J. Cohen, A. Yoo, W. M. Miller, A. Jacob, C. Ulmer, and R. Pearce. Hardware technologies for high-performance data-intensive scientific computing. *Computer*, **41**, 60 (2008).
- [180] C. C. Gonzalez and R. G. Ross. Performance measurement reference conditions for terrestrial photovoltaics. In *Proceedings of the International Solar Energy Society Conference*, pages 1401–1405, 1980.
- [181] A. Gopinath, S. V. Boriskina, B. M. Reinhard, and L. Dal Negro. Deterministic aperiodic arrays of metal nanoparticles for surface-enhanced Raman scattering (SERS). *Org. Electron.*, **17**, 3741 (2009).
- [182] E. M. Gordon, R. W. Barrett, W. J. Dower, S. P. A. Fodor, and M. A. Gallop. Applications of combinatorial technologies to drug discovery. 2. Combinatorial organic synthesis, library screening strategies, and future directions. *J. Med. Chem.*, **37**, 1385 (1994).

- [183] E. M. Gordon, M. A. Gallop, and D. V. Patel. Strategy and tactics in combinatorial organic synthesis. Applications to drug discovery. *Acc. Chem. Res.*, **29**, 144 (1996).
- [184] M. S. Gordon, J. M. Mullin, S. R. Pruitt, L. B. Roskop, L. V. Slipchenko, and J. A. Boatz. Accurate methods for large molecular systems. *J. Phys. Chem. B*, **113**, 9646 (2009).
- [185] I. Gorton, P. Greenfield, A. Szalay, and R. Williams. Data-intensive computing in the 21st century. *Computer*, **41**, 30 (2008).
- [186] N. Govindaraju, J. Gray, R. Kumar, and D. Manocha. Gputerasort: High performance graphics co-processor sorting for large database management. In *Proceedings of the 2006 ACM SIGMOD international conference on Management of data*, page 325, Chicago, IL, USA, 2006. ACM.
- [187] J. Greeley, J. K. Nørskov, and M. Mavrikakis. Electronic structure and catalysis on metal surfaces. *Annu. Rev. Phys. Chem.*, **53**, 319 (2002).
- [188] J. Green. Vibrational spectra of benzene derivatives-III. Anisole, ethylbenzene, phenetole methyl phenyl sulphide and ethyl phenyl sulphide. *Spectrochim. Acta*, **18**, 39 (1962).
- [189] M. A. Green. Third generation photovoltaics: Solar cells for 2020 and beyond. *Physica E*, **14**, 65 (2002).
- [190] R. Green, A. Morpha, A. J. Ferguson, N. Kopidakis, G. Rumbles, and S. E. Shaheen. Performance of bulk heterojunction photovoltaic devices prepared by airbrush spray deposition. *Appl. Phys. Lett.*, **92**, 33301 (2008).
- [191] B. A. Gregg. Excitonic solar cells: The physics and chemistry of organic-based photovoltaics. In L. Marya, editor, *Molecules as Components of Electronic Devices*, chapter 19, pages 243–257. ACS, Washington, DC, 2003.
- [192] B. A. Gregg and M. C. Hanna. Comparing organic to inorganic photovoltaic cells: Theory, experiment, and simulation. *J. Appl. Phys.*, **93**, 3605 (2003).
- [193] P. Gribbon and S. Andreas. High-throughput drug discovery: What can we expect from HTS? *Drug Discovery Today*, **10**, 17 (2005).
- [194] S. Grimme. Semiempirical hybrid density functional with perturbative second-order correlation. *J. Chem. Phys.*, **124**, 034108 (2006).
- [195] R. L. Grossman, C. Kamath, P. Kegelmeyer, V. Kumar, and R. Namburu. *Data Mining for Scientific and Engineering Applications*. Springer, Berlin, 2001.
- [196] C. Gueymard, D. Myers, and K. Emery. Proposed reference irradiance spectra for solar energy systems testing. *Sol. Energy*, **73**, 443 (2002).

- [197] Y. Gui and T. Kuwana. Long optical path length thin-layer spectroelectrochemistry: Quantitation and potential dependence of electroinactive species absorbed on platinum. *J. Electroanal. Chem. Interfacial Electrochem.*, **222**, 321 (1987).
- [198] J. Gummaraju and M. Rosenblum. Stream programming on general-purpose processors. In *Proceedings of the 38th annual IEEE/ACM International Symposium on Microarchitecture*, MICRO 38, pages 343–354, Washington, DC, USA, 2005. IEEE Computer Society.
- [199] G. Guntas, C. Purbeck, and B. Kuhlman. Engineering a protein-protein interface using a computationally designed library. *Proc. Natl. Acad. Sci.*, **107**, 19296 (2010).
- [200] J. Hachmann, J. J. Dorando, M. Avilés, and G. K.-L. Chan. The radical character of the acenes: A density matrix renormalization group study. *J. Chem. Phys.*, **127**, 134309 (2007).
- [201] J. Hachmann, R. Olivares-Amaya, S. Atahan-Evrenk, C. Amador-Bedolla, R. S. Sánchez-Carrera, A. Gold-Parker, L. Vogt, A. M. Brockway, and A. Aspuru-Guzik. The Harvard Clean Energy Project: Large-scale computational screening and design of organic photovoltaics on the World Community Grid. *J. Phys. Chem. Lett.*, **2**, 2241 (2011).
- [202] J. Halls, C. Walsh, N. Greenham, E. Marseglia, R. Friend, S. Moratti, and A. Holmes. Efficient photodiodes from interpenetrating polymer networks. *Nature*, **376**, 498 (1995).
- [203] T. Hamada and T. Iitaka. The Chamomile Scheme: An optimized algorithm for N-body simulations on programmable graphics processing units. *astro-ph/0703100* (2007).
- [204] S. Hamel, P. Duffy, M. E. Casida, and D. R. Salahub. Kohn-Sham orbitals and orbital energies: Fictitious constructs but good approximations all the same. *J. Electron. Spectrosc. Relat. Phenom.*, **123**, 345 (2002).
- [205] A. Hamelin, S. Morin, J. Richer, and J. Lipkowski. Adsorption of pyridine on the (110) face of silver. *J. Electroanal. Chem. Interfacial Electrochem.*, **272**, 241 (1989).
- [206] A. Hamelin, S. Morin, J. Richer, and J. Lipkowski. Adsorption of pyridine on the (311) face of silver. *J. Electroanal. Chem. Interfacial Electrochem.*, **285**, 249 (1990).
- [207] C. Hansch and T. Fujita. p - σ - π analysis. A method for the correlation of biological activity and chemical structure. *J. Am. Chem. Soc.*, **178**, 1616 (1964).
- [208] M. Haranczyk and J. Sethian. Automatic structure analysis in high-throughput characterization of porous materials. *J. Chem. Theory Comput.*, **6**, 3472 (2010).
- [209] M. Harb, F. Rabilloud, D. Simon, A. Rydlo, S. Lecoultré, F. Conus, V. Rodrigues, and C. Félix. Optical absorption of small silver clusters: Ag_n , ($n=4-22$). *J. Chem. Phys.*, **129**, 194108 (2008).

- [210] C. Hättig. Beyond Hartree-Fock: MP2 and coupled-cluster methods for large systems. In J. Grotendorst, S. Blügel, and D. Marx, editors, *Computational Nanoscience: Do It Yourself!*, volume 31, pages 245–278. John von Neumann Institute for Computing, Jülich, 2006.
- [211] G. Hautier, C. Fischer, V. Ehrlicher, A. Jain, and G. Ceder. Data mined ionic substitutions for the discovery of new compounds. *Inorg. Chem.*, **50**, 656 (2011).
- [212] E. Havinga, W. Hovee, and H. Wynberg. A new class of small band gap organic polymer conductors. *Polym. Bull.*, **29**, 119 (1992).
- [213] Y. He and Y. Li. Fullerene derivative acceptors for high performance polymer solar cells. *Phys. Chem. Chem. Phys.*, **13**, 1970 (2011).
- [214] M. Head-Gordon and E. Artacho. Chemistry on the computer. *Phys. Today*, **61**, 58 (2008).
- [215] M. Head-Gordon, A. M. Grana, D. Maurice, and C. A. White. Analysis of electronic transitions as the difference of electron attachment and detachment densities. *J. Phys. Chem.*, **99**, 14261 (1995).
- [216] M. Head-Gordon, J. A. Pople, and M. J. Frisch. MP2 energy evaluation by direct methods. *Chem. Phys. Lett.*, **153**, 503 (1988).
- [217] A. Heeger. Low-cost ‘plastic’ solar cells: A dream becoming a reality. In H. J. Schellnhuber, M. Molina, N. Stern, V. Huber, and S. Kadner, editors, *Global Sustainability — A Nobel Cause*. Cambridge University Press, Cambridge, UK, 2010.
- [218] A. J. Heeger. Semiconducting polymers: The third generation. *Chem. Soc. Rev.*, **39**, 2354 (2010).
- [219] W. J. Hehre, R. Ditchfield, R. F. Stewart, and J. A. Pople. Self-consistent molecular orbital methods. IV. use of Gaussian expansions of Slater-type orbitals. extension to second-row molecules. *J. Chem. Phys.*, **52**, 2769 (1970).
- [220] W. J. Hehre, R. F. Stewart, and J. A. Pople. Self-consistent molecular-orbital methods. I. use of Gaussian expansions of Slater-type atomic orbitals. *J. Chem. Phys.*, **51**, 2657 (1969).
- [221] G. Heimel, I. Salzmann, S. Duhm, and N. Koch. Design of organic semiconductors from molecular electrostatics. *Chem. Mater.*, **23**, 359 (2011).
- [222] T. Helgaker, P. Jørgensen, and J. Olsen. *Molecular Electronic-Structure Theory*. Wiley, Chichester, 2000.
- [223] E. J. Heller. The semiclassical way to molecular spectroscopy. *Acc. Chem. Res.*, **14**, 368 (1981).
- [224] A. Henemann. BIPV: Built-in solar energy. *Renew. Energy Focus*, **9**, 16 (2008).

- [225] P. Heremans, D. Cheyns, and B. P. Rand. Strategies for increasing the efficiency of heterojunction organic solar cells: Material selection and device architecture. *Acc. Chem. Res.*, **42**, 1740 (2009).
- [226] Y. Hida, X. S. Li, and D. H. Bailey. Algorithms for quad-double precision floating point arithmetic. In *ARITH '01: Proceedings of the 15th IEEE Symposium on Computer Arithmetic*, page 155, Washington, DC, USA, 2001. IEEE Computer Society.
- [227] A. Y. Hirakawa and M. Tsuboi. Molecular geometry in an excited electronic state and a preresonance Raman effect. *Science*, **188**, 359 (1975).
- [228] P. Hohenberg and W. Kohn. Inhomogeneous electron gas. *Phys. Rev.*, **136**, B864 (1964).
- [229] H. Houili, J. D. Picon, L. Zuppiroli, and M. N. Bussac. Polarization effects in the channel of an organic field-effect transistor. *J. Appl. Phys.*, **100**, 023702 (2006).
- [230] J. Hummelen, B. Knight, F. LePeq, F. Wudl, J. Yao, and C. Wilkins. Preparation and characterization of fulleroid and methanofullerene derivatives. *J. Org. Chem.*, **60**, 532 (1995).
- [231] G. R. Hutchison, M. A. Ratner, and T. J. Marks. Accurate prediction of band gaps in neutral heterocyclic conjugated polymers. *J. Phys. Chem. A*, **106**, 10596 (2002).
- [232] J. Idrobo, S. Ögüt, and J. Jellinek. Size dependence of the static polarizabilities and absorption spectra of Ag_n ($n=2-8$) clusters. *Phys. Rev. B*, **72**, 085445 (2005).
- [233] J. Idrobo, S. Ögüt, K. Nemeth, J. Jellinek, and R. Ferrando. First-principles isomer-specific absorption spectra of Ag_{11} . *Phys. Rev. B*, **75**, 233411 (2007).
- [234] O. Inganäs, M. Svensson, A. Gadisa, F. Zhang, N. Persson, X. Wang, and M. Andersson. Low bandgap alternating polyfluorene copolymers in plastic photodiodes and solar cells. *Appl. Phys. A*, **79**, 31 (2004).
- [235] W. G. S. Initiative. http://wgsi.org/files/equinoxcommunique_june9_2011.pdf.
- [236] International Energy Agency. *World Energy Outlook 2010*. Organization for Economic Development, 2010.
- [237] N. Isaacs. *Physical Organic Chemistry (2nd Edition)*. Prentice Hall, 1996.
- [238] J. D. Jackson. *Classical Electrodynamics Third Edition*. Wiley, 3 edition, Aug. 1998.
- [239] M. Z. Jacobson and M. A. Delucchi. A plan to power 100 percent of the planet with renewables. *Sci. Am.*, **301**, 58 (2009).
- [240] D. Jacquemin, E. A. Perpète, G. Scalmani, M. J. Frisch, R. Kobayashi, and C. Adamo. Assessment of the efficiency of long-range corrected functionals for some properties of large compounds. *J. Chem. Phys.*, **126**, 144105 (2007).

- [241] D. M. Jaffey and R. J. Madix. Reactivity of sulfur-containing molecules on noble metal surfaces. 4. Benzenethiol on Au(110). *J. Am. Chem. Soc.*, **116**, 3020 (1994).
- [242] A. Jain, G. Hautier, C. J. Moore, S. P. Ong, C. C. Fischer, T. Mueller, K. A. Persson, and G. Ceder. A high-throughput infrastructure for density functional theory calculations. *Comput. Mater. Sci.*, **50**, 2295 (2011).
- [243] M. Jaiswal and R. Menon. Polymer electronic materials: A review of charge transport. *Polym. Int.*, **55**, 1371 (2006).
- [244] D. L. Jeanmaire and R. P. Van Duyne. Surface Raman spectroelectrochemistry Part I. Heterocyclic, aromatic, and aliphatic amines adsorbed on the anodized silver electrode. *J. Electroanal. Chem.*, **84**, 1 (1977).
- [245] S. A. Jenekhe, L. Lu, and M. M. Alam. New conjugated polymers with donor-acceptor architectures: Synthesis and photophysics of carbazole-quinoline and phenothiazine-quinoline copolymers and oligomers exhibiting large intramolecular charge transfer. *Macromolecules*, **34**, 7315 (2001).
- [246] L. Jensen, C. M. Aikens, and G. C. Schatz. Electronic structure methods for studying surface-enhanced Raman scattering. *Chem. Soc. Rev.*, **37**, 1061 (2008).
- [247] L. Jensen, L. L. Zhao, J. Autschbach, and G. C. Schatz. Theory and method for calculating resonance Raman scattering from resonance polarizability derivatives. *J. Chem. Phys.*, **123**, 174110 (2005).
- [248] L. Jensen, L. L. Zhao, and G. C. Schatz. Size-dependence of the enhanced Raman scattering of pyridine adsorbed on Ag_n ($n = 2-8, 20$) clusters. *J. Phys. Chem. C*, **111**, 4756 (2007).
- [249] E. Kaasschieter. Techn. Rep. 86-21, Delft University of Technology, Delft, 1986.
- [250] K. Kalyanasundaram. *Dye-sensitized Solar Cells*. CRC Press, Boca Raton, 2010.
- [251] U. J. Kapasi, S. Rixner, W. J. Dally, B. Khailany, J. H. Ahn, P. Mattson, and J. D. Owens. Programmable stream processors. *Computer*, **36**, 54 (2003).
- [252] S. R. Kass. Zwitterion-dianion complexes and anion-anion clusters with negative dissociation energies. *J. Am. Chem. Soc.*, **127**, 13098 (2005).
- [253] A. Katritzky, M. Kuanar, S. Slavov, C. Hall, M. Karelson, I. Kahn, and D. Dobchev. Quantitative correlation of physical and chemical properties with chemical structure: Utility for prediction. *Chem. Rev.*, **110**, 5714 (2010). cited By (since 1996) 0.
- [254] S. Keinan, M. J. Therien, D. N. Beratan, and W. Yang. Molecular design of porphyrin-based nonlinear optical materials. *J. Phys. Chem. A*, **112**, 12203 (2008).
- [255] B. Kennedy, S. Spaeth, and M. Dickey. Determination of the distance dependence and experimental effects for modified SERS substrates based on self-assembled monolayers formed using alkanethiols. *J. Phys. Chem. B*, **103**, 3640 (1999).

- [256] E. H. Kerns. High throughput physicochemical profiling for drug discovery. *J. Pharm. Sci.*, **90**, 1838 (2001).
- [257] J. Y. Kim, S. H. Kim, H.-H. Lee, K. Lee, W. Ma, X. Gong, and A. J. Heeger. New architecture for high-efficiency polymer photovoltaic cells using solution-based titanium oxide as an optical spacer. *Adv. Mater.*, **18**, 572 (2006).
- [258] M.-S. Kim, B.-G. Kim, and J. Kim. Effective variables to control the fill factor of organic photovoltaic cells. *ACS Appl. Mater. Interfaces*, **1**, 1264 (2009).
- [259] W. Y. Kim, Y. C. Choi, S. K. Min, Y. Cho, and K. S. Kim. Application of quantum chemistry to nanotechnology: electron and spin transport in molecular devices. *Chem. Soc. Rev.*, **38**, 2319 (2009).
- [260] W. Y. Kim and K. S. Kim. Tuning molecular orbitals in molecular electronics and spintronics. *Acc. Chem. Res.*, **43**, 111 (2010).
- [261] C. Kingsford and S. L. Salzberg. What are decision trees? *Nature Biotechnol.*, **26**, 1011 (2008).
- [262] B. Kippelen and J.-L. Brédas. Organic photovoltaics. *Energy Environ. Sci.*, **2**, 251 (2009).
- [263] K. Kitaura, E. Ikeo, T. Asada, T. Nakano, and M. Uebayasi. Fragment molecular orbital method: An approximate computational method for large molecules. *Chem. Phys. Lett.*, **313**, 701 (1999).
- [264] A. Klamt. Conductor-like screening model for real solvents: A new approach to the quantitative calculation of solvation phenomena. *J. Phys. Chem.*, **99**, 2224 (1995).
- [265] A. Klamt and G. Schüürmann. COSMO: A new approach to dielectric screening in solvents with explicit expressions for the screening energy and its gradient. *J. Chem. Soc., Perkin Trans. 2*, pages 799–805 (1993).
- [266] N. Kleinhenz, L. Yang, H. Zhou, S. C. Price, and W. You. Low-band-gap polymers that utilize quinoid resonance structure stabilization by thienothiophene: Fine-tuning of HOMO level. *Macromolecules*, **44**, 872 (2011).
- [267] M. Kline. *Calculus: An intuitive and physical approach*. Dover books on mathematics. Dover, 1998.
- [268] G. Klopman, J.-Y. Li, S. Wang, and M. Dimayuga. Computer automated log P calculations based on an extended group contribution approach. *J. Chem. Inf. Comput. Sci.*, **34**, 752 (1994).
- [269] K. Kneipp, M. Moskovits, and H. Kneipp, editors. *Surface-Enhanced Raman Scattering: Physics and Applications*. Springer, Berlin, New York, 2006.

- [270] K. Kneipp, Y. Wang, H. Kneipp, L. T. Perelman, I. Itzkan, R. R. Dasari, and M. S. Feld. Single molecule detection using surface-enhanced Raman scattering (SERS). *Phys. Rev. Lett.*, **78**, 1667 (1997).
- [271] W. Koch and M. C. Holthausen. *A Chemist's Guide to Density Functional Theory*. Wiley-VCH, Weinheim, 2nd edition, 2001.
- [272] A. Köhler, D. A. dos Santos, D. Beljonne, Z. Shuai, J.-L. Brédas, A. B. Holmes, A. Kraus, K. Müllen, and R. H. Friend. Charge separation in localized and delocalized electronic states in polymeric semiconductors. *Nature*, **392**, 903 (1998).
- [273] W. Kohn and L. Sham. Self-consistent equations including exchange and correlation effects. *Phys. Rev.*, **140**, A1133 (1965).
- [274] F. B. Kooistra, J. Knol, F. Kastenberg, L. M. Popescu, W. J. H. Verhees, J. M. Kroon, and J. C. Hummelen. Increasing the open circuit voltage of bulk-heterojunction solar cells by raising the LUMO level of the acceptor. *Org. Lett.*, **9**, 551 (2007).
- [275] L. J. A. Koster, V. D. Mihailetschi, and P. W. M. Blom. Ultimate efficiency of polymer/fullerene bulk heterojunction solar cells. *Appl. Phys. Lett.*, **88**, 093511 (2006).
- [276] S. E. Krakiwsky, L. E. Turner, and M. M. Okoniewski. Graphics processor unit (GPU) acceleration of finite-difference time-domain (FDTD) algorithm. In *ISCAS (5)*, page 265, 2004.
- [277] F. C. Krebs. *Polymer Photovoltaics: A Practical Approach*. SPIE Publications, Bellingham, WA, 2008.
- [278] F. C. Krebs, T. Tromholt, and M. Jørgensen. Upscaling of polymer solar cell fabrication using full roll-to-roll processing. *Nanoscale*, **2**, 873 (2010).
- [279] C. Kreisbeck, T. Kramer, M. Rodriguez, and B. Hein. High-Performance Solution of Hierarchical Equations of Motion for Studying Energy Transfer in Light-Harvesting Complexes. *Journal of Chemical Theory and Computation*, **7**, 2166 (2011).
- [280] L. Kronik, R. Fromherz, E. Ko, G. Ganteför, and J. R. Chelikowsky. Highest electron affinity as a predictor of cluster anion structures. *Nature Mater.*, **1**, 49 (2002).
- [281] J. Krüger and R. Westermann. Linear algebra operators for GPU implementation of numerical algorithms. In *ACM SIGGRAPH 2005 Courses*, pages 234–242, Los Angeles, California, 2005. ACM.
- [282] M. Kryder and C. S. Kim. After hard drives; what comes next? *IEEE Trans. Magn.*, **45**, 3406 (2009).
- [283] S. Kuhn, G. Mori, M. Agio, and V. Sandoghdar. Modification of single molecule fluorescence close to a nanostructure: Radiation pattern, spontaneous emission and quenching. *Mol. Phys.*, **106**, 893 (2008).

- [284] Y. N. Kukushkin and V. A. Yurinov. Stability of platinum(II) complexes with secondary heterocyclic amines. *Zh. Neorg. Khim.*, **18**, 182 (1973).
- [285] P. S. Kutchukian, D. Lou, and E. I. Shakhnovich. FOG: Fragment Optimized Growth algorithm for the *de novo* generation of molecules occupying druglike chemical space. *J. Chem. Inf. Model.*, **49**, 1630 (2009).
- [286] P. S. Kutchukian and E. I. Shakhnovich. *De novo* design: Balancing novelty and confined chemical space. *Expert Opin. Drug Discovery*, **5**, 789 (2010).
- [287] J. J. Ladik. Recent developments in the quantum theory of organic polymers. *J. Mol. Struct. THEOCHEM*, **230**, 127 (1991).
- [288] E.-W. Lameijer, T. Bäck, J. Kok, and A. D. Ijzerman. Evolutionary algorithms in drug design. *Natural Comput.*, **4**, 177 (2005).
- [289] N. D. Lang and W. Kohn. Theory of metal surfaces: Charge density and surface energy. *Phys. Rev. B*, **1**, 4555 (1970).
- [290] H. P. Langtangen. *Python Scripting for Computational Science*. Springer, Berlin, 3rd edition, 2010.
- [291] R. M. Lazorenko-Manevich. Adatom hypothesis as a predominant mechanism of surface enhanced Raman scattering: A review of experimental argumentation. *Russian Journal of Electrochemistry*, **41**, 799 (2005).
- [292] T. Le Bahers, T. Pauporte, G. Scalmani, C. Adamo, and I. Ciofini. A TD-DFT investigation of ground and excited state properties in indoline dyes used for dye-sensitized solar cells. *Phys. Chem. Chem. Phys.*, **11**, 11276 (2009).
- [293] E. C. Le Ru, B. E., M. Meyer, and P. G. Etchegoin. Surface enhanced Raman scattering enhancement factors: A comprehensive study. *J. Phys. Chem. C*, **111**, 13794 (2007).
- [294] E. C. Le Ru and P. G. Etchegoin. *Principles of Surface-Enhanced Raman Spectroscopy and Related Plasmonic Effects*. Elsevier, Amsterdam; Boston, 2008.
- [295] A. R. Leach and V. Gillet. *An Introduction to Chemoinformatics*. Springer, 2003.
- [296] C. Lee, W. Yang, and R. G. Parr. Development of the Colle-Salvetti correlation-energy formula into a functional of the electron density. *Phys. Rev. B*, **37**, 785 (1988).
- [297] S.-Y. Lee and E. J. Heller. Time-dependent theory of Raman scattering. *J. Chem. Phys.*, **71**, 4777 (1979).
- [298] M. Lenes, G.-J. a. H. Wetzelaer, F. B. Kooistra, S. C. Veenstra, J. C. Hummelen, and P. W. M. Blom. Fullerene bisadducts for enhanced open-circuit voltages and efficiencies in polymer solar cells. *Adv. Mater.*, **20**, 2116 (2008).

- [299] L. W. H. Leung and M. J. Weaver. Extending surface-enhanced Raman spectroscopy to transition-metal surfaces: Carbon monoxide adsorption and electrooxidation on platinum- and palladium-coated gold electrodes. *J. Am. Chem. Soc.*, **109**, 5113 (1987).
- [300] L. W. H. Leung and M. J. Weaver. Adsorption and electrooxidation of carbon monoxide on rhodium- and ruthenium-coated gold electrodes as probed by surface-enhanced Raman spectroscopy. *Langmuir*, **4**, 1076 (1988).
- [301] X. Q. Lewell, D. B. Judd, S. P. Watson, and M. M. Hann. RECAP—retrosynthetic combinatorial analysis procedure: A powerful new technique for identifying privileged molecular fragments with useful applications in combinatorial chemistry. *J. Chem. Inf. Comput. Sci.*, **38**, 511 (1998).
- [302] N. S. Lewis. Toward cost-effective solar energy use. *Science*, **315**, 798 (2007).
- [303] N. S. Lewis and D. G. Nocera. Powering the planet: Chemical challenges in solar energy utilization. *Proc. Natl. Acad. Sci.*, **103**, 15729 (2006).
- [304] X. Li, J. Demmel, D. Bailey, G. Henry, Y. Hida, J. Iskandar, W. Kahan, S. Kang, A. Kapur, M. Martin, B. Thompson, T. Tung, and D. Yoo. Design, implementation and testing of extended and mixed precision BLAS. *ACM T. Math. Software*, **28**, 152 (2002).
- [305] W. Liang, M. P. Shores, M. Bockrath, J. R. Long, and H. Park. Kondo resonance in a single-molecule transistor. *Nature*, **417**, 725 (2002).
- [306] Y. Liang, D. Feng, J. Guo, J. M. Szarko, C. Ray, L. X. Chen, and L. Yu. Regioregular oligomer and polymer containing thieno[3,4- b]thiophene moiety for efficient organic solar cells. *Macromolecules*, **42**, 1091 (2009).
- [307] Y. Liang, D. Feng, Y. Wu, S.-T. Tsai, G. Li, C. Ray, and L. Yu. Highly efficient solar cell polymers developed via fine-tuning of structural and electronic properties. *J. Am. Chem. Soc.*, **131**, 7792 (2009).
- [308] Y. Liang, D. Feng, Y. Wu, S.-T. Tsai, G. Li, C. Ray, and L. Yu. Highly efficient solar cell polymers developed via fine-tuning of structural and electronic properties. *J. Am. Chem. Soc.*, **131**, 7792 (2009).
- [309] Y. Liang, Y. Wu, D. Feng, S.-T. Tsai, H.-J. Son, G. Li, and L. Yu. Development of new semiconducting polymers for high performance solar cells. *J. Am. Chem. Soc.*, **131**, 56 (2009).
- [310] C. A. Lipinski and A. Hopkins. Navigating chemical space for biology and medicine. *Nature*, **432**, 855 (2004).
- [311] C. A. Lipinski, F. Lombardo, B. W. Dominy, and P. J. Feeney. Experimental and computational approaches to estimate solubility and permeability in drug discovery and development settings. *Adv. Drug Del. Rev.*, **46**, 3 (2001).

- [312] J. Liu, I. A. Mikhaylov, J. Zou, I. Osaka, A. E. Masunov, R. D. McCullough, and L. Zhai. Insight into how molecular structures of thiophene-based conjugated polymers affect crystallization behaviors. *Polymer*, **52**, 2302 (2011).
- [313] Y. Liu, J. Fan, Y.-P. Zhao, S. Shanmukh, and R. A. Dluhy. Angle dependent surface enhanced Raman scattering obtained from a Ag nanorod array substrate. *Appl. Phys. Lett.*, **89**, 173134 (2006).
- [314] J. R. Lombardi, R. L. Birke, T. Lu, and J. Xu. Charge-transfer theory of surface enhanced Raman spectroscopy: Herzberg-Teller contributions. *J. Chem. Phys.*, **84**, 4174 (1986).
- [315] D. A. Long. *The Raman Effect*. Wiley, Chichester, 2002.
- [316] M. Loukides. What is data science? In M. Slocum, editor, *Big Data Now: Current Perspectives from O'Reilly Radar*, pages 9–52. O'Reilly Media, 2011.
- [317] P.-O. Löwdin. A note on the quantum-mechanical perturbation theory. *J. Chem. Phys.*, **19**, 1396 (1951).
- [318] P.-O. Löwdin. Correlation problem in many-electron quantum mechanics I. Review of different approaches and discussion of some current ideas. In I. Prigogine, editor, *Advances in Chemical Physics*, volume 2, pages 207–322. John Wiley & Sons, Inc., Hoboken, NJ, 2007.
- [319] N. Luehr, I. S. Ufimtsev, and T. J. Martinez. Dynamic Precision for Electron Repulsion Integral Evaluation on Graphical Processing Units (GPUs). *J. Chem. Theory Comput.*, **7**, 949 (2011).
- [320] J. Luo, Z. Q. Xue, W. M. Liu, J. L. Wu, and Z. Q. Yang. Koopmans' theorem for large molecular systems within density functional theory. *J. Phys. Chem. A*, **110**, 12005 (2006).
- [321] D. J. C. MacKay. *Information Theory, Inference and Learning Algorithms*. Cambridge University Press, 2003.
- [322] G. Madsen, C. Gatti, B. Iversen, L. Damjanovic, G. Stucky, and V. Srdanov. F center in sodium electrosodalite as a physical manifestation of a non-nuclear attractor in the electron density. *Phys. Rev. B*, **59**, 12359 (1999).
- [323] S. A. Maier. *Plasmonics—Fundamentals and Applications*. Springer, New York, 2007.
- [324] N. T. Maitra. Undoing static correlation: Long-range charge transfer in time-dependent density-functional theory. *J. Chem. Phys.*, **122**, 234104 (2005).
- [325] M. Mamada, J. Nishida, D. Kumaki, S. Tokito, and Y. Yamashita. High performance organic field-effect transistors based on [2,2']bi[naphtho[2,3-b]thiophenyl] with a simple structure. *J. Mater. Chem.*, **18**, 3442 (2008).

- [326] M. Manceau, A. Rivaton, J.-L. Gardette, S. Guillerez, and N. Lemaître. Light-induced degradation of the P3HT-based solar cells active layer. *Sol. Energy Mater. Sol. Cells*, **95**, 1315 (2011).
- [327] G. Marsh. BIPV innovation puts spotlight on solar. *Renew. Energy Focus*, **9**, 62 (2008).
- [328] M. Marsman, J. Paier, A. Stroppa, and G. Kresse. Hybrid functionals applied to extended systems. *J. Phys. Condens. Matter*, **20**, 064201 (2008).
- [329] R. L. Martin. Natural transition orbitals. *J. Chem. Phys.*, **118**, 4775 (2003).
- [330] R. M. Martin. *Electronic Structure: Basic Theory and Practical Methods*. Cambridge University Press, Cambridge, 2004.
- [331] T. J. Martinez and S. Patel. <http://cms.mcc.uiuc.edu/wiki/display/mccfiles/findings+2007> (accessed 2007).
- [332] B. V. C. Martins, G. Brunetto, F. Sato, V. R. Coluci, and D. S. Galvão. Designing conducting polymers using bioinspired ant algorithms. *Chem. Phys. Lett.*, **453**, 290 (2008).
- [333] L. Maschio, D. Usvyat, F. R. Manby, S. Casassa, C. Pisani, and M. Schültz. Fast local-MP2 method with density-fitting for crystals. I. Theory and algorithms. *Phys. Rev. B*, **76**, 075101 (2007).
- [334] D. J. Masiello and G. C. Schatz. Many-body theory of surface-enhanced Raman scattering. *Phys. Rev. A*, **78**, 042505 (2008).
- [335] D. J. Masiello and G. C. Schatz. On the linear response and scattering of an interacting molecule-metal system. *J. Chem. Phys.*, **132**, 064102 (2010).
- [336] C. Massobrio, H. Bulou, and C. Goyhenex, editors. *Advances in the Atomic-Scale Modeling of Nanosystems and Nanostructured Materials*, volume 795 of *Lecture Notes in Physics*. Springer, Heidelberg, 2010.
- [337] A. D. McFarland, M. A. Young, J. A. Dieringer, and R. P. Van Duyne. Wavelength-scanned surface-enhanced Raman excitation spectroscopy. *J. Phys. Chem. B*, **109**, 11279 (2005).
- [338] C. McInnes. Virtual screening strategies in drug discovery. *Curr. Opin. Chem. Biol.*, **11**, 494 (2007).
- [339] J. M. McMahon, S. K. Gray, and G. C. Schatz. Nonlocal optical response of metal nanostructures with arbitrary shape. *Phys. Rev. Lett.*, **103**, 097403 (2009).
- [340] J. M. McMahon, S. K. Gray, and G. C. Schatz. Optical properties of nanowire dimers with a spatially nonlocal dielectric function. *Nano Lett.*, **10**, 3473 (2010).

- [341] L. McMurchie and E. Davidson. One- and two-electron integrals over cartesian Gaussian functions. *J. Comput. Phys.*, **26**, 218 (1978).
- [342] R. McWeeny. Separability of quantum systems: A density matrix approach. In J. R. Sabin, M. C. Zerner, E. Brändas, S. Wilson, J. Maruani, Y. G. Smeyers, P. J. Grout, and R. McWeeny, editors, *Advances in Quantum Chemistry*, volume 31, pages 15–35. Academic Press, New York, 1998.
- [343] G. Meller and T. Grasser. *Organic Electronics*. Springer, Berlin, 2009.
- [344] H. Meng, F. Sun, M. Goldfinger, G. Jaycox, Z. Li, W. Marshall, and G. Blackman. High-performance, stable organic thin-film field-effect transistors based on bis-5'-alkylthiophen-2'-yl-2,6-anthracene semiconductors. *J. Am. Chem. Soc.*, **127**, 2406 (2005).
- [345] B. Mennucci. Continuum solvation models: What else can we learn from them? *J. Phys. Chem. Lett.*, **1**, 1666 (2010).
- [346] J. P. Merrick, D. Moran, and L. Radom. An evaluation of harmonic vibrational frequency scale factors. *J. Phys. Chem. A*, **111**, 11683 (2007).
- [347] J.-B. Michel, Y. K. Shen, A. P. Aiden, A. Veres, M. K. Gray, J. P. Pickett, D. Hoiberg, D. Clancy, P. Norvig, J. Orwant, S. Pinker, M. A. Nowak, and E. L. Aiden. Quantitative analysis of culture using millions of digitized books. *Science*, **331**, 176 (2011).
- [348] A. D. Miller, I. Bezel, K. J. Gaffney, S. Garrett-Roe, S. H. Liu, P. Szymanski, and C. B. Harris. Electron solvation in two dimensions. *Science*, **297**, 1163 (2002).
- [349] K. J. Miller and J. Savchik. A new empirical method to calculate average molecular polarizabilities. *J. Am. Chem. Soc.*, **101**, 7206 (1979).
- [350] P. W. Milonni and M.-L. Shih. Casimir forces. *Contemp. Phys.*, **33**, 313 (1992).
- [351] A. Mishra, M. K. R. Fischer, and P. Bäuerle. Metal-free organic dyes for dye-sensitized solar cells: From structure-property relationships to design rules. *Angew. Chem. Int. Ed.*, **48**, 2474 (2009).
- [352] S. Mitra, S. Datta, T. Perkins, and G. Michailidis. *Introduction to Machine Learning and Bioinformatics*. CRC Press, Boca Raton, 2008.
- [353] M. Mitsui, A. Nakajima, K. Kaya, and U. Even. Mass spectra and photoelectron spectroscopy of negatively charged benzene clusters, $(\text{benzene})_n^-$ ($n=53-124$). *J. Chem. Phys.*, **115**, 5707 (2001).
- [354] C. Møller and M. S. Plesset. Note on an approximation treatment for many-electron systems. *Phys. Rev.*, **46**, 618 (1934).
- [355] R. Mondal, N. Miyaki, H. A. Becerril, J. E. Norton, J. Parmer, A. C. Mayer, M. L. Tang, J.-L. Bredas, M. D. McGehee, and Z. Bao. Synthesis of acenaphthyl and phenanthrene based fused-aromatic thienopyrazine co-polymers for photovoltaic and thin film transistor applications. *Chem. Mater.*, **21**, 3618 (2009).

- [356] R. Mondal and A. Sokolow. Personal communication, 2009.
- [357] O. Morton. Solar energy: A new day dawning? Silicon Valley sunrise. *Nature*, **443**, 19 (2006).
- [358] S. M. Morton and L. Jensen. Understanding the molecule-surface chemical coupling in SERS. *J. Am. Chem. Soc.*, **131**, 4090 (2009).
- [359] S. M. Morton, D. W. Silverstein, and L. Jensen. Theoretical studies of plasmonics using electronic structure methods. *Chem. Rev.*, **111**, 3962 (2011).
- [360] M. Moskovits. Surface-enhanced spectroscopy. *Rev. Mod. Phys.*, **57**, 783 (1985).
- [361] M. Moskovits. Surface-enhanced spectroscopy. *Rev. Mod. Phys.*, **57**, 783 (1985).
- [362] M. Moskovits. Surface-enhanced Raman spectroscopy: A brief retrospective. *J. Raman Spectrosc.*, **36**, 485 (2005).
- [363] M. F. Mrozek, S. A. Wasileski, and M. J. Weaver. Periodic trends in electrode-chemisorbate bonding: Benzonitrile on platinum-group and other noble metals as probed by surface-enhanced Raman spectroscopy combined with density functional theory. *J. Am. Chem. Soc.*, **123**, 12817 (2001).
- [364] A. Muñoz-Losa, S. Vukovic, S. Corni, and B. Mennucci. Nonplasmonic metal particles as excitation energy transfer acceptors: An unexpected efficiency revealed by quantum mechanics. *J. Phys. Chem. C*, **113**, 16364 (2009).
- [365] D. Mühlbacher, M. Scharber, M. Morana, Z. Zhu, D. Waller, R. Gaudiana, and C. Brabec. High photovoltaic performance of a low-bandgap polymer. *Adv. Mater.*, **18**, 2884 (2006).
- [366] R. S. Mulliken. Electronic population analysis on LCAO-MO molecular wave functions. I. *J. Chem. Phys.*, **23**, 1833 (1955).
- [367] A. Munshi. OpenCL specification version 1.0, 2008, <http://khronos.org/registry/cl/>.
- [368] K. Nalwa, J. Park, K. Ho, and S. Chaudhary. On realizing higher efficiency polymer solar cells using a textured substrate platform. *Adv. Mater.*, **23**, 112 (2011).
- [369] J. Nara, S. Higai, Y. Morikawa, and T. Ohno. Density functional theory investigation of benzenethiol adsorption on Au(111). *J. Chem. Phys.*, **120**, 6705 (2004).
- [370] J. Nelson. *The Physics of Solar Cells (Properties of Semiconductor Materials)*. Imperial College Press, 2003.
- [371] J. Nelson, J. J. Kwiatkowski, J. Kirkpatrick, and J. M. Frost. Modeling charge transport in organic photovoltaic materials. *Acc. Chem. Res.*, **42**, 1768 (2009).
- [372] J. Nelson, J. J. Kwiatkowski, J. Kirkpatrick, and J. M. Frost. Modeling charge transport in organic photovoltaic materials. *Acc. Chem. Res.*, **42**, 1768 (2009).

- [373] I. Nenner and G. Schulz. Temporary negative ions and electron affinities of benzene and n-heterocyclic molecules: Pyridine, pyridazine, pyrimidine, pyrazine, and s-triazine. *J. Chem. Phys.*, **62**, 1747 (1975).
- [374] NERSC. www.nersc.gov (accessed august 10, 2011).
- [375] H. Neven, V. S. Denchev, G. Rose, and W. G. Macready. Training a binary classifier with the quantum adiabatic algorithm. arXiv:0811.0416, page 11 (2008).
- [376] S. Nie and S. R. Emory. Probing single molecules and single nanoparticles by surface-enhanced Raman scattering. *Science*, **275**, 1102 (1997).
- [377] NIST. NIST Computational Chemistry Comparison and Benchmark Database, NIST Standard Reference Database No 101, Rel. 15a, April 2010, Editor: Russell D. Johnson III, <http://cccbdb.nist.gov/> (accessed August 10, 2011).
- [378] A. Nitzan and M. A. Ratner. Electron transport in molecular wire junctions. *Science*, **300**, 1384 (2003).
- [379] C. Noguez, C. E. Román-Velázquez, R. Esquivel-Sirvent, and C. Villarreal. High-multipolar effects on the Casimir force: The non-retarded limit. *Europhys. Lett.*, **67**, 191 (2004).
- [380] K. Norrod, L. Sudnik, D. Rousell, and K. Rowlen. Quantitative comparison of five SERS substrates: Sensitivity and limit of detection. *Appl. Spectrosc.*, **51**, 994 (1997).
- [381] J. K. Nørskov. Chemisorption on metal surfaces. *Rep. Progr. Phys.*, **53**, 1253 (1990).
- [382] NVIDIA. CUBLAS Library 0.8, <http://developer.download.nvidia.com>.
- [383] NVIDIA. CUBLAS Library 1.0, <http://developer.download.nvidia.com>.
- [384] NVIDIA. CUDA Programming Guide 1.0, <http://developer.download.nvidia.com>.
- [385] NVIDIA. CUDA Programming Guide 2.0, <http://developer.download.nvidia.com>.
- [386] N. M. O’Boyle, C. M. Campbell, and G. R. Hutchison. Computational design and selection of optimal organic photovoltaic materials. *J. Phys. Chem. C*, **115**, 16200 (2011).
- [387] O. Obrezanova, G. Csanyi, J. M. R. Gola, and M. D. Segall. Gaussian processes: A method for automatic QSAR modeling of ADME properties. *J. Chem. Inf. Model.*, **47**, 1847 (2007).
- [388] C. Ochsenfeld, J. Kussmann, and D. Lambrecht. Linear-Scaling Methods in Quantum Chemistry. In K. B. Lipkowitz and T. R. Cundari, editors, *Reviews in Computational Chemistry*, volume 23, pages 1–82. John Wiley & Sons, Hoboken, NJ, USA, 2007.
- [389] T. Okamoto and Z. Bao. Synthesis of solution-soluble pentacene-containing conjugated copolymers. *J. Am. Chem. Soc.*, **129**, 10308 (2007).

- [390] Y. Okiyama, T. Nakano, K. Yamashita, Y. Mochizuki, N. Taguchi, and S. Tanaka. Acceleration of fragment molecular orbital calculations with Cholesky decomposition approach. *Chem. Phys. Lett.*, **490**, 84 (2010).
- [391] R. Olivares-Amaya, C. Amador-Bedolla, J. Hachmann, S. Atahan-Evrenk, R. S. Sánchez-Carrera, L. Vogt, and A. Aspuru-Guzik. Accelerated computational discovery of high-performance materials for organic photovoltaics by means of cheminformatics. *Energy Environ. Sci.*, **4**, 4849 (2011).
- [392] R. Olivares-Amaya, M. Stopa, X. Andrade, M. A. Watson, and A. Aspuru-Guzik. Anion stabilization in electrostatic environments. *J. Phys. Chem. Lett.*, **2**, 682 (2011).
- [393] R. Olivares-Amaya, M. A. Watson, R. G. Edgar, L. Vogt, Y. Shao, and A. Aspuru-Guzik. Accelerating correlated quantum chemistry calculations using graphical processing units and a mixed precision matrix multiplication library. *J. Chem. Theory Comput.*, **6**, 135 (2010).
- [394] R. Olivares-Amaya et al. Combinatorial generation of molecular libraries for organic photovoltaics: Exploring chemical spaces via SMILES and SMARTS. *In Preparation* (2011).
- [395] M. O'Neill and S. M. Kelly. Ordered materials for organic electronics and photonics. *Adv. Mater.*, **23**, 566 (2011).
- [396] Optibrium. StarDrop 5.0, 2011, <http://www.optibrium.com/stardrop/>.
- [397] B. O'Regan and M. Grätzel. A low-cost, high-efficiency solar cell based on dye-sensitized colloidal TiO₂ films. *Nature*, **353**, 737 (1991).
- [398] A. Otto. The chemical (electronic) contribution to surface-enhanced Raman scattering. *J. Raman Spectrosc.*, **36**, 497 (2005).
- [399] A. Otto, I. Mrozek, H. Grabhorn, and W. Akemann. Surface-enhanced Raman scattering. *J. Phys. Cond. Mat.*, **4**, 1143 (1992).
- [400] M. Pagliaro, R. Ciriminna, and G. Palmisano. Flexible solar cells. *ChemSusChem*, **1**, 880 (2008).
- [401] M. Pagliaro, G. Palmisano, and R. Ciriminna. *Flexible Solar Cells*. Wiley-VCH, Weinheim, 2008.
- [402] P. Paoletti, A. Vacca, and D. Arenare. Computer calculation of stepwise stability constants and heat changes from calorimetric data. System silver(i)pyridine. *J. Phys. Chem.*, **70**, 193 (1966).
- [403] S. Park, A. Roy, S. Beaupré, S. Cho, N. Coates, J. Moon, D. Moses, M. Leclerc, K. Lee, and A. Heeger. Bulk heterojunction solar cells with internal quantum efficiency approaching 100%. *Nature Photon.*, **3**, 297 (2009).

- [404] J. Parkhill, D. Rappoport, and A. Aspuru-Guzik. Modeling coherent anti-stokes Raman scattering with time-dependent density functional theory: Vacuum and surface enhancement. *J. Phys. Chem. Lett.*, **2**, 1849 (2011).
- [405] R. Parr and W. Yang. *Density-Functional Theory of Atoms and Molecules*. Oxford University Press, New York, 1989.
- [406] W. Paszkowicz. Genetic algorithms, a nature-inspired tool: Survey of applications in materials science and related fields. *Mater. Manuf. Processes*, **24**, 174 (2009).
- [407] M. J. G. Peach, P. Benfield, T. Helgaker, and D. J. Tozer. Excitation energies in density functional theory: An evaluation and a diagnostic test. *J. Chem. Phys.*, **128**, 044118 (2008).
- [408] M. J. G. Peach, T. Helgaker, P. Salek, T. W. Keal, O. B. Lutnaes, D. J. Tozer, and N. C. Handy. Assessment of a Coulomb-attenuated exchange-correlation energy functional. *Phys. Chem. Chem. Phys.*, **8**, 558 (2006).
- [409] A. Pecchia and A. D. Carlo. Atomistic theory of transport in organic and inorganic nanostructures. *Rep. Progr. Phys.*, **67**, 1497 (2004).
- [410] J. Peet, J. Y. Kim, N. E. Coates, W. L. Ma, D. Moses, a. J. Heeger, and G. C. Bazan. Efficiency enhancement in low-bandgap polymer solar cells by processing with alkane dithiols. *Nature Mater.*, **6**, 497 (2007).
- [411] R. Pennington, T. El-Ghazawi, J. Dongarra, P. Woodard, W. mei Hwu, and D. Post. (super)computing on fpgas, gpus, cell and other exotic architectures: Challenges and opportunities. Panel at Supercomputing 2007, November 2007.
- [412] J. Perdew, K. Burke, and M. Ernzerhof. Generalized gradient approximation made simple. *Phys. Rev. Lett.*, **77**, 3865 (1996). *Phys. Rev. Lett.* **78**, 1396(E) (1997).
- [413] J. P. Perdew. Density-functional approximation for the correlation energy of the inhomogeneous electron gas. *Phys. Rev. B*, **33**, 8822 (1986).
- [414] J. P. Perdew, M. Ernzerhof, and K. Burke. Rationale for mixing exact exchange with density functional approximations. *J. Chem. Phys.*, **105**, 9982 (1996).
- [415] J. P. Perdew, V. N. Staroverov, J. Tao, and G. E. Scuseria. Density functional with full exact exchange, balanced nonlocality of correlation, and constraint satisfaction. *Phys. Rev. A*, **78**, 052513 (2008).
- [416] J. P. Perdew, J. Tao, V. N. Staroverov, and G. E. Scuseria. Meta-generalized gradient approximation: Explanation of a realistic nonempirical density functional. *J. Chem. Phys.*, **120**, 6898 (2004).
- [417] B. N. J. Persson. On the theory of surface-enhanced Raman scattering. *Chem. Phys. Lett.*, **82**, 561 (1981).

- [418] B. N. J. Persson, K. Zhao, and Z. Zhang. Chemical contribution to surface-enhanced Raman scattering. *Phys. Rev. Lett.*, **96**, 207401 (2006).
- [419] C. H. Peters, I. T. Sachs-Quitana, J. P. Kastrop, S. Beaupré, M. Leclerc, and M. D. McGehee. High efficiency polymer solar cells with long operating lifetimes. *Adv. Energy Mater.*, **1**, 491 (2011).
- [420] H. Phillips, A. Prociuk, and B. D. Dunietz. Bias effects on the electronic spectrum of a molecular bridge. *J. Chem. Phys.*, **134**, 054708 (2011).
- [421] J. Poater, M. Duran, M. Solà, and B. Silvi. Theoretical evaluation of electron delocalization in aromatic molecules by means of atoms in molecules (AIM) and electron localization function (ELF) topological approaches. *Chem. Rev.*, **105**, 3911 (2005).
- [422] H. A. Pohl. Theories of electronic behavior in macromolecular solids. *J. Polym. Sci. C: Polym. Symp.*, **17**, 13 (1967).
- [423] T. Pradeep. Noble metal nanoparticles for water purification: A critical review. *Thin Solid Films*, **517**, 6441 (2009).
- [424] S. C. Price, A. C. Stuart, L. Yang, H. Zhou, and W. You. Fluorine substituted conjugated polymer of medium band gap yields 7% efficiency in polymer-fullerene solar cells. *J. Am. Chem. Soc.*, **133**, 4625 (2011).
- [425] S. C. Price, A. C. Stuart, and W. You. Low band gap polymers based on benzo[1,2-*b*:4,5-*b'*]dithiophene: Rational design of polymers leads to high photovoltaic performance. *Macromolecules*, **43**, 4609 (2010).
- [426] A. Pron and P. Rannou. Processible conjugated polymers: From organic semiconductors to organic metals and superconductors. *Prog. Polym. Sci.*, **27**, 135 (2002).
- [427] P. Pulay. Convergence acceleration of iterative sequences. The case of scf iteration. *Chem. Phys. Lett.*, **73**, 393 (1980).
- [428] E. M. Purcell and C. R. Pennypacker. Scattering and absorption of light by nonspherical dielectric grains. *Astrophys. J.*, **186**, 705 (1973).
- [429] R Development Core Team. *R: A Language and Environment for Statistical Computing*. R Foundation for Statistical Computing, Vienna, Austria, 2008.
- [430] K. Rajan. Combinatorial materials sciences: Experimental strategies for accelerated knowledge discovery. *Annu. Rev. Mater. Sci.*, **38**, 299 (2008).
- [431] B. G. Ramsey. A correction to the Hückel localization energy approximation of aromatic substitution rates. *J. Am. Chem. Soc.*, **87**, 2502 (1965).
- [432] D. Rappoport and F. Furche. Lagrangian approach to molecular vibrational Raman intensities using time-dependent hybrid density functional theory. *J. Chem. Phys.*, **126**, 201104 (2007).

- [433] D. Rappoport, S. Shim, and A. Aspuru-Guzik. Simplified sum-over-states approach for predicting resonance raman spectra. Application to nucleic acid bases. *J. Phys. Chem. Lett.*, **2**, 1254 (2011).
- [434] C. E. Rasmussen and C. K. I. Williams. *Gaussian Processes for Machine Learning (Adaptive Computation and Machine Learning series)*. The MIT Press, 2005.
- [435] P. Rebentrost, M. Stopa, and A. Aspuru-Guzik. Förster coupling in nanoparticle excitonic circuits. *Nano Lett.*, **10**, 2849 (2010).
- [436] A. E. Reed, L. A. Curtiss, and F. Weinhold. Intermolecular interactions from a natural bond orbital, donor-acceptor viewpoint. *Chem. Rev.*, **88**, 899 (1988).
- [437] A. E. Reed and F. Weinhold. Natural bond orbital analysis of near-Hartree-Fock water dimer. *J. Chem. Phys.*, **78**, 4066 (1983).
- [438] A. E. Reed and F. Weinhold. Natural localized molecular orbitals. *J. Chem. Phys.*, **83**, 1736 (1985).
- [439] A. E. Reed, R. B. Weinstock, and F. Weinhold. Natural population analysis. *J. Chem. Phys.*, **83**, 735 (1985).
- [440] M. Reed, C. Zhou, C. Muller, T. Burgin, and J. Tour. Conductance of a molecular junction. *Science*, **278**, 252 (1997).
- [441] M. Reyes-Reyes, K. Kim, and D. Carroll. High-efficiency photovoltaic devices based on annealed poly(3-hexylthiophene) and 1-(3-methoxycarbonyl)-propyl-1-phenyl-(6,6)C-61 blends. *Appl. Phys. Lett.*, **87**, 083506 (2005).
- [442] M. Riede, T. Mueller, W. Tress, R. Schueppel, and K. Leo. Small-molecule solar cells — status and perspectives. *Nanotechnology*, **19**, 424001 (2008).
- [443] I. Riedel, E. von Hauff, J. Parisi, N. Martín, F. Giacalone, and V. Dyakonov. Diphenylmethanofullerenes: New and efficient acceptors in bulk-heterojunction solar cells. *Adv. Funct. Mater.*, **15**, 1979 (2005).
- [444] J. Rienstra-Kiracofe, C. Barden, S. Brown, and H. Schaefer III. Electron affinities of polycyclic aromatic hydrocarbons. *J. Phys. Chem. A*, **105**, 524 (2001).
- [445] J. C. Rienstra-Kiracofe, G. S. Tschumper, H. F. Schaefer, S. Nandi, and G. B. Ellison. Atomic and molecular electron affinities: Photoelectron experiments and theoretical computations. *Chem. Rev.*, **102**, 231 (2002).
- [446] C. Risko, M. D. McGehee, and J.-L. Brédas. A quantum-chemical perspective into low optical-gap polymers for highly-efficient organic solar cells. *Chem. Sci.*, **2**, 1200 (2011).
- [447] A. Rivaton, S. Chambon, M. Manceau, J.-L. Gardette, N. Lemaître, and S. Guillerez. Light-induced degradation of the active layer of polymer-based solar cells. *Polym. Degrad. Stab.*, **95**, 278 (2010).

- [448] M. R. Rizhikov, S. G. Kozlova, and S. N. Konchenko. Electron structure of iron chalcogenide clusters Fe₃Q from aim and elf data: Effect of hydrogen atoms on interatomic interactions. *J. Phys. Chem. A*, **113**, 474 (2009).
- [449] J. Roncali. Synthetic principles for bandgap control in linear [π]-conjugated systems. *Chemical Reviews*, **97**, 173 (1997).
- [450] J. Roncali. Molecular engineering of the band gap of π -conjugated systems: Facing technological applications. *Macromolecular Rapid Communications*, **28**, 1761 (2007).
- [451] R. B. Ross, C. M. Cardona, D. M. Guldi, S. G. Sankaranarayanan, M. O. Reese, N. Kopidakis, J. Peet, B. Walker, G. C. Bazan, E. Van Keuren, B. C. Holloway, and M. Drees. Endohedral fullerenes for organic photovoltaic devices. *Nature Mater.*, **8**, 208 (2009).
- [452] F. Ruetter, editor. *Quantum Chemistry Approaches to Chemisorption and Heterogeneous Catalysis*. Kluwer, 1992.
- [453] E. Runge and E. K. U. Gross. Density-functional theory for time-dependent systems. *Phys. Rev. Lett.*, **52**, 997 (1984).
- [454] J. Sadowski, J. Gasteiger, and G. Klebe. Comparison of automatic three-dimensional model builders using 639 X-ray structures. *J. Chem. Inf. Comput. Sci*, **34**, 1000 (1994).
- [455] S. K. Saikin, Y. Chu, D. Rappoport, K. B. Crozier, and A. Aspuru-Guzik. Separation of electromagnetic and chemical contributions to surface-enhanced Raman spectra on nanoengineered plasmonic substrates. *J. Phys. Chem. Lett.*, **1**, 2740 (2010).
- [456] S. K. Saikin, R. Olivares-Amaya, D. Rappoport, M. Stopa, and A. Aspuru-Guzik. On the chemical bonding effects in the Raman response: Benzenethiol adsorbed on silver clusters. *Phys. Chem. Chem. Phys.*, **11**, 9401 (2009).
- [457] E. San-Fabián, A. Guijarro, J. Vergés, G. Chiappe, and E. Louis. PPP hamiltonian for polar polycyclic aromatic hydrocarbons. *Eur. Phys. J. B*, **81**, 253 (2011).
- [458] R. S. Sánchez-Carrera, S. Atahan, J. Schrier, and A. Aspuru-Guzik. Theoretical Characterization of the Air-Stable, High-Mobility Dinaphtho[2,3-b:2'3'-f]thieno[3,2-b]-thiophene Organic Semiconductor. *J. Phys. Chem. C*, **114**, 2334 (2010).
- [459] R. S. Sánchez-Carrera, M. C. R. Delgado, C. C. Ferrón, R. M. Osuna, V. Hernández, J. T. L. Navarrete, and A. Aspuru-Guzik. Optical absorption and emission properties of end-capped oligothienoacenes: A joint theoretical and experimental study. *Org. Electron.*, **11**, 1701 (2010).
- [460] R. S. Sánchez-Carrera, P. Paramonov, G. M. Day, V. Coropceanu, and J.-L. Brédas. Interaction of charge carriers with lattice vibrations in oligoacene crystals from naphthalene to pentacene. *J. Am. Chem. Soc.*, **132**, 14437 (2010).

- [461] A. Sánchez-González, A. Muñoz Losa, S. Vukovic, S. Corni, and B. Mennucci. Quantum mechanical approach to solvent effects on the optical properties of metal nanoparticles and their efficiency as excitation energy transfer acceptors. *J. Phys. Chem. C*, **114**, 1553 (2010).
- [462] J. E. Sanhueza, O. Tapia, W. G. Laidlaw, and M. Trsic. On the application of the variational principle to a type of nonlinear “Schrödinger equation”. *J. Chem. Phys.*, **70**, 3096 (1979).
- [463] A. Savin, A. Becke, J. Flad, and R. Nesper. A new look at electron localization. *Angew. Chem. Int. Ed. Engl.*, **30**, 409 (1991).
- [464] A. Savin, R. Nesper, S. Wengert, and T. F. Fässler. ELF: The electron localization function. *Angew. Chem. Int. Ed. Engl.*, **36**, 1808 (1997).
- [465] A. Schäfer, H. Horn, and R. Ahlrichs. Fully optimized contracted Gaussian basis sets for atoms Li to Kr. *J. Chem. Phys.*, **97**, 2571 (1992).
- [466] M. C. Schalnatz, A. M. Hawkrige, and J. E. Pemberton. Raman Spectroscopy of the Reaction of Thin Films of Solid-State Benzene with Vapor-Deposited Ag, Mg, and Al. *J. Phys. Chem. C*, **115**, 13717 (2011).
- [467] M. C. Scharber, D. Mühlbacher, M. Koppe, P. Denk, C. Waldauf, A. J. Heeger, and C. J. Brabec. Design Rules for Donors in Bulk-Heterojunction Solar Cells—Towards 10% Energy-Conversion Efficiency. *Adv. Mater.*, **18**, 789 (2006).
- [468] G. C. Schatz. Theoretical studies of surface enhanced Raman scattering. *Acc. Chem. Res.*, **17**, 370 (1984).
- [469] G. C. Schatz. Using theory and computation to model nanoscale properties. *Proc. Natl. Acad. Sci.*, **104**, 6885 (2007).
- [470] C. W. Schlenker and M. E. Thompson. The molecular nature of photovoltage losses in organic solar cells. *Chem. Commun.*, **47**, 3702 (2011).
- [471] D. Schnur, B. R. Beno, A. Good, and A. Tebben. Approaches to target class combinatorial library design. *Methods Mol. Biol.*, **275**, 355 (2004).
- [472] G. D. Scholes and G. Rumbles. Excitons in nanoscale systems. *Nature Mater.*, **5**, 683 (2006).
- [473] M. B. Schubert and J. H. Werner. Flexible solar cells for clothing. *Mater. Today*, **9**, 42 (2006).
- [474] A. Schweig, F. Diehl, K. Kesper, and H. Meyer. The electronic spectra of benzo[b]thiote and transient o-thiobenzoquinonemethide. spectral assignments on the basis of the electronic spectra of aniline, thiophenol, thioanisole, all-trans-octatetraene and transient o-xylylene in conjunction with quantum-chemical calculations. *J. Mol. Struct.*, **198**, 307 (1989).

- [475] SCIGPU. scigpu-gemm v0.8, <http://scigpu.org>.
- [476] H. M. Senn and W. Thiel. QM/MM methods for biological systems. In M. Reiher, editor, *Atomistic Approaches in Modern Biology*, volume 268, pages 173–290. Springer, Berlin Heidelberg, 2007.
- [477] J. D. Servaites, M. a. Ratner, and T. J. Marks. Practical efficiency limits in organic photovoltaic cells: Functional dependence of fill factor and external quantum efficiency. *Appl. Phys. Lett.*, **95**, 163302 (2009).
- [478] R. F. Service. Solar energy. Outlook brightens for plastic solar cells. *Science*, **332**, 293 (2011).
- [479] S. E. Shaheen, D. S. Ginley, and G. E. Jabbour. Organic-based photovoltaics: Toward low-cost power generation. *MRS Bull.*, **30**, 10 (2005).
- [480] Y. Shao, L. F. Molnar, Y. Jung, J. Kussmann, C. Ochsenfeld, S. T. Brown, A. T. Gilbert, L. V. Slipchenko, S. V. Levchenko, D. P. O'Neill, R. A. DiStasio Jr, R. C. Lochan, T. Wang, G. J. Beran, N. A. Besley, J. M. Herbert, C. Yeh Lin, T. Van Voorhis, S. Hung Chien, A. Sodt, R. P. Steele, V. A. Rassolov, P. E. Maslen, P. P. Korambath, R. D. Adamson, B. Austin, J. Baker, E. F. C. Byrd, H. Dachsel, R. J. Doerksen, A. Dreuw, B. D. Dunietz, A. D. Dutoi, T. R. Furlani, S. R. Gwaltney, A. Heyden, S. Hirata, C.-P. Hsu, G. Kedziora, R. Z. Khalliulin, P. Klunzinger, A. M. Lee, M. S. Lee, W. Liang, I. Lotan, N. Nair, B. Peters, E. I. Proynov, P. A. Pieniazek, Y. Min Rhee, J. Ritchie, E. Rosta, C. David Sherrill, A. C. Simmonett, J. E. Subotnik, H. Lee Woodcock III, W. Zhang, A. T. Bell, A. K. Chakraborty, D. M. Chipman, F. J. Keil, A. Warshel, W. J. Hehre, H. F. Schaefer III, J. Kong, A. I. Krylov, P. M. W. Gill, and M. Head-Gordon. Advances in methods and algorithms in a modern quantum chemistry program package. *Phys. Chem. Chem. Phys.*, **8**, 3172 (2006).
- [481] C. She, S. Easwaramoorthi, P. Kim, S. Hiroto, I. Hisaki, H. Shinokubo, A. Osuka, D. Kim, and J. T. Hupp. Excess polarizability reveals exciton localization/delocalization controlled by linking positions on porphyrin rings in butadiyne-bridged porphyrin dimers. *J. Phys. Chem. A*, **114**, 3384 (2010).
- [482] W. Shockley and H. J. Queisser. Detailed balance limit of efficiency of p-n junction solar cells. *J. Appl. Phys.*, **32**, 510 (1961).
- [483] V. Shrotriya. Organic photovoltaics: Polymer power. *Nat. Photonics*, **3**, 447 (2009).
- [484] Z. Shuai, L. Wang, and Q. Li. Evaluation of charge mobility in organic materials: From localized to delocalized descriptions at a first-principles level. *Adv. Mater.*, **23**, 1145 (2011).
- [485] B. Silvi and A. Savin. Classification of chemical bonds based on topological analysis of electron localization functions. *Nature*, **371**, 683 (1994).
- [486] J. Simons. Molecular anions. *J. Phys. Chem. A*, **112**, 6401 (2008).

- [487] R. Singh and M. Mishra. Electronic structure analysis and vertical ionization energies of thiophene and ethynylthiophenes. *J. Chem. Sci.*, **121**, 867 (2009).
- [488] A. Slaoui and R. T. Collins. Advanced inorganic photovoltaics. *MRS Bull.*, **32**, 211 (2007).
- [489] L. H. Slooff, S. C. Veenstra, J. M. Kroon, D. J. D. Moet, J. Sweelssen, and M. M. Koetse. Determining the internal quantum efficiency of highly efficient polymer solar cells through optical modeling. *Appl. Phys. Lett.*, **90**, 143506 (2007).
- [490] M. B. Smith and J. Michl. Singlet fission. *Chem. Rev.*, **110**, 6891 (2010).
- [491] A. N. Sokolov, S. Atahan-Evrenk, R. Mondal, H. B. Akkerman, R. S. Sánchez-Carrera, S. Granados-Focil, J. Schrier, S. C. Mannsfeld, A. P. Zoombelt, Z. Bao, and A. Aspuru-Guzik. From computational discovery to experimental characterization of a high hole mobility organic crystal. *Nature Commun.*, **2**, 437 (2011).
- [492] G. C. Solomon, C. Herrmann, T. Hansen, V. Mujica, and M. A. Ratner. Exploring local currents in molecular junctions. *Nature Chem.*, **2**, 223 (2010).
- [493] S. Solomon, D. Qin, M. Manning, Z. Chen, M. Marquis, K. B. Averyt, M. Tignor, and H. L. Miller, editors. *Climate Change 2007 - The Physical Science Basis: Working Group I Contribution to the Fourth Assessment Report of the IPCC*. Cambridge University Press, Cambridge, UK, 2007.
- [494] G. A. Somorjai and Y. Li. *Introduction to Surface Chemistry and Catalysis*. Wiley, Hoboken, NJ, 2nd edition, 2010.
- [495] P. Sonneveld. Techn. Rep. 84-16, Delft University of Technology, Delft, 1986.
- [496] V. Staemmler. Introduction to Hartree-Fock and CI methods. In J. Grotendorst, S. Blügel, and D. Marx, editors, *Computational Nanoscience: Do It Yourself!*, volume 31, pages 1–18. John von Neumann Institute for Computing, Jülich, 2006.
- [497] K. X. Steirer, M. O. Reese, B. L. Rupert, N. Kopidakis, D. C. Olson, R. T. Collins, and D. S. Ginley. Ultrasonic spray deposition for production of organic solar cells. *Sol. Energy Mater. Sol. Cells*, **93**, 447 (2009).
- [498] P. L. Stiles, J. A. Dieringer, N. C. Shah, and R. P. Van Duyne. Surface-enhanced Raman spectroscopy. *Annu. Rev. Anal. Chem.*, **1**, 601 (2008).
- [499] M. Stockman. Electromagnetic theory of SERS. In K. Kneipp, M. Moskovits, and H. Kneipp, editors, *Surface-Enhanced Raman Scattering*, volume 103, chapter 3, pages 47–65. Springer, Berlin Heidelberg, 2006.
- [500] J. E. Stone, D. J. Hardy, I. S. Ufimtsev, and K. Schulten. GPU-accelerated molecular modeling coming of age. *Journal of molecular graphics & modelling*, **29**, 116 (2010).

- [501] J. E. Stone, J. C. Phillips, P. L. Freddolino, D. J. Hardy, L. G. Trabuco, and K. Schulten. Accelerating molecular modeling applications with graphics processors. *J. Comput. Chem.*, **28**, 2618 (2007).
- [502] M. Stopa. Coulomb oscillation amplitudes and semiconductor quantum-dot self-consistent level structure. *Phys. Rev. B*, **48**, 18340 (1993).
- [503] M. Stopa. Quantum dot self-consistent electronic structure and the Coulomb blockade. *Phys. Rev. B*, **54**, 13767 (1996).
- [504] M. Stopa, Y. Aoyagi, and T. Sugano. Multiple-capacitance magnetic-field-dependent Coulomb blockade energetics. *Phys. Rev. B*, **51**, 5494 (1995).
- [505] R. Stowasser and R. Hoffmann. What do the Kohn-Sham orbitals and eigenvalues mean? *J. Am. Chem. Soc.*, **121**, 3414 (1999).
- [506] C. Suh and K. Rajan. Virtual screening and QSAR formulations for crystal chemistry. *QSAR Comb. Sci.*, **24**, 114 (2005).
- [507] C. Suh and K. Rajan. Data mining and informatics for crystal chemistry: Establishing measurement techniques for mapping structure-property relationships. *Mater. Sci. Technol.*, **25**, 466 (2009).
- [508] G. Sun and G. Grundmeier. Surface-enhanced Raman spectroscopy of the growth of ultra-thin organosilicon plasma polymers on nanoporous Ag/SiO₂-bilayer films. *Thin Solid Films*, **515**, 1266 (2006).
- [509] S.-S. Sun and N. S. Sariciftci. *Organic Photovoltaics: Mechanisms, Materials, and Devices*. CRC Press, Boca Raton, 2005.
- [510] R. Susukita, T. Ebisuzaki, B. G. Elmegreen, H. Furusawa, K. Kato, A. Kawai, Y. Kobayashi, T. Koishi, G. D. McNiven, T. Narumi, and K. Yasuoka. Hardware accelerator for molecular dynamics: MDGRAPE-2. *Comput. Phys. Commun.*, **155**, 115 (2003).
- [511] M. Svensson, F. Zhang, S. Veenstra, W. Verhees, J. Hummelen, J. Kroon, O. Inganäs, and M. Andersson. High-Performance Polymer Solar Cells of an Alternating Polyfluorene Copolymer and a Fullerene Derivative. *Adv. Mater.*, **15**, 988 (2003).
- [512] V. J. Sykora and D. E. Leahy. Chemical descriptors library (CDL): A generic, open source software library for chemical informatics. *J. Chem. Inf. Model.*, **48**, 1931 (2008).
- [513] A. Szabo and N. Ostlund. *Modern Quantum Chemistry*. Dover, New York, 1996.
- [514] A. Taflove and S. C. Hagness. *Computational Electrodynamics: The Finite-Difference Time-Domain Method*. Artech House, Norwood, MA, 3rd edition, 2005.
- [515] Talete. Dragon 6, 2011, <http://www.talete.mi.it/index.htm>.

- [516] C. W. Tang. Two-layer organic photovoltaic cell. *Appl. Phys. Lett.*, **48**, 183 (1986).
- [517] J. Tao, J. P. Perdew, V. N. Staroverov, and G. E. Scuseria. Climbing the density functional ladder: Nonempirical meta-generalized gradient approximation designed for molecules and solids. *Phys. Rev. Lett.*, **91**, 146401 (2003).
- [518] D. Tempel, J. Yuen-Zhou, and A. Aspuru-Guzik. Open quantum systems: Density matrix formalism and applications. In M. A. Marques, N. T. Maitra, F. M. S. Nogueira, E. K. U. Gross, and A. Rubio, editors, *Fundamentals of Time-Dependent Density Functional Theory*, volume 837 of *Lecture Notes in Physics*, pages 211–229. Springer Berlin Heidelberg, 2012.
- [519] L. Terfloth and J. Gasteiger. Neural networks and genetic algorithms in drug design. *Drug Discovery Today*, **6**, 102 (2001).
- [520] K. Theisen, B. Smit, and M. Haranczyk. Chemical hieroglyphs: Abstract depiction of complex void space topology of nanoporous materials. *J. Chem. Inf. Model.*, **50**, 461 (2010).
- [521] B. C. Thompson and J. M. J. Frechet. Organic photovoltaics — Polymer-fullerene composite solar cells. *Angew. Chem. Int. Ed.*, **47**, 58 (2008).
- [522] H. Tian, J. Wang, J. Shi, D. Yan, L. Wang, Y. Geng, and F. Wang. Novel thiophene-aryl co-oligomers for organic thin film transistors. *J. Mater. Chem.*, **15**, 3026 (2005).
- [523] Z.-Q. Tian, B. Ren, J.-F. Li, and Z.-L. Yang. Expanding generality of surface-enhanced Raman spectroscopy with borrowing SERS activity strategy. *Chem. Commun.*, pages 3514–3534 (2007).
- [524] Z. Q. Tian, B. Ren, and B. W. Mao. Extending surface Raman spectroscopy to transition metal surfaces for practical applications. 1. Vibrational properties of thiocyanate and carbon monoxide adsorbed on electrochemically activated platinum surfaces. *J. Phys. Chem. B*, **101**, 1338 (1997).
- [525] Z.-Q. Tian, B. Ren, and D.-Y. Wu. Surface-enhanced Raman scattering: From noble to transition metals and from rough surfaces to ordered nanostructures. *J. Phys. Chem. B*, **106**, 9463 (2002).
- [526] Z.-Q. Tian, Z.-L. Yang, B. Ren, J.-F. Li, Y. Zhang, X.-F. Lin, J.-W. Hu, and D.-Y. Wu. Surface-enhanced Raman scattering from transition metals with special surface morphology and nanoparticle shape. *Faraday Discuss.*, **132**, 159 (2006).
- [527] Z.-Q. Tian, Z.-L. Yang, B. Ren, and D.-Y. Wu. SERS from transition metals and excited by ultraviolet light. In K. Kneipp, M. Moskovits, and H. Kneipp, editors, *Surface-Enhanced Raman Scattering — Physics and Applications*, volume 103 of *Topics Appl. Phys.*, pages 125–146. Springer, Berlin, Heidelberg, 2006.
- [528] D. Tilman, K. G. Cassman, P. A. Matson, R. Naylor, and S. Polasky. Agricultural sustainability and intensive production practices. *Nature*, **418**, 671 (2002).

- [529] R. Tipnis, J. Bernkopf, S. Jia, J. Krieg, S. Li, M. Storch, and D. Laird. Large-area organic photovoltaic module – fabrication and performance. *Sol. Energy Mater. Sol. Cells*, **93**, 442 (2009).
- [530] R. Todeschini and V. Consonni. *Handbook of Molecular Descriptors*. Wiley-VCH, Weinheim, 2002.
- [531] J. Tomasi, B. Mennucci, and R. Cammi. Quantum mechanical continuum solvation models. *Chem. Rev.*, **105**, 2999 (2005).
- [532] J. Tomasi and M. Persico. Molecular interactions in solution: An overview of methods based on continuous distributions of the solvent. *Chem. Rev.*, **94**, 2027 (1994).
- [533] T. Trevethan, A. Shluger, and L. Kantorovich. Modelling components of future molecular devices. *J. Phys. Condens. Matter*, **22**, 084024 (2010).
- [534] A. Troisi. Charge transport in high mobility molecular semiconductors: Classical models and new theories. *Chem. Soc. Rev.*, **40**, 2347 (2011).
- [535] N. Troullier and J. Martins. Efficient pseudopotentials for plane-wave calculations. *Phys. Rev. B*, **43**, 1993 (1991).
- [536] M. Tsutsui, M. Taniguchi, K. Yokota, and T. Kawai. Identifying single nucleotides by tunnelling current. *Nature. Nanotech.*, **5**, 286 (2010).
- [537] TURBOMOLE GmbH. TURBOMOLE V5.10 2008, a development of University of Karlsruhe and Forschungszentrum Karlsruhe GmbH, 1989-2007, TURBOMOLE GmbH, since 2007; available from <http://www.turbomole.com>.
- [538] I. S. Ufimtsev and T. J. Martinez. Graphical processing units for quantum chemistry. *Comput. Sci. Eng.*, **10**, 26 (2008).
- [539] I. S. Ufimtsev and T. J. Martinez. Quantum chemistry on graphical processing units. 1. Strategies for two-electron integral evaluation. *J. Chem. Theory Comput.*, **4**, 222 (2008).
- [540] I. S. Ufimtsev and T. J. Martinez. Quantum chemistry on graphical processing units. 2. Direct self-consistent-field implementation. *J. Chem. Theory Comput.*, **5**, 1004 (2009).
- [541] I. S. Ufimtsev and T. J. Martinez. Quantum chemistry on graphical processing units. 3. Analytical energy gradients, geometry optimization, and first principles molecular dynamics. *J. Chem. Theory Comput.*, **5**, 2619 (2009).
- [542] D. Vak, S. Kim, J. Jo, S. Oh, S. Na, J. Kim, and D. Kim. Fabrication of organic bulk heterojunction solar cells by a spray deposition method for low-cost power generation. *Appl. Phys. Lett.*, **91**, 081102 (2007).
- [543] C. Van Caillie and R. D. Amos. Raman intensities using time dependent density functional theory. *Phys. Chem. Chem. Phys.*, **2**, 2123 (2000).

- [544] C. Van Caillie and R. D. Amos. Static and dynamic polarisabilities, Cauchy coefficients and their anisotropies: An evaluation of DFT functionals. *Chem. Phys. Lett.*, **328**, 446 (2000).
- [545] M. W. van der Kamp, R. D. Schaeffer, A. L. Jonsson, A. D. Scouras, A. M. Simms, R. D. Toofanny, N. C. Benson, P. C. Anderson, E. D. Merkley, S. Rysavy, D. Bromley, D. A. C. Beck, and V. Daggett. Dynameomics: A comprehensive database of protein dynamics. *Structure*, **18**, 423 (2010).
- [546] P. T. van Duijnen and M. Swart. Molecular and atomic polarizabilities: Thole's model revisited. *J. Phys. Chem. A*, **102**, 2399 (1998).
- [547] R. P. Van Duyne and J. P. Haushalter. Surface-enhanced Raman spectroscopy of adsorbates on semiconductor electrode surfaces: tris(bipyridine)ruthenium(II) adsorbed on silver-modified n-gallium arsenide(100). *J. Phys. Chem.*, **87**, 2999 (1983).
- [548] H. Van Mullekom, J. Vekemans, E. Havinga, and E. Meijer. Developments in the chemistry and band gap engineering of donor-acceptor substituted conjugated polymers 1. *Mater. Sci. Eng. R*, **32**, 1 (2001).
- [549] J. A. Vergés, E. San-Fabián, G. Chiappe, and E. Louis. Fit of Pariser-Parr-Pople and Hubbard model Hamiltonians to charge and spin states of polycyclic aromatic hydrocarbons. *Phys. Rev. B*, **81**, 085120 (2010).
- [550] B. O. Villoutreix, R. Eudes, and M. A. Miteva. Structure-Based Virtual Ligand Screening: Recent Success Stories. *Comb. Chem. High Throughput Screening*, **12**, 1000 (2009).
- [551] V. N. Viswanadhan, A. K. Ghose, G. R. Revankar, and R. K. Robins. Atomic physicochemical parameters for three dimensional structure directed quantitative structure-activity relationships. 4. Additional parameters for hydrophobic and dispersive interactions and their application for an automated superposition of certain naturally occurring nucleoside antibiotics. *J. Chem. Inf. Comput. Sci*, **29**, 163 (1989).
- [552] L. Vogt, R. Olivares-Amaya, S. Kermes, Y. Shao, C. Amador-Bedolla, and A. Aspuru-Guzik. Accelerating resolution-of-the-identity second-order Møller-Plesset quantum chemistry calculations with graphical processing units. *J. Phys. Chem. A*, **112**, 2049 (2008).
- [553] T. Vosgröne and A. J. Meixner. Surface- and resonance-enhanced micro-Raman spectroscopy of xanthene dyes: From the ensemble to single molecules. *ChemPhysChem*, **6**, 154 (2005).
- [554] S. Vukovic, S. Corni, and B. Mennucci. Fluorescence enhancement of chromophores close to metal nanoparticles. optimal setup revealed by the polarizable continuum model. *J. Phys. Chem. C*, **113**, 121 (2009).
- [555] V. P. Vysotskiy and L. S. Cederbaum. Accurate Quantum Chemistry in Single Precision Arithmetic: Correlation Energy. *J. Chem. Theory Comput.*, **7**, 320 (2011).

- [556] B. Walker, C. Kim, and T.-Q. Nguyen. Small molecule solution-processed bulk heterojunction solar cells. *Chem. Mater.*, **23**, 470 (2011).
- [557] C. Walter. Kryder's Law. *Sci. Am.*, **293**, 32 (2005).
- [558] E. Wang, L. Wang, L. Lan, C. Luo, W. Zhuang, J. Peng, and Y. Cao. High-performance polymer heterojunction solar cells of a polysilafuorene derivative. *Appl. Phys. Lett.*, **92**, 033307 (2008).
- [559] L. Wang, Q. Li, Z. Shuai, L. Chen, and Q. Shi. Multiscale study of charge mobility of organic semiconductor with dynamic disorders. *Phys. Chem. Chem. Phys.*, **12**, 3309 (2010).
- [560] L. Wang, G. Nan, X. Yang, Q. Peng, Q. Li, and Z. Shuai. Computational methods for design of organic materials with high charge mobility. *Chem. Soc. Rev.*, **39**, 423 (2010).
- [561] M. Wang, X. Hu, D. N. Beratan, and W. Yang. Designing molecules by optimizing potentials. *J. Am. Chem. Soc.*, **128**, 3228 (2006).
- [562] X. Wang, W. Shi, G. She, and L. Mu. Using Si and Ge nanostructures as substrates for surface-enhanced Raman scattering based on photoinduced charge transfer mechanism. *J. Am. Chem. Soc.*, **133**, 16518 (2011).
- [563] X. Wang, W. Shi, G. She, and L. Mu. Surface-Enhanced Raman Scattering (SERS) on transition metal and semiconductor nanostructures. *Phys. Chem. Chem. Phys.* (2012).
- [564] D. R. Ward, N. J. Halas, J. W. Ciszek, J. M. Tour, Y. Wu, P. Nordlander, and D. Natelson. Simultaneous measurements of electronic conduction and Raman response in molecular junctions. *Nano Lett.*, **8**, 919 (2008).
- [565] A. Warshel and M. Levitt. Theoretical studies of enzymic reactions: Dielectric, electrostatic and steric stabilization of the carbonium ion in the reaction of lysozyme. *J. Mol. Biol.*, **103**, 227 (1976).
- [566] S. Wasileski, S. Zou, and M. Weaver. Surface-enhanced Raman scattering from substrates with conducting or insulator overlayers: Electromagnetic model predictions and comparisons with experiment. *Appl. Spectrosc.*, **54**, 761 (2000).
- [567] M. Watson, R. Olivares-Amaya, R. G. Edgar, and A. Aspuru-Guzik. Accelerating correlated quantum chemistry calculations using graphical processing units. *Comput. Sci. Eng.*, **12**, 40 (2010).
- [568] M. A. Watson, Y. Kurashige, T. Nakajima, and K. Hirao. Linear-scaling multipole-accelerated Gaussian and finite-element Coulomb method. *J. Chem. Phys.*, **128**, 054105 (2008).

- [569] M. A. Watson, D. Rappoport, E. M. Y. Lee, R. Olivares-Amaya, and A. Aspuru-Guzik. Electronic structure calculations in arbitrary electrostatic environments. *J. Chem. Phys.*, **136**, 024101 (2012).
- [570] M. Weaver, S. Zou, and H. Y. H. Chan. The new interfacial ubiquity of surface-enhanced Raman spectroscopy. *Anal. Chem.*, **72**, 38A (2000).
- [571] F. Weigend and R. Ahlrichs. Balanced basis sets of split valence, triple zeta valence and quadruple zeta valence quality for H to Rn: Design and assessment of accuracy. *Phys. Chem. Chem. Phys.*, **7**, 3297 (2005).
- [572] F. Weigend, M. Häser, H. Patzelt, and R. Ahlrichs. RI-MP2: Optimized auxiliary basis sets and demonstration of efficiency. *Chem. Phys. Lett.*, **294**, 143 (1998).
- [573] F. Weigend, A. Köhn, and C. Hättig. Efficient use of the correlation consistent basis sets in resolution of the identity MP2 calculations. *J. Chem. Phys.*, **116**, 3175 (2002).
- [574] D. Weininger. SMILES, a chemical language and information system. 1. Introduction to methodology and encoding rules. *J. Chem. Inf. Comput. Sci.*, **28**, 31 (1988).
- [575] G. C. Welch, L. A. Perez, C. V. Hoven, Y. Zhang, X.-D. Dang, A. Sharenko, M. F. Toney, E. J. Kramer, T.-Q. Nguyen, and G. C. Bazan. A modular molecular framework for utility in small-molecule solution-processed organic photovoltaic devices. *J. Mater. Chem.*, **21**, 12700 (2011).
- [576] H. J. Werner and F. R. Manby. Explicitly correlated second-order perturbation theory using density fitting and local approximations. *J. Chem. Phys.*, **124**, 054114 (2006).
- [577] H.-J. Werner, F. R. Manby, and P. J. Knowles. Fast linear scaling second-order Møller-Plesset perturbation theory (MP2) using local and density fitting approximations. *J. Chem. Phys.*, **118**, 8149 (2003).
- [578] C. M. Whelan, C. J. Barnes, C. G. H. Walker, and N. M. D. Brown. Benzenethiol adsorption on Au(111) studied by synchrotron ARUPS, HREELS and XPS. *Surf. Sci.*, **425**, 195 (1999).
- [579] K. B. Wiberg and P. R. Rablen. Comparison of atomic charges derived via different procedures. *J. Comp. Chem.*, **14**, 1504 (1993).
- [580] K. A. Willets. Surface-enhanced Raman scattering (SERS) for probing internal cellular structure and dynamics. *Analytical and bioanalytical chemistry*, **394**, 85 (2009).
- [581] J. H. Williams. The molecular electric quadrupole moment and solid-state architecture. *Acc. Chem. Res.*, **26**, 593 (1993).
- [582] E. B. Wilson. The normal modes and frequencies of vibration of the regular plane hexagon model of the benzene molecule. *Phys. Rev.*, **45**, 706 (1934).

- [583] E. B. Wilson, J. Decius, and P. C. Cross. *Molecular Vibrations: The Theory of Infrared and Raman Vibrational Spectra (Dover Books on Chemistry)*. Dover Publications, 1980.
- [584] D. Wöhrle and D. Meissner. Organic solar cells. *Adv. Mater.*, **3**, 129 (1991).
- [585] R. A. Wolkow and M. Moskovits. Enhanced photochemistry on silver surfaces. *J. Chem. Phys.*, **87**, 5858 (1987).
- [586] World Community Grid. www.worldcommunitygrid.org (accessed August 10, 2011).
- [587] D.-Y. Wu, B. Ren, X. Xu, G.-K. Liu, Z.-L. Yang, and Z.-Q. Tian. Periodic trends in the bonding and vibrational coupling: Pyridine interacting with transition metals and noble metals studied by surface-enhanced Raman spectroscopy and density-functional theory. *J. Chem. Phys.*, **119**, 1701 (2003).
- [588] Q. Wu and T. Van Voorhis. Constrained density functional theory and its application in long-range electron transfer. *J. Chem. Theory Comput.*, **2**, 765 (2006).
- [589] S. Xiao, S. C. Price, H. Zhou, and W. You. Recent progress on highly efficient bulk heterojunction polymer solar cells. In W. Qing and Z. Lei, editors, *Functional Polymer Nanocomposites for Energy Storage and Conversion*, chapter 7, pages 71–80. ACS, Washington, DC, 2010.
- [590] T. Xu and Q. Qiao. Conjugated polymer-inorganic semiconductor hybrid solar cells. *Energy Environ. Sci.* (2011).
- [591] L. Xue and J. Bajorath. Molecular descriptors in chemoinformatics, computational combinatorial chemistry, and virtual screening. *Comb. Chem. High Throughput Screening*, **3**, 363 (2000).
- [592] L. Yang, H. Zhou, and W. You. Quantitatively analyzing the influence of side chains on photovoltaic properties of polymer- fullerene solar cells. *J. Phys. Chem. C*, **114**, 16793 (2010).
- [593] W. Yang, J. Hulteen, G. Schatz, and R. Van Duyne. A surface-enhanced hyper-Raman and surface-enhanced Raman scattering study of trans-1,2-bis(4-pyridyl)ethylene adsorbed onto silver film over nanosphere electrodes. Vibrational assignments: Experiment and theory. *J. Chem. Phys.*, **104**, 4313 (1996).
- [594] W.-H. Yang, G. C. Schatz, and R. P. Van Duyne. Discrete dipole approximation for calculating extinction and Raman intensities for small particles with arbitrary shapes. *The Journal of Chemical Physics*, **103**, 869 (1995).
- [595] Z. R. Yang. *Machine Learning Approaches to Bioinformatics*. World Scientific, Singapore, 2010.
- [596] K. Yasuda. Accelerating density functional calculations with graphics processing unit. *J. Chem. Theory Comput.*, **4**, 1230 (2008).

- [597] K. Yasuda. Two-electron integral evaluation on the graphics processor unit. *J. Comput. Chem.*, **29**, 334 (2008).
- [598] K. Yee. Numerical solution of initial boundary value problems involving maxwell's equations in isotropic media. *IEEE Trans. Antennas Propag.*, **14**, 302 (1966).
- [599] R. H. Young and J. J. Fitzgerald. Dipole moments of hole-transporting materials and their influence on hole mobility in molecularly doped polymers. *J. Phys. Chem.*, **99**, 4230 (1995).
- [600] G. Yu, J. Gao, J. Hummelen, F. Wudl, and A. Heeger. Polymer photovoltaic cells: Enhanced efficiencies via a network of internal donor-acceptor heterojunctions. *Science*, **270**, 1789 (1995).
- [601] G. Yu and A. J. Heeger. Charge separation and photovoltaic conversion in polymer composites with internal donor/acceptor heterojunctions. *J. Appl. Phys.*, **78**, 4510 (1995).
- [602] J. Yuen-Zhou, D. G. Tempel, C. A. Rodríguez-Rosario, and A. Aspuru-Guzik. Time-dependent density functional theory for open quantum systems with unitary propagation. *Phys. Rev. Lett.*, **104**, 043001 (2010).
- [603] S. S. Zade and M. Bendikov. From oligomers to polymer: Convergence in the HOMO-LUMO gaps of conjugated oligomers. *Org. Lett.*, **8**, 5243 (2006).
- [604] S. S. Zade, N. Zamoshchik, and M. Bendikov. From short conjugated oligomers to conjugated polymers. Lessons from studies on long conjugated oligomers. *Acc. Chem. Res.*, **44**, 14 (2011).
- [605] V. M. Zamarion, R. A. Timm, K. Araki, and H. E. Toma. Ultrasensitive SERS nanoprobe for hazardous metal ions based on trimercaptotriazine-modified gold nanoparticles. *Inorg. Chem.*, **47**, 2934 (2008).
- [606] A. T. Zayak, Y. S. Hu, H. Choo, J. Bokor, S. Cabrini, P. J. Schuck, and J. B. Neaton. Chemical Raman enhancement of organic adsorbates on metal surfaces. *Phys. Rev. Lett.*, **106**, 083003 (2011).
- [607] P. Zelenay and L. Rice-Jackson. Adsorption of pyridine on polycrystalline gold electrode studied by radioactive-labeling method. *Langmuir*, **6**, 974 (1990).
- [608] C.-G. Zhan, J. A. Nichols, and D. A. Dixon. Ionization potential, electron affinity, electronegativity, hardness, and electron excitation energy: Molecular properties from density functional theory orbital energies. *J. Phys. Chem. A*, **107**, 4184 (2003).
- [609] X. Zhan and D. Zhu. Conjugated polymers for high-efficiency organic photovoltaics. *Polym. Chem.*, **1**, 409 (2010).
- [610] G. Zhang and C. B. Musgrave. Comparison of DFT methods for molecular orbital eigenvalue calculations. *J. Phys. Chem. A*, **111**, 1554 (2007).

- [611] Q. Zhang and M. James. Alternating donor/acceptor repeat units in polythiophenes. intramolecular charge transfer for reducing band gaps in fully substituted conjugated polymers. *J. Am. Chem. Soc.*, **120**, 5355 (1998).
- [612] X. Zhang, N. C. Shah, and R. P. Van Duyne. Sensitive and selective chem/bio sensing based on surface-enhanced Raman spectroscopy (SERS). *Vib. Spectrosc.*, **42**, 2 (2006).
- [613] Y. Zhang and W. Yang. Comment on “generalized gradient approximation made simple”. *Phys. Rev. Lett.*, **80**, 890 (1998).
- [614] J. Zhao, J. A. Dieringer, X. Zhang, G. C. Schatz, and R. P. Van Duyne. Wavelength-scanned surface-enhanced resonance Raman excitation spectroscopy. *J. Phys. Chem. C*, **112**, 19302 (2008).
- [615] J. Zhao, A. Wang, M. A. Green, and F. Ferrazza. 19.8% efficient “honeycomb” textured multicrystalline and 24.4% monocrystalline silicon solar cells. *Appl. Phys. Lett.*, **73**, 1991 (1998).
- [616] L. Zhao, L. Jensen, and G. C. Schatz. Pyridine-Ag₂₀ cluster: A model system for studying surface-enhanced Raman scattering. *J. Am. Chem. Soc.*, **128**, 2911 (2006).
- [617] Y. Zhao and D. G. Truhlar. Density functionals with broad applicability in chemistry. *Acc. Chem. Res.*, **41**, 157 (2008).
- [618] Y. Zhao and D. G. Truhlar. The M06 suite of density functionals for main group thermochemistry, thermochemical kinetics, noncovalent interactions, excited states, and transition elements: Two new functionals and systematic testing of four m06 functionals and twelve other functionals. *Theor. Chem. Acc.*, **120**, 215 (2008).
- [619] H. Zhou, L. Yang, S. C. Price, K. J. Knight, and W. You. Enhanced photovoltaic performance of low-bandgap polymers with deep lumo levels. *Angew. Chem. Int. Ed.*, **49**, 7992 (2010).
- [620] H. Zhou, L. Yang, S. Stoneking, and W. You. A weak donor-strong acceptor strategy to design ideal polymers for organic solar cells. *ACS Appl. Mater. Interfaces*, **2**, 1377 (2010).
- [621] H. Zhou, L. Yang, A. C. Stuart, S. C. Price, S. Liu, and W. You. Development of fluorinated benzothiadiazole as a structural unit for a polymer solar cell of 7% efficiency. *Angew. Chem. Int. Ed. Engl.*, **50**, 2995 (2011).
- [622] X.-Y. Zhu, Q. Yang, and M. Muntwiler. Charge-transfer excitons at organic semiconductor surfaces and interfaces. *Acc. Chem. Res.*, **42**, 1779 (2009).
- [623] S. Zou and M. J. Weaver. Surface-enhanced Raman scattering on uniform transition-metal films: Toward a versatile adsorbate vibrational strategy for solid-nonvacuum interfaces? *Anal. Chem.*, **70**, 2387 (1998).

-
- [624] S. Zou, M. J. Weaver, X. Q. Li, B. Ren, and Z. Q. Tian. New strategies for surface-enhanced Raman scattering at transition-metal interfaces: Thickness-dependent characteristics of electrodeposited Pt-group films on gold and carbon. *J. Phys. Chem. B*, **103**, 4218 (1999).
- [625] S. Zou, M. J. Weaver, X. Q. Li, B. Ren, and Z. Q. Tian. New strategies for surface-enhanced Raman scattering at transition-metal interfaces: thickness-dependent characteristics of electrodeposited Pt-group films on gold and carbon. *J. Phys. Chem. B*, **103**, 4218 (1999).
- [626] S. Zou, C. T. Williams, E. K.-Y. Chen, and M. J. Weaver. Probing molecular vibrations at catalytically significant interfaces: A new ubiquity of surface-enhanced Raman scattering. *J. Am. Chem. Soc.*, **120**, 3811 (1998).
- [627] K. Zweibel, J. Mason, and V. Fthenakis. A solar grand plan. *Sci. Am.*, **298**, 64 (2008).